Investigations on the effect of thermal history, particle size and SHI irradiation on some physical properties of Y^{3+}-substituted YIG

THESIS

Submitted to the

Saurashtra University, Rajkot, India

For the Degree of

Doctor of Philosophy

in Science

in the subject of Physics

By

Pooja U. Sharma

Under the supervision of

Dr. Kunal B. Modi

Assistant Professor

Department of Physics

Saursashtra University

Rajkot,(Gujarat)

June 2009

STATEMENT UNDER O. Ph.D. 7 OF THE SAURASHTRA UNIVERSITY

This is to certify that the work presented in the thesis is my own work, carried out under the supervision of Dr. Kunal B. Modi and leads to some important contributions in Physics supported by necessary references.

Date: 09/06/09 **Pooja U. Sharma**

Place: Rajkot (Research Scholar)

This is to certify that the work submitted for Ph.D. degree in Physics to Saurashtra University, Rajkot by Ms. Pooja U. Sharma has been the result of more than four years of work under my supervision and is a valuable contribution in the field of Solid State Physics and Materials Science.

Date: 09/06/09 **Dr. Kunal B. Modi**

Place: Rajkot

Assistant Professor
Department of Physics
Saurashtra University
Rajkot

Acknowledgement

Finally the day has come when flight of my ambitions is ready to take off with the blessings of God. First of all, I bow my head before almighty for his endless blessings and giving me patience, encouragement and strength to achieve this academic milestone.

With great pleasure, I take this opportunity to put on record my gratitude to all those who have helped me during the tenure of my Ph.D Work.

My first and largest dept is to my mother Mrs. Santosh Sharma, my father Dr. Uttam Prakash Sharma and my brother Mr. Ankur Sharma for their efforts in supporting me throughout my life with all the hardships they have faced for me. My words dry up to sum up the unconditional love, advice, care and emotional support given by my maternal Grandfather Mr. Rishikumar Mudgal, my grandmother Mrs. Shakuntla Mudgal and my brother Mr. Deepak Mudgal during entire duration of my course. My heartfelt regards to my parents, Grandparents and all my family members without whom this day would not have been possible.

This is the most appropriate time to put in words my hearty feelings and best regards to my respected teacher and guide **Dr. Kunal B. Modi**, which I could not express during my research work. I am deeply indebted to my research supervisor for his constant encouragement, perennial interest, mentoring, research support and untiring help during entire tenure. His guidance proved to be a source of inspiration in my academic as well as my personal life. I am deeply grateful to him for giving me a chance to work in IUAC research project.

I feel very fortunate for having Mr. Jayesh V. Raval as my Husband who has given me invaluable cooperation in my academic and personal matters. He has always helped me solving problems, whether academic or personal and is always a source of encouragement for me. I have no words to express my thanks to him for sharing all my sorrows and joys.

I wish to express my warm and sincere thanks to Professor Hiren H. Joshi whose valuable suggestions proved to be very helpful throughout my research work. His ideas and concepts have had a remarkable influence on my entire career not only in the field of research but also in other aspects of life. I extend my thanks to Professor K.N. Iyer, Professor Mihir J. Joshi, Dr. G.J. Baldha for their encouraging words and all the other faculty members of the Department for their moral support.

I wish to express special thanks to Inter University Accelerator Center, New Delhi for providing me financial support in the form of UFUP-project scheme. I am thankful to Dr. Ravi Kumar, our project collaborator at IUAC, for his kind cooperation, during entire course of work. Acknowledgements are due to all the groups of scientists and students of IUAC associated with the irradiation experiments.

I thankfully acknowledge Our Research collaborators, who have helped to accomplish this work by providing various characterization facilities. I express my sincere thanks to the following:

Professor H.C. Verma and Dr. M.K. Roy, IIT, Kanpur for providing Mössbauer characterization facility.

Professor P.V.Reddy, Department of Physics, Osmania University, Hyderabad for providing Ultrasonic measurements.

Dr. S. N. Dolia, Department of Physics, University of Rajasthan, Jaipur for low temperature VSM measurement facility.

I thankfully acknowledge Professor Ajay Gupta, Centre Director, IUC-DAE-CSR, Indore for providing Mossbauer Characterization facility and Dr. Alok Banerjee from the same department for providing Dielectric measurements.

I extend my thanks to SICART, Vallabh Vidya-nagar for providing various characterization facilities.

I am deeply grateful to Ms. Smita Gohil, Tata Institute of fundamental research, Mumbai for her kind help in getting various experimental facilities from TIFR, Mumbai. My hearty thanks to Ms. Paramani Rajput, IUC-DAE-CSR, Indore, who has guided me Mossbauer analysis.

I acknowledge the help provided by Dr. R.B.Jotania and Dr. Chetna Makwana, for getting VSM measurements of few of my samples. I feel pleasure to express my thanks to my research colleagues Ms. Manisha Chhantbar, Mrs. Daksha Mehta, for their friendly help and advice. I extend my thanks to all the former and present members of ferrite laboratory and all other research students of the department for their cooperation. My hearty thanks to all my friends and research colleagues from other institutes and Universities who have helped me directly or indirectly in completion of this work.

I expect to be pardoned if I have missed the name of any body inadvertently who helped me to accomplish this work.

June 2009 **Pooja U. Sharma**

Rajkot

With due regards…

I thankfully acknowledge Inter- University Accelerator Center ***(IUAC),*** *New Delhi for providing financial support in the form of Junior Research Fellowship (JRF) under UFUP-project of* ***Dr. Kunal B. Modi*** *and Material Research Society of India* ***(MRSI),*** *IISc, Banglore for providing partial support under Students' projects Scheme.*

June 2009 ***Pooja U. Sharma***

Rajkot

Projects

(1) I have worked as a junior research fellow in the project entitled **"Study of SHI induced modification in Elastic behaviour of magnetic oxide materials through X-ray diffraction and infrared spectroscopic measurement"** funded by Inter- University Accelerator Center, New Delhi since April -2005 to April-2008.
(2) A Project entitled **"Grain Size dependent dielectric performance of Spinel ferrites"** is approved for partial support from Material Research Society of India (MRSI) under Students' projects Scheme on 15th September 2006.

Academic Achievements

(1) 2nd prize winner for best paper presentation (oral) at 19th Gujarat Science Congress (2004) held at S. P. University, Vallabh Vidyanagar.

Oxygen does not play any role in governing Elastic properties of Oxide Compositions.
P.U.Sharma, V.K. Lakhani, M.C. Chhantbar, K. B. Modi and H.H.Joshi

(2) 1st prize winner for best paper presentation (poster) at Indian Physics Association and World Year of Physics-Intermeeting, held at Veer Narmad South Gujarat University, Surat.

A Novel application of Raman spectroscopy
P.U.Sharma, M.C.Chhantbar, K.B.Modi and H.H.Joshi

(3) Prize winner for best paper presentation (oral) at One Day Seminar on Celebration of International Year of Physics 2005, organized jointly by Physics Dept. Saurashtra University and IAPT- Regional Council- Gujarat, held during 8th January 2006 at Pradeshik Lok Vigyan Kendra,Rajkot

A Novel Approach for elastic constant determination of polycrystalline oxide compositions.
P.U.Sharma, K.B. Zankat and K.B.Modi

(4) Project selected for "Student research convention west zone" organized by Rashtrasant Tukdoji Maharaj Nagpur University and Association of Indian Universities held during 14th-16th march 2008 at Rashtrasant Tukdoji Maharaj Nagpur University, Nagpur.

Fabrication of Ferrite based anti-cellphone wood

P. U. Sharma and K. B. Modi

(5) Shri Natvarbhai motibhai Patel research Award for "Best research Paper" for the year 2006-2007, published by students in the subject of "Materials Science and Nanotechnology" instituted by Chandubhai Patel (Vikil) foundation, USA and Sardar Patel University, Vallabh Vidyanagar.

Study on electrical and dielectric behaviour of Zn-substituted cobalt-ferri- aluminates

N.H. Vasoya, V.K. Lakhani, **P.U. Sharma**, K.B. Modi, Ravi kumar, and H H Joshi

List of Publications in International / National Journals and proceedings

(1)**Thermoelectric Power study of Fe^{3+} Substituted YIG**
Proceedings of DAE-SSPS **49**(2004) 730-731
P. U. Sharma, R. P. Vara, M. P. Pandya, K.B. Zankat and K.B. Modi

(2) **Elastic constant determination for Fe^{3+} substituted YIG through infrared spectroscopy and heterogeneous metal mixture rule**
Journal of material science **40(5)** (2005) 1247-1249.
K.B. Modi, M.C.Chhantbar, **P.U.Sharma** and H.H.Joshi

(3)**Ultrasonic studies of aluminium substituted Bi (Pb)-2223 Superconductors**
Pramana-Journal of Physics **65(3)** (2005) 481-490
M.B. Solunke, **P.U.Sharma**, M.P. Pandya, K.B. Modi, P.Venugopal Reddy and S.S.Shah, Pramana- Journal of Physics (2005)

(4) **Study of elastic properties of fine particle copper-zinc ferrite through infrared spectroscopy**
Indian journal of pure and journal of physics **44**(2006) 165-168
K.B. Modi, U.N. Trivedi, **P.U. Sharma**, V.K. Lakhani, M. C. Chhantbar and H. H. Joshi

(5) **Study on electrical and dielectric behaviour of Zn-substituted cobalt-ferri- aluminates**
Journal of physics: condensed matter **18**(2006) 8063-8092
N.H. Vasoya, V.K. Lakhani, **P.U. Sharma**, K.B. Modi, Ravi kumar, and H H Joshi

(6) **Study of electric and dielectric properties of Mn^{4+}-substituted cobalt ferrite**

Indian Journal of Physics **80(8)**, (2006) 789-796
V K Lakhani, **P.U. Sharma**, K G Saija, K B Zankat and K B Modi

(7) **Master Curve generation of some experiment data for Zinc-substituted Cobalt Ferri-aluminates**
Proceedings of DAE –SSPS **51,** (2006) 681-682
K.B.Modi, I.G.Jhala, T.K.Pathak, J.U.Buch, **P.U.Sharma** and G.J.Baldha

(8) **Elastic properties of gallium substituted Bi (Pb)-2212 superconducting system at 300K**
Ceramic International **33**(2007)21-25
M.B. Solunke, **P.U. Sharma**, V.K. Lakhani ,M.P. Pandya, K.B. Modi, P.V. Reddy and S.S. Shah

(9) **Mossbauer Studies of Fe^{3+} substituted YIG**
Ceramic International **33**, (2007)1543-1546
P. U. Sharma,V. K.Lakhani, K.B.Zankat and K.B.Modi

(10) **Effect of Nickel substitution on structural, infrared and elastic properties of Lithium Ferrite**
Indian Journal of Pure and Applied Physics **45,** (2007)596-608
S.S. Bhatu, V.K.Lakhani, N.H.Vasoya, J.U.Buch, **P.U.Sharma** ,U.N.Trivedi,H.H.Joshi and K.B.Modi

(11)**Effect of Ag^{+} addition on Elastic behaviour of Bi-2212 superconductors**
Indian Journal of Pure and Applied Physics **45**, (2007) 764-766
M.B. Solunke, K B Modi, V. K. Lakhani, K.B. Zankat, **P.U. Sharma**, P.V. Reddy and S.S. Shah

(12)**Dielectric Performance of Nanocrystalline Yttrium Iron Garnet**
Proceedings of DAE –SSPS **52,** (2007)293-294
P.U. Sharma, K.B. Zankat, V.V. Siva Kumar, Ravi Kumar and K.B. Modi

(13) **Effect of SHII on Bulk and Microscopic Magnetic Properties of YIG**
Proceedings of the National Conference on Recent Advances in Material Science (2007) 241-245
P.U. Sharma, M.C. Chhantbar, Ravi Kumar, H.C. Verma, M.K. Roy, H.H. Joshi and K.B.Modi

(14)**SHI-Induced ion beam mixing in Y^{3+}: YIG revelation through X-ray diffraction and Mossbauer spectroscopy**
Hyperfine interactions (2008) 187,117-124
P.U. Sharma, M. K. Roy, Ravi Kumar, H.C.Verma H.H. Joshi and K.B.Modi

(15) **Effect of SHII on M-H loop characteristics of Y^{3+}-substituted YIG**
Proceedings of DAE-SSPS **53**, (2008)1157-1158
P.U. Sharma, J.V. Raval, K.B. Zankat, S.N. Dolia, Ravikumar and K.B. Modi

Conferences/Seminars (Presentations)

(1) **Thermoelectric Power study of Fe^{3+} Substituted YIG (poster presentation)**

49th DAE Solid State Physics Symposium (2004) held at Guru Nanak Dev University, Amritsar.
P. U. Sharma, R. P. Vara, M. P. Pandya, K.B. Zankat and K.B. Modi

(2) **Oxygen does not play any role in governing Elastic properties of Oxide**
Compositions (2nd prize winner for best paper presentation (oral))

19th Gujarat Science Congress (2004), S. P. University, Vallabh Vidyanagar.
P.U.Sharma, V.K. Lakhani, M.C. Chhantbar, K. B. Modi and H.H.Joshi

(3) **A Novel application of Raman spectroscopy (1st prize winner for best paper presentation (poster))**

Indian Physics Association and World Year of Physics-Intermeeting (2005), Veer Narmad South Gujarat University, Surat.
P.U.Sharma, M.C.Chhantbar, K.B.Modi and H.H.Joshi

(4) **A Novel Approach for elastic constant determination of polycrystalline oxide compositions (prize winner for best paper presentation (oral))**

One Day Seminar on Celebration of International Year of Physics 2005, organized jointly by Physics Dept. Saurashtra University and IAPT-Regional Council- Gujarat, held during 8th January 2006 at Pradeshik Lok Vigyan Kendra,Rajkot.
P.U.Sharma and K.B. Zankat

(5) **Effect of SHll on Magnetic Properties of Fe^{3+} Substituted YIG (Oral presentation)**
One Day National Seminar on Recent Advances in Condensed matter and Space Physics held on 21st march 2006 at Department of Physics, Saurashtra University, Rajkot.
P.U.Sharma and K. B. Zankat

(6) **Effect of SHll on bulk and Microscopic Magnetic Properties of YIG (Oral presentation)**

Workshop on Functional Oxide Materials held during 25th-26th September 2006 at Inter -University Accelerater Center, New Delhi.
P. U. Sharma, Ravi Kumar and K. B. Modi.

(7) **Effect of SHll on bulk and Microscopic Magnetic Properties of YIG (poster presentation)**

National Conference on Recent Advances in Material Science (RAMS-06) held during 27th -29th September 2006 at department of physics, Kurukshetra University, Kurukshetra.

P. U. Sharma, M.C.Chhantbar, Ravi Kumar, H.C.Verma, M.K.Roy, H. H. Joshi and K. B. Modi

(8) **Effect of SHII, Quenching and Grain Size reduction On Elastic Properties of Copper Ferrite. (Poster presentation)**

Indian National Science Academy of Sciences sponsored Workshop on Condensed Matter Research and Magnetic Materials held on 4th December 2006 at School of Physics, University of Hyderabad, Hyderabad.
P. U. Sharma

(9) **Master Curve generation of some experiment data for Zinc-substituted Cobalt Ferri-aluminates**

51th DAE Solid State Physics Symposium (2006) held at Barkatullah Univesity,Bhopal.
K.B.Modi, I.G.Jhala, T.K.Pathak, J.U.Buch, **P.U.Sharma** and G.J.Baldha

(10) **Dielectric performance of Nanocrystalline yttrium Iron Garnet (Poster presentation)**

National conference on Physics of Nanostructure and biomolecules held during 22nd-24th January 2007 at Physics Department, M.S. University, Vadodra.
P.U. Sharma, K.B. Zankat, V.V. Siva Kumar and K.B. Modi

(11) **SHI-Induced ion beam mixing in Y^{3+}: YIG revelation through X-ray diffraction and Mossbauer spectroscopy (Poster presentation)**

International Conference on the Applications of the Mössbauer Effect held during 15th –19th October 2007 at IITK-Kanpur.
P.U. Sharma, M. K. Roy, Ravi Kumar, H.C.Verma H.H. Joshi and K.B.Modi

(12) **Dielectric Performance of Nanocrystalline Yttrium Iron Garnet (Poster presentation)**

52nd DAE Solid State Physics Symposium (2007) held at Mysore University, Mysore, during 26-30,December,2007.
P.U. Sharma, K.B. Zankat, V.V. Siva Kumar, Ravi Kumar and K.B. Modi

(13) **Effect of SHII on M-H loop characteristics of Y^{3+}-substituted YIG**

53rd DAE Solid State Physics Symposium (2008) held at Bhabha Atomic Research Centre and Tata Institute of Fundamental Research, Mumbai, during 16-20, December, 2008.
P.U. Sharma, J.V. Raval, K.B. Zankat, S.N. Dolia, Ravi Kumar and K.B. Modi

Workshops/School/teaching programme attended

(I) "National Workshop on prospects of Astronomy research in universities" held during
25-27 February 2004 at Department of Physics, Saurashtra University, Rajkot.

(2) "National Workshop on Advanced techniques for Characterization of Nanomaterials" held during 28th June-2nd July '2005 at Department of Physics, Pune University, Pune.

(3) "IUAC Ph.D teaching programme on Vacuum techniques (grade-A^+) and Ion- sources (grade-B),held during 7th-24th February -2006.

(4) "School on X-ray technique in Material Science" held during 12th- 16th June '2006 at Inter University Accelerator Center, New Delhi.

(5) " 4th SERC School in Condensed Matter and Materials Physics (Special Theme: Magnetism and Superconductivity)" held during 13th November-9th December 2006 at School of Physics, University of Hyderabad, Hyderabad.

(6) "Student research convention west zone" organized by Rashtrasant Tukdoji Maharaj Nagpur University and Association of Indian Universities held during 14th-16th march 2008 at Rashtrasant Tukdoji Maharaj Nagpur University, Nagpur.

CONTENTS

Chapter 6

On the effect of thermal history and Swift heavy ion (SHI) - irradiation on physical properties Y^{3+}-substituted Yttrium iron garnet: $Y_{3+x}Fe_{5-x}O_{12}$; Y-(Fe(Y)-O system

Effect of SHI-Irradiation on 1500 °C sintered samples of Y-Fe(Y)-O system

Chapter 7

Grain size dependent structural, Infrared spectral, magnetic, electrical and dielectric properties of Yttrium iron garnet (YIG)

This thesis is dedicated to

My Family

Chapter 1

Introduction

1.1 Introduction

We are dependent on material to the extent that is not apparent at a first glance. It may not be an exaggeration to state that we have survived and consolidated our position amongst the many other animal species inhabiting the earth because we decided to manipulate material around us. From the naturally occurring flint of the stone age to the silicon chip of the space age, materials have had a very important role in our lives. So, it should be of interest to know something about the nature and properties of new exciting materials that are being developed.

Materials Science today assumes various manifestations. The study of the science of different types of material has led to the development of variety of devices that have found application in man's everyday life. Much of the recent progress in science and technology is due to the advances made in physics and chemistry of condensed matter. It not only draws attention to the chemical composition, atomic configuration etc of the solid but also correlates the physical properties of the solids and helps in solving variety of problems of practical and technological importance.

Magnetic materials find wide technological applications in magnetic memories, high density magnetic recording medium, millimeter wave frequency devices etc. The two principle groups of magnetic materials of interest to the microwave engineer are the ferromagnets and ferrimagnets. Alongside the metals, principally iron, cobalt, nickel and their alloys, oxides constitute the main groups of magnetic materials. Magnetic oxides, due to their properties like very low conductivities, low dielectric loss tangents ($\sim 10^{-4}$) and low magnetic losses away from resonance permit the penetration of

microwave radiation with negligible attenuation and hence are applicable at microwave frequencies. The principal classes of oxide materials are the cubic spinel ferrites, hexagonal ferrites and ferrimagnetic garnets.

Ferrites are complex magnetic oxides that contain the ferric oxide (Fe_2O_3) as their main magnetic component. They can be classified into four main groups based on their crystal structure viz. spinel, garnet, hexa-ferrite and orthoferrite. Ferrite materials are known for a long time for a number of communication and defense applications. Of this development in the technology of ferrite material, the scientists still prefer to examine the structural, magnetic, electric and dielectric properties of these materials in a systematic manner to evolve correlation between them. Ferrites possess high values of magnetization due to the imbalanced magnitude of magnetic moments. The high value of resistivity, low dielectric loss, high as well as moderate saturation magnetization and high Neel temperature, have made ferrites the most versatile material for various technological application in the field like microwave technology, Radars, space technologies, communication etc. The interesting electrical and magnetic properties of these compounds are governed critically by their chemical compositions, preparative parameters, treatment employed etc. Hence, preparation of ferrite composites with specific properties has gained much importance.

Garnet refer to a group of minerals which have the same type of composition as $Mg_3Al_2(SiO_4)_3$ which is a common metamorphic mineral crystallizing in the cubic system. By replacing Si atoms with Fe, we obtain a group of ferrimagnetic garnet $M_3Fe_5O_{12}$ where, M is rare earth elements such as Dy, Eu, Gd, Er, Tm, Yb, Lu, or Y. All these metal ions are trivalent. The

garnets of the rare earth elements and iron were first prepared by Bertaut and Forrats in (1956) [1], as well as by Geller and Gilleo in (1957) [2]. The fundamental properties of garnet structure materials concerning the nature of origin of ferrimagnetisms are closely connected with the possibilities of their applications. They are widely used in electrical, telecommunication, computer and microwave industries. Apart from these, they have wide range of applications [3].

Garnets are well-established magnetic oxide materials having interesting properties of applied and basic research point of view. Garnets substituted with different cations have gained importance because of their very low losses at microwave frequency [4]. It is well known that when magnetic insulators are subjected to swift heavy ion irradiation (SHII), it leads to the creation of a wide variety of defect states such as point/cluster and columnar defects in the materials [5] resulting to the modifications on their physical properties.

The interest in the SHI irradiation on garnets is because of the effect of irradiation on the magnetic interactions, especially the super-exchange and hyperfine interactions that are highly sensitive to any change in the bond angle and the cation distribution. SHI-irradiation is a good source to generate defects that can further be responsible for re-distribution of cations and production of stress-strain in the structure thereby modifying the structural, magnetic, electrical and dielectric properties. Nanomaterials are materials possessing grain size of the order of 1-100 nm; they manifest extremely fascinating and useful properties. The nanoscience research mainly deals with synthesis, understand and explore new nanomaterials and the related

phenomena. Nanoparticles of spinel ferrites and garnets are of great interest in fundamental science for addressing relationship between physical properties and their crystal structure and chemistry. Due to their reduced sizes, these nanoparticles may possess novel and /or improved properties in comparison to its coarse grain counterpart. This has renewed interest to study different properties of pure and substituted garnet systems in nanocrystalline regime. A wide variety of techniques are being used to synthesize nanostructured materials including co-precipitation, sol-gel [6, 7], Microwave induced combustion [8], gas condensation, rapid solidification, electro-deposition, sputtering, crystallization of amorphous phases [9]. Mechanical attrition-ballmilling is a technique which has also been used widely for preparation of Nanostructured materials [10-12]. This has become a popular method to make nanocrystalline materials because of its simplicity and relatively inexpensive equipment needed and the applicability to essentially all classes of materials. The major disadvantage often quoted is the possibility for easily scaling up to tonnage quantities of material for various applications. In fact contamination problem is often given as a reason to dismiss the method at least for some materials. In the past the effectiveness of milling process has been assessed in terms of changes in the particle shape, size and size distribution. Recently, it has become apparent that in order to characterize a powder more fully, account must be taken of the strain content induced during the milling process.

The wet-chemical routes, for growing nano-crystallites (bottom-up technique) of ferrite materials are prone to loss of compositional stoichiometry. Moreover, it is difficult to obtain consistency in the physical

properties of electro-ceramics synthesized by systems containing more than three cations; percentage substitution is very small, tetravalent/pentavalent cation substituted systems.

Therefore, the study of ballmilled (bottom down technique) ceramically prepared magnetic oxides will definitely lead to easy synthesis of required material for fundamental as well as applied research. It is important to note that the materials produced by ballmilling technique have two fold advantage of having better control in obtaining fine particles and surety of stoichiometry of the products with good homogeneity and densification. At the same time mechanical milling induced stress-strain should be taken into account.

- For fine communication dry lab samples of solids in suspension down to colloidal fineness.
- For mixing and perfect homogenization of emulsions or pastes.
- For mechanical alloying are the fields of application of ballmilling.

The usefulness of garnets is influenced by the physical and chemical properties of the material. Yttrium iron garnet (YIG) is a prototype of new ferrimagnetic materials, which have provoked great interest since their discovery [13, 2].The combination of low dielectric and magnetic losses has been lead to the development and use of YIG in many tunable microwave devices. These materials have been widely used as both transmitter and transducer of acoustic energy, laser host and in memory devices. It has been reported that YIG is suitable for colloidal particles for transport magnetic fluids [14]. On the other hand YAG (Yttrium aluminum garnet): Nd compositions are utilized as laser materials [15]. In recent year only, a large number of research

articles describing various physical properties of substituted Yttrium iron garnet are available in the literature [16-25].

In short, even after sixty years of first preparation of garnet, still it carries lots of potential from both fundamental and applied research point of view.

1.2 Motivation, aim and outline of the present work

The basic structural and hence various physical properties like magnetic, electric –dielectric and elastic properties of Yttrium Iron Garnet is sensitive to many factors like substitution of various magnetic and non-magnetic ions, methods of preparation, particle size etc. Owing to the importance of YIG material from basic research and application point of view, magnetic materials considered in the present investigations are Fe^{3+}- and Y^{3+}-substituted Yttrium iron garnet respectively. A series of Fe^{3+}- substituted YIG and a series of Y^{3+} -substituted YIG with general formula $Y_{3-x}Fe_{5+x}O_{12}$ and $Y_{3+x}Fe_{5-x}O_{12}$ respectively, are prepared by usual double sintering ceramic technique. The systems under investigation seem to be simple but it posses certain qualities:

(1) Only two cations are present, i.e Y^{3+} and Fe^{3+} in the systems, it is always easy to deals with systems with small number of cations.

(2) Y^{3+} is non-magnetic ($0\mu_B$) while Fe^{3+} is magnetic ($5\mu_B$), thus all the magnetic properties are govern by magnetic Fe^{3+} ions only.

(3) Y^{3+} is known for valency stabilization; on the other hand Fe^{3+} may be converted into Fe^{2+} or Fe^{4+} or both, depending on the preparative parameters, responsible for conduction and other electrical/dielectric behaviour.

(4) Ionic radius of Y^{3+} is 0.89 Å while it is 0.64 Å for Fe^{3+}, thus observe changes in structural and other related parameters can be well understood.

The polycrystalline pure and substituted YIG is a subject of interest from various applications and physics point of view. Many research reports are available on various properties of non-magnetic cation substituted on a- and d-sites of YIG [26-28]. Majority of the work deals with substitution of tetravalent and pentavalent cations on a- and d-sites along with divalent cations on c-site in order to maintain charge neutrality [26, 27]. Few reports are available on magnetic ion substitution on a- and d-sites [30, 31]. However, rare earth magnetic cation doped on c-site of YIG is very common [26, 28]. So far no work has been reported on exclusive c-site substitution, with cations other than rare earths, except In^{3+} and Fe^{3+}-substituted YIG [32]. Since no work has been reported on detailed analysis of garnet systems in general and $Y_{3-x}Fe_{5+x}O_{12}$ system in particular, the present work is important from fundamental research point of view. It becomes interesting and complex too, when all the three sites of crystal lattice possess magnetic ions like Fe^{3+} as in the present case, to study the compositional dependence of cation distribution, hyperfine interactions and other physical properties.

The yttrium iron garnet: $Y_3Fe_5O_{12}$ (YIG) has been found to be a relevant material for the purpose of irradiation because of its stability, well known magnetic properties and the possibility to find it in polycrystalline, single crystal or thin epitaxial film form [33]. However, majority of the work available in the literature deals with irradiation effect on various properties of single crystal and thin films of YIG [33-35]. Some facts to be mentioned are (i) to obtain pure garnet phase, temperatures of the order of 1400^{o}C are required

(at 1300^{o}C, even for a prolong heat treatment the materials contain only 90% of the garnet phase [36], (ii) in yttrium substituted yttrium iron garnets excess yttrium may be accommodated by formation of the perovskite $YFeO_3$ rather than non- stoichiometric phases, as there is very little difference in the lattice energies of the two phases [37]. In view of these facts, we have studied polycrystalline Y^{3+}- substituted yttrium iron garnet system with general formula : Y_{3+x} Fe_{5-x} O_{12} (x=0.0, 0.2,0.4 and 0.6), sintered at two different temperatures i. e. 1300 ^{o}C and 1500 ^{o}C, for effects of Swift heavy ion irradiation on their various physical properties.

Considering all the above mentioned facts and findings, the present work aims:

1. To synthesize magnetic Fe^{3+}-ions-substituted $Y_3Fe_5O_{12}$ ($Y_{3-x}Fe_{5+x}O_{12}$; x = 0.0, 0.1, 0.3, and 0.5) and non-magnetic Y^{3+}-ion substituted $Y_3Fe_5O_{12}$ ($Y_{3+x}Fe_{5-x}O_{12}$; x=0.0, 0.2, 0.4 and 0.6) by usual double sintering ceramic technique.
2. To study the effect of swift heavy ion irradiation (Li^{3+}, 50 MeV, fluence: $5*10^{13}$ ions/cm^2) on various physical properties of $Y_{3+x}Fe_{5-x}O_{12}$ system.
3. To study the grain size dependent structural, magnetic, electrical and dielectric behaviour of pristine $Y_3Fe_5O_{12}$ compositions. A series of nanoparticles of $Y_3Fe_5O_{12}$ was obtained using conventional high energy ball mill (SPEX 8000 D). The milling process was carried out for 3hrs, 6hrs, 9hrs and 12 hrs durations.

The following investigative techniques have been employed for the detailed study.

(a) Energy dispersive analysis of X-rays (300 K).

(b) Powder X-ray diffractometry (300 K).

(c) Infrared spectroscopy (300 K, 400-1000 cm^{-1}).

(d) Scanning electron microscopy (300 K).

(e) Transmission electron microscopy (300 K).

(f) High field magnetization (300 K and 20 K, H=9 kOe), DC magnetization (20K-273K, H = 200 Oe).

(g) Low field ac susceptibility (0.5 Oe, 300 K-700 K).

(h) Mössbauer spectroscopy (300 K).

(i) Permeability (300 K-573 K, f=100Hz-13 MHz).

(j) DC Resistivity (300 K-673 K).

(k) Thermo electric power (300 K-673 K).

(l) AC resistivity, dielectric constant and impedance spectroscopy (300 K-673K, f=100 Hz-1 MHz).

References

1. F. Bertaut and F. Forrat, Compt. Rend. 242,382 (1956).
2. S. Geller and M. A. Gilleo, J. Phys. Chem. Solids. 3, 30(1957).
3. T.Aichele, A.Lorenz, R.Herot and P.Goornet, Cryst. Res. Technol. 38, 575 (2003), http:www.compusprogram.com (6/1/2004).
4. M.A. Gilleo and S.Geller, Phys. Rev. 110, 1(1958).
5. Thompson, M.W.: Defects and radiation damage in metals. Cambridge University press, Cambridge (1969).
6. M. Ristic, I. Nowik, S. Popovic, I. Felner and S. Music, Mater. Lett. 57(2003)2584.
7. Haitao Xu and Hua Yang, Mater. Manu. Process. 23(2008)1.
8. Y.P.Fu. C.H. Lin and K.Y. Pan, J. Magn. Magn. Mater. 272-276(2004)2202.
9. C. C. Koch, Nanostructured materials 9(1997)13.
10. B.P.Richards and A.C. Greenham Brit. J. Appl. Phys. (J.Phys.D)2(1)(1968)1297.
11. R.J. Joseyphus, A. Narayansamy, N. Sivakumar, M.Guyot, R. Krishnan, N.Ponpandian and K.Chattopadhyay, J. Magn. Mag. Mater. 272(2004)2257.
12. R.J. Joseyphus, A. Narayansamy, A.K. Nigam and R. Krishnan, J. Magn. Magn. Mater. 296(2006)57.
13. M. Bonnet, A. Delapalme, H. Fuess and M. Thomas, Acta Cryst. B31 (1975)2233.
14. Taketani, K. Kawasaki, Y. Ozaki, S. Yuash and H Miyajim, J. Magn. Magn. Mater. 122 (1993) 6.

15. A. Ikesue, T. Kinoshita, K. Kamata and K.Yoshida, J. Am. Ceramic. Soc. 78 (1995)1035.

16. V.D. Murumkar, D. R. Shengule, G.K. Bichile and K.M. Jadhav, Hyperfine Interactions 192(2009)93.

17. M. Erol, Y.Ozturk, I. Avgin and E. Celik, J. Phys: Conf. Seri. 153(2009)01204.

18. Y.J. Wu, H.P. Fu, R.Y. Hong, Y. Zheng and D.G. Wei, J.Alloy. Comp. 470(1-2)(2009)49.

19. Y. J. Wu, R.Y. Hong, L.S. Wang, G.Q. Di, H.Z. Li, B.Xu, Y.Zheng and D.G. Wei, J.Alloy. Comp. (doi: 10.1016/J.jallcom. 2009.03.060).

20. Y.P. Fu, D.S. Hung, C.W. Cheng, F.Y. Tsai and Y.D. Yao. Ceram. Int. 35(2)(2009)559.

21. Z. A. Motlagh, M. Mozaffari and J. Amighian, J. Magn. Magn. Mater. 321 (13)(2009)1980.

22. A.S. El-Said, NIM B ,267,6(2009)953.

23. Huseyin Sozeri and Nader Ghazanfari, Mater. Chem. Phys. 113, (2-3) (2009)977.

24. S.S. Balabanov, E.M. Gavrishchuk, V. V. Drobotenko, A.M. Kut'in, V.S. Polyakov and T.I. Strozheva, Inorg. Mater. 45,(2)(2009)157.

25. Noorhana Yahya, Ramadan Al Habashi Masoud, Hanita Daud, Azizuddin A. Aziz and Hasnah Mohd Zaid Am. J. Eng. Appl. Sci. 2(1)(2009)76.

26. K.J. Standly, Oxide Magnetic Materials, second ed., Clerendon Press, Oxford, 1974, and references therein.

27. T.T. Shrinivasan, Om Prakash, M.J. Patni, Trans. Ind. Ceram. Soc. 40 (1) (1981) 1.

28. K.C. Patil, K. Suresh, J. Alloys. Compd. 209 (1994) 203.

29. C.M. Srivastava, S.N. Shringi, B. Uma Rao, D. Bahadur and Om Prakash,Bull. Mater. Sci. 6 (1) (1984) 17.

30. V.D. Murumkar, K.B. Modi, K.M. Jadhav, G.K. Bichile and R.G. Kulkarni, Mater. Lett. 32 (1997) 281.

31. J. Smith and H.P. Wijn, Ferrites, Cleaver–Hame Press, London, 1959.

32. Sung Ho Lee, Kwang Pyo Chae, Seok Won Hong and Young Bae Lee, Solid State Commun. 83 (2) (1992) 97.

33. F.Studer, C.Houpert, D. Groult and M. Toulemonde, Radiation Effects and defects in solids, 110, (1989) 55-59.

34. M.Toulemonde, G.Fuchs, N.Nguyen, F.Studer and D.Groult, Phys.Rev. B. 35(13), (1987)6560-6569 and references therein.

35. C.Houpert, M.Hervieu, D.Groult, F.Studer and M.Toulmonde, NIM B. 32, (1988)393-396.

36. P.Grosseau, A.Bachiorrini and B. Guilhot, Powder technology, 93, (1997)247-251.

37. H.Donnerberg and C.R.A.Catlow, J. Phys. Condens. Matter. 5, (1993)2947-2960.

Chapter 2

Crystal Structure, Classification of Ferrites and Magnetism in Garnets

2.1 Historical Background

The history of ferrites (magnetic oxides) began centuries before the birth of Christ with the discovery of stones that attract iron. The deposits of these stones were found in the districts of Magnesia in Asia Minor, hence the mineral's name became magnetite (Fe_3O_4). Much later, the first application of magnetite was as 'Lodestones' used by early navigators to locate magnetic North. In 1600 William Gilbert published De Magnete, the first scientific study of magnetism.

The term "ferrite" is derived from the Latin word "ferrum", meaning iron. Ferrites are homogeneous ceramic materials composed of various oxides containing iron oxide as their main constituent [1]. The term "ferrite' means different to different scientists. To metallurgists, ferrite means pure iron. To geologists, ferrites are a group of minerals based on iron oxide. To an electrical engineer, ferrites are a group of materials based on iron oxide, but one that have particular useful properties: magnetic and dielectric.

Magnetite or lodestone is a naturally occurring iron oxide that is considered a ferrite by both geologists and engineers. Over 2,000 years ago, the Greeks recognized the strange properties of lodestone, and almost 1,000 years ago the Chinese used it to invent the magnetic compass. Dielectric properties mean that even though electromagnetic waves can pass through ferrites, they do not readily conduct electricity. This gives them an advantage over iron, nickel and other transition metals that have magnetic properties ("ferromagnetic") in many applications because these metals also conduct electricity.

Magnetite, i.e., $Fe^{2+}Fe_2^{3+}O_4$ (Fe_3O_4) is a naturally occurring ferrite. The first artificial ferrite was actually made in 1909 by Hilpert. Since the method of producing ferrite involves more chemistry than physics, it was not until 1940 that methods of controlling the ferrite composition were developed. Snoek, the father of ferrites with the help of scientists at Philips Laboratory, Holland developed first ever-commercial ferrites during Second World War [2]. Philips even today is the leading manufacturer of commercial ferrites and has the biggest market share in the international ferrite industry, only to be followed by Japan. Scientific research on ferrite began in the mid of nineteenth century. Two Japanese scientists Dr. Kato Yogoro and Dr. Takei Takeshi took the initiative in conducting serious research oriented to industrial applications [3]. Their series of research results on Cu ferrite and Co ferrite in the year beginning 1932 become the nucleus and motive force which, as is well known led to the world's first application of ferrite on a commercial basis. Subsequently, J.L. Snoek and his colleagues at N.V. Philips Gloeilampenfabrieken, published systematic fundamental research on ferrite [4] and Louis Neel of France published his theory of ferrimagnetism [5]. Neel provided the theoretical key to an understanding of ferrites, and the word ferrimagnetism is due to him. With these publications and results, ferrite holds the main position in worldwide research on magnetism, which it retains to this day.

2.2 Classification of Ferrites

In the commercial world, ferrites are usually classified as soft ferrites and hard ferrites depending upon their magnetic properties. The

distinguishing characteristic of the first group is high permeability. Its flux – multiplying power made it suitable for their job in machines and devices. Magnetically hard materials, on the other hand are made into permanent magnets having high coercivity as it once magnetized may be able to resist the demagnetizing action of stray fields including its own. Naturally occurring magnetite is a weak 'hard' ferrite. Hard ferrites possess magnetism, which is essentially permanent. Man-made hard ferrites with superior properties were developed but producing an analogous 'soft' magnetic material in the laboratory proved elusive.

2.2.1 Soft Ferrites

The research on soft ferrites continued since 1930, primarily in Japan and the Netherlands. However, it was in the year 1945 that J.L. Snoek of the Philips Research Laboratories in the Netherlands succeeded in producing a soft ferrite for commercial applications. Soft ferrites are ceramic electromagnetic material dark grey or black in appearance and very hard and brittle. The terms "SOFT" has nothing to do with their physical properties but refers to their magnetic characteristics. Soft ferrite dose not retain significant magnetization whereas hard ferrite magnetization is considered permanent. Soft ferrite is the general term to a class of ceramic and electromagnetic materials. From the crystallographic aspect, soft ferrites are inverse spinels and belong to the cubic crystal system. In other words, we can say they have a homogenous cubic spinel crystalline structure and are composed of iron oxide with divalent metal oxides. The most important type in terms of output are MnZn ferrite ($MnZnFe_2O_4$) and NiZn ferrite ($NiZnFe_2O_4$).

A soft ferrite's magnetic properties arise from interactions between metallic ions occupying particular positions relative to the oxygen ions in its spinel crystalline structure. The magnetic domain theory suggests these interactions create magnetic domains, which are microscopic magnetized regions within the material. When no magnetizing force is present, the magnetic domains are random and the net flux contribution is zero even though local domains are fully magnetized. When a magnetizing force is present the magnetic domains align in the direction of the magnetizing force resulting in a large net flux contribution. Soft ferrites are also semi – conductors meaning they are somewhere between conductors and insulators in their ability to conduct electron flow through the material.

The advantages which the soft ferrites have over other electromagnetic materials include their inherent high resistivity which results in low eddy current losses over wide frequency ranges, high magnetic permeability and stability over wide temperature ranges. For inductor cores, transformer cores and other applications where electromagnetic materials are required to operate at high frequencies, these advantages makes soft ferrites paramount over all other magnetic materials.

Uses of Soft Ferrites

Soft ferrites are used mainly in radio and television engineering, telephony and telegraphy. For example, ferrite coils, shell cores, pot cores, E – cores, cross cores, loading coils etc., of ferrite materials, are used in telephone engineering. The development of modern radio, television and telecommunications engineering would have been impossible in the absence of such ferrite components as U – cores for transformers, yoke rings,

intermediate frequency band filters and balancing transformers. In electronic computers, ferrites serve as storage elements and thus form the centre – piece of the whole machine. They also serve as magnetostriction vibrators in high frequency heating devices and many other electrical apparatus. Microwave ferrites are used in telecommunications and radar units as non – reciprocal waveguides.

2.2.2 Hard Ferrite

In the case of hard ferrites, a strong magnetization remains after a magnetizing field has been removed and residual magnetization is stable even if certain strength of demagnetizing field is applied. These characteristics are valuable in making permanent magnets. For hard ferrites, however, there is a considerable difference between the B – H curve and the M – H curve, in which M shows the magnetization. The M – H is important in magnet design and the evaluation of hard magnetic materials. These ferrites form a large class of ceramic materials. Hard ferrites vary from dark grey to black in colour, very hard and brittle. Naturally occurring magnetite is a weak hard ferrite. Hard ferrites possess magnetism, which is essentially permanent. These hard ferrites play a dominant role in the permanent magnet market that is mainly due to the low price per unit of available energy, the wide availability of the raw materials and the high chemical stability. M – type ferrites can be regarded as the more common type of the hard ferrites. They adopt the magnetoplumbite structure characterized by close packing of oxygen and Metal ions with Fe atoms at the interstitial positions. Alternatively, one may describe this crystal structure as being built up of cubic blocks with the spinel structure and hexagonal blocks containing the Metal ions.

The most important of these permanent magnetic materials in practical use are barium ferrite ($BaO.\ 6Fe_2O_3$) and strontium ferrite ($SrO.\ 6Fe_2O_3$). Since they have a larger coercive force than metallic magnetic materials, it is possible to design very thin magnets. Compared with soft magnetic ferrite, hard magnetic ferrite is weak in structural sensitivity, and is relatively little influenced by impurities and by firing conditions. Two classes of hard magnets, comprising oriented (anisotropic) and non – oriented (isotropic) ferrites, are distinguished. The magnetic properties, e.g., remanence B_r and energy product $(BH)_{max.}$ of anisotropic ferrites are superior to those of isotropic ferrites, and for this reason anisotropic ferrites enjoy a considerable large share in the market.

Uses of Hard Ferrites (Permanent Ferrites)

Permanent magnets have become indispensable components in modern technology. They play an important role in many electromechanical and electronic devices used in domestic and professional appliances. For example, an average home contains more than fifty of such devices, and least ten are in a standard family car. Magnetic resonance imaging used, as a medical diagnostic tool is an example of professional appliance where large amounts of permanent magnets are used. Apart from the many domestic and professional appliances, information technology, automotive and aerospace systems are significant users of permanent magnets, in particular actuators and motion systems. The most common types of magnets applied at present are alnico type magnets, hard ferrite magnets and rare – earth based magnets (SmCo, NdFeB). Of these the alnico magnets have only a modest coercivity which leads to non – linear demagnetization characteristics. For this

reason, their applicability is very limited compared to the other two types. The hard ferrites have higher coercivity than the alnico magnets. Their demagnetizing characteristics are linear but their Remanence is fairly low. Ferrite permanent magnets currently dominate the automotive applications and many of the other applications due to low cost and proven long-term stability.

2.3 Structural Classification of Ferrites

However, in most of the research work done on ferrites, scientists classify the ferrites according to their crystal structure. Hence technically speaking, we have four important classes of ferrites: (i) spinel, (ii) garnet (iii) hexaferrite and (iv) orthoferrite.

2.3.1 Spinel Ferrites

Such ferrites are in fact a prototype of naturally occurring ferrite i.e., $FeO.Fe_2O_3$. The spinel is by far the most widely used ferrite, so much so that the term is almost synonymous with the word “ferrite”. The spinel structure is derived from the mineral spinel ($MgAl_2O_4$ or $MgO.Al_2O_3$), that crystallizes in the cubic system. This crystal structure was first determined by Bragg [6] and by Nishikawa [7]. Analogous to the mineral

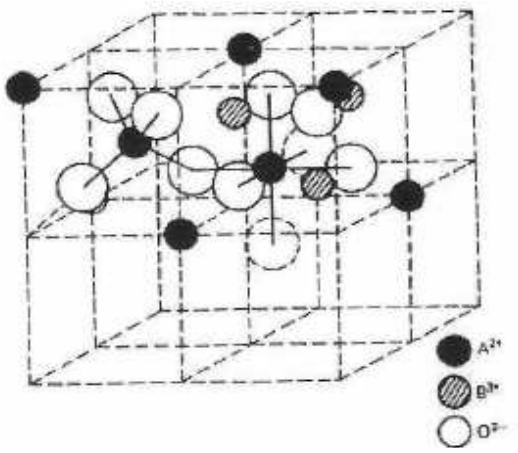

Fig.2.1 Unit cell of spinel structure

spinel, the magnetic spinel has the general formula $MeO.Fe_2O_3$ or $MeFe_2O_4$ where Me is the divalent metal ion.

The smallest cell of the spinel lattice that has cubic symmetry contains eight "molecules" of $MeFe_2O_4$. The relatively large oxygen ions (radius about 1.4 Å) form *fcc* lattice, and the much smaller metal ions (radii from about 0.7 to 0.8 Å) occupy the spaces between them. In this cubic close – packed structure two kinds of interstitial sites occur, the tetrahedral and the octahedral sites, which are surrounded by 4 and 6 oxygen ions respectively. In the above – mentioned cubic unit cell, 64 tetrahedral (A-) sites and 32 octahedral (B-) sites are present, of which only 8 and 16 respectively are occupied by metal ions (called A and B sites respectively).

In the mineral spinel, the Mg^{2+} ions are in A - sites and the Al^{3+} ions are in the B - sites. Some ferrites $MeO.Fe_2O_3$ have exactly this structure with Me^{2+} in A - sites and Fe^{3+} in B - sites. It is called the normal spinel structure. In case of Zinc ferrite, the tetrahedral sites are occupied by zinc ions, which, being non-magnetic (having no unpaired electronic spins), produce no antiferromagnetic orientation of the ions on the octahedral sites that are occupied by Fe^{3+} ions. The Fe^{3+} (B – B) interactions are so weak as to be unimportant, therefore, zinc ferrite is not ferrimagnetic. Both zinc and cadmium ferrite have this structure and they both are non-magnetic i.e., paramagnetic. Barth and Posnjak [8] found many cases in which the trivalent ions preferred the tetrahedral or A - sites and filled these first. Many other ferrites, however, have the inverse spinel structure in which the divalent ions are on B - sites, and the trivalent ions are equally divided between A - and B - sites. Iron, cobalt and nickel ferrites have the inverse structure and they are all

ferrimagnetic. Many of the commercially important ferrites are inverse spinel. Finally, it should be noted that ferrites can be prepared containing two different kinds of divalent ions, e.g., $(NiZn)O.Fe_2O_3$. This is called a mixed ferrite although actually it is a solid solution of $NiO.Fe_2O_3$ and $ZnO.Fe_2O_3$. Most of the cubic ferrites used commercially are mixed ferrites.

2.3.2 Garnet Ferrites

These are the ferrites that can accommodate large trivalent rare earth ions with large magnetic moments. Garnet ferrites have the structure of the silicate mineral garnet. Magnetic garnets crystallize in the dodecahedral or 12 – sided structure related to the mineral garnet. The general formula is $Me_3Fe_5O_{12}$. It is to be noted that in this case all the metal ions are trivalent in contrast to the other two classes. In the important magnetic garnets, Me is usually Yttrium (Y) or one of the rare earth ions. The crystal structure and the unit cell dimensions of the rare earth iron garnets were first reported by Bertaut and Forrat [9], then by Geller and Gilleo [10] and Gilleo and Geller [11, 12].

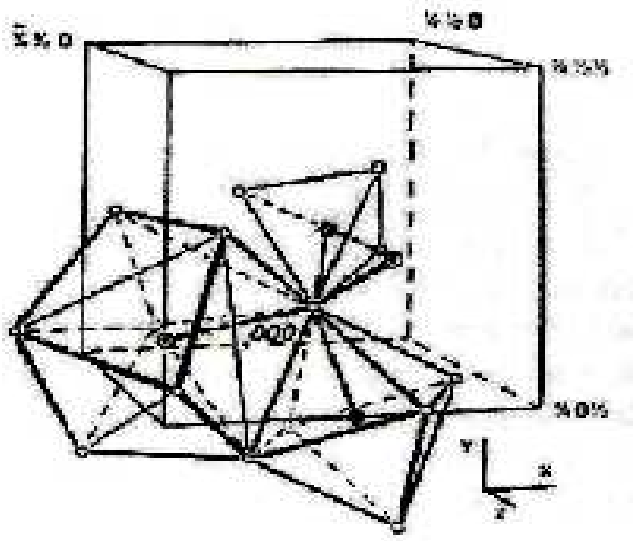

Fig. 2.2 Unit cell of garnet structure

Following the discovery by Menzer [13, 14] of the structure of the natural garnet $Mn_3Al_2Si_3O_{12}$, Yoder and Keith [15] indicated the possibility of

substitution of Y^{3+} and Al^{3+} and Si^{4+} and obtained for the first time the garnet $Y_3Al_5O_{12}$ free from silicon. The garnet structure is particularly stable because all the sites are occupied by cations. This contributes to the high stability of this compound.

2.3.3 Hexagonal Ferrites

This class of magnetic oxides have magnetoplumbite structure [16] which comes from the mineral of the same name. The so – called hexagonal ferrites have the formula $MeFe_{12}O_{19}$, where Me is usually Ba, Sr or Pb. The symmetry of the magnetoplumbite structure is hexagonal. Thus, it has a major preferred axis called the c – axis and a minor axis called a – axis. The preferred direction is used to good advantage as a permanent magnet material. Most of these compounds are ferrimagnetic but some are antiferromagnetic. They were first developed by Went et al [16], Fahlenbrach and Heister [17]. The best known compounds in this class are $BaFe_{12}O_{19}$, $SrFe_{12}O_{19}$ and $PbFe_{12}O_{19}$. Further studies in the ternary system BaO – FeO – Fe_2O_3 have led to the discovery of many other compounds having related hexagonal structures [18]. The complex crystal structures of these compounds were established by Braun [19]. The workers

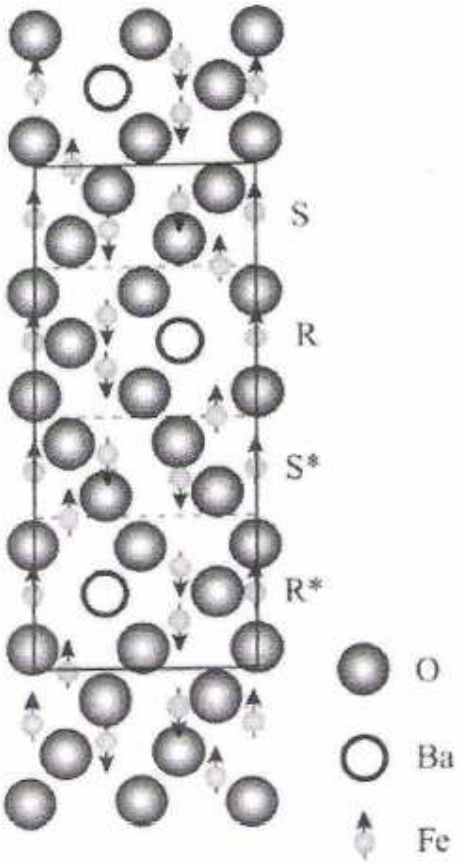

Fig. 2.3 Hexagonal ferrite structure

at Philips Research Laboratories found a series of other compounds possessing the hexagonal structure, in addition to the magnetoplumbite type structure. These compounds were made by combining the magnetoplumbite composition with various spinel ferrite compositions in various ratios. Thus, layers of spinel are sandwiched between layers of magnetoplumbite.

2.3.4 Orthoferrites

Apart from the hexagonal, spinel, and garnet ferrites, the next important structure is the orthoferrite or perovskite structure. The formula is $RFeO_3$ where R is usually Yttrium or a rare earth ion. These are also cubic ferrites but having a slightly distorted perovskite structure. Perovskite structure is the name given to the atomic arrangement of the oxides having the formula RMO_3 e.g., $BaTiO_3$, $PbTiO_3$ etc. This structure is often acquired by a material, which have a complicated molecular arrangement consistent with cubic symmetry.

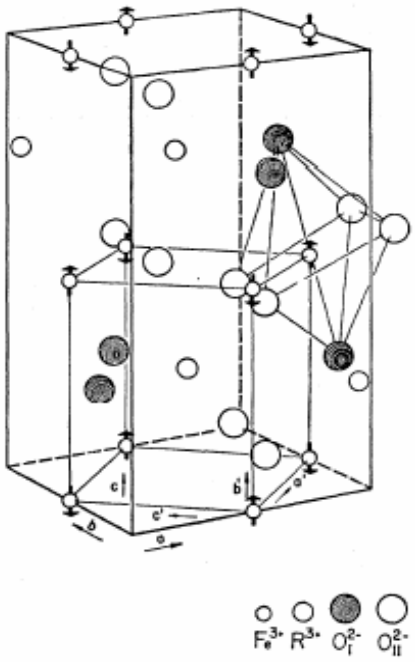

Fig.2.4 The unit cell of Ortho ferrite $RFeO_3$, monoclinic pseudo cell is indicated by a'b'c', the vectors indicate the magnetic ordering of iron ion.

The structure is orthorhombic rather than cubic. The canting or non – parallel alignment of the antiferromagnetically coupled ions leads to weak ferromagnetism in the perovskite structured materials. These compounds have the structure formed by the superposition of a canted spin antiferromagnetic sublattice M and sublattice R that is magnetically ordered at

low temperature and is paramagnetic at higher temperature. The rare earth iron perovskites are also known as “Orthoferrite” [20]. They were first studied by Forestier and Guillot – Guillain [21] and then by Pauthenet and Blum [22]. They observed that these rare earth iron perovskites have a parasitic ferromagnetic moment at room temperature and the curie points are about 700 ^{0}K. Real progress in the magnetic properties was achieved with the successful growth of perovskite single crystals [23] and the structure determination of $GdFeO_3$ [24]. The crystal structure of $GdFeO_3$ and $YFeO_3$ has been refined by Coppens and Eibschutz [25]. The magnetic properties of single crystals were measured by Bozorth et al [26, 27], Bozorth and Kramer [28] and Treves [29], and the magnetic structure was established with neutron diffraction by Koehler and Wollan [30]. Mossbauer studies were reported by Eibschutz et al [31]. The practical importance of the orthoferrites rested in their applications in the original bubble memory structures.

2.4 General Properties of Ferrites

Ferrite materials have properties which vary widely, and correspondingly their uses cover a considerable range. The properties of all the ferrites not only depend on their chemical composition but also on the methods of preparation. However variations in the different properties can be made by adding a little bit of impurity. Following are the properties of the ferrites:

- Ferrites are generally black or grey in appearance. Most ferrites are opaque. This can be attributed to the approximately equal energies of the

3d and 4s states. This is also because the absorption in case of ferrites crystal structure occur only in visible range thus making them black [2].

- Ferrites have high dielectric constant. Its values are generally of the order of thousands at lower frequencies, falling to about ten to twenty at microwave frequencies. This is due to the close – packed structure of oxygen ions [1, 2, 32].
- Ferrites are very hard and brittle and have high melting point. Again this is due to the fact that oxygen ions have a close – packed spatial formation, thus making the ionic bonds very strong [2]. The ferrite melting points are difficult to measure because they lose oxygen at high temperatures. However Van Arkel [33] measured their melting point with an oxyhydrogen flame.
- Ferrites are non – conductors of electricity but behave as semiconductors under the influence of an applied electric field [2, 34].
- Ferrites are best known for their magnetic properties. The important are:
  * Magnetic Anisotropy: Most of the ferrites have an ability to get completely magnetized along a preferred axis on the application of magnetic field.

  * Hysteresis and Permeability: Ferrites have either thin hysteresis loop or square loops. The ferrites with this loop come under the class of soft ferrites and finds applications in devices like transformers and inductors. The other with square loop are classified as hard ferrites which find applications in memory devices [1, 35] and switching devices [2].

2.5 Crystallography of Yttrium iron garnet

2.5.1 Crystallographic structure of YIG.

Yttrium iron garnet $Y_3Fe_5O_{12}$ (YIG) is isomorphic with the naturally occurring garnet Ca_3Fe_2 $(SiO_4)_3$. The general formula of the YIG can be represented schematically by $\{Y_3\}[Fe_2](Fe_3)O_{12}$.The garnets are cubic compounds with O_h^{10}-Ia3d symmetry, unit cell parameter a= 12.376 Á and 8 formula units per unit cell or 160 atoms, which can be described as a spatial arrangement of 96 O ions with cations in the “interstices”. The X-ray density of Y_3Fe_2 $(FeO_4)_3$ is 5.17 g /cm^3 with a volume of 236.9 A^3 per formula unit. The rare earth ions are large, and so they occupy dodecahedral sites. One formula unit, $3Me_2O_3.5Fe_2O_3$, is distributed as follows:

$3Me_2O_3$ Dodecahedral; $3Fe_2O_3$ Tetrahedral and $2Fe_2O_3$ Octahedral

In the garnet structure each of three positive- ion positions is associated with a different co- ordination polyhedron of oxygen ions: for Y^{3+}[24(c)] an eight-cornered twelve-sided figure (Figure 2.5); for Fe^{3+} [16(a)] an octahedron (Figure 2.6); for Fe^{3+}[24(d)] a tetrahedron (Figure 2.7).Thus Y^{3+} ions occupy positions 24(c), Fe^{3+} ions occupy positions 24(d) and 16(a), and oxygen ions occupy positions 96(h).

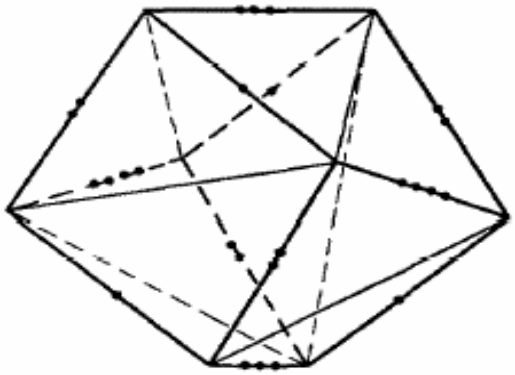

Fig. 2.5 Co-ordination polyhedron of oxygen ions about the Y^{3+} (d) ion (• 2.68, •• 2.81, ••• 2.87, •••• 2.96Å).

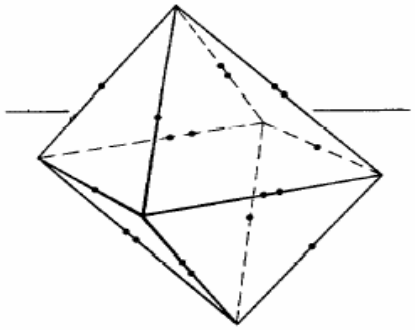

Fig. 2.6 Co-ordination octahedron of oxygen ions about Fe^{3+} (a) ion (• 2.68, •• 2.99 Å).

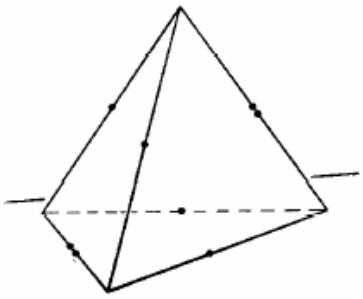

Fig. 2.7 Co-ordination tetrahedron of oxygen ions about Fe^{3+}(d) ion (• 3.16 , ••2.87 Å)

None of the polyhedra in YIG is regular with respect to edge length even though the oxygen parameters would permit the octahedra and tetrahedra to be regular simultaneously [36]. However in the latter two polyhedra all center-to-corner (Fe^{3+}-0^{2-}) distances are equal (Table 2.1): for the octahedra 2.00 Á ; for the tetrahedra I .88 Á and the yttrium-oxygen distances are 2.37 and 2.43 Á. The oxygen parameters are x = -0.0275, y = 0.0572 and z = 0.1495.

There are two different angles in each case: for octahedra 87.2˚ and 96.6˚ ; for tetrahedra 99.9˚ and 114.3˚ . Each oxygen ion is common to two eight-cornered polyhedra, one octahedron and one tetrahedron. Thus each oxygen ion has as nearest positive-ion neighbours two Y^{3+}, one Fe^{3+}(a) and one Fe^{3+}(d) ions (Tables 2.1 and 2.2). This feature of the structure is most important to the magnetic properties.

Table 2.1 Nearest-neighbour interionic distances in yttrium-iron garnet

Ion	Interionic distances (Å)
Y^{3+}	$4Fe^{3+}(a)$ at 3·46 $6Fe^{3+}(d)$ at 3·09(2), 3·79(4) $8O^{2-}$ at 2·37(4), 2·43(4)
$Fe^{3+}(a)$	$2Y^{3+}$ at 3·46 $6Fe^{3+}(d)$ at 3·46 $6O^{2-}$ at 2·00
$Fe^{3+}(d)$	$6Y^{3+}$ at 3·09(2), 3·79(4) $4Fe^{3+}(a)$ at 3·46 $4Fe^{3+}(d)$ at 3·79 $4O^{2-}$ at 1·88
O^{2-}	$2Y^{3+}$ at 2·37, 2·43 $1Fe^{3+}(a)$ at 2·00 $1Fe^{3+}(d)$ at 1·88 $9O^{2-}$ at 2·68(2), 2·81, 2·87, 2·96, 2·99(2), 3·16(2)

Table 2.2 Interionic angles in yttrium-iron garnet

Ions	Angles (°)
$Fe^{3+}(a)$–O^{2-}–$Fe^{3+}(d)$	126·6
$Fe^{3+}(a)$–O^{2-}–Y^{3+}*	102·8
$Fe^{3+}(a)$–O^{2-}–Y^{3+}†	104·7
$Fe^{3+}(d)$–O^{2-}–Y^{3+}*	122·2
$Fe^{3+}(d)$–O^{2-}–Y^{3+}†	92·2
Y^{3+} –O^{2-}–Y^{3+}	104·7
$Fe^{3+}(a)$–O^{2-}–$Fe^{3+}(a)$ (4·41)‡	147·2
$Fe^{3+}(d)$–O^{2-}–$Fe^{3+}(d)$ (3·41)	86·6
$Fe^{3+}(d)$–O^{2-}–$Fe^{3+}(d)$ (3·68)	78·8
$Fe^{3+}(d)$–O^{2-}–$Fe^{3+}(d)$ (3·83)	74·7
$Fe^{3+}(d)$–O^{2-}–$Fe^{3+}(d)$ (3·83)	74·6

* Y^{3+}–O^{2-} distance = 2·43 Å.

† Y^{3+}–O^{2-} distance = 2·37 Å.

‡ Numbers in parentheses are the longer $Fe^{3+}(a$ or $d)$–O^{2-} distances. The shorter distances (Table 4) are $Fe^{3+}(a)$–O^{2-} = 2·00, $Fe^{3+}(d)$–O^{2-} = 1·88 Å.

2.5.2 Ferrimagnetism in Garnets

The first magnetic measurements of the rare earth garnets were reported by Pauthenet [37]. The early magnetic measurements on the iron garnets have a historical value because many physicists became interested in this class of materials. The data were taken on polycrystalline materials and at least some of the samples did not have the purity, which was achieved several years later. More refined magnetic measurements were reported later by Geller et al [38] and Harrison et al [39].

These measurements were made on pure single crystals. In bubble memory applications, specially substituted rare earth garnets are used to form the cylindrical bubble domains.

In YIG, Y^{3+}, with no 4f electrons, does not have a magnetic moment; three Fe^{3+} ions on tetrahedral sites align antiparallel with two Fe^{3+} on octahedral sites. The antiferromagnetic exchange between these two types of Fe^{3+} results in a net magnetic moment of $5\mu_B$ per formula unit. This can be represented in following manner;

$$M^{3+}(2Fe^{3+})(3Fe^{3+})O^{2-}{}_{12}$$

$$2(5\uparrow)+3(5\downarrow)=5\ \mu_B\downarrow$$

When a rare earth ion or other magnetic cation replaces Yttrium, the c-sublattice magnetization must be subtracted from that due to the ferric ions and resultant magnetic moment can be represented as follows:

$$M = [Md - Ma] - Mc$$

where Md, Ma and Mc, are magnetic moment of d, a- and c-site respectively.

In pure Yttrium iron garnet a- and d- sites are occupied by magnetic Fe^{3+} ions and therefore total three interactions takes place i.e a-a, d-d and a-d. When

the c-site ion is magnetic, there are three interacting sublattices and therefore six interactions a-a, d-d, c-c, a-c and c-d comes into the consideration. The crystal geometry appears to be quite unfavorable to super exchange interaction between a-c and d-c sites. The interactions between them are considered to be weak. In a formula unit of garnet each of two octahedral ions, 16(a), interacts with six tetrahedral ions, 24(d), and each of three tetrahedral ions interacts with four octahedral ions, corresponding to a total of twenty-four interactions. There is probably no appreciable interaction between magnetic ions in equivalent sites in a garnet structure since either oxygen-magnetic ion distances are too large or the Me-O-Me, angle is nearly 90° (Table 2.2). In the garnet each Fe^{3+} (a) ion interacts only with Fe^{3+} (d) ions, i.e. all 16(a) or 24(d) ions are not only crystallographically but also magnetically equivalent.

The "exchange" interaction of two magnetic ions, Me, through an oxygen ion between them was first conceived by Kramers [40] and has since been more extensively studied by Anderson [41] and Van Vleck [42]. In this interaction the overlap of the 2p electrons (with dumbbell-shaped distribution) of the oxygen ion with the electronic distribution of the magnetic ions is an important feature The interaction increases with the overlap and, accordingly, will be greatest for short Me-O distances and for Me1-O-Me2 angles near 180°. Therefore, in yttrium-iron garnet the strongest interaction (Table 2.2) will probably occur between Fe^{3+}(a) and Fe^{3+}(d) for which the Fe^{3+}(a)-O^{2-}-Fe^{3+}(d) angle is 126.6". Because interaction of this type is known to be negative in ferrites, as was first recognized by Neel [43] and because there are $3Fe^{3+}$ (d) and $2Fe^{3+}$ (a) ions per formula unit, there should be a net magnetic moment

corresponding to that of one Fe^{3+}, i.e. 5 μ_B. Verification of this expectation is found in measurements of the saturation magnetization, $\sigma_{\infty,0}$ reported by Albonard et. al.[44] and by Geller and Gilleo [45].

Generally in garnets, rare earth metal ions Me^{3+} have large magnetic moments, but are loosely coupled. They behave paramagnetically in the exchange field produced strong Fe^{3+} coupling. So at low temperature, the Me^{3+} sublattices moment decreases sharply and Fe^{3+} coupling dominate. Therefore, compensation, T_{cmp}, will be observed in the magnetization curve, when the sign of the spontaneous magnetization reverses.

The Neel temperature of the garnet ferrites is approximately 553K. Substitution for rare earth ion for Yttrium does not affect the Neel temperature but other trivalent ion may substitute for iron in a- or d-sites where they can change strength as well as the magnitude of magnetic interactions between the tetrahedral and octahedral sites.

The magnetic properties of YIG can be tailored in a very wide range, since all three different crystallographic sites are available for substitutions by different cations with various valence states. The substitution of non-magnetic Al^{3+} or Ga^{3+} at the octahedral sites can lower $4\pi Ms$ to 300 Gauss; a- site substitutions by Sc raise $4\pi Ms$ up to 1900 Gauss; when compared with $4\pi Ms$~1760 Gauss for pure YIG. The substitution of rare earths increases the anisotropy.

2.5.3 Substitution in Garnet

The {24c} sites are the largest cation positions and are occupied by rare earth ions from Sm – Lu, Y or Ca. Larger ions such as La, Pr, Nd or Bi

can only partly substitute for the {24c} sites. The octahedral [16a] sites are the second largest cation positions and are occupied by the divalent ions of Mg, Mn, Fe, Co and Ni, the trivalent ions of Cr, Fe, In or Sc, the tetravalent ions of Sn, Zr and Hf, and the pentavalent Sb. The smallest tetrahedral (24d) sites are occupied by Fe^{3+}, Si^{4+}, Ge^{4+} and V^{5+}. Small amounts of the ions Al^{3+} and Ga^{3+} prefer the tetrahedral sites but may gradually occupy also the octahedral sites.

If one Fe^{3+} per formula unit could be replaced by a heavier Y^{3+} with no structure change the density of the resulting $4YFeO_3$, would be 5.40 g/cm^3. Actually the density of the perovskite-like compound, $YFeO_3$, is 5.67 g/cm^3 and the volume 225.9 $Å^3$ [46].

The garnets are mentioned in literature in various ways, the compound Yttrium iron garnet ($Y_3Fe_5O_{12}$) is called by the Grenoble French School of Neel, Bertaut and Pauthenet as $5Fe_2O_3.3Y_2O_3$; most American physicists mention it as YIG whereas Geller and coworkers write the formula as $\{Y_3\}[Fe_2](Fe_3)O_{12}$. The latter nomenclature is advantageous as it shows the various crystallographic sites, i.e., {3c}, [2a] and (3d) positions per formula unit corresponding to the {24c}, [16a] and (24d) sites per unit cell which contains eight formula units.

References

1. R.S. Tebble and D.J. Craik, “Magnetic Materials”, Wiley Interscience Publications (1969)
2. R.S. Waldron, “Ferrites – An Introduction for Microwave Engineers”, D. Va. Nostrand Company Ltd., Canada (1961)
3. Kato Yogoro and Takei Takeshi, Japanese Patent 98 (1932) 844.
4. J.L. Snoek, New Developments in ferromagnetic Materials, New York; Elsevier (1947)
5. L. Neel, Magnetic Properties of Ferrites: Ferrimagnetism and Antiferromagnetism, 3 (12) (1948) 137
6. W.H. Bragg, Nature 95 (1915) 561; Phil. Mag. 30 (1915) 305
7. S. Nishikawa, Proc. Tokyo Math. Phys. Soc. 8 (1915) 199
8. T.F.W. Barth, and Posnjak, Z. Krist. 82 (1932) 325
9. E.F. Bertaut and F. Forrat, Compt. Rend. 242 (1956) 382
10. S. Geller and M.A. Gilleo, Acta Cryst. 10 (1957) 239
11. M.A. Gilleo and S. Geller, J. Appl. Phys. 29 (1958) 380
12. M.A. Gilleo and S. Geller, J. Phys. Chem. Solids 10 (1959) 187
13. G. Menzer, Die Kristtallstruktur von granat centrlbl. Min. (A), 344-345 1925.
14. G. Menzer and Z. Kristallogr 63,157-158,1926
15. H. Yoder and M.L.Keith, Amer. Mineral, 36,519-533, 1951
16. J.J. Went, G.W. Rathenau, E.W. Gorter and G.W. van Oosterhout, Philips tech. Rev. 13 (1951/52) 194
17. H.Fahlenbrach and W. Heister, Arch. Eisenhiittenw 29 (1953) 523

18. G.H. Jonker, H.P. Wijn and P.B. Braun, Philips Tech. Rev. 18 (1956/7) 145
19. P.B. Braun, Philips Res. Rept. 6 (1957) 491
20. S. Geller, J. Chem. Phys. 24 (1956) 1256
21. H. Forestier and G. Guillot – Guillain, Compt. Rend. 230 (1950) 1844
22. R. Pauthenet and P. Blum, Compt. Rend. 239 (1954) 33
23. J.P. Remeika, J. Am. Chem. Soc. 78 (1956) 4259
24. S. Geller, J. Chem. Phys. 24 (1956) 1256
25. P. Coppens and M. Eibschutz, Acta Cryst. 19 (1965) 524
26. R.M. Bozorth, A.J. Williams and D.E. Walsh, Phys. Rev. 103 (1956) 574
27. R.M. Bozorth, D.E. Walsh and A.J. Williams, Phys. Rev. 108 (1957) 157
28. R.M. Bozorth and V. Kramer, J. Phys. Radium 20 (1959) 393
29. D. Treves, J. Appl. Phys. 36 (1965) 1033
30. W.C. Koehler and E.O. Wollan, Phys. Rev. 118 (1960) 58
31. M. Eibschiitz, S. Shtrikman and D. Treves, Solid State Commun. 4 (1966) 141
32. N.C. Tombs and J. Watkins, Proc. of the Institution of Electrical Engineers, 104B (5) (1957) 145
33. A.E. Van Arkel, Rec. Trav. Chim 55 (1936) 331
34. A.J.E. Welch, Proc. of the Institution of Electrical Engineers, 104B (5) (1957) 159
35. C.G. Koops, Phys. Rev. 83 (1953) 121
36. G. Menzer, 2. Krist. 69, 300 (1929)

37. R. Pauthenet, Ann. Phys. Paris 3 (1958) 424
38. S. Geller, J.P. Remeika, R.C. Sherwood, H.J. Williams and G.P. Espinoza, Phys. Rev. 137 (1965) A1034
39. F.W. Harrison, J.F.A. Thompson and K. Tweedale (1965), Proc. Intern. Conf. Magnetism, Nottingham 1964 (Phys. Soc. London) p. 664
40. H. A Kramers, Physica, 182(1934)
41. P. W Anderson, Phys. Rev. 79, (1950) 350
42. J. H. Van Vleck, J. Phys. Radium 12, (1951) 262
43. L. Neel, Ann. Phys., Paris 3, (1948) 137
44. R. Albonard, J.C. Barbier, and R Pauthenet. C.R. Acad. Sci., Paris 242, (1956) 2531
45. S.Geller and M. A. Gilleo, Acta Cryst. 10, (1957) 239
46. S. Geller and E. A. Wood, Acta Cryst. 9, 563 (1956)

2(b) Magnetism

2.6 History of Magnetism

The history of magnetism dates back over many centuries. The earliest observations of magnetism can be traced back to the Greek philosopher Thales in the 6th century B.C. In the middle ages, a host of superstitions gathered around the magnet, but the true founder of science of magnetism was William Gilbert in 1600. It was not until 1600 that the modern understanding of magnetism began. The following is the chronology of events related with magnetism.

1600: Dr. William Gilbert published the first systematic experiments on magnetism in “De Magnete”.

1819: Oersted accidentally made the connection between magnetism and electricity discovering that a current carrying coil produces a magnetic field after observing deflection in a compass needle. Next, Michael Faraday discovered the opposite effect that an electric voltage can be produced when there is a change in magnetic flux.

1825: Sturgeon invented the electromagnet.

1880: Warburg produced the first hysteresis loop for iron.

1895: The Curie law was proposed.

1905: Langevin first explained the theory of diamagnetism and paramagnetism.

1906: Weiss proposed ferromagnetic theory.

1920: The physics of magnetism was developed with the theories involving electron spins and exchange interactions; the beginnings of Quantum mechanics.

1932: Van Vleck developed Modern magnetism based on quantum mechanics.

Neel (Ferrimagnetism), Kittel (Ferromagnetism and Antiferromagnetism), Anderson (Exchange interactions) etc. made many significant contributions in this field. One has to analyze the nature of interactions at atomic/ electronic level to understand the basic concepts in magnetism.

2.6.1 Origin of Magnetism

Basically every material is magnetic in nature, as it possesses charged particles which are in continuous motion. Magnetism is present mainly due to the motion of electrons. According to Bohr (1913) theory of magnetism, the electrons are revolving around the nucleus of an atom in orbits similar to those of the planets around the sun. Figure 2.8 shows the orbit of a spinning electron about the nucleus of an atom. Here the magnetic behaviour of an atom was considered due to the orbital motion of the electrons, an effect that is similar to current carrying wire loop [1]. The basic unit of electron magnetism is Bohr Magneton. This includes not only a fundamental electric charge but also a magnetic quantity associated with the electron.

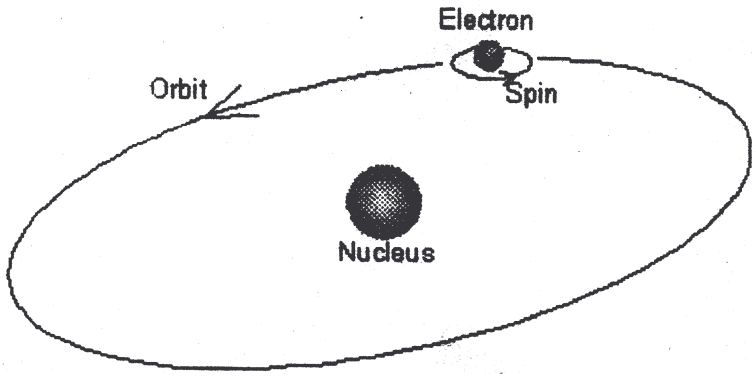

Fig. 2.8 Orbit of a spinning electron about the nucleus of an atom

Glasstone (1946) explained in classical electrodynamics, that the magnetic moment (μ), resulting due to motion of electron in its orbit can be given by

$$\mu = \frac{ep}{2mc} \tag{1}$$

where e is the electronic charge (C); p is the total angular momentum of the electron; m is the mass of the electron (g); c is the speed of light (cm/s).

In Bohr theory, the orbital angular momentum is quantized in units of h/2π. So the resulting magnetic moment can be expressed as

$$\mu = \frac{eh}{4\pi mc} \tag{2}$$

Substituting the known values and constants, we get

$$\mu_B = 9.27 \times 10^{-21} \text{ erg/oersted} \tag{3}$$

This constant, Bohr Magneton, is the fundamental unit of magnetic moment in Bohr theory.

In 1925, Goudsmit and Uhlenbeck (1926) postulated the electron spin. At about the same time, Heisenberg (1926) and Schrodinger (1929) developed wave mechanics, which was more successful in accounting for magnetic phenomena. In Quantum Mechanics, the advanced source of magnetism is the spin of the electron on its own axis similar to that of the earth. Since the electron contains electric charge, the spin leads to the movement of this charge or electric current, which produces a magnetic moment. It has been found both experimentally as well as theoretically that the magnetic moment associated with the spin moment is equal to One Bohr

Magneton. Some other important concepts related to magnetic moments are explained below [2-13].

The orbital magnetic moment is given by

$$\mu_l = \frac{-e\omega_0 r^2}{2c} \qquad \text{OR} \qquad (4)$$

$$\mu_l = \frac{-e}{2mc} P_l \qquad (5)$$

where e is the electronic charge; ω_0 is the angular velocity of electron; r is the radius of the circular orbit; c is the velocity of light; P_l is the orbital angular momentum of electron.

Similarly spin magnetic moment is given by

$$\mu_s = \left(\frac{-e}{2mc}\right).2.P_s \qquad (6)$$

where P_s is spin angular momentum of the electron.

Here negative sign indicates that the magnetic moment directs in a direction opposite to vector representing the angular momentum.

The main interactions, which arise because of the relative orientations of the orbital and spin moments of various electrons, are as follows:

(a) The coupling of orbital motion of electrons and spin moment leads to Coulomb interaction.

(b) Spin – orbit interactions, which magnetically couple the orbital motion of each electron to its own spin.

(c) Interactions produced because of electric field of neighbouring ions of the crystalline lattice.

Today we cannot think of modern technology without magnetic materials and magnetic phenomena. Magnetic disks or tapes, motors, generators, telephones, transformers, electromagnets, permanent magnets, loudspeakers and magnetic strips on credit cards are only a few examples of their applications. Due to many common mechanisms such as dipoles, field lines, attraction/ repulsion, field strength etc., magnetism and electricity can be considered to be siblings. These two phenomena are linked to each other by the famous Maxwell equations.

2.7 Classification of Magnetic Materials

The origin of magnetism lies in the orbital and spin motions of electrons and how the electrons interact with one another. With this background on origin of magnetism, it is appropriate to switch over to the magnetic behaviour of solids. Figure 2.9 shows the different spin arrangements in various types of materials. This is divided into two categories.

- **Non – Cooperative phenomena**

Where there is no collective magnetic interaction of atomic magnetic moments with each other and are not magnetically ordered.

For example: (i) Diamagnetic materials (ii) Paramagnetic materials

- **Cooperative phenomena**

Where the magnetic dipoles interact with each other introduces three types of behaviour, For example: (i) Ferromagnetism (ii) Antiferromagnetism (iii) Ferrimagnetism. These materials exhibit long range magnetic order below a certain critical temperature.

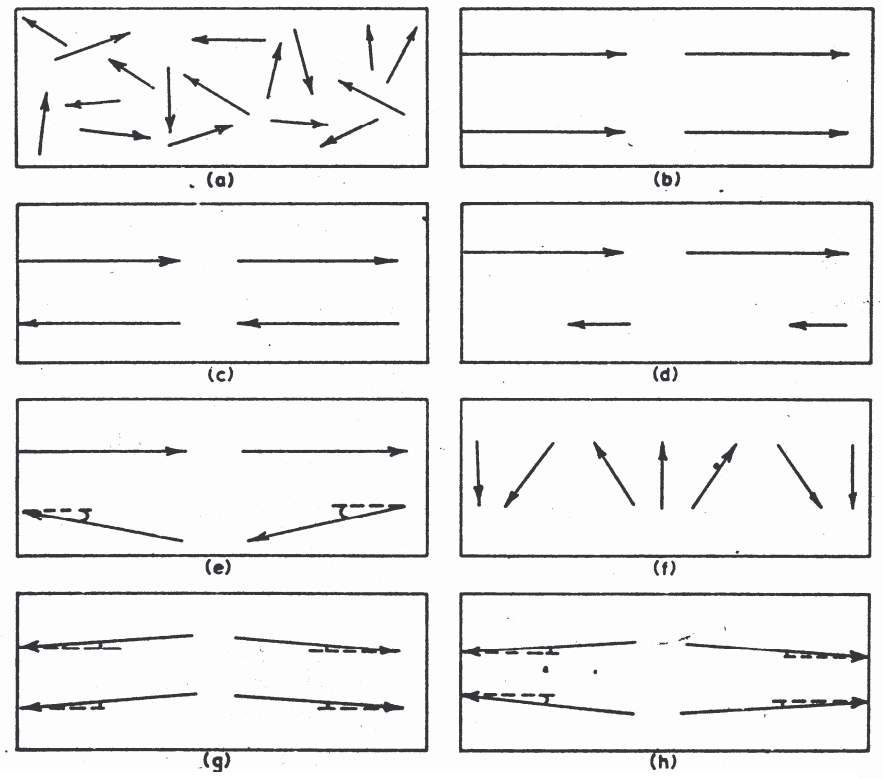

Fig. 2.9 Schematic representation of spin arrangements

(a)	Paramagnetic state	(b)	ferromagnetism
(c)	Neel type antiferromagnetism	(d)	Neel type ferrimagnetism
(e)	Yafet – Kittel type ferrimagnetism	(f)	helical spiral structures
(g)	canted spin weak ferromagnets	(h)	canted spin compensated antiferromagnets

The different types of magnetism existing in materials can be characterized by the magnitude and the sign of the susceptibility. Since every material responds in a different way to an applied magnetic field (H), different mechanisms must be responsible for the magnetic properties. A certain amount of magnetization (M) develops which is defined as magnetic moment per unit volume and is given by $M = \chi H$ where χ is known as magnetic

susceptibility when a solid is placed in a magnetic filed (H). For isotropic materials, χ is scalar as M and H are in the same direction whereas χ is a tensor in case of anisotropic materials as M and H is not necessarily in the same direction. The magnetic induction (B) is defined as

$$B = H + 4\pi M \tag{7}$$

And the permeability (μ) of the material is given as

$$\mu = \frac{B}{H} = 1 + 4\pi\chi \tag{8}$$

2.7.1 Non – Cooperative Phenomenon

(i) Diamagnetic materials

Diamagnetism is a fundamental property of all materials; however, it is very weak and is generally masked by the larger paramagnetic or ferromagnetic term. It is produced inside a material due to non – cooperative magnetic interactions between orbiting electrons on the application of a magnetic field. Diamagnetic substances have no net magnetic moments, as there are no unpaired electrons. Under the influence of an applied field (H), the precessional motion of the spinning electrons which is a type of electric current produces a magnetization (M) in the opposite direction to that of H. so these materials have a negative susceptibility. As shown in Figure 2.10 (a), the magnetization is zero when the applied field is zero. The other important feature of these materials is that the value of susceptibilty is temperature independent as shown in Figure 2.11(a). The order of χ_d is $\approx -10^{-5}$ emu. The theory of diamagnetism, developed by Langevin in 1905, is based upon Lenz's law which states that the magnetic filed produced by an induced current opposes the change in magnetic field which produces it. The

susceptibilty in superconductors is therefore –1 compared to about -10^{-5} in the normal state. This strong diamagnetism can be used for frictionless bearings for support of loads by a repelling magnetic force.

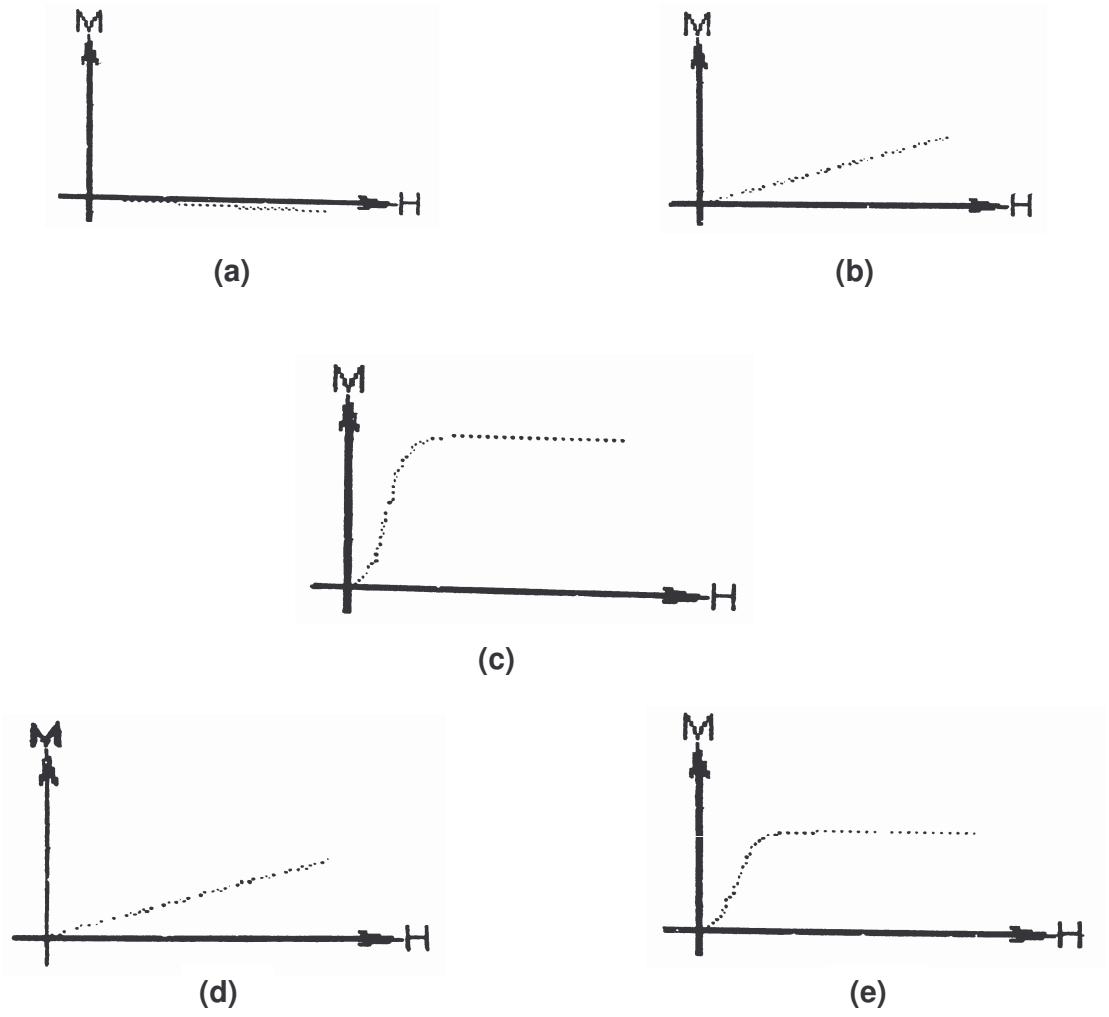

Fig. 2.10 M – H curves depicting different types of magnetic behaviour (a) diamagnetism (b) paramagnetism (c) ferromagnetism (d) antiferromagnetism (e) ferrimagnetism

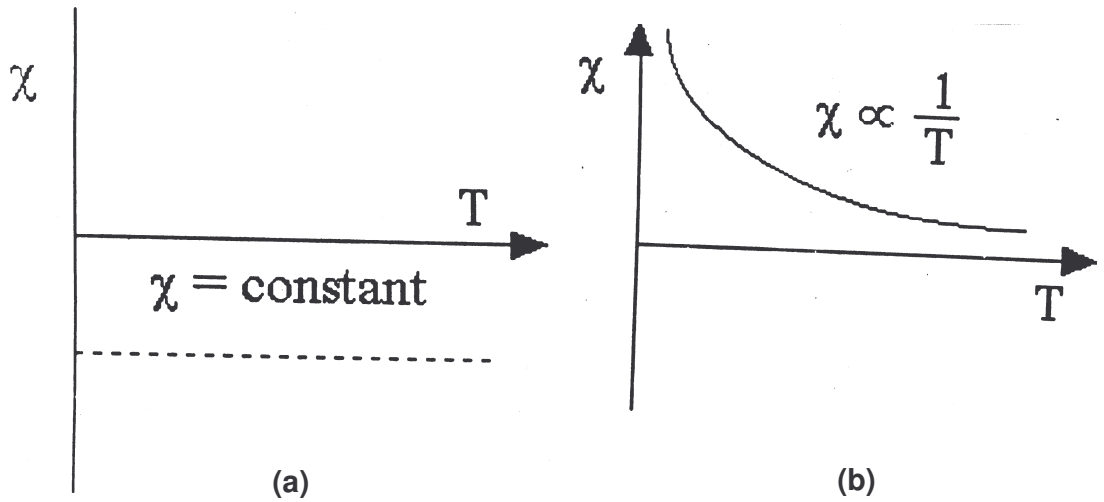

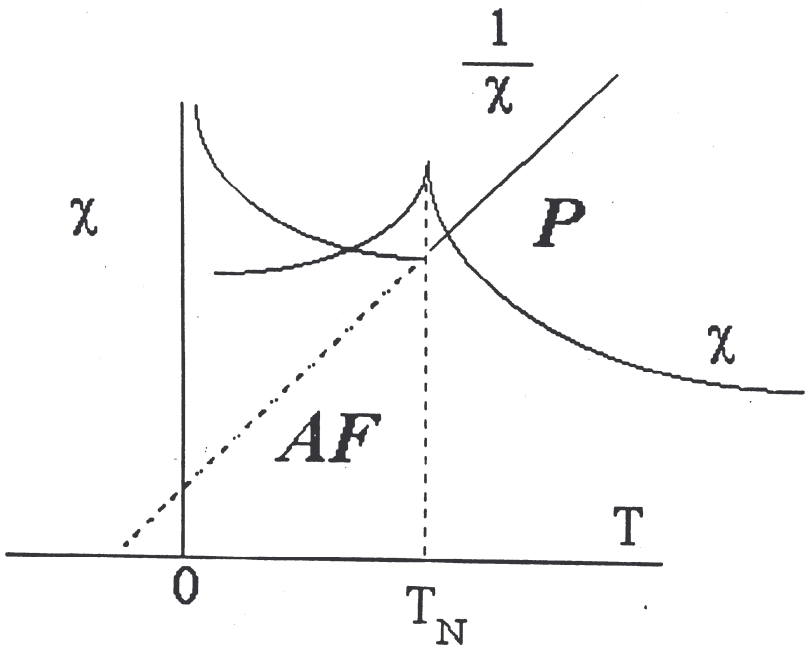

Fig. 2.11 Temperature dependence of susceptibility showing different types of magnetic behaviour.
(a) diamagnetism (b) paramagnetism (c) antiferromagnetism

(ii) Paramagnetic materials

Paramagnetic magnetization arises from the partial alignment of magnetic moments in the same direction as that of the applied field. They have net magnetic moment due to presence of unpaired electrons in the partially filled orbitals. Iron is one of the most important atoms with unpaired electrons. Paramagnetism in solids arises when the electrons spin around their own axis and the spin magnetic moments are randomly oriented such that no net magnetic moment results. Like diamagnetism, the magnetization is zero when the applied field is zero and on the application of field (H), there is partial alignment of the atomic magnetic moments in the field direction resulting a net positive magnetization as shown in Figure 2.10(b) and positive susceptibility shown in Figure 2.11(b). The increase in temperature increases the thermal agitation in these materials. With this, the efficiency of the field in aligning the magnetic moments is opposed by the randomizing effects of temperature i.e., it becomes harder to align the atomic magnetic moments and hence the susceptibilty decreases. This leads to the temperature dependent susceptibility, known as Curie law and is given as

$$\chi = \frac{C}{T} \tag{9}$$

where C is a material constant called the Curie constant. The materials obeying Curie law have magnetic moments localized at the atomic or ionic sites and no interaction between neighbouring magnetic moments. For example: hydrated salts of the transition metals ($CuSO_4.5H_2O$) have a magnetic moment and no interaction between neighbouring magnetic moments as it is surrounded by non – magnetic ions/ atoms.

The more general relation known as Curie – Weiss law, given by equation (10) incorporates interactions between neighbouring magnetic moments i.e.,

$$\chi = \frac{C}{T - \theta} \tag{10}$$

It incorporates a temperature constant (θ) which is derived from Weiss theory, proposed for ferromagnetic materials. This is related with the interaction between magnetic moments.

In equation (10), θ can be positive, negative or zero. So when θ is non – zero, then there is an interaction between neighbouring magnetic moments, and the materials is paramagnetic above a certain transition temperature. If θ is positive, material is ferromagnetic below the transition temperature and θ corresponds to transition temperature (Curie Temperature T_c). If θ is negative, materials is antiferromagnetic below transition temperature (Neel temperature T_N), however the value of θ does not relate to the Neel temperature (T_N).

It is important to note that this equation (10) is only valid when the material is in a paramagnetic state.

2.7.2 Cooperative Phenomenon

(i) Ferromagnetic materials

The intense response to an applied magnetic field is known as ferromagnetism. Ferromagnetic materials are those in which atoms are arranged in a lattice and the interacting magnetic moments align parallel to each other. The real progress in understanding ferromagnetism was not made until Pierre Weiss in 1906 advanced his hypothesis of the molecular field [14].

The first classical theory of ferromagnetism explaining the presence of a molecular field was postulated by Weiss in 1907 [15]. This molecular field magnetizes the materials to saturation. The regions in the ferromagnetic materials where the cooperative effect extends are known as magnetic domains. Weiss in 1907 proposed the existence of these domains in ferromagnetic materials (Figure 2.12) to account for certain magnetic phenomena.

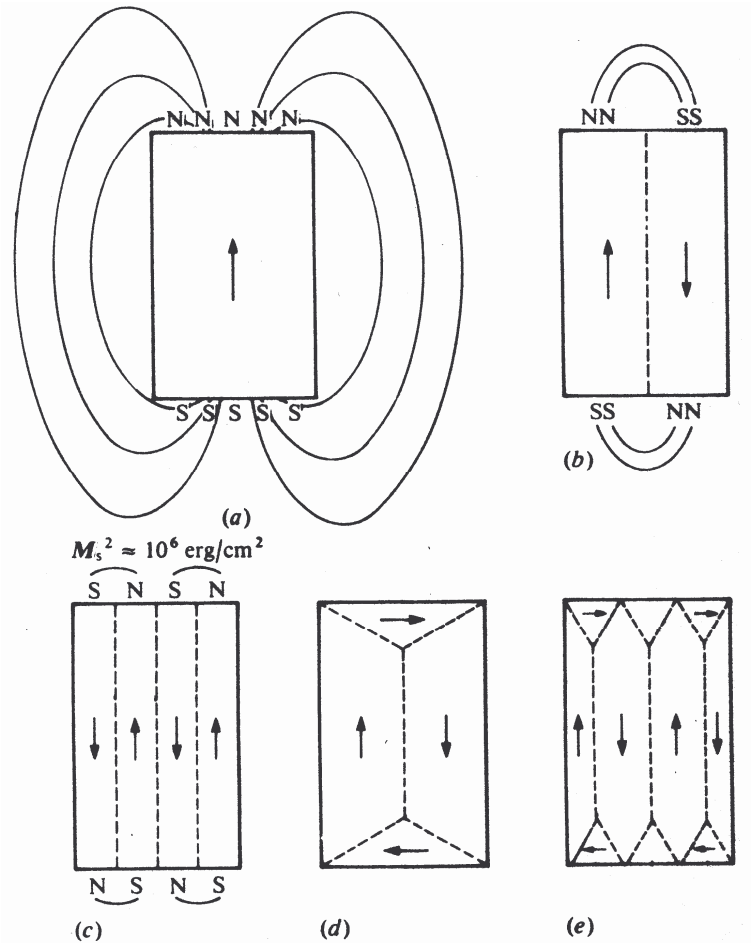

Fig. 2.12 Different kinds of magnetic domains

The strong internal fields which align the magnetic moments or spins are known as molecular field and this alignment is only due to one quantum

mechanical process known as exchange interactions. This quantum mechanical model was given by Heisenberg in 1928. The magnitude of the Weiss or molecular field is of the order of 10^5 – 10^7 Oe. Ferromagnetic materials exhibit parallel alignment of moments resulting in large net magnetization even in the absence of field. Figure 2.13 shows the M – H plot for a ferromagnetic material. The movement of these domains determines how the material responds to an applied field. So these materials are usually compared in terms of saturation magnetization rather than susceptibility.

Two main features of ferromagnetic materials are:

(a) Spontaneous Magnetization (b) Existence of magnetic ordering temperature

(a) Spontaneous Magnetization

It is the net magnetization, which exists inside a magnetized material in the absence of field. Another closely related term is saturation magnetization that is the measure of maximum induced magnetic moment on applying a magnetic field (H_{sat}) beyond which no further increase in magnetization occurs. The main difference between the two terms is that saturation magnetization is the intrinsic property independent of particle size but depends strongly on temperature.

(b) Magnetic Ordering Temperature (Curie Temperature)

Ferromagnetic materials exhibits very strong electronic exchange forces, but increase in temperature leads to thermal agitation which overcomes the exchange and produce randomizing effect. So, the degree of alignment of magnetic moments decreases and hence also the saturation magnetization.

All this occurs at a particular temperature called the Curie temperature (T_c) where the materials become paramagnetic. Below T_c ferromagnetic is ordered and above T_c, it is completely disordered. The value of saturation magnetization becomes almost zero at T_c. The Curie temperature is also an intrinsic property and is a diagnostic parameter for mineral identification. Above the Curie temperature, the materials becomes paramagnetic, then the susceptibility decreases with temperature i.e., above T_c, the susceptibility varies according to Curie – Weiss law.

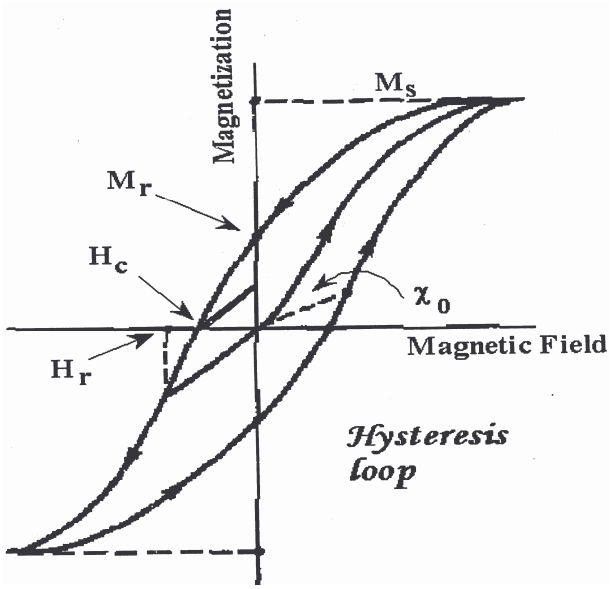

Fig. 2.13 Hysteresis loop of a permanent magnet

In addition with the above said properties, ferromagnetic materials exhibits hysteresis loop. Hysteresis is derived from the greek word meaning “to lag”. The lagging of the magnetic flux in a magnetic material behind the magnetizing force which is producing it, is known as magnetic hysteresis. A plot of the variation of magnetization with magnetic field forms a closed figure when the magnetizing force is taken through a complete cycle of increasing values (upto saturation magnetization). Figure 2.13 shows a typical hysteresis

loop of a ferromagnetic material. The area of this loop is proportional to the magnetic hysteresis loss. This hysteresis loop is the main feature of ferromagnetic materials because this M – H variation is always linear in case of diamagnetic as well as paramagnetic materials. When the magnetic field is increased, the magnetization also increases reaching a saturation value. If the field is reversed, the magnetization does not follow the same path. Even at the zero fields, the material persists as a saturation remanenece (M_r). It is also called residual magnetization or retentivity. So the value of reverse field which reduces the residual magnetism to zero is called the coercive field or coercivity of the material.

Various hysteresis parameters are not solely intrinsic properties but dependent on grain size, domain state, stresses and temperature.

(ii) Antiferromagnetic materials

In ferromagnetism, there exist exchange interactions which are aligned parallel in a domain. Figure 2.10(c) shows the variation of magnetization (M) with applied field (H). Neel [16] in 1932 observed that some alloys do not obey Curie law at low temperatures but follow Curie – Weiss law at higher temperature.

$$\chi = \frac{C}{(T + \theta)} \tag{11}$$

Also $\chi = \frac{C}{(T - T_N)}$ where T_N = Neel Temperature

When the high temperature linear slope of χ vs T was extrapolated, (Figure 2.11(c)) it resulted into a negative value i.e., negative Curie point. To explain this, Neel postulated a negative exchange interaction, which aligned

the neighbouring magnetic moments antiparallel. At lower temperatures this negative exchange interaction prevents normal paramagnetic alignment. At higher temperatures, this negative exchange interaction diminished and then susceptibility increases upto Neel point where this negative exchange disappears. After this the system follows Curie – Weiss law dependence.

Such type of negative exchange behaviour exhibited by a material is known as antiferromagnetism. If the two sublattices A and B are having magnetic moments equal but directed opposite to each other, the net moment is zero i.e., $M_a = M_b$, such type of ordering is known as antiferromagnetism. The main distinction to antiferromagnetism is its behaviour of susceptibility above Neel temperature (T_N).

Antiferromagnetic materials have no hysteresis, zero remanence but a small positive susceptibility. But in some cases, there is slight deviation from ideal antiferromagnetism i.e., the spins are slightly tilted ($< 1^0$) or canted resulting into small net magnetization. Such type of canted antiferromagnets exhibit magnetic characteristics like ferro – and ferrimagnetics (e.g., hysteresis, remanence, Curie point). Hematite is best known example of canted antiferromagnetism.

(iii) Ferrimagnetic materials

At the same time when Neel gave the theory of antiferromagnetism, Snoek [17, 18] obtained interesting properties in some oxides materials called ferrites which find wide applications at higher frequencies. Neel then extended his theory of antiferromagnetism to include ferrites. In these crystal structures, two magnetic sublattice (called A and B with negative exchange interaction) are separated by oxygen ions. In this magnetic structure, the exchange

interactions are mediated by the oxygen anions known as indirect or superexchange interactions. These strongest superexchange results into alignment of spins between A and B sublattices. The difference between antiferromagnetism and ferrimagnetism is that the moments on the two sites are equal in case of antiferromagnetism whereas not equal in case of ferrimagnetism. Thus moments on A and B sublattices are not equal resulting in a net magnetic moment which is due to the difference in the moments on the two sites. This difference is usually due to difference in the number of magnetic ions on the two types of sites. That's why this behaviour is known as ferrimagnetism or uncompensated antiferromagnetism. Neel [19] published his theory in 1948 based on these two phenomenons. Because of the presence of net magnetic moment in these materials, ferrimagnetism is similar to ferromagnetism. Thus these materials break down into magnetic domains similar to ferromagnetic materials. It exhibits all the hallmarks of ferromagnetic behaviour i.e., spontaneous magnetization, Curie temperature, hysteresis and remanence although both ferro and ferrimagnets have very different magnetic ordering. Magnetite is a well-known ferrimagnetic material. It was considered ferromagnetic until Neel in 1940's explained the phenomenon of ferrimagnetism. Ferrimagnetic materials also have Curie temperature and thus, these materials exhibit similar paramagnetic behaviour above Curie point. The variation of $1/\chi$ vs T would be concave because of presence of negative exchange interactions as in case of antiferromagnetic materials which approaches to an asymptotic value that extrapolate to give a negative value. This type of behaviour strongly confirms the Neel's theory.

The variation of $1/\chi$ vs T for all the types of magnetic materials is shown in Figure 2.14.

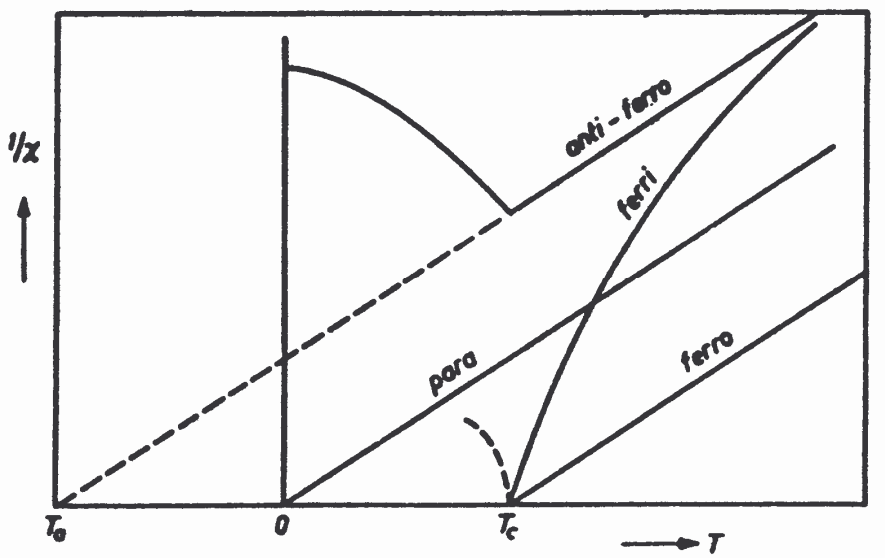

Fig. 2.14 Comparison of the temperature dependencies of the reciprocal susceptibilities of paramagnetic, ferromagnetic, antiferromagnetic, and ferrimagnetic materials. (Smit & Wijn) [2]

2.8 Intrinsic Properties of Magnetic Materials

These are the properties, which denotes the characteristics of a material and are independent of the microstructure i.e., grain size, orientation of these grains in a crystal. Intrinsic properties include Curie temperature, saturation magnetization and magnetocrystalline anisotropy.

2.8.1 Saturation magnetization

When all the dipole moments associated with all the molecules in the material are aligned in the direction of the applied field at 0 K, then the net resultant dipole moment per unit volume is known as the saturation magnetization ($4\pi M_s$). The M_s is expressed as

$$M_s = N.\ \mu_m \qquad (12)$$

where N is the number of dipoles per unit volume and μ_m is the dipole moment of each molecule. Saturation magnetization mainly depends on the chemical composition and electronic structure of the constituents. The contribution to net magnetic moment in ferrites come from the orbital motion of the electrons and the parallel uncompensated electron spins of the individual metal ions. In the ionic materials, major contribution to magnetic moment comes from the spin motion of the electrons. However the contribution due to the orbital motion is negligibly small in most cases due to quenching effect of crystalline field [20]. Since the oxygen ions have got the zero magnetic moment they do not contribute the net magnetic moment, Therefore the magnetic moment in the ferrites arises only due to the uncompensated electron spins of the metal ions, in the sublattices.

In case of ferromagnetic material, M_s depends on the alignment of the moments as their alignment can be destroyed by thermal vibration that results in reduction in the value of saturation magnetization (M_s). In case of ferrimagnetism, it depends upon the relative alignment of moments as all the moments don't align parallel even at zero Kelvin.

2.8.2 Magnetic Anisotropy

The simplest meaning of this term is that the magnetic properties depend on the direction in which they are measured. In other words, we can say the magnetic properties vary depending on the crystallographic direction in which the dipoles are aligned. Anisotropy is of great interest as it is exploited in the design of most magnetic materials of commercial importance.

Kinds of Anisotropy

(i) Crystal Anisotropy, also called magnetocrystalline anisotropy (Intrinsic)

(ii) Shape Anisotropy

(iii) Stress Anisotropy

(iv) Anisotropy induced by: (a) Magnetic annealing (b) Plastic deformation (c) Irradiation

(v) Exchange Anisotropy

The first type i.e., crystal anisotropy also known as magnetocrystalline anisotropy is an intrinsic property where all the other types come under extrinsic properties. Magnetocrystalline anisotropy depends upon the structure of the crystal whereas shape and stress anisotropy depends upon grain shape and applied or residual stresses respectively.

(i) Magnetocrystalline Anisotropy

This is an intrinsic property of ferrites independent of grain size and shape. It can be regarded as a force, which tends to bind the magnetization to certain preferred directions in the crystal. So, it can be observed by measuring magnetization curves along different crystallographic directions. To understand crystal anisotropy, we need to know about the anisotropy field denoted by H_a. We can define this anisotropy field in different ways:

Crystal anisotropy forces that bind the magnetization (M_s) of any domain to an easy direction can be expressed in terms of anisotropy field (H_a), which is in turn related to anisotropy constants. It is also defined as the field required to turn the magnetization vector from certain preferred direction to other direction, i.e., from easy direction to hard direction. Fig. 2.15 shows magnetization vector along easy as well as hard directions for Cobalt crystal.

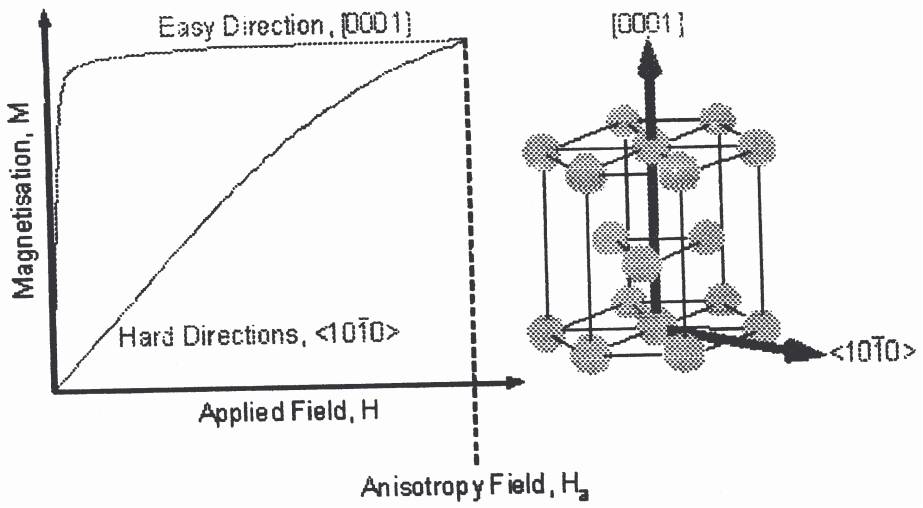

Fig. 2.15 The magnetocrystalline anisotropy of cobalt

In case of single crystal, magnetocrystalline anisotropy can be defined as the energy, which is required to deflect the magnetic moments from the easy to the hard direction. The crystal anisotropy is originated mainly due to spin – orbit coupling. This term coupling means a kind of interaction. So the exchange interaction between two spins leads to spin – spin coupling. This is very strong as it helps to keep spins parallel or antiparallel with respect to each other. Now the exchange energy associated with this interaction is isotropic as it depends only on the angle between adjacent spins but not at all on the direction of spin axis with respect to crystal lattice. That's why spin – spin coupling don't contribute to the anisotropy.

The orbit – lattice coupling is also very strong. This is due to the fact that the orbital magnetic moments are almost entirely quenched (when orbital magnetic moment of the electron is much smaller than the spin moment; it is said that orbital magnetic moment is quenched). This means that the orientations of the orbits are very strongly fixed to the lattice that even large

fields cannot change them. One more coupling between spin and the orbital motion of electron exist. On the application of an external field, the field tries to reorient the spin of an electron with the result; the orbit also tries to be reoriented. But orbit is strongly fixed to lattice thus resist the rotation of spin axis. Now the anisotropy energy is the energy required to rotate the spin system of a domain from the easy axis i.e., energy required to overcome the spin – orbit coupling. This coupling is relatively weaker as field of few hundred Oersted are usually enough (strong) to rotate the spins. Spin – lattice coupling is also a weak interaction. All the above said relationships are summarized and shown in Figure 2.16.

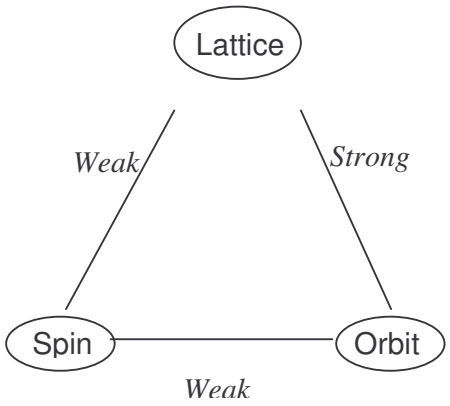

Fig. 2.16 Spin – lattice – orbit interaction

The strength of the anisotropy in any crystal is measured by the magnitude of the anisotropy constant K_1 and K_2. The magnetic anisotropy of a cubic single crystal can be expressed in terms of anisotropy free energy, which is a function of direction cosines α_1, α_2 and α_3 of the magnetization vector M.

$$E_A = K_0 + K_1 (\alpha_1^2\alpha_2^2 + \alpha_2^2\alpha_3^2 + \alpha_3^2\alpha_1^2) + (\alpha_1^2\alpha_2^2\alpha_3^2 + \ldots.) + \ldots. \quad (2.13)$$

where α_1 is the referred cubic axis; K_1 & K_2 are the magnetocrystalline anisotropy constants.

Here in this equation for a cube $\alpha_1^2 + \alpha_2^2 + \alpha_3^2 = 1$ and odd powers are missing because of even symmetry.

In case of antiferromagnetic crystals,

$$E_A = \frac{1}{2} K\left(\sin^2\theta_1 + \sin^2\theta_2\right) \qquad (2.14)$$

where θ_1 & θ_2 are the angles which sublattice magnetization M_1 and M_2 make with the easy axis of magnetization.

In hexagonal close – packed structures, the c – axis is the easy magnetization direction and within accuracy of measurements, any direction in the basal plane is equally hard. In that case, the anisotropy energy E, depends on a single angle (θ) between M_s vector and the c- axis. Therefore,

$$E = K_0^{/} + K_1^{/}\cos^2\theta + K_2^{/}\cos^4\theta + \ldots. \qquad (2.15)$$

To rewrite above equation in terms of $\sin\theta$. Put $\cos^2\theta = 1 - \sin^2\theta$

$$E = K_0 + K_1\sin^2\theta + K_2\sin^4\theta + \ldots. \qquad (2.16)$$

When K_1 is positive and $K_2 > -K_1$, the energy E is a minimum for $\theta = 0$ and the c – axis is one of the easy magnetization axis which is true in case of single crystal of Co and hexagonal barium ferrite and strontium ferrite etc. So a single crystal with a single easy axis, along which the magnetization point either upwards or downwards is known as uniaxial crystal.

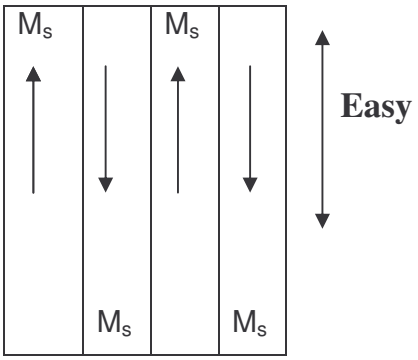

Fig. 2.17 Domain structure of a uniaxial crystal

This energy E will have a minimum for $\theta = 90^0$ if K_1 is negative and $K_2 < |K_1|/2$, or if K_1 is positive and $K_2 < -K_1$. In this case, basal plane will be the easy plane of magnetization.

The magnetic potential energy is

$E_p = -M_s H \cos(90^0 - \theta)$

The condition for minimum total energy is

$2K_1 \sin\theta\cos\theta + 4K_2 \sin^3\theta\cos\theta - M_s H\cos\theta = 0$

Also $M = M_s \cos(90^0 - \theta)$

Elimination of θ from these two equations gives

$$H = \frac{2K_1}{M_s}\left(\frac{M}{M_s}\right) + \frac{4K_2}{M_s}\left(\frac{M}{M_s}\right)^3 \qquad (2.17)$$

With saturation being attained a field given by

$$H = \frac{2K_1 + 4K_2}{M_s} \qquad (2.18)$$

If $K_2 = 0$, the magnetization curve becomes a straight line.

$$H = \frac{2K_1 M}{M_s^{\,2}} \tag{2.19}$$

And the saturating field becomes $H = \frac{2K_1}{M_s}$ (2.20)

From above equation, the value of K_1 can be calculated. The crystal anisotropy is structure insensitive property as it is due to spin – orbit coupling but various crystal imperfections like residual strain, lattice vacancy, inclusion deviate it from accuracy and it becomes effectively structure sensitive. Anisotropy constant depend on temperature variation as it decreases with the increase in temperature and attains zero value at or even before Curie point.

2.9 Magnetic Interactions

In magnetic materials, generally two types of magnetic interactions occurs:

(a) Direct exchange interactions (b) Indirect exchange interactions

Direct exchange interactions involve the direct overlapping of the orbitals of two interacting magnetic ions. In first transition series, there is involvement of T_{2g} and E_g orbitals.

Indirect exchange interactions are also known as superexchange interactions. The direct exchange interactions used to explain the origin of strong Weiss field was ruled out to explain the Neel molecular field because of large separation between the magnetic ions. Kramers in 1934 and Anderson in 1950 proposed a new mechanism called superexchange. This involves the coupling between the magnetic ions by higher order interactions involving the

intervening anions. Superexchange interactions is applicable between the cations which are separated by a larger distances. Hence direct exchange interaction is not possible or can be ignored as direct interactions becomes important only when the separation is very small so that overlapping between T_{2g} or E_g becomes possible. In ferrites, the active participation of anions makes the coupling possible between cations. Since the extent of overlapping of the orbitals decreases exponentially with distance. This superexchange between 3d ions involves the overlap of the T_{2g} and E_g orbitals with the 2p orbitals of the anions. T_{2g} orbitals consist of d_{xy}, d_{yz} and d_{xz} orbitals while E_g orbitals are the d_z^2 and the $d_{x^2-y^2}$. The anion orbitals which participate in these interactions are essentially P_x, P_y and P_z orbitals which are highly directional. The sign and strength of these interactions depend upon the bond angles and bond distances between two cations and the intervening anions. The semi – empirical rules were given by Goodenough [92] and Kanamori [93]. These interactions were originally formulated 180^0 and 90^0 configurations.

2.10 Neel's Theory of Antiferromagnetism & Ferrimagnetism

Antiferromagnetic and ferrimagnetic materials have low electrical conductivity and so their magnetic moments may be regarded as completely localized in their particular ions. Therefore a molecular field (localized – moment) theory is therefore expected to be valid. Also the exchange forces between the metal ions in a ferrimagnetic material act through oxygen ions by means of indirect exchange (superexchange) mechanism just like in antiferromagnets. In ferromagnetic materials, the AA interactions differ from BB interactions although the ions are identical because the number and

arrangement of neighbouring ions on both the sites differ with respect to each other.

Neel in 1948 gave a modification of Weiss model of ferromagnetism and replaced it with new theory. This theory is based on the following assumptions:

- The crystal lattice is subdivided into two or more sublattices such as tetrahedral (A) and octahedral (B) sites each possessing uniform magnetism.
- There exists 'n' number of identical magnetic ions per unit volume, with a fraction 'λ' located on A site and a fraction ν (1-λ) on B sites i.e., $\lambda + \nu = 1$.
- The interactions A – B and B – A are identical and predominant over A – A and B – B interactions.
- An internal Weiss molecular field acts on the ions.

Neel defined that the magnetic field acting upon an ion can be written as

$$H = H_0 + H_m \qquad (2.21)$$

where H_0 is the external applied field and H_m is the internal molecular field that arises due to interactions among other atoms or ions.

Let μ_A and μ_B be the average moment of an A and B ions respectively. $\mu_A \neq \mu_B$ because these ions being on different sites are exposed to different molecular fields. Then magnetization of A sublattice is $M_A = \lambda n \mu_A$

Put $n\mu_A = M_a$ then $M_A = \lambda M_a$ and $M_B = \nu M_b$

The total magnetization is $M = M_A + M_B = \lambda M_a + \nu M_b$ (2.22)

The molecular field acting on sublattice A is

$$H_{mA} = - \gamma_{AB} M_B + \gamma_{AA} M_A \qquad (2.23)$$

The molecular field coefficient is negative (antiparallel) between A and B ions and a positive (parallel) interaction between A ions.

Similarly $H_{mB} = - \gamma_{AB} M_A + \gamma_{BB} M_B$ (2.24)

The coefficient γ_{AA} and γ_{BB} are now unequal and can be expressed as fractions of γ_{AB}.

$$\alpha = \frac{\gamma_{AA}}{\gamma_{AB}} \quad \text{and} \quad \beta = \frac{\gamma_{BB}}{\gamma_{AB}} \tag{2.25}$$

The molecular fields are then

$H_{mA} = \gamma_{AB} (\alpha\lambda M_a - \nu M_b)$ (2.26)

$H_{mB} = \gamma_{AB} (\beta\nu M_b - \lambda M_a)$ (2.27)

These equations are valid above and below the Curie temperature.

Here γ's are the appropriate molecular field coefficients. It may be shown that $\gamma_{AB} = \gamma_{BA}$ but $\gamma_{AA} \neq \gamma_{BB}$ unless the two sublattice are identical.

If $M_a = M_b$, the system is antiferromagnetic and if $M_a \neq M_b$, the system is ferrimagnetic.

The subdivision of ferrites into different sublattices made it easy for Neel (1948) to explain the magnetic moment of inverse spinel ferrites. Gorter further extended the validity of the collinear Neel structure to more complicated ferrites. The validity of Neel's theory for three sublattices is confirmed by Pauthenet. At T = 0 if $M_a \neq M_b$ then the compound is ferrimagnetic and the total magnetic moment can be given as the algebraic sum of M_a and M_b i.e., $M = M_a + M_b$. However, the temperature variation of M_a and M_b may be different and the resultant M (= $M_a + M_b$) may pass through

zero as shown in Fig. 2.18. Here the point of zero magnetization is called the compensation point and was predicted by Neel (1948).

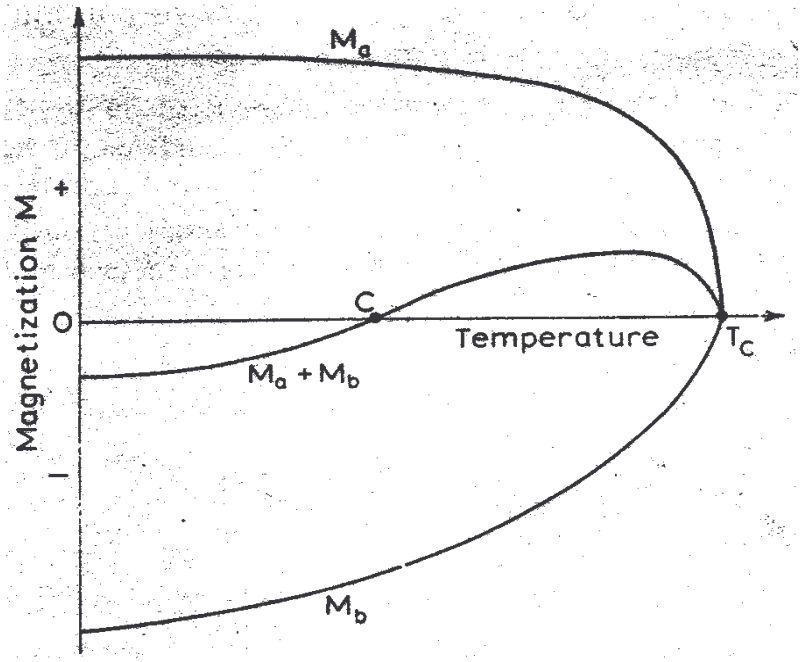

Fig. 2.18 Temperature variation of the opposite sublattice magnetizations M_a and M_b. C is the compensation temperature which lies below Curie temperature T_c.

References

1. A. Goldman, “Modern ferrite Technology”, Van Nostrand Reinhold, New York (1990).
2. J. Smith and H.P.J. Wijn, “Ferrites”, John Wiley Publications, New York (1959)
3. D.H. Martin, Magnetism in Solids (1967) Iliffe Books Ltd., London.
4. A.J. Dekker, Solid State Physics (1952) McMillan and Co. Ltd. London.
5. M.M.Schieber, “Experimental Magnetochemistry” (1967) North Holland Publishing Company Amsterdam.
6. Ing. C. Heck, “Magnetic Materials and Their Applications” (1974) Butterworth and Co. (Publishers) Ltd.
7. G.T. Rado and H. Suhl, Magnetism (1963 – 1966) Academic Press, New York.
8. J.B. Goodenough, Magnetism and Chemical Bond (1963) Interscience, New York.
9. C.P. Poole, Jr. and H.A. Farach, “The Theory of Magnetic Resonance (1972) John Wiley and Sons Inc., New York.
10. A.S. Chakravarty, “Introduction to the Magnetic Properties of Solids” (1980) A Wiley – Interscience Publication, New York.
11. J.S. Grifith, “The Theory of Transition Metal Ions” (1961) Cambridge University Press, London.
12. D. Hadfield, “PermanentMagnets and Magnetism” (1962) Iliffe Books Ltd., London.

13. D.J. Craik, “Magnetic Oxides (1975) John Wiley and Sons Ltd., New York.
14. P. Weiss, “La Variation du Ferromagnetisme avec la temperature”, Compt. Rend., 143 (1906) 1136.
15. P. Weiss, J. de Physique 6 (1907) 661.
16. L. Neel, Ann. De Phys. 17 (1932) 61.
17. J.L. Snoek, New Developments in ferromagnetic Materials, New York; Elsevier (1947).
18. J.L Snoek, Physics (Amsterdam) 3 (1936) 463.
19. L. Neel, Magnetic Properties of Ferrites: Ferrimagnetism and Antiferromagnetism, 3 (12) (1948) 137.
20. J. Smit and H.P.J. Wijn, “Ferrites”, Philips Technical library, eindhoven, Holland (1959)

Chapter 3

Synthesis, Theoretical and Experimental aspects of Characterization Techniques

The chapter presents relevant background, theoretical and experimental concepts of the characterization techniques used for the present work. The different sections in the chapter describe the sample preparation methods and different techniques employed to study the structural, elastic, electrical, dielectric, magnetic and optical properties of various garnet compositions.

3.1 Synthesis process for Bulk and Nanomaterials

The properties of ferrites are much sensitive to the preparation conditions. Various methods are developed for preparing solid solution series; depending on the form of the desired product namely;

- Ceramic method (solid-state reaction route)
- Wet Chemical method
- Sol-gel method
- Combustion method
- Citrate precursor method
- Hydrothermal synthesis
- Reverse micelles technique

Different synthesis techniques have their own advantages and disadvantages.

3.1.1 Solid state reaction route

This is the conventional powder processing method which is commercially accepted since it is possible to maintain the stoichiometry of the final product even at large scale industrial production. In this method, the preparation of ferrites takes place at about 1000°C by solid state reaction. The finely grained

powder of the required composition is shaped by pressing and finally sintered to obtain ceramically prepared ferrites. The solid-state reaction route can be divided into four major steps:

(i) Initial mixing, grinding and pelletizing of powder

(ii) Pre- sintering

(iii) Regrinding and re-pelletizing

(iv) Final Sintering

(a) Mixing of powder

The following factors are basically considered in the choice of raw materials:

(1)High purity (2) small particle size (3) cost effectiveness

The selected starting chemicals should be dried thoroughly prior to weighing, especially hygroscopic ingredient. Fine-grained materials should be used if possible in order to maximize surface areas and hence reaction rates. After the reactants have been weighed out in the required amounts, they are mixed together. For manual mixing of starting materials, this may be done with an agate mortar and pestle. Homogenization of the mixture is aided greatly by adding sufficient amount of a volatile organic liquid like acetone to form a paste. During the process of grinding and mixing the organic liquid gradually volatizes and after 10 – 15 minutes it gets usually evaporated completely. Grinding for several hours is necessary for the better homogeneity of the powder.

(b) Pelletizing

Once the samples have been prepared in the powder form, it is imperative to give them a definite shape for practical purpose. Unlike metals,

ceramics are generally shaped prior to firing rather than after firing. The axial pressure applied with a hydraulic press to powder in a die can form pellets of the powder. Normally, pressure is required before sintering so as to ensure large areas of surface between grains, it also tend to increase the density and strength of the final product. The grain morphologies of the product depend on processing conditions and determine their mechanical and electrical properties.

(c) Additives (binder/lubricant)

The main purpose of the binders is to form samples with complex shapes which can be transported for further processing without breaking. The most common binder for the ferrites is polyvinyl alcohol (PVA). The PVA, when dried, creates a hard shell around the particle aggregates that may be difficult to crush in the pressing operation. Another additive is stearic acid powder that can act as die lubricant to aid in pressing.

(d) Calcination

The decomposition of the starting chemicals by heating below melting point is known as calcinations. Calcination achieves three objectives;

(i) Raw materials such as carbonates decompose and oxides react to form required phase.

(ii) Improves the density of the powder and reduces subsequent shrinkage during final sintering (firing) and

(iii) Give out the product to be shaped after additional process steps.

The neighbouring grains in the material react in the furnace (heated to temperature between 800 ˚C and 1000 ˚C in air) to form new stable phase.

(e) Re-grinding

The solid-state reaction is often greatly facilitated by double sintering method i.e. cooling and grinding the sample periodically. This is because during heating, sintering and grain growth of both reactant and product phases, usually occur in addition to the main reaction, causing a reduction in the surface area of the mixture. The effect of regrinding is to maintain a high surface area as well as to bring fresh surfaces into contact. The reaction rate may also be speeded up by palletizing the samples prior to heating, thereby increasing the area of contact between the grains. In some cases where the chemical homogeneity is critical, a second calcination and additional milling may follow the milling step.

(f) Final Sintering

The final sintering process can attain the variable objectives;

(i) Complete formation of the lattice

(ii) Attainment of the chemical homogeneity and

(iii) Attainment of the uniform microstructure

Various parameters like temperature, pressure (for the pelletization), time and atmosphere etc affect the sintering process and the dominant parameter is temperature. Typically sintering temperature is three quarters of the melting temperature for the formation of traditional ceramics. Any change in above mentioned parameters can modify properties of the sintered materials significantly. For example, an increase in sintering temperature increases the density of the material due to increase in rate of diffusion. An increase in the pressure increases the elastic stress at inter-particle contacts and provides the driving force for sintering. Thus sintering can be

accomplished at lower temperatures and in reduced time. An increase in pressure does not alter the driving force for grain growth whereas it acts to reduce porosity to large extent.

Synthesis of nanomaterials

The research in nano-science can be framed with three aims: to synthesize, understand and explore new nano-materials and the related phenomena.Nano-scale particles are known to exhibit unique physical and chemical properties. The novel properties of nano-crystalline materials are the result of their small residual pore sizes, limited grain sizes, phase or domain dimensions, and large fraction of atoms residing at surfaces. The possibilities for reacting, coating, and mixing various types of nano-materials create the potential for fabricating new compositions/composites with nano-sized phases and novel properties. Not only is the structure different from those exhibited by their bulk counterparts, but also the mechanical, electronic, optical, magnetic and thermal properties of nano-crystalline materials are different from those exhibited by their bulk counterparts. Specifically, ceramics fabricated from ultra-fine particles are known to possess high strength and toughness because of their ultra-fine intrinsic defect sizes and the ability for their grain boundaries to undergo a large plastic deformation. Ultra-fine particles can be sintered at much lower temperatures also. Known techniques for generating nanosized particles may be divided into four broad techniques, including:

1) a vacuum technique,
2) a gas-phase technique,
3) a condensed-phase synthesis technique and
4) a mechanical grinding technique.

The vacuum synthesis techniques include sputtering, laser ablation, and liquid-metal ion source. Additionally, the gas-phase technique includes

inert gas condensation, oven sources (for direct evaporation into a gas to produce an aerosol or smoke of clusters), laser-induced vaporization, laser pyrolysis, and flame hydrolysis. Furthermore, the condensed-phase synthesis technique includes reduction of metal ions in an acidic aqueous solution, liquid phase precipitation of semiconductor clusters, and decomposition-precipitation of ionic materials for ceramic clusters. Most of these prior-art techniques suffer from a severe drawback: extremely low production rates. Vacuum sputtering, for instance, only produces small amounts of particles at a time. Laser ablation and laser-assisted chemical vapor deposition techniques are also well-known to be excessively slow processes. These low production rates generally result in high product costs, which limit the utility value of nano-phase materials. Some processes require expensive precursor materials to produce ceramic powders and could result in a harmful gas. Most of the prior-art processes are capable of producing one particular type of metallic or ceramic powder at a time, but do not permit the preparation of a uniform mixture of two or more types of nano-scaled powders at a predetermined proportion. Also, most of the prior art processes require heavy and/or expensive equipment, resulting in high production costs. Additionally, during the precipitation of ultra-fine particles from the vapor phase, when using thermal plasmas or laser beams as energy sources, the particle sizes and size distribution can not precisely be controlled. Also, the reaction conditions usually lead to a broad particle size distribution as well as the appearance of individual particles having diameters that are multiples of the average particle size.

3.1.2 Mechanical grinding technique

Mechanical grinding technique deals with a ball mill by which the powders in the mill pots can be ground into ultra-fine particles. This technique can be used to produce nanosized powders at industrial level. Unlike many of the methods mentioned above, mechanical attrition produces its nanostructures not by cluster assembly but by the structural decomposition of coarser grained structures as a result of plastic deformation. It is important to note that the materials produced by ballmilling technique have two fold advantages of having better control in obtaining fine particles and surety of stoichiometry of the products with good homogeneity and densification. At the same time mechanical milling induced stress-strain should be taken into account. The ball milling and rod milling techniques belong to the mechanical alloying process which has received much attention as a powerful tool for the fabrication of several advanced materials. Mechanical alloying is a unique process, which can be carried out at room temperature. The process can be performed on high energy mills, centrifugal type mill and vibratory type mill, and low energy tumbling mill.

Examples of High Energy Mills

High energy mills include:

- Attrition Ball Mill
- Planetary Ball Mill
- Vibrating Ball Mill
- Low Energy Tumbling Mill
- High Energy Ball Mill

A typical photograph of high energy planetary ballmill (Pulverisette 6) is shown in the Figure.

Basic principle of a conventional Ballmill

A ballmill, a type of grinder, is a cylindrical device used in grinding (or mixing) materials like ores, chemicals, ceramic raw materials and paints. Ball mills rotate around a horizontal axis, partially filled with the material to be ground plus the grinding medium. Different materials are used as media, including ceramic balls, pebbles, stainless steel balls and zirconia balls. Careful selection of the milling media is required to avoid the contamination of the samples by the media. An internal cascading effect reduces the material to a fine powder. Large to medium-sized ball mills are mechanically rotated on their axis, but small ones normally consist of a cylindrical capped container that sits on two drive shafts (pulleys and belts are used to transmit rotary

motion).Balls or cylinders of selected materials are mixed with the ceramic compounds in a volatile organic lubricant (e.g. Acetone, Propanol etc), and the mixture is poured into suitable jars. These jars are sealed and made to rotate for long periods, e.g., several hours on motorized rollers.

In the present work, nanoscale polycrystalline samples of Yttrium Iron Garnet ($Y_3Fe_5O_{12}$) are obtained using conventional High energy ballmill (SPEX 8000D) at IUAC, New-Delhi.

Experimental details

The polycrystalline samples of substituted Fe^{3+}-and Y^{3+}-substituted Yttrium iron garnet system with general formula:

(i) $Y^{3+}_{3-x}Fe^{3+}_{5+x}O^{2-}_{12}$ (x=0.0,0.1,0.3 and 0.5)

(ii) $Y^{3+}_{3+x}Fe^{3+}_{5-x}O^{2-}_{12}$ (x=0.0,0.2,0.4 and 0.6)

were synthesized by the double sintering ceramic technique. The starting materials were analytical grade powders of Fe_2O_3 and Y_2O_3; all 99.9 % pure supplied by Thomas & Backer. The oxides were mixed thoroughly in stoichiometric proportions to yield the desired compositions, then compressed in the form of pellets and pre-sintered at 1000 ˚C for 24 hrs. The pre-sintered pellets were re-grinded and the resulting powders were re-pelletized. The binder used was acetone, which evaporates at 300 ˚C. The pellets for the samples of first and second series were finally sintered in air at 1500 ˚C for 24 hours and furnace-cooled at the rate of 2 ˚C /min.

The garnet material with nominal composition $Y_3Fe_5O_{12}$ used to study grain size dependent various physical properties was kept at 1300 ˚C for 24 hours in final sintering process. The as prepared (unmilled) sample was milled upto 12 hours using high energy ballmill (SPEX-8000D) with steel vials and balls. The milling intensity was 400 rotations per minute and a ball to powder ratio of 8:1 was chosen. Water was added to container to improve particle mobility during milling. The milling process was interrupted after selected time period (3hrs, 6hrs, 9hrs, 12hrs) to take out small amount of powder, which were heated in air at 50 ˚C until it get dried completely. The powder was initially dark brown, becomes a lighter and lighter brown during milling. The initial change is thought to be associated mainly with particle size reduction.

3.2 Structural Characterization and chemical analysis

The high temperature, prolong sintering may results in loss of ingredient and hence lead to non-stoichiometric composition, which shows unexpected behaviour, that can not be explained on the basis of normal stoichiometry. Thus, it was essential to check the chemical stoichiometry of each composition after the synthesis. Energy dispersive analysis of x-rays (EDAX) is an important tool for this purpose.

3.2.1 EDAX measurements

If any element is bombarded with the X- rays of high enough energy, it will emit its 'characteristic lines'. In most cases they are the K_α and K_β lines. They are called the characteristic lines to emphasize that the wavelengths of them are fixed and characteristic to the emitting element. The phenomena are called the fluorescence. It provides a basis for a method of chemical analysis. If the different elements in the sample are bombarded with X – rays they will emit their characteristic lines of different wavelengths thus providing identification of the elements. The X–ray spectrometer is used for this purpose in two different modes:

Wavelength dispersive

In this mode the wavelengths of the emitted radiation from sample are analyzed by diffracting the radiations through a single crystal of known d value and obtaining the wavelength distribution.

Energy dispersive

In this mode diffraction of the radiation is not involved in the process of analyzing the emitted radiation from the sample. The emitted radiation is analyzed on the basis of their energies rather than their wavelength.

Fluorescence Spectroscopy

Suppose that monochromatic primary radiation of constant intensity and wavelength λ is incident on an element, which has K absorption edge λ_k. As we decrease λ, the fluorescence will not occur until λ is just shorter than λ_k where the fluorescence intensity will be maximum. For further decrease in λ, the fluorescence intensity will decrease in much the same manner as absorption coefficient.

There are many other phenomena occurring along with the fluorescence. They are ejection of an Auger electron, coherent and incoherent diffracted radiations. The auger effect plays crucial role when the emitter is any light element. The probability of fluorescence emission is much less in such case. The other radiations contribute to the background in energy dispersive spectrum.

The wavelength range generally used in fluorescence extends from 0.2Å to 20Å. The lower limit is generally imposed by the maximum voltage that can be applied to the tube. The radiation of 0.2 Å wavelength would cause the K fluorescence in H_f (Z = 72). For heavier elements than H_f, we can use the L rather than K fluorescence. The upper limit on wavelength depends upon the equipment used. It is imposed due to the large absorption of long wavelength fluorescence caused by just anything if encounters, such as air, counter wind etc. The more important is the absorption by the elements it self in this limit, particularly for the lighter elements. In case of the lighter

elements, the fluorescence radiation comes only from the surface because the fluorescence radiation coming out from the interior is absorbed by the element atoms. Thus, the total fluorescence intensity is only meager. This puts limit on the detection of the lighter elements. Generally, commercial spectrometer detect F (Z = 13), which is the lower limit of detection of elements.

Design of the Spectrometer

The essential parts of the Energy Dispersive spectrometer are shown in the diagram below. It consists of i). The X – ray tube, ii) Specimen, iii) Si (Li) counter & a FET preamplifier, both cooled by liquid Nitrogen and iv) Multi-channel Analyzer (MCA).

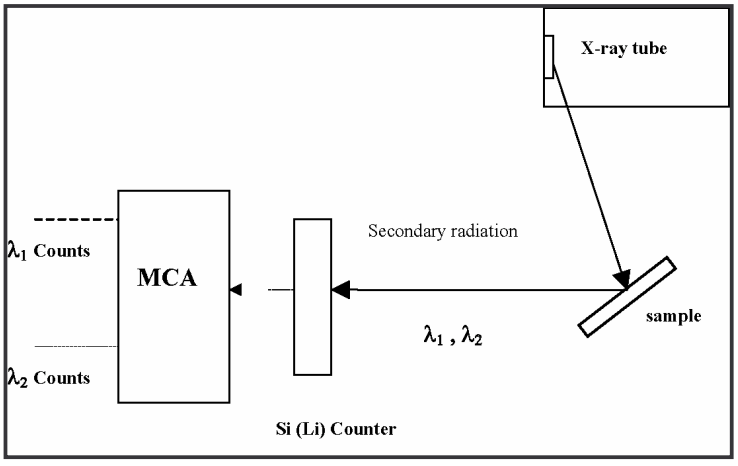

Fig.1 Schematic diagram of Energy Dispersive spectrometer

The sample specimen is bombarded with X – rays of enough high energy generated from the X – ray tube. The fluorescence radiation, emitted by the sample comprising of various wavelengths according to the various elements present in the sample is analyzed and various wavelengths are separated on the basis of their energies by means of a Si (Li) counter and a

multi-channel analyzer (MCA). The counter produces the pulses proportional in height to the energies in the incident beam and MCA sorts out the various pulse heights. The excellent energy resolution of the Si (Li) counter with FET preamplifier [1] and the ability of the MCA to perform rapid pulse height analysis make the spectrometer to measure the intensities of all the spectral lines from the sample in about a minute, unless there are elements in very low concentration are to be determined.

Chemical analysis

The energy dispersive spectrometer is used to make a rapid chemical analysis qualitatively. It can also be used for a semi quantitative, if not quantitative, analysis. The energy dispersive spectrum one gets from this spectrometer is the intensity (in counts) v/s energy spectrum. The energies in k eV cover all the K and L lines emitted by the samples. The analysis is done with the help of the computer software. There is a table or chart of the energies of all K and L lines arranged in consequent manner of all the elements. The information from it is retrieved by the computer for assigning any energy peak in the diagram with the respective element. Thus, from the peak energy the elements present in the sample can be detected. The semi quantitative analysis can be done with calculating the total number of counts recorded for a particular energy. This examination is difficult to do manually since all the energy peaks may not be well separated and may be diffused with each other. Since the analysis needs the total area under the curve and not the height of the peak, it is difficult to separate the contributions of each peak. But computer software simulates the peaks with different areas under the curve and it checks their resultant effect when merged. It can separate out

the contribution from each peak in this manner. The relative concentrations of the elements can be known, if not the absolute, from this analysis. All the samples of the present study were characterized with EDAX at SICART, V.V.Nagar (Gujarat state, India).

It is very essential to study structural properties of any material in order to verify single phase structure before carrying out further studies on the material. Structural properties are closely related to the chemical characteristics of the atoms in the material and thus form the basics on which detailed physical understanding is built. There are various techniques known to explore the science related to structure of a material. These are used to ascertain single phase samples and detect deviations from the main structure as well as extracting the actual structure. The different techniques have different advantages and disadvantages and thus complement each other. In present study, X-Ray diffraction measurements are used to study the crystalline formation of a material.

3.2.2 X-ray Diffraction (XRD)

The easy availability and accessibility of x-ray diffraction makes it a useful technique not only for phase identification, but also for initial identification of lattice structure and for modeling of the basic unit cell.

The wavelength of x-rays (λ~ 0.5-2.5Å) is of the order of the inter-atomic distances and hence get diffracted when interacts with a crystalline substance (phase). The x-ray diffraction pattern of a pure substance is, therefore, like a fingerprint of the substance. While passing through a crystal, x-rays are diffracted by atoms at specific angles depending on the x-ray wavelength, the crystal orientation and the structure of the crystal. X-rays are predominantly diffracted by electrons and analysis of the diffraction angles produces an electron density map of the crystal. Crystalline materials can be described by their unit cell. This is the smallest unit describing the material. In the material

this unit cell is then repeated over and over in all directions. This will result in planes of atoms at certain intervals. The diffraction method is based on this fact of repetition and on Bragg's law which gives a relation between the distance from one atomic plane to the next, d, and the angle, θ, in which constructive interference of a reflected monochromatic beam is seen. The Bragg's law follows the equation given below.

$2d_{hkl} \times \sin\theta_{hkl} = n\,\lambda$,

where d = inter planar distance, n = order of reflection (Integer value), λ = wave length of x-rays, θ = angle between incident/reflected beam and particular crystal planes under consideration.

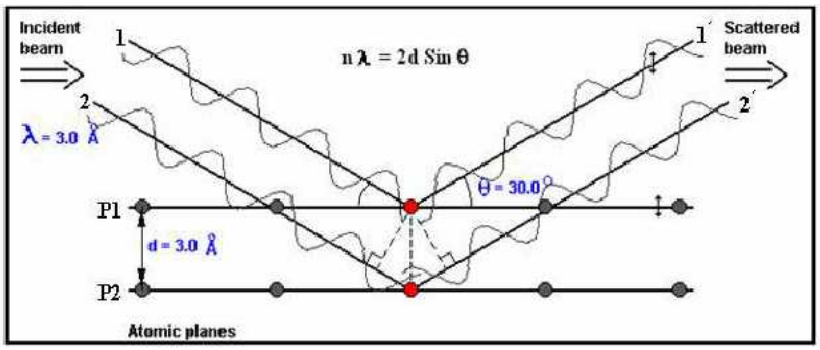

Fig.2 Diffraction of X-rays by a crystal planes (Bragg's law)

Bragg law is consequence of the periodicity of the lattice. Reflection (or diffraction) occurs from planes set at angle, θ, with respect to the incident beam and generates a reflected beam at an angle, 2θ, from the incident beam. The possible d-spacing defined by the indices h, k, l are determined by the shape of the unit cell. Therefore the possible 2θ values where we can have reflections are determined by the unit cell dimensions. Notice that the law does not refer to the composition of the basis atoms associated with every lattice point. However, the composition of the basis determines the relative

intensities of the various orders of diffraction from a given set of parallel planes. Therefore, the intensities depend on what kind of atoms we have and where in the unit cell they are located. Planes going through areas with high electron density will reflect strongly, planes with low electron density will give weak intensities. A typical powder diffraction spectrum consists of a plot of reflected intensities versus the detector angle 2θ. The detailed description of XRD is given in references. [1, 2].

X-ray diffractometer

There are several methods of getting the X –ray diffraction using a crystal specimen, such as Laue method, rotating – crystal diffractometer method, powder diffractometer method etc. The powder diffractometer method in particular is relevant to the present study.

The geometrical diagram of the diffractometer based on this method is shown in the Figure 3 and three main components are discussed in brief.

X-ray tube

The X-ray tube is a high vacuum, sealed off unit, usually with a copper, iron or molybdenum target. During the process of X-ray generation, the target is cooled by the water circulation. The generated X-rays beam is passed through thin beryllium window.

Detector

In addition to photographic film, the Geiger counter, the proportional counter, the scintillation counter and some times semiconductors are used in X-ray detection. The Scintillation counter is widely used. They have shortest dead time of around 0.25 μsec and have nearly uniform and high quantum efficiency throughout the important wavelength region.

Goniometer

It comprises of two circular tracks. On outer track the X-ray tube is usually made fixed. Detector is mounted on the arm moving on outer track. The sample holder is fixed on the inner track. The inner track rotates at half the angular distance than the outer arm. The movement of both the inner track and outer arm is controlled by mechanical motors.

Since the mass of powder is equivalent to a single crystal rotated not only about the one axis but in fact, about all possible axes, it has simplified to get signature of all the planes in one shot. The specimen for this method is a flat thin layer of powdered sample on a glass or a silicon single crystal holder. The randomness in the orientations of small crystals (or crystallites in the case of polycrystalline material) with respect to each other is such that there is a presence of all possible orientations of crystals.

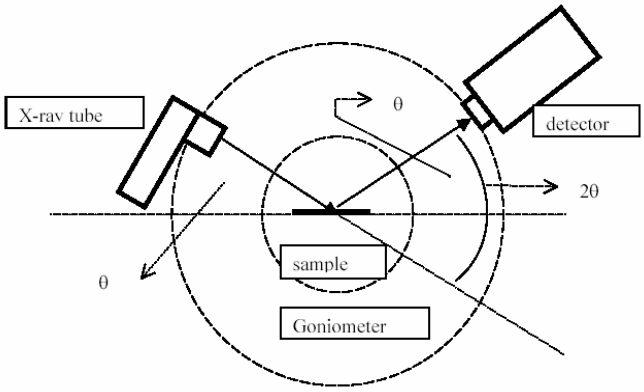

Fig.3 Schematic diagram of powder X-Ray diffractometer

In other words, there is a presence of a set of all permissible (hkl) planes with different d value and oriented parallel to flat surface of the specimen. Assume that the size of each crystal is such that it possesses enough number of planes necessary for perfect constructive and destructive interference. Now for any incident X-rays beam at angle θ, the detector is set at angle 2θ with

respect to the incident beam. At a particular value of 2θ, the d spacing of any of the (hkl) planes fulfilling the Bragg's condition will give constructive interference and all other (hkl) planes will give perfect destructive interference. If the specimen and detector are now moved in such a way that the specimen rotates half the angular distance than the detector in the same angular direction, the incident angle θ can be changed and each time the presence of Bragg peak can be detected. Thus, whole spectra of diffracted intensities by various planes at different angles will be traced. The experimental particulars regarding the X-ray diffractometer along with data acquisition electronics is discussed at length in reference [2].

Structural Analysis of the X-Rays

The investigation into the structure of an unknown compound involves many stages. First one is the data acquisition and secondly the analysis of this data to retrieve the relevant information and finally proper interpretation of the analyzed data. The powder x-ray diffraction pattern of all the garnet compositions has been recorded at 300 K with a Philips (PW 1700) diffractometer using CuKα radiation (λ=1.54056 Å).The analysis of the X-ray data has been done using various computer softwares. The software used prominently in the present work are Powder-X [3] for peak indexing and evaluation of the phases present in the samples under study and GSAS (General Structural Analysis Software) for structural refinement of few samples.

The Rietveld refinement method

There are six factors affecting the relative intensities of the diffraction lines on a powder pattern, namely, i) polarization factor, ii) structure factor, iii)

multiplicity factor, iv) Lorentz factor, v) absorption factor and vi) temperature factor. A very important technique for analysis of powder diffraction data is the whole pattern fitting method proposed by Rietveld (1969) [4, 5].The Rietveld method is an extremely powerful tool for the structural analysis of virtually all types of crystalline materials not available as single crystals. The method makes use of the fact that the peak shapes of Bragg reflections can be described analytically and the variations of their width (FWHM) with the scattering angle 2θ. The analysis can be divided into number of separate steps. While some of these steps rely on the correct completion of the previous one(s), they generally constitute independent task to be completed by experimental and depending on the issue to be addressed by any particular experiment, one, several or all of these tasks will be encountered [6].

The parameters refined in the Rietveld method fall into mainly three classes: peakshape function, profile parameters and atomic and structural parameters. The peak shapes observed are function of both the sample (e.g. domain size, stress/train, defects) and the instrument (e.g. radiation source, geometry, slit sizes) and they vary as a function of 2θ. The profile parameters include the lattice parameters and those describing the shape and width of Bragg peaks (changes in FWHM and peak asymmetry as a function of 2θ, 2θ correction, unit cell parameters). In particular, the peak widths are smooth function of the scattering angle 2θ. It uses only five parameters (usually called U, V, W, X and Y) to describe the shape of all peaks in powder pattern. The structural parameters describe the underlying atomic model include the positions, types and occupancies of the atoms in the structural model and

isotropic or anisotropic thermal parameters. The changes in the positional parameters cause changes in structure factor magnitudes and therefore in relative peak intensities, whereas atomic displacements (thermal) parameters have the effect of emphasizing the high angle region (smaller thermal parameters) or de-emphasizing it (larger thermal parameters). The scale, the occupancy parameters and the thermal parameters are highly correlated with one another and are more sensitive to the background correction than are the positional parameters. Thermal parameter refinement with neutron data is more reliable and even anisotropic refinement is sometimes possible. Occupancy parameters are correspondingly difficult to refine and chemical constraints should be applied whenever possible [7].

Once the structure is known and a suitable starting model is found, the Rietveld method allows the least-squares refinement [chi-square (χ^2) minimization] of an atomic model (crystal structure parameters) combined with an appropriate peak shape function, i.e., a simulated powder pattern, directly against the measured powder pattern without extracting structure factor or integrated intensities. With a complete structural model and good starting values of background contribution, the unit cell parameters and the profile parameters, the Rietveld refinement of structural parameters can begin. A refinement of structure of medium complexity can require hundred cycles, while structure of high complexity may easily require several hundreds. The progress of a refinement can be seen from the resultant profile fit and the values of the reliability factors or R-values. The structure should be refined to convergence. All parameters (profile and structural) should be refined

simultaneously to obtain correct estimated standard deviations (e.s.d.) can be given numerically in terms of reliability factors or R-values [8].

The weighted -profile R value, Rwp, is defined as,

$$R_{wp} = 100\left[\frac{\sum_{i=1,n} w_i \left|y_i - y_{c,i}\right|^2}{\sum_{i=1,n} w_i y_i^2}\right]^{1/2}$$

Ideally, the final Rwp, should approach the statistically expected R value, Rexp,

$$R_{exp} = 100\left[\frac{n-p}{\sum_i w_i y_i^2}\right]^{1/2}$$

where, N is the number of observations and P the number of parameters. Rexp reflects the quality of data. Thus, the ratio between the two (goodness of fit),

$$\chi_v^2 = \left[\frac{R_{wp}}{R_{exp}}\right]^2 = S^2$$

An R value is observed and calculated structure factors, F_{hkl}, can also be calculated by distributing the intensities of the overlapping reflections according to the structural model,

$$R_F = 100\frac{\sum_h \left|\sqrt{F_{obs,h}}' - F_{calc,h}\right|}{\sum_h \sqrt{F_{obs,h}}'}$$

Similarly, the Bragg-intensity R value can be given as,

$$R_B = 100 \frac{\sum_{\mathbf{h}} \left| {}' I_{obs,\mathbf{h}} {}' - I_{calc,\mathbf{h}} \right|}{\sum_{\mathbf{h}} \left| {}' I_{obs,\mathbf{h}} {}' \right|}$$

R values are useful indicators for the evaluation of refinement, especially in the case of small improvements to the model, but they should not be over interpreted. The most important criteria for judging the quality of a Rietveld refinement are (i) the fit of the calculated pattern to the observed data and (ii) the chemical sense of structural model.

3.2.3 Infrared Spectroscopy

The infrared region of the electromagnetic spectrum extends from 14,000 cm^{-1} to 10 cm^{-1}. The region of most interest for chemical analysis is the mid-infrared region (4,000 cm^{-1} to 400 cm^{-1}) which corresponds to changes in vibrational energies within molecules. The far infrared region (400 cm^{-1} to 10 cm^{-1}) is useful for molecules containing heavy atoms such as inorganic compounds but requires rather specialized experimental techniques.

Use of the Technique

It is rarely, if ever, possible to identify an unknown compound by using IR spectroscopy alone. Its principal strengths are: (i) it is a quick and relatively cheap spectroscopic technique, (ii) it is useful for identifying certain functional groups in molecules and (iii) an IR spectrum of a given orgainc compound is unique and can therefore serve as a fingerprint for this compound.

Sample Preparation

There are a variety of techniques for sample preparation dependent on the physical form of the sample to be analyzed.

Solids

There are two main methods for sample preparation involving the use of Nujol mull or potassium bromide disks. However there is also a third option of preparing a solution in a suitable solvent (not infrared active in the region of interest).

Nujol Mull

The sample is ground using an agate mortar and pestle to give a very fine powder. A small amount is then mixed with nujol to give a paste and several

drops of this paste are then applied between two sodium chloride plates (these do not absorb infrared in the region of interest). The plates are then placed in the instrument sample holder ready for scanning.

Potassium Bromide disk

A very small amount of the solid (approximately 1-2 mg) is added to pure potassium bromide powder (approximately 200 mg) and ground up as fine as possible. This is then placed in a small die and put under pressure mechanically. The pressure is maintained for several minutes before removing the die and the KBr disk formed. The disk is then placed in a sample holder ready for scanning.

The success of this technique is dependent on the powder being ground as fine as possible to minimize infrared light scattering off the surface of the particles. It is also important that the sample be dry before preparation. KBr has no infrared absorption in the region 4000 - 650 cm^{-1}.

Instrumentation

The Double Beam Infrared Spectrometer

This instrument uses a source of infrared radiation such as a nichrome wire or cooled rod of silicon carbide to produce a range of frequencies which are then separated into individual frequencies using a monochromator diffraction grating. The beam produced is then split into two and one passes through the sample whilst the other is used as a reference beam. The two beams then converge on the detector which measures the difference in intensity and then sends a proportional signal to the recorder. The resulting plot is a measure of transmission against frequency which is usually plotted

as wavenumber (cm^{-1}). Wavenumber can be related to the frequency by using the following equations:-

Wavenumber = 1/ Wavelength (l)*

*The units for wavenumber are cm^{-1} therefore wavelength should be converted to cm rather thanmetres for this calculation. and wavelength is related to frequency as:-

Velocity of light (C) = Frequency (v)/ Wavelength (l)

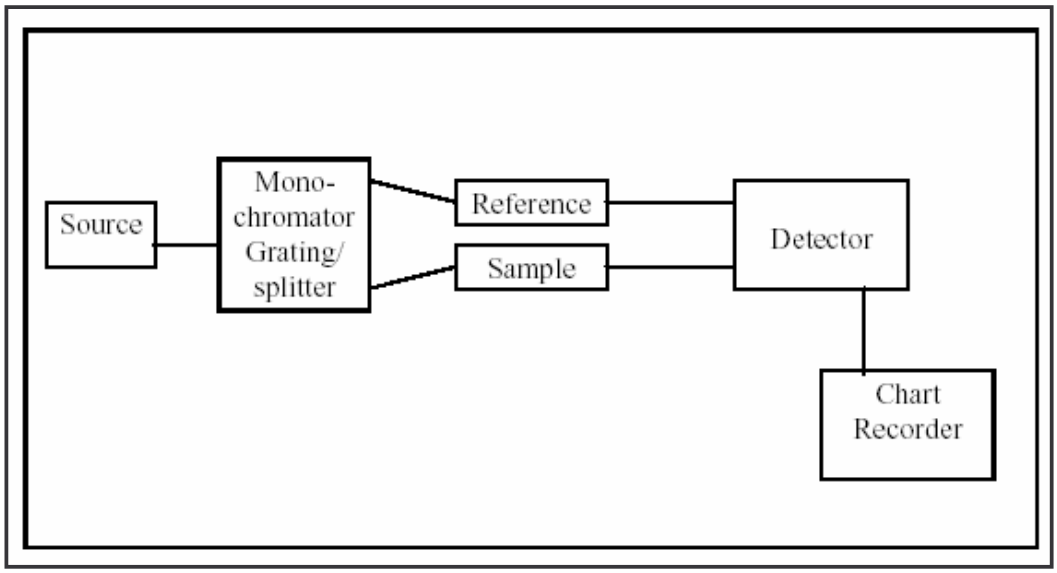

Fig.4 Schematic Diagram of an Infrared Spectrometer

Fig.5 Fourier Transform Infrared Spectrometer

Slow scans using diffraction gratings are inefficient. Almost all modern IR spectrometers use a different approach, the Fourier transform method, to scan the full spectral range at the same time. The details of this method are quite complex and will not be covered here.

However, this method has some obvious advantages. Firstly, it is much quicker, taking seconds instead of minutes to record a complete spectrum. A further advantage is that it is possible to get a spectrum from very small or very dilute samples by performing multiple scans and adding the data to improve the signal-to-noise ratio.

Infrared spectroscopic measurements of few of the compositions were carried out at Inter-University accelerator centre, New-Delhi and few at SICART, Vallabh-Vidyanagar.

3.3 Surface Morphology

3.3.1 Scanning electron microscopy (SEM)

The scanning electron microscope (SEM) is a type of electron microscope that images the sample surface by scanning it with a high-energy beam of electrons in a raster scan pattern. The electrons interact with the atoms that make up the sample producing signals that contain information about the sample's surface topography, phase distribution, crystal orientation, presence and location of defects [9, 10] and other properties such as conductivity. It is one of the most widely used techniques to examine surfaces. Its resolution is a few thousand angstroms depending on the nature of the sample.

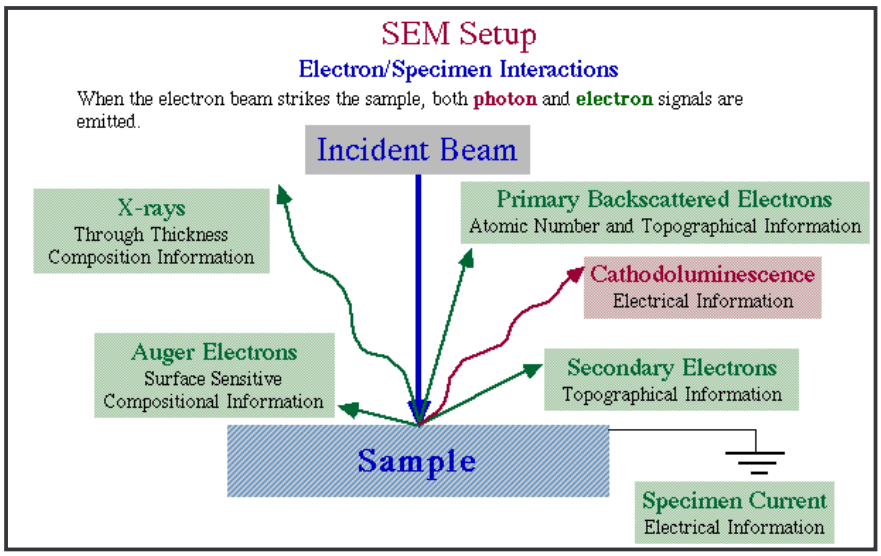

Fig.6 Block diagram of Scanning Electron Microscope

The types of signals made by an SEM can include secondary electrons, back scattered electrons, characteristic X-rays and light (cathodoluminescence). These signals come from the beam of electrons striking the surface of the specimen and interacting with the sample at or near

its surface. In its primary detection mode, secondary electron imaging, the SEM can produce very high-resolution images of a sample surface, revealing details about 1 to 5 nm in size. Due to the way these images are created, SEM micrographs have a very large depth of focus yielding a characteristic three-dimensional appearance useful for understanding the surface structure of a sample.

Scanning process and image formation

In a typical SEM, electrons are thermionically emitted from a tungsten filament cathode and are accelerated towards an anode. Tungsten is normally used in thermionic electron guns because it has the highest melting point and lowest vapour pressure of all metals, thereby allowing it to be heated for electron emission. Other electron sources include lanthanum hexaboride (LaB_6) cathodes, which can be used in a standard tungsten filament SEM if the vacuum system is upgraded. Electrons can also be emitted using a field emission gun (FEG), which may be of the cold-cathode type or the thermally-assisted Schottky type.

The electron beam, which typically has an energy ranging from a few hundred eV to 40 keV, is focused by one or two condenser lenses into a beam with a very fine focal spot sized 0.4 nm to 5 nm. The beam passes through pairs of scanning coils or pairs of deflector plates in the electron column, typically in the final lens, which deflect the beam horizontally and vertically so that it scans in a raster fashion over a rectangular area of the sample surface.

When the primary electron beam interacts with the sample, the electrons lose energy by repeated scattering and absorption within a teardrop-

shaped volume of the specimen known as the interaction volume, which extends from less than 100 nm to around 5 µm into the surface. The size of the interaction volume depends on the electron's landing energy, the atomic number of the specimen and the specimen's density. The energy exchange between the electron beam and the sample results in the reflection of high-energy electrons by elastic scattering, emission of secondary electrons by inelastic scattering and the emission of electromagnetic radiation which can be detected to produce an image.

Fig.7 SEM sample Chamber

Electronic devices are used to detect and amplify the signals and display them as an image on a cathode ray tube in which the raster scanning is synchronized with that of the microscope. The image displayed is therefore a distribution map of the intensity of the signal being emitted form the scanned area of the specimen. The image may be captured by photography from a high resolution cathode ray tube, but in modern machines is digitally captured and displayed on a computer monitor.

Resolution of the SEM

The spatial resolution of the SEM depends on the size of the electron spot, which in turn depends on both the wavelength of the electrons and the magnetic electron-optical system which produces the scanning beam. The resolution is also limited by the size of the interaction volume, or the extent to which the material interacts with the electron beam. The spot size and the interaction volume both might be large compared to the distances between atoms, so the resolution of the SEM is not high enough to image individual atoms, as is possible in the shorter wavelength (i.e. higher energy) transmission electron microscope (TEM). The SEM has compensating advantages, though, including the ability to image a comparatively large area of the specimen; the ability to image bulk materials (not just thin films or foils); and the variety of analytical modes available for measuring the composition and nature of the specimen. Depending on the instrument, the resolution can fall somewhere between less than 1 nm and 20 nm. The world's highest SEM resolution is obtained with the Hitachi S-5500. Resolution is 0.4nm at 30kV and 1.6nm at 1kV.

SEM Images for all the samples were obtained from TIFR, Mumbai and SICART, Vallabh Vidyanagar.

3.3.2 Transmission Electron microscopy

TEM can be used to obtain information about the samples Morphology i.e. size, shape and arrangement of the particles as well as their relationship to each other on the scale of atomic diameters.

Transmission electron microscopy (TEM) is a microscopy technique whereby a beam of electrons is transmitted through an ultra thin specimen, interacting with the specimen as it passes through it. An image is formed from the electrons transmitted through the specimen, magnified and focused by an objective lens and appears on an imaging screen, a fluorescent screen in most TEMs, plus a monitor, or on a layer of photographic film, or to be detected by a sensor such as a CCD camera. The first practical transmission electron microscope was built by Albert Prebus and James Hillier at the University of Toronto in 1938 using concepts developed earlier by Max Knoll and Ernst Ruska.

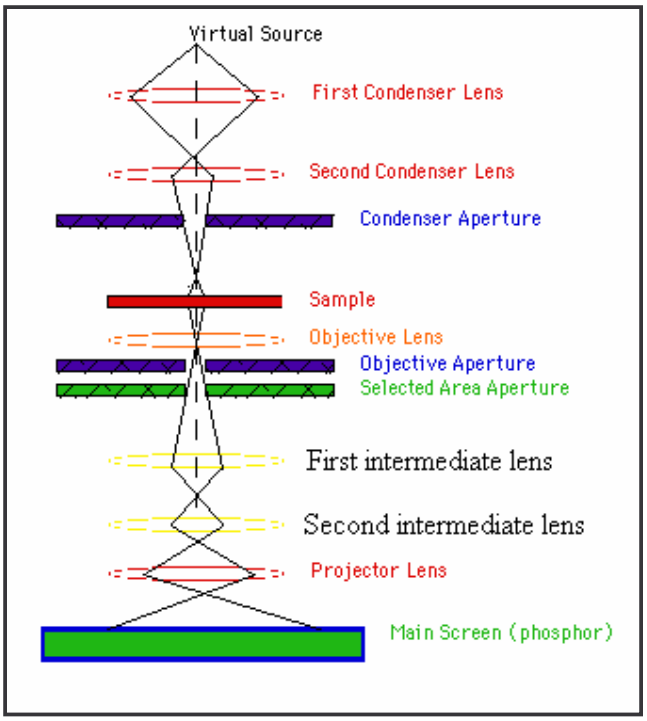

Fig.8 Schematic of Transmission Electron Microscope

Imaging in TEM

1. The "Virtual Source" at the top represents the electron gun, producing a stream of monochromatic electrons.
2. This stream is focused to a small, thin, coherent beam by the use of condenser lenses 1 and 2. The first lens (usually controlled by the "spot size knob") largely determines the "spot size"; the general size range of the final spot that strikes the sample. The second lens (usually controlled by the "intensity or brightness knob" actually changes the size of the spot on the sample; changing it from a wide dispersed spot to a pinpoint beam.
3. The beam is restricted by the condenser aperture (usually user selectable), knocking out high angle electrons (those far from the optic axis, the dotted line down the center)
4. The beam strikes the specimen and parts of it are transmitted
5. This transmitted portion is focused by the objective lens into an image
6. Optional Objective and Selected Area metal apertures can restrict the beam; the Objective aperture enhancing contrast by blocking out high-angle diffracted electrons, the Selected Area aperture enabling the user to examine the periodic diffraction of electrons by ordered arrangements of atoms in the sample
7. The image is passed down the column through the intermediate and projector lenses, being enlarged all the way
8. The image strikes the phosphor image screen and light is generated, allowing the user to see the image. The darker areas of the image represent those areas of the sample that fewer electrons were

transmitted through (they are thicker or denser). The lighter areas of the image represent those areas of the sample that more electrons were transmitted through (they are thinner or less dense).

Particle size of all the ballmilled compositions was confirmed using Transmission Electron Microscopy (TEM) (Model: PHILIPS-TECHNAI, using EHT potentials at 200kV) recorded at SICART, Vallabh Vidyanagar, Gujarat.

3.4 Ultrasonic pulse transmission technique for elastic wave velocities and elastic constants determination

Ultrasound is the strain wave propagating through a solid. The velocity of longitudinal and transverse elastic waves thus produced is a characteristic feature of a solid. The change in wavelength of ultrasonic waves in different mediums is due to elastic properties and the induced particle vibrations in the medium. The basic idea is that if there is any distortion of the solid from its equilibrium shape (Figure 9), the average separation of the atoms within the solid is no longer optimal. Some atoms will be too close to their neighbours and some too far apart. In either case there will be a restoring force, which will act to return the atoms to their equilibrium separations. The dynamics of the elastic wave will be affected by the way the solid responds to the restoring force. The two factors most critical in determining this response are the restoring force per unit displacement (the natural “springiness” of the substance), and the density of the substance. The restoring force on a small region of a solid depends on the type of the distortion (strain) that has taken place during synthesis process. The parameters that describe the restoring force per unit strain are known as the elastic moduli of a substance [11]. In the present work we have employed the Ultrasonic pulse transmission technique as a tool to get an idea about such stress/strain ratio.

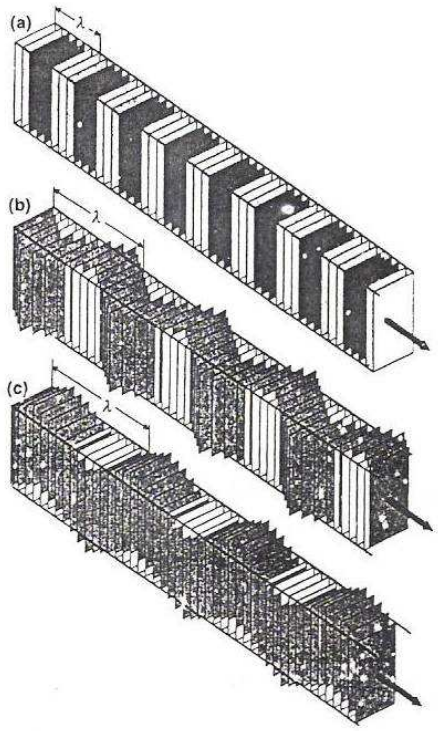

Fig. 9 Sound waves in solids (a) longitudinal (b) and (c) transverse waves

3.4.1 Ultrasonic Pulse Transmission (UPT) Technique

The longitudinal and transverse wave velocity measurements were undertaken by the ultrasonic pulse transmission (UPT) technique. The Schematic diagram (Figure 10) shows the block diagram of UPT Technique.

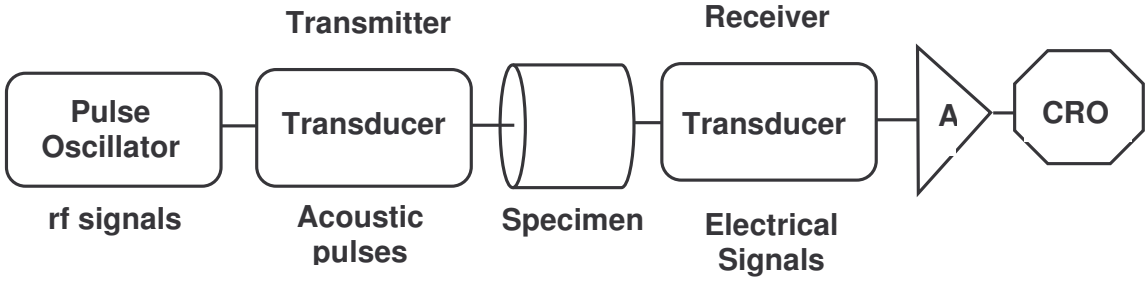

Fig. 10 Schematic diagram showing working of UPT Technique

The radio frequency (r.f) pulses generated by the pulse oscillator were applied to the transmitting transducer, which converts them into acoustic pulses, these in turn, after propagating through the test samples, were converted into electrical signals by the receiving transducer. The amplified output signal was then displayed on a storage oscilloscope. The cuboid shaped garnet samples with 10mm diameter and 5-7 mm thickness were polished to have flat and parallel faces. Ultrasonic pulse were generated and detected by X- and Y-cut (for longitudinal and transverse waves respectively) 1 MHz transducer. The sample was bounded to the transducer using the Nonaq stopcock grease such that intimate contact (no air gap) is established. A transducer correction was applied to the ultrasonic wave velocities. In all the cases, the measurement was made on both sides of the specimen. The transit time of the ultra sound was measured upto an accuracy of 1μs using a 100 MHz digital storage oscilloscope (Tektronix model: 2221). The overall accuracy of these measurements is about 0.25% in velocity and about 0.5% in elastic moduli. Bulk densities (ρ) of the samples have been determined by employing the Archimedes principle using Xylene (ρ = 0.87 g/cm^3) as buoyant to get fairly good results.

The longitudinal wave velocity (V_l) and shear or transverse wave velocity (V_s) measurements were carried out at Department of Physics, Osmania University, Hyderabad.

3.4.2 Young's modulus, E

This characterizes the restoring forces appropriate to longitudinal extensions of a substance. Figure 11 shows two rigid planes of area "A" separated by a distance "a" and held together by "springs" (analogous to

planes within a solid held together by atomic bonds). Young's modulus is defined by:

$$\frac{F}{A} = E\frac{\Delta x}{a}$$

where F is the force exerted on each plane. Notice that if a rod of material is stretched in this way, it will 'neck' i.e. its cross- sectional area will be reduced (Figure12). This tendency is characterized by the Poisson ratio, σ, of a substance. If we apply stress S_x (force per unit area) in the x-direction, we induce stress Sy in the y-direction. The Poisson ratio is defined as:

$$\sigma = \frac{S_y}{S_x}$$

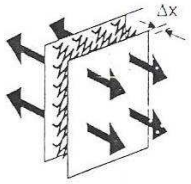

Fig. 11

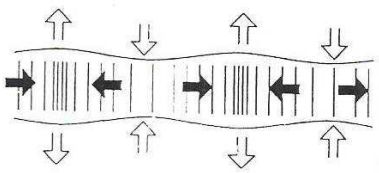

Fig. 12 Illustration of the way in which a rod of material necks and bulges as a compressive sound waves travels along a long thin rod

3.4.3 Shear or rigidity modulus, G

This characterizes the restoring forces appropriate to shear or transverse deformations of the substance. Figure13 shows two rigid planes of area "A" held together by "springs" (analogous to planes within a solid held together by atomic bonds). The rigidity modulus is defined by :

$$\frac{F}{A} = G\theta$$

where F is the force on each plane.

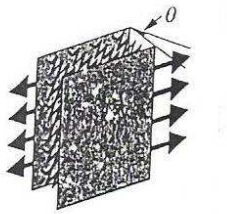

Fig. 13

3.4.4 Bulk modulus, B

Here it should be noted that the bulk modulus (and its inverse, the compressibility K) describes the restoring forces appropriate to volume compressions of the substance. It is defined by:

$$B = -V \frac{\partial P}{\partial V}$$

Where P is the pressure and V is the volume of the substance.

If the material is easily compressed or easily sheared, then for a given strain, the restoring force will be small. In other words, a high modulus (E,G, or B) indicates that the corresponding deformation of the solid is difficult and the solid has a strong tendency to 'spring' back to its equilibrium position.

The bulk modulus (B) for various garnets calculated by considering IR sum and determined experimentally [12], are given below:

Composition	B(GPa)	
	(Theoretical)	(Experimental)
$Y_3Al_5O_{12}$	220.0	185.2
$Y_3Ga_5O_{12}$	~ 195.0	174.7
$Y_3Fe_5O_{12}$	183.0	164.0

3.5.5 Poisson's ratio, σ

Poisson's ratio (σ) is the ratio of transverse contraction strain to longitudinal extension strain in the direction of stretching force. Tensile deformation is considered positive and compressive deformation is considered negative. The definition of Poisson's ratio contains a minus sign so that normal materials have a positive Poisson's ratio.

Poisson's ratio: Why usually positive?

Virtually all common materials become narrower in cross section when they are stretched. The reason why, in the continuum view, is that most materials resist a change in volume as determined by the bulk modulus B more than they resist a change in shape, as determined by the shear modulus G. In the structural view, the reason for the usual positive Poisson's ratio is that inter-atomic bonds realign with deformation.

The theory of isotropic elasticity allows Poisson's ratios in the range from -1 to 0.5. Physically the reason is that for the material to be stable, the stiffness must be positive; the bulk and shear stiffness are interrelated by formulae which incorporate Poisson's ratio.

Poisson's ratio, waves and deformation

The Poisson ratio of a material influences the speed of propagation and reflection of stress waves. In geological applications, the ratio of compressional to shear wave speed is important in inferring the nature of the rock deep in the earth. This wave speed ratio depends on Poisson's ratio.

Practical example-cork in a bottle

An example of the practical application of a particular value of Poisson's ratio is the cork of a wine bottle. The cork must be easily inserted,

yet it also must withstand the pressure from with in the bottle. Rubber, with a Poisson's ratio of 0.5, could not be used for this purpose because it would expand when compressed into the neck of the bottle and jam. Cork, by contrast, with a Poisson's ratio of nearly zero, is ideally in this application.

The inter relationship between various elastic constants are given below. Just by knowing any two elastic moduli, we can able to find other one using given formulae. Here it is important to note that Bulk modulus, rigidity modulus and Young's modulus are measure in dynes/cm^2 (CGS unit system), Newton/m^2 (MKS unit system), or Pascal (SI unit system), while 'σ' is unit less quantity.

Young's modulus

$$E = \frac{G(3\lambda + 2G)}{\lambda + G}$$

$$E = \frac{\lambda(1+\nu)(1-2\nu)}{\nu}$$

$$E = \frac{9K(K-\lambda)}{3K-\lambda}$$

$$E = 2G(1+\nu)$$

$$E = \frac{9KG}{3K+G}$$

$$E = 3K(1-2\nu)$$

Shear Modulus

$$G = \frac{\sqrt{(E+\lambda)^2 + 8\lambda^2} + (E-3\lambda)}{4}$$

$$G = \frac{\lambda(1-2\nu)}{2\nu}$$

$$G = \frac{3(K - \lambda)}{2}$$

$$G = \frac{E}{2(1 + \nu)}$$

$$G = \frac{3EK}{9K - E}$$

$$G = \frac{3K(1 - 2\lambda f)}{2(1 + \nu)}$$

Lamb's constant

$$\lambda = \frac{G(2G - E)}{E - 3G}$$

$$\lambda = \frac{2G\nu}{1 - 2\nu}$$

$$\lambda = \frac{3K - 2G}{3}$$

$$\lambda = \frac{\nu E}{(1 + \nu)(1 - 2\nu)}$$

$$\lambda = \frac{3K(3K - E)}{9K - E}$$

$$\lambda = \frac{3K\nu}{1 + \nu}$$

Poisson's ratio

$$\nu = \frac{\lambda}{2(\lambda + G)}$$

$$\nu = \frac{\sqrt{(E + \lambda)^2 + 8\lambda^2} - (E + \lambda)}{4\lambda}$$

$$\nu = \frac{\lambda}{3K - \lambda}$$

$$\nu = \frac{E - 2G}{2G}$$

$$\nu = \frac{3K - 2G}{2(3K + G)}$$

$$\nu = \frac{3K - E}{6K}$$

Bulk Modulus

$$K = \frac{3\lambda + 2G}{3}$$

$$K = \frac{\sqrt{(E + \lambda)^2 + 8\lambda^2} + (3\lambda + E)}{6}$$

$$K = \frac{\lambda(1 + \nu)}{3\nu}$$

$$K = \frac{GE}{3(3G - E)}$$

$$K = \frac{2G(1 + \nu)}{3(1 - 2\nu)}$$

$$K = \frac{E}{3(1 - 2\nu)}$$

3.5 Magnetic studies

For strongly magnetic materials, magnetic moment is the most important physical property for determination of their application. Magnetic moment measurements provide information about spin structure, anisotropy and phase transitions.

Various methods of Magnetometry can be used to measure the magnetic properties of the materials [1] Vibrating sample magnetometer (VSM) and superconducting quantum interference device (SQUID) are well-known methods to measure the magnetization of the material.

3.5.1 Vibrating sample magnetometer

The magnetization of different materials can be measured mainly in three ways: (i) the induction method, (ii) the force method, and (iii) the methods based on the detection of the dipole field of a magnetized specimen. Among all these methods, Vibrating Sample Magnetometer is a convenient and popular form of the induction method. It was first described by Foner in 1959 and now it has almost completely superseded the Vibrating Coil device. It is a device in which sample is vibrated in a uniform magnetizing field, and the magnetization of the sample is detected. This instrument allows precise magnetization measurements to be made as a function of temperature, magnetic field strength and crystallographic orientation. The sensitivity of this instrument is limited. A VSM is a goniometer, measuring the differences in magnetic induction between a region of space with and without specimen. Therefore, it gives a direct measure of magnetization of the specimen.

The growing importance for modern media is the analysis of the magnetization vector rather than the magnetization in the direction of the

applied field because of the importance of the oblique anisotropy direction. The instrument, which is most suitable for such investigations, is vibrating sample magnetometer and is widely used for characterizing ferromagnetic materials. In a VSM, the sample, either in the form of a single crystal, powder or thin film is mounted on the end of a rigid rod attached to mechanical resonator which oscillates the sample (usually in a vertical direction) at a fixed frequency. A set of sensing coils are surrounding the sample. When a uniform magnetic field is applied, a magnetization (M) is induced in the sample that is equal to the product of susceptibility and applied magnetic field. This magnetization further alters the magnetic flux through the coils. This produces AC voltage and this electric signal is directly proportional to magnetic moment, the vibrational amplitude and the vibrational frequency, which can be amplified and detected using a lock – in amplifier. The external magnetizing field is usually provided by a horizontal electromagnet. The design of a VSM must be in such a way that sample vibration should produce no vibration of the sensing coils relative to the magnet because it may result into large spurious signals. However this problem can be overcomed if the applied field is very homogeneous. So that's why VSM typically use large electromagnets with large pole piece diameters.

VSM can easily measure permanent moments, hysteresis curves of ferromagnetic materials and strongly paramagnetic salts. However their moments sensitivity (typically 10^{-4} emu of moment with a 1 second time constant) is not really adequate for weakly magnetic systems or very small samples.

In the commercial system available from Princeton Applied Research, a transducer unit with beryllium – copper springs is used to vibrate the sample. The transducer assembly is mounted on a rotating platform, and the sample is mounted on a rigid, but readily demountable rod.

Operation of VSM

The materials used in the present work are in the form of powder. The required quantity is mounted on a rigid rod so that it rests centered in a pair of sensing pick – up coils between the poles of a field magnet. The rod is mounted in a transducer assembly that passes through the centre of the driving coil. The transducer is driven by a power amplifier which itself is driven by an oscillator. The large electromagnet produces uniform magnetic field. The magnetic sample under study is constrained to vibrate vertically only along the z – axis at 80 Hz. When the field is ON, the sample gets magnetized and thus produces its own magnetic field. Since the sample vibrates, it's surrounding experiences a continuous change in the magnetic field, which in turn, can induce emf in the sensor coils. Because of this vibration, it induces a signal in the sample pick – up coil. The magnitude of this signal is dependent on the magnetic properties of the sample itself. Various parameters like field, sweep time, time constant, temperature etc. are fed to the software, and the run is started. The signal derived from the vibrating transducer assembly is proportional to the amplitude and frequency of the sample motion. The signal derived is amplified and used to control the motion of the sample.

The output of the sample coil is fed to the differential input of a lock – in amplifier. The reference input of the lock – in comes from the sine wave oscillator used to drive the sample holder. This new drive and lock – in

configuration allows time constants as short as 10 ms for faster measurements of higher moment samples.

The output of the lock – in goes to an analog to digital converter and is stored in a curve buffer. The x – axis of the curve buffer is the field as measured by the built in gaussmeter. The y – axis is directly proportional to the magnetic moment of the sample. Thus magnetization produced in the sample can be against the change in the applied field thus giving a characteristic curve called hysteresis loop. By measuring various parameters of this hysteresis loop, the materials can be characterized magnetically whether it is hard/ soft, or strong/ weak etc. This study helps in characterizing the magnetic to non – magnetic transitions. The working temperature range is 78 K to 1000 K with additional attachments like cryostat/ oven etc.

Vibrating Sample Magnetometer (EG&G PARC Model 4500)

Fig.14 Fully computer – controlled vibrating sample magnetometer (EG&G PARC Model 4500)

The vibrating sample magnetometer is both convenient and versatile. The Model 4500 vibrating sample magnetometer (VSM) is a fully computer – controlled device which is capable of conducting a wide range of susceptibility measurements as shown in Figure 14. This particular system has a greater flexibility to specific application requirements because of its state of the art design, augmented with a comprehensive applications software package. The model 4500 can measure the room temperature magnetic moments of a sample ranging from $1x10^{-3}$ moment to $1x10^{+3}$ moment. The temperature dependent magnetic moment from a few degrees Kelvin to approximately 1270 K can be measured with the help of available accessories. Requested sample zone temperature entered via the keyboard can cause the temperature controller to slow up or down as required. The temperature may be held constant during moment vs Oersted scans. Samples may be interchanged rapidly even at extreme temperatures.

The system is established with a two – way communications between the Model 4500 and various host computers with both an IEEE – 488 (GPIB) parallel link and an RS 232 C serial link which allows computer control of all the 4500's functions. The system is offered with a flexible (458A) applications software package for the IBM PC or IBM XT.

The EG&G PARC vibrating sample magnetometer (VSM) allows the measurement of magnetic characterization of a large variety of sample material under extremely diverse temperature conditions. The flexible design of VSM combines extremely high sensitivity with ease of sample mounting, orientation and exchange. The magnetic moments as small as $5x10^{-5}$ emu can be measured in magnetic fields ranging from zero to 2T with conventional

laboratory electromagnets or 9T with superconducting solenoids. With the available accessories, the EG&G PARC vibrating sample magnetometer is operable over a temperature range from 2.0 K to1323 K. The use of model 153 cryostat, which is helium – vapour shielded unit, enables temperature of sample environment to be reduced to liquid helium temperature. It also includes a flexible transfer line and liquid helium level indicator. Addition of the M 151H oven assembly enables sample temperatures of 1050 °C to be achieved.

Magnets having a diameter of $6^{//}$ or greater are recommended, although $4^{//}$ diameter magnets can be used. Magnet air gap must be set for $2^{//}$ access to field region to accept standard pick – up coil mounting hardware. Magnet ripple should be minimal to prevent overload problems on the more sensitive ranges.

The instrument also features automatic polarity sensing which provides bipolar readout for hysteresis and similar studies, in addition to digital and analog readout directly in electromagnetic units. A built – in Hall effect gaussmeter continuously monitors the applied magnetic field and provides a feedback signal to the magnet power supply during “field sweep” and “static” measurement conditions. The system’s high sensitivity coupled with its inherent ease of operation make it equally attractive for use in research and development or meeting the high volume requirements of a manufacturing environment.

In the present work, EG&G PARC Model 4500 vibrating sample magnetometer has been used to characterize all the compositions of $Y_{3-x}Fe_{5+x}O_{12}$(i.e Y(Fe)-Y-O) system at 300K for magnetization measurements

at National Chemical Laboratory (NCL), Pune and the saturation magnetization of all the compositions of $Y_{3+x}Fe_{5-x}O_{12}$ (i.e Y-Fe(Y)-O) system and ballmilled samples (at T=300 K and 20 K) were recorded at Department of Physics, University of Rajasthan, Jaipur. Thermal variation of magnetization of the 9hrs milled sample of YIG was obtained with an applied field of 200 Oe after zero field cooling (ZFC) from 273 K to 20 K.

3.5.2 Low field AC Susceptibility

The thermal variation of the low field ac susceptibility of samples was obtained by using the instrument, which consists of (i) magnetic field unit (ii) magnetization unit and (iii) temperature unit. The magnetic field is produced by a double coil set up i.e. Helmholtz coil, operating at a frequency of 263 Hz with rms field varying between 0 to 10 Oe. The two coils are oppositely wound relative to each other producing uniform magnetic field along the axis perpendicular to the coils. For the magnetization measurement a pick up coil is provided at the centre of a Helmholtz coil.

The temperature variation from 300K to 600K was achieved using a platinum wire wound silica tube, which acts as a furnace to heat the sample. The over heating of the coil is avoided by water circulars system as a precaution against the burning or leaking of the coil. The temperature was sensed by Platinum – Rhodium (Pt(Rh)) thermocouple calibrated against the current in the heating element. Variable current was provided to the heating element by a variable power supply. The sample tube is held in such a way that the sample material can be located in the middle of the pick up coil. By applying the current to the Helmholtz coil, the change in magnetization of the sample produces EMF in the pick up coil. The signal is then digitized by an analog to digital converter (ADC) and then fed to a digital panel meter. The block diagram/internal circuit diagram and the photograph of the susceptibility instrument are shown in the Figures 15 and 16 respectively.

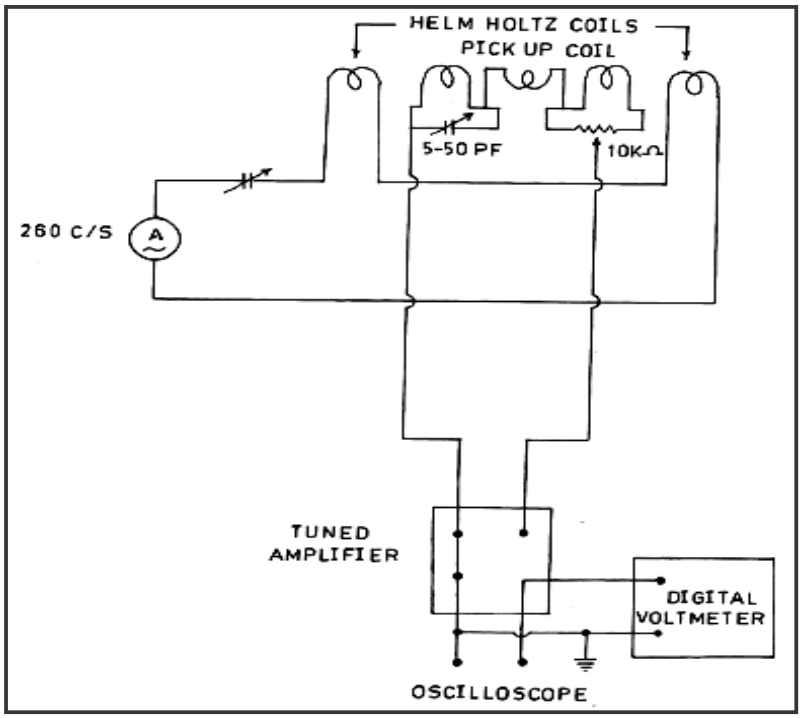

Fig.15 Block diagram of ac Susceptibility setup

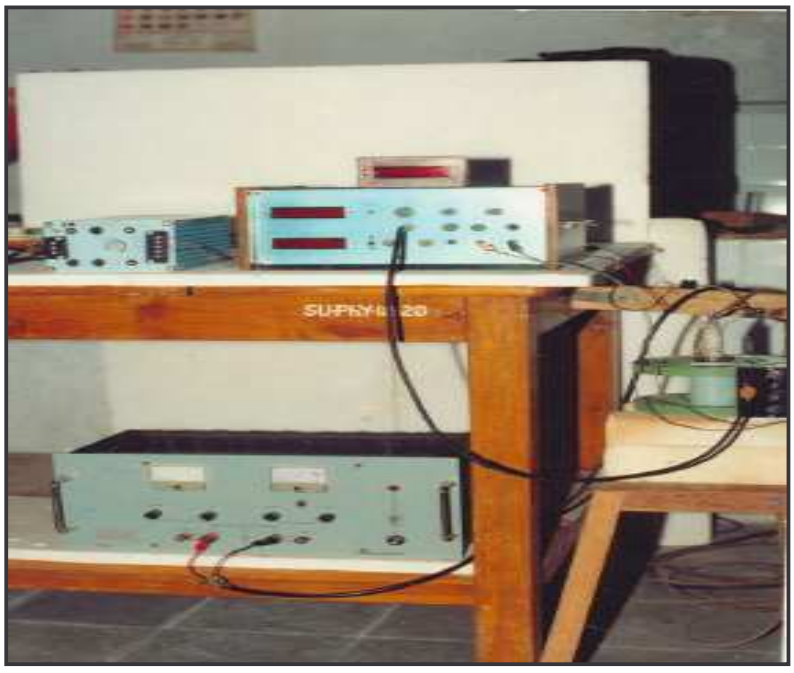

Fig.16 Photograph of ac susceptibility measurement instrument

Thermal variation of ac susceptibility of all the powdered samples of $Y_{3-x}Fe_{5+x}O_{12}$ (x=0.0, 0.1, 0.3, 0.5) and $Y_{3+x}Fe_{5-x}O_{12}$ (x=0.0-0.6, step=0.2) series and ballmilled samples of YIG composition was obtained in the temperature range 300-600K using a double coil setup [13] (Figure 16) operating at a frequency of 263 Hz and in an rms field of 40A/m at Department of Physics, Saurashtra University, Rajkot.

3.5.3 Mössbauer Spectroscopy:

Mössbauer spectroscopy is a versatile technique that can be used to provide information in many areas of science such as Physics, Chemistry, Biology and Metallurgy. It can give very precise information about the chemical, structural, magnetic and time-dependent properties of a material. Key to the success of the technique is the discovery of recoilless gamma ray emission and absorption, now referred to as the 'Mössbauer Effect', after its discoverer Rudolph Mössbauer, who first observed the effect in 1957 and received the Nobel Prize in Physics in 1961 for his work.

The Mössbauer Effect

Nuclei in atoms undergo a variety of energy level transitions, often associated with the emission or absorption of a gamma ray. These energy levels are influenced by their surrounding environment, both electronic and magnetic, which can change or split these energy levels. These changes in the energy levels can provide information about the atom's local environment within a system and ought to be observed using resonance-fluorescence. There are, however, two major obstacles in obtaining this information: the 'hyperfine' interactions between the nucleus and its environment are extremely small, and the recoil of the nucleus as the gamma-ray is emitted or absorbed prevents resonance.

In a free nucleus during emission or absorption of a gamma ray it recoils due to conservation of momentum, just like a gun recoils when firing a bullet, with a recoil energy E_R. This recoil is shown in Figure 17. The emitted gamma ray has E_R less energy than the nuclear transition but to be resonantly absorbed it must be E_R greater than the transition energy due to the recoil of

the absorbing nucleus. To achieve resonance the loss of the recoil energy must be overcome in some way.

Fig. 17 Recoil of free nuclei in emission or absorption of a gamma-ray

As the atoms will be moving due to random thermal motion the gamma-ray energy has a spread of values E_D caused by the Doppler effect. This produces a gamma-ray energy profile as shown in Figure 18. To produce a resonant signal the two energies need to overlap and this is shown in the red-shaded area. This area is shown exaggerated as in reality it is extremely small, a millionth or less of the gamma-rays are in this region, and impractical as a technique.

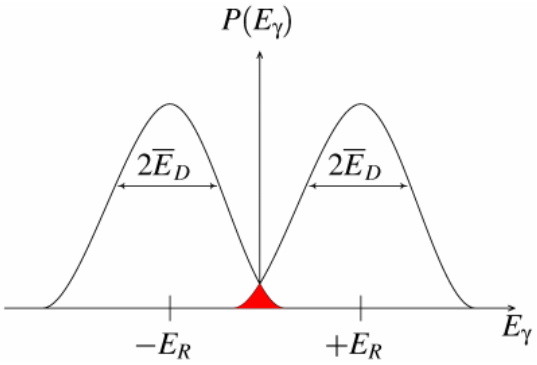

Fig.18 Resonant overlap in free atoms. The overlap shown shaded is greatly exaggerated

What Mössbauer discovered is that when the atoms are within a solid matrix the effective mass of the nucleus is very much greater. The recoiling mass is now effectively the mass of the whole system, making E_R and E_D very small. If the gamma-ray energy is small enough the recoil of the nucleus is too low to be transmitted as a phonon (vibration in the crystal lattice) and so the whole

system recoils, making the recoil energy practically zero: a recoil-free event. In this situation, as shown in Figure 19, if the emitting and absorbing nuclei are in a solid matrix the emitted and absorbed gamma-ray energy is the same hence resonance absorption can take place.

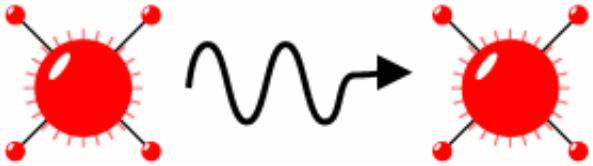

Fig.19 Recoil-free emission or absorption of a gamma-ray when the nuclei are in a solid matrix such as a crystal lattice

If emitting and absorbing nuclei are in identical, cubic environments then the transition energies are identical and this produces a spectrum as shown in Figure 20 a single absorption line.

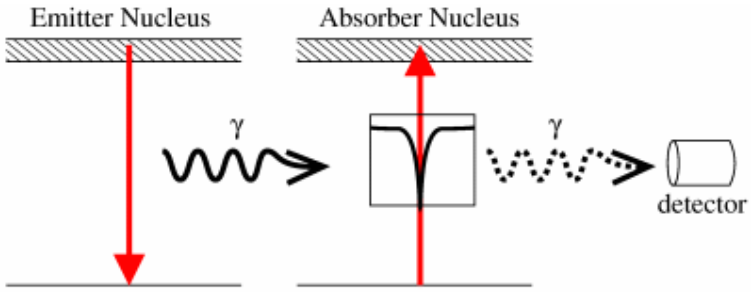

Fig.20 Simple Mössbauer spectrum from identical source and absorber

Now that we can achieve resonant emission and absorption can we use it to probe the tiny hyperfine interactions between an atom's nucleus and its environment? The limiting resolution now that recoil and doppler broadening have been eliminated is the natural linewidth of the excited nuclear state. This is related to the average lifetime of the excited state before it decays by emitting the gamma-ray. For the most common Mössbauer isotope, ^{57}Fe, this

linewidth is $5x10^{-9}$ eV. Compared to the Mössbauer gamma-ray energy of 14.4 keV this gives a resolution of 1 in 10^{12}, or the equivalent of a small speck of dust on the back of an elephant or one sheet of paper in the distance between the Sun and the Earth. This exceptional resolution is of the order necessary to detect the hyperfine interactions in the nucleus.

As resonance occurs only when the transition energy of the emitting and absorbing nucleus matches exactly, the effect is isotope specific. The relative number of recoil-free events (and hence the strength of the signal) is strongly dependent upon the gamma-ray energy and so the Mössbauer effect is only detected in isotopes with very low lying excited states. Similarly the resolution is dependent upon the lifetime of the excited state. These two factors limit the number of isotopes that can be used successfully for Mössbauer spectroscopy. The most used is ^{57}Fe, which has both a very low energy gamma-ray and long-lived excited state, matching both requirements well. Figure 21 shows the isotopes in which the Mössbauer effect has been detected.

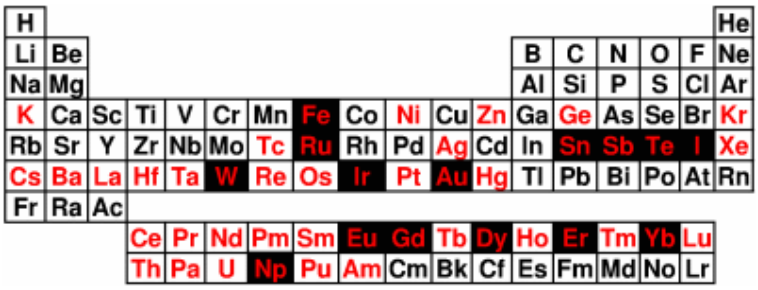

Fig.21 Elements of the periodic table which have known Mössbauer isotopes (shown in red font).Those which are used the most are shaded with black

Fundamentals of Mössbauer Spectroscopy

As shown previously the energy changes caused by the hyperfine interactions we will want to look at are very small, of the order of billionths of an electron volt. Such miniscule variations of the original gamma-ray are quite easy to achieve by the use of the Doppler Effect. In the same way that when an ambulance's siren is raised in pitch when it's moving towards you and lowered when moving away from you, our gamma-ray source can be moved towards and away from our absorber. This is most often achieved by oscillating a radioactive source with a velocity of a few mm/s and recording the spectrum in discrete velocity steps. Fractions of mm/s compared to the speed of light ($3x10^{11}$mm/s) gives the minute energy shifts necessary to observe the hyperfine interactions. For convenience the energy scale of a Mössbauer spectrum is thus quoted in terms of the source velocity, as shown in Figure 22.

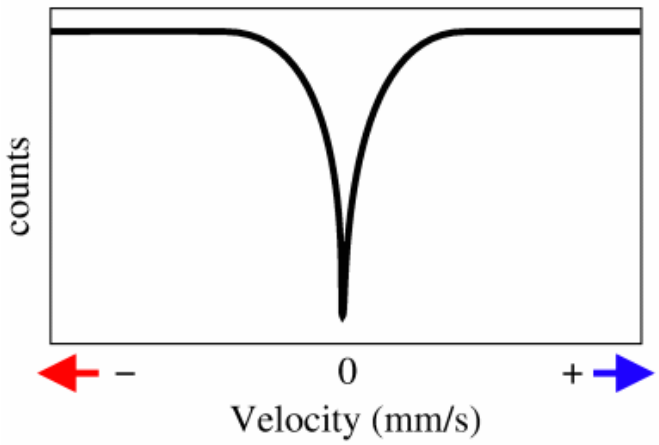

Fig.22 Simple spectrum showing the velocity scale and motion of source relative to the absorber

With an oscillating source we can now modulate the energy of the gamma-ray in very small increments. Where the modulated gamma-ray energy matches precisely the energy of a nuclear transition in the absorber the gamma-rays

are resonantly absorbed and we see a peak. As we're seeing this in the transmitted gamma-rays the sample must be sufficiently thin to allow the gamma-rays to pass through, the relatively low energy gamma-rays are easily attenuated.

In Figure 22 the absorption peak occurs at 0mm/s, where source and absorber are identical. The energy levels in the absorbing nuclei can be modified by their environment in three main ways: by the Isomer Shift, Quadrupole Splitting and Magnetic Splitting.

Isomer Shift

The isomer shift arises due to the non-zero volume of the nucleus and the electron charge density due to s-electrons within it. This leads to a monopole (Coulomb) interaction, altering the nuclear energy levels. Any difference in the s-electron environment between the source and absorber thus produces a shift in the resonance energy of the transition. This shifts the whole spectrum positively or negatively depending upon the s-electron density, and sets the centroid of the spectrum.

As the shift cannot be measured directly it is quoted relative to a known absorber. For example ^{57}Fe Mössbauer spectra will often be quoted relative to alpha-iron at room temperature.

The isomer shift is useful for determining valency states, ligand bonding states, electron shielding and the electron-drawing power of electronegative groups. For example, the electron configurations for Fe^{2+} and Fe^{3+} are $(3d)^6$ and $(3d)^5$ respectively. The ferrous ions have less s-electron at

the nucleus due to the greater screening of the d-electrons. Thus ferrous ions have larger positive isomer shifts than ferric ions.

Quadrupole Splitting

Nuclei in states with an angular momentum quantum number I>1/2 have a non-spherical charge distribution. This produces a nuclear quadrupole moment. In the presence of an asymmetrical electric field (produced by an asymmetric electronic charge distribution or ligand arrangement) this splits the nuclear energy levels. The charge distribution is characterized by a single quantity called the Electric Field Gradient (EFG).

In the case of an isotope with I=3/2 excited state, such as ^{57}Fe or ^{119}Sn, the excited state is split into two substates m_I=±1/2 and m_I=±3/2. This is shown in Figure 23, giving a two line spectrum or 'doublet'.

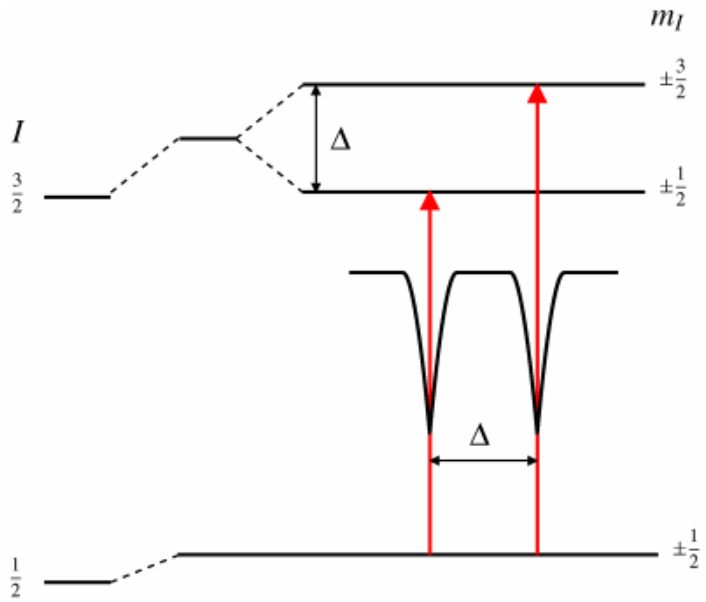

Fig.23 Quadrupole splitting for a 3/2 to 1/2 transition

The magnitude of splitting, Delta, is related to the nuclear quadrupole moment, Q, and the principle component of the EFG, V_{zz}, is shown by the relation Delta=eQV_{zz}/2.

Magnetic Splitting

In the presence of a magnetic field the nuclear spin moment experiences a dipolar interaction with the magnetic field ie Zeeman splitting. There are many sources of magnetic fields that can be experienced by the nucleus. The total effective magnetic field at the nucleus, B_{eff} is given by:

$$B_{eff} = (B_{contact} + B_{orbital} + B_{dipolar}) + B_{applied}$$

the first three terms being due to the atom's own partially filled electron shells. $B_{contact}$ is due to the spin on those electrons polarizing the spin density at the nucleus, $B_{orbital}$ is due to the orbital moment on those electrons, and $B_{dipolar}$ is the dipolar field due to the spin of those electrons.

This magnetic field splits nuclear levels with a spin of I into (2I+1) substates. This is shown in Figure 24 for ^{57}Fe. Transitions between the excited state and ground state can only occur where m_I changes by 0 or 1. This gives six possible transitions for a 3/2 to 1/2 transition, giving a sextet as illustrated in Figure 24, with the line spacing being proportional to B_{eff}.

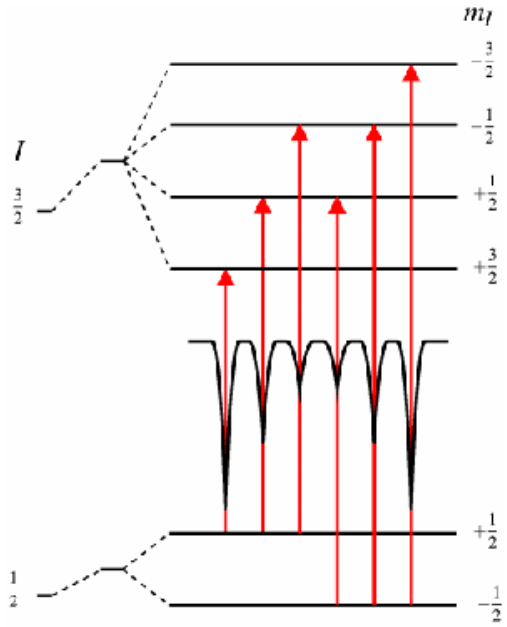

Fig.24 Magnetic splitting of the nuclear energy levels

The line positions are related to the splitting of the energy levels, but the line intensities are related to the angle between the Mössbauer gamma-ray and the nuclear spin moment. The outer, middle and inner line intensities are related by:

$3 : (4\sin^2\theta)/(1+\cos^2\theta) : 1$

meaning the outer and inner lines are always in the same proportion but the middle lines can vary in relative intensity between 0 and 4 depending upon the angle the nuclear spin moments make to the gamma-ray. In polycrystalline samples with no applied field this value averages to 2 (as shown in Figure 24) but in single crystals or under applied fields the relative line intensities can give information about moment orientation and magnetic ordering.

These interactions, Isomer Shift, Quadrupole Splitting and Magnetic Splitting, alone or in combination are the primary characteristics of many Mössbauer spectra.

Mössbauer Spectrometer

The major components are a radioactive source, an electro-mechanical transducer (Doppler scanning device), an absorber, an energy sensitive gamma-ray detector and a data acquisition system. The source is specifically prepared using the nuclides appropriate for giving Mössbauer effect. For example, ^{57}Fe nuclide is widely used nuclide. Its precursor ^{57}Co radioactive nuclides are embedded in a matrix of crystalline structure of different elements such as Pd, Rh, Cu, etc.

If the transition energy of the source and the absorber nuclides are different as a result of different hyperfine interactions in both, its effect will be

to destroy the resonance. To restore the resonance the respective additional energy must be applied to or subtracted from the gamma radiation of the source. Relative motion between the absorber and the source adds Doppler motion energy to the system. The Doppler velocity required to demonstrate the natural width of ^{57}Fe nuclide is $\Delta E/E = v/c$; v comes out to be 1.4×10^{-2} cm/sec. The velocity is then changed and if the total scan of all intermediate velocity between 0 and 1.4×10^{-2} cm/sec (in both the directions) is done, a spectrum demonstrating the natural line width of resonance can be achieved.

The modern commercial equipments operate in a constant-acceleration mode rather where a whole range of velocities is scanned from zero to a preset maximum value. This scanning is accomplished in synchronization with the multi channel analyzer. Each channel accumulates the number of transmitted counts for the same given velocity increment during each cycle. The device for this includes constant acceleration cams, electromechanical transducers such as high fidelity loudspeakers.

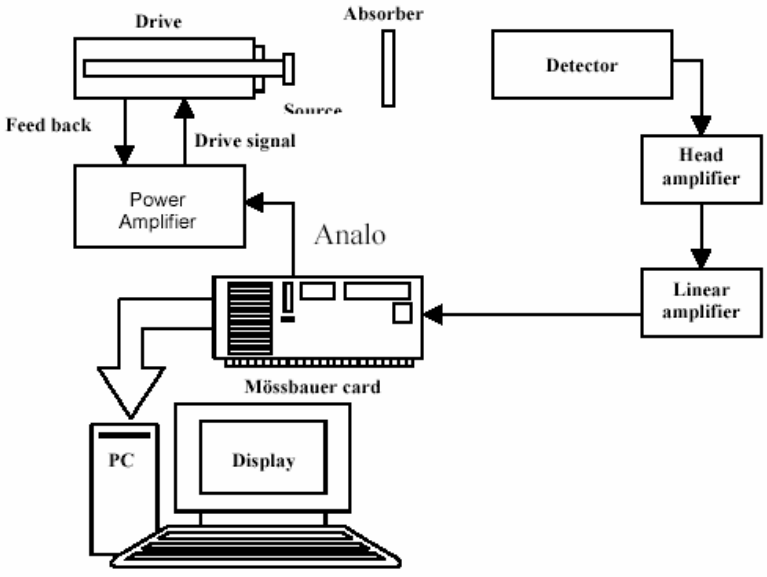

Fig.25 Block Diagram of Mössbauer measurement setup

The Mössbauer detectors are energy sensitive detectors. Different types of detectors are used depending on the specifics of the application. Commonly used detectors are Proportional counters and Scintillation detectors.

Mössbauer line shape and analysis of spectra:

The Mössbauer line has the Lorentzian or Breit-Winger shape and can be described by,

$$I(E) = \frac{f_s \cdot f_a \cdot n \cdot \sigma_0 \cdot d \cdot (\Gamma/2)}{(E - E_0)^2 + (\Gamma/2)^2}$$

where $\Gamma = 2\Gamma_0 = 2\leftarrow/ ı$ is the measured line width

E_0 = the transition energy

d = absorber thickness

σ_0 = the resonance absorption cross section

f_s and f_a are the resonace fractions for the source and the absorber.

The analysis of the Mössbauer spectra is done for accurate determination of line positions, line widths and area under the resonant peak. This is done using the standard computational method for curve fitting the Mössbauer spectra according to constrained least square analysis of the different parameters of the theoretical model provided. This is done with using computer software [14-16].

The above equation for Lorentzian profile to account for observed spectrum can be given by,

$$Y(x) = b - \frac{Y(0)}{1 + \left(\frac{x - x(0)}{\Gamma_{ex}/2} \right)^2}$$

Here b is the baseline intensity, Y(0) is the amplitude of the peak located at resonance energy (or velocity) x(0) which is nothing but $Y(0) = f_s.f_a.n.\sigma_0.d.(\Gamma/2)$ and Γex is the F.W.H.M. for the line. This equation is for fitting any one Mössbauer line. But for n lines, the equation becomes,

$$Y(x) = b - \sum_{i=1}^{n} \frac{Y(0)_i}{1 + \left(\frac{x - x(0)_i}{\Gamma_{ex}/2} \right)^2}$$

The least square fitting of observed and calculated profile is done as follows: goodness of fit is given by χ^2.

$$\chi^2 = \sum_{r=1}^{n} W_r \left[Y_r - Y\left(x_r / q \right) \right]^2$$

Where Y_r is observed count at channel r, $Y\left(\frac{X_r}{q}\right)$ is the function given above.

Wr is the inverse of variance for channel r. the q is the parameter to be corrected for fitting. The least square fitting is then;

$$d\chi^2 / dq_i = 0$$

This is one iteration, the value of q_i are corrected until the change in χ^2 is minimized. The computer software generally does constrained analysis where the theoretical relationship has been established between various q values and so the parameters to be controlled by the users are reduced.

The Mössbauer spectra were recorded at 300K on the Mössbauer spectrometer at Indian Institute of Tecnology, Kanpur and at IUC-DAE UGC CSR, Indore. The spectra were obtained using constant acceleration

transducer and 512 multi-channel analyze, operating in time mode. A gamma ray source of ^{57}Co in Pd matrix of 25 mCi was used. The spectra were obtained in transmission geometry and 14.4 keV gamma rays were detected by Xenon-Methane filled proportional detector. The absorbers were made using the samples in powder form of the thickness around 20 – 30 mg/cm^2.

The Mössbauer spectra were analyzed using NORMOS computer software. The program is developed by R.A. Brand, Laboratorium fuer Angewandte Physik, Universitaet Duisburg, Lotharstr. 1, D-4100 Duisburg 1. The NORMOS programs are for fitting a wide variety of different Mossbauer spectra. There are two versions NORMOS/SITE is for fitting spectra composed of a certain number of discrete sub-spectra. The program uses nonlinear least-squares minimization with the Levenberg-Marquardt method.

The program gives the final parameters after best fitting the observed spectra with the one theoretical generated by it using the parameters provided by user and then after refined by it. The goodness of fit can be checked by the χ^2 value. The refined parameters and the statistical errors in them can be obtained along with the observed and fitted spectra in format of plot file, which can be plotted by user. The detailed discussion is given in [17-19].

3.5.4 Initial permeability

Initial permeability (μ_i) is considered to be an important parameter of a magnetic material, which describes the effect of the applied magnetic field on the state of magnetization of the material. Initial permeability is defined as ratio of the magnetic induction B to an infinitesimally small applied field H, applied to initially unmagnetized material and given as

$$\mu_i = \frac{1}{\mu_0} \lim_{H \to 0} \frac{B}{H}$$

where μ_0 is the permeability of the free space (~$4\pi \times 10^{-7}$ Henry/meter). In the case of alternating applied field, the magnetization produced in the material does not remain in phase with the applied field due to the damping and results in dissipation of the energy. Therefore the initial permeability can generally expressed in the complex quantity,

$\mu_i = \mu_i' - j\mu_i''$

μ_i' is the dispersive part and μ_i'' is the dissipative part of the initial permeability. Both are frequency and temperature dependent. The magnetization mechanism contributing initial permeability can be attributed to the presence of the ferromagnetic domains as per in the molecular field theory. The spins are lined parallel to one another in domains. The layer that separates the adjacent domains is termed as domain wall or Bloch wall [20]. In Bloch wall the direction of magnetization gradually changes from one orientation to another. The magnetization mechanism which contribute to initial permeability are contributed to the simultaneous rotation of spins in each Weiss domain, known as domain rotation or to the reversible displacement of bulging of domain walls, known as domain wall motion[20,21]. It is also well known that initial permeability is a grain size

dependent parameter [22]. Globus explained the contribution of the various processes of magnetization [23].according to him the rotational permeability is isotropic in ferrimagnetic materials and is given by the relation

$$\mu_{ir} = 1 + 8\pi \frac{M_s}{Ha}$$

where μ_{ir} represents the contribution of domain rotations to initial permeability, M_s is the saturation magnetization and H_a represents the field due to the various types of anisotropies present in the material. H_a in case of polycrystalline material, consisting of randomly oriented crystallites, without any magnetic interaction and having small crystal anisotropy is given by

$$H_a = \frac{2K_1}{M_s} (K_1 > 0)$$

where K_1 is magneto-crystalline anisotropy constant.

Thus the polycrystalline materials with small anisotropy, permeability can be rewritten as,

$$\mu_{ir} = 1 + \frac{4\pi M_s^2}{K_1}$$

A Weiss domain structure is stable only as a whole, that is to say the walls are strongly coupled to each other, and in general a particular wall will only be able to move provided that all the others or at least a number of them move too. The initial permeability resulting from a number of walls at a distance d_s apart is given by

$$\mu_{rw} = \frac{4M_s^2 D^2}{\sigma_w d_s}$$

where μ_{rw} represents the domain wall contribution to initial permeability, D is the span of the wall spacing. From the above equations, it follows that initial

permeability increases with increase in saturation magnetization and with decrease in the anisotropy constant K_1. Initial permeability also depends on the preparation method of the material as it depends on the grain size and the porosity. Larger the grain size higher will be the initial permeability.[24,25].

Dispersion of Initial permeability

The initial permeability varies with the frequency of the applied field. Different groups have explained variations in different ferrite materials. Snoek [26,27] observed a broad natural ferromagnetic resonance in several compositions of Mn-Zn ferrites for radio frequencies between 1 and 100MHz, and attributed it to the rotation of domains. His explanation was based on the theory proposed by Landau and Lifshitz [28].The fundamental idea of this theory is that the crystalline anisotropy is equivalent to an effective static magnetic field, H_a, acting inside each crystallite, which produces larmour precession of the appropriate electron spins. Since the rotation of spins is the subject to damping, it is apparent that resonance absorption will occur in any given crystallite, if a small magnetic field, oscillating near the Larmour frequency is applied to crystallite along a direction different from that of H_A. The expression of resonance frequency, ω_r, due to domain rotations, neglecting all the magnetic interactions and attributing H_A to the crystalline anisotropy is written as $\varpi_r = 2\gamma \frac{K_1}{M_s}$

where γ=ge/2mc, is the magneto-mechanical ratio and g is the spectroscopic splitting factor. This equation implies that resonance due to domain rotation occurs at higher frequency in a material having large crystalline anisotropy and low saturation magnetization. It has also been reported that the

resonance is not only due to crystalline anisotropy but also due to internal demagnetization field [29,30].Two resonance peaks in case of commercial ferrites have been reported by Rado [31].One of the peak lies in radio frequency region and other in microwave region. It has been concluded from various observations that the resonance peak appearing in the radio frequency region is primarily due to domain wall displacement while the peak appearing in the microwave frequency range is primarily due to domain rotation. Globus et. al. [32, 33] has reported that radio frequency susceptibility consists of a constant but negligible small part due to domain rotation whereas the major contribution comes from domain wall motion. The domain wall contribution is found to be well described by the classic harmonic oscillator model, with a resonance around 10 MHz [34]. However, the domain wall contribution is found to be negligible above 50 MHz. In contradiction to Snoek's classical interpretation, the domain wall displacement and the uniform rotation have been found to contribute equally to the static susceptibility. Rado et. al. [29] derived an expression for the resonance frequency, $\omega_{r,}$ due to domain wall displacement, which is given as

$$\varpi_w = \left(\frac{\gamma M_s}{\chi_{\sigma w}}\right)\left[\frac{8\pi\chi_{\sigma w}\delta}{d}\right]^{1/2}$$

$\chi_{\sigma w}$ is the static susceptibility due to domain wall displacements, δ is the wall thickness parameter, and d is the average domain size. Thus it follows from the above expression that unlike ω_r the resonance frequency due to wall displacement ω_w does not depend upon the anisotropy constant but depends upon the value of saturation magnetization M_s. The sintered ferrite contains a wall resonance as well as rotation resonance. However, the single domain

particles and in suitably oriented monocrystals, the domain theory excludes the possibility of both the resonance mechanisms. The appearance of single broad resonance is also observed the two resonances coalesce [31]. For example, the presence of zinc in a mixed ferrite decreases the value of K_1 thereby reducing the value of ω_r. Since ω_w does not depend on the anisotropy constant, its value remains almost constant. Hence both the resonance peaks overlap each other yielding single broad resonance.

Figure 26 shows permeability spectra of pure YIG with different grain size and Al^{3+}-substituted YIG at 300K.

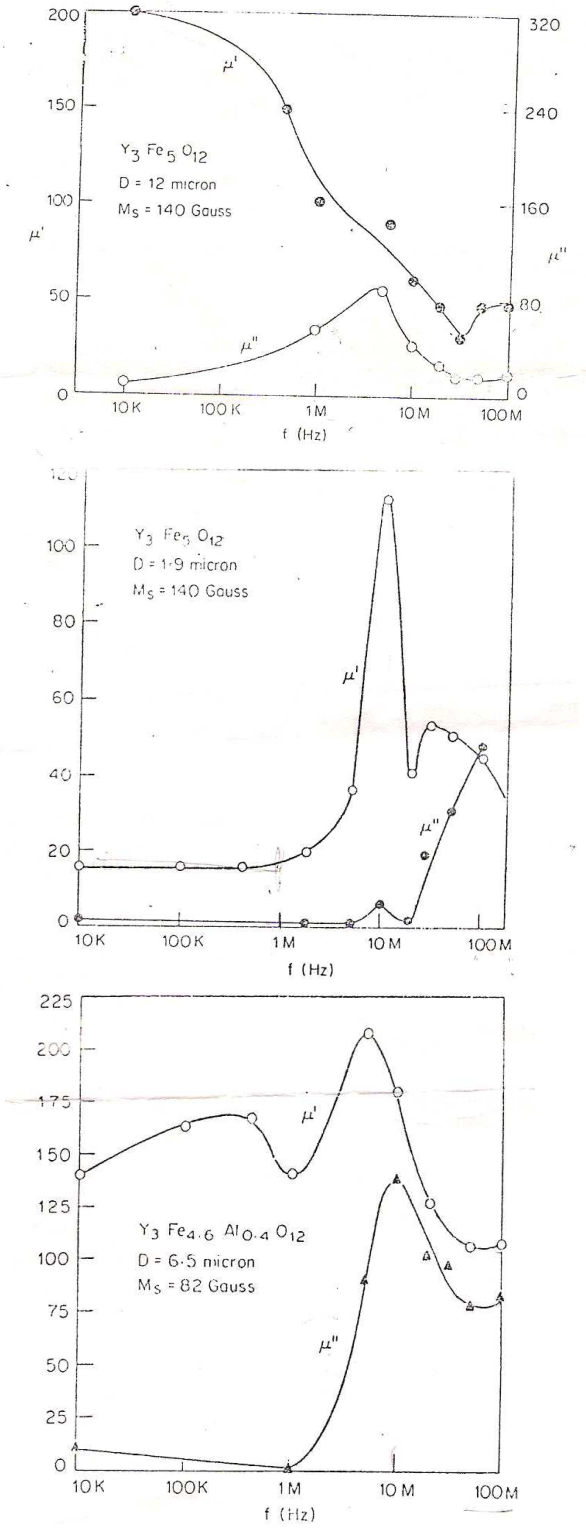

Fig.26 Permeability spectra of pure YIG with different grain size and Al^{3+}-substituted YIG at 300 K

Experimental details

Heck [35] gave an easy technique to measure the initial permeability. It can be determined by measuring the inductance of the toroidal sample as a function of frequency. In present work initial permeability as a function of frequency from 100 Hz to 13 MHz was determined by measuring the inductance of toroids using a 4192 A impedance analyzer. The initial permeability is expressed as

$\mu_i = L/L_0$

where the air core inductance L_0 (in Henry) is given as

$$L_0 = 4.6N^2 d \log\left(\frac{r_0}{r_i}\right) x10^{-9}$$

where N is the number of turns, d the thickness of the toroid in meters, r_0 and r_i are the outer and inner radii of the toroid.

3.6 Electrical resistivity, Thermo-Electric power and Dielectric constant

3.6.1 Hopping Model of Electrons

Most of the oxide spinels not containing transition metal ions are very good insulators at room temperature [36]. This behaviour may be understood as due to a large energy gap (often of several eV) between the occupied valence band primarily formed by the oxygen 2p states and the empty conduction band. The actual values of electrical conductivity and the activation energies are then usually controlled by impurity levels within the gap. With the presence of the transition metal ions additional energy levels and/or narrow bands are introduced usually also lying in the gap. This need not necessarily change the picture of the electronic charge transport very much provided that transport within the partially occupied d levels (bands) themselves does not dominate. In particular, many oxide spinels with $3d^n$ ions in the tetrahedral positions only possess a very low conductivity. The same is true for pure stoichiometric spinels having only one kind of ions on equivalent crystallographic sites such as the normal spinels $ZnFe_2O_4$ and $CdFe_2O_4$ or ordered $Li_{0.5}Fe_{2.5}O_4$. A considerable increase of the electrical resistivity is usually connected with the combined effect of disorder and the presence of cations able to change easily their valence states or actually coexisting with different valencies in the material. Typical examples are divalent and trivalent Fe or Co ions in the octahedral positions. The charge transfer may then be effectuated by hopping of electrons or holes between equivalent ions (valency exchange) which is a rather easy process. The sign of Seebeck coefficient

(Thermo-electric power) is often helpful in clarifying the nature of the dominating charge carriers and the mechanism of their motion.

The magnetite Fe_3O_4 has high value of DC conductivity at room temperature ~ 250 $\Omega^{-1}cm^{-1}$ and peculiar character of the conductivity versus temperature dependence. The substitution in magnetite may lead to hindrance to the free motion of electronic charge carriers after exceeding certain critical concentration of substituent due to Anderson localization [37]. At finite temperatures they may be thermally activated to hop to other ions and contribute to the electrical transport. The range of resistivity values of ferrite and garnet materials is wide from 10^{-4} to 10^{9} Ω.m at room temperature [38]. In ferrites, the high value of resistivity is associated with the simultaneous presence of ferrous and ferric ions on equivalent lattice sites (usually the octahedral sites). In nickel-zinc ferrite it was found that the resistivity was about 10 Ω.m when the material contained 0.42 percent by weight of ferrous oxide but this resistivity increased approximately one thousand fold when the specimen was more completely oxidized [38].

A mechanism of conduction in stoichiometric ferrites is due to thermally activated electron hopping. The extra electron on a ferrous ion requires little energy to move to a similarly situated adjacent ferric ion. The valence states of the two ions are interchanged. Under the influence of an electric field, these extra electrons can be considered to constitute the conduction current, jumping or hopping from one iron ion to the next.

Polaron Model

When an electron is excited to the conduction band in an ionic crystal, it interacts with the longitudinal optical lattice vibration. The Physical origin of

this interaction is that the electric field arising from the electron induces displacements of positive and negative ions and consequently the restoring force acting on the longitudinal wave changes. On the other hand, electric polarization in the crystal induced by an electron affects conversely the motion of the electron. Electron moves accompanied by a phonon cloud around it. Thus, electron and phonon cloud compose a kind of composite particle called polaron. The polaron is one of the elementary excitations in a solid. Because of the presence of the phonon cloud, the polaron mass becomes larger than the band mass, i.e renormalization of the mass takes place. If m* represents the mass of the polaron, then

m* = m/(1-α/6)

$$\frac{m^*}{m} = 1 + \frac{\alpha}{6} (\alpha << 1)$$

where $\alpha = \frac{1}{2}\left(\frac{1}{\varepsilon_\infty} - \frac{1}{\varepsilon_0}\right)\frac{e^2}{\hbar\omega}\left(\frac{2m\omega}{\hbar}\right)^{\frac{1}{2}}$

is a non-dimensional quantity and a coupling constant which describes the strength of interaction between the electron and the phonon.

The polaron comprises the electron plus its surrounding lattice deformation. Polarons can also be formed from holes in the valence band. If the deformation extends over many lattice sites, the polaron is “large”, and the lattice can be treated as a continuum. Charge carriers inducing strongly localized lattice distortions form “small” polarons.

Small polaron

For a small polaron the spatial extent of its self-trapped charge is comparable to or smaller than interionic distances. In particular atoms surrounding an excess charge are displaced to new equilibrium positions and

produce a potential well which traps the excess particles. Small polaron formation is typically associated with the interaction of the excess charge with the atoms in its immediate vicinity. Thus, unlike the case of the large polaron, the self trapping is not primarily associated with the long range interaction of an excess charge with the dipolar fields of polar materials. Hence, the name polaron, coined to reflect this latter situation, is a misnomer for the small polaron. Electron and hole small polarons are found in both polar and non-polar semiconductors and insulators. This includes numerous oxides and molecular solids.

Small polaron motion proceeds relatively slowly via a succession of phonon- assisted hopping events. As a result, the small polaron drift mobility increases as a thermal agitation of the solid increase. Above a temperature comparable to the solid's phonon temperature, the diffusivity increase in an Arrhenious manner with reciprocal temperature.

The migration of small polaron requires the hopping of both the electron and the polarized atomic configuration from one site to an adjacent one . The drift mobility can be given as;

$$\mu = (1-c)ea^{2\Gamma/KT}$$

where, e is the electronic charge, a the lattice parameter, c is the fraction of sites which contain an electron (c=n/N), n is the number of electrons and N the number of available sites per unit volume. The quantity Γ is the jump rate of the polaron from one site to a specific neighbouring site.

The small polaron model also explains the low value of mobility, temperature independent, Seebeck coefficient and thermally activated hopping. In addition to these properties if the hopping electron becomes

localized by virtue of its interaction with phonons, then a small polaron is formed and the electrical conduction is due to hopping motion of small polarons.

Large polaron

The concept of the large polaron is most useful when the carrier mobility is high and the carrier density and temperature both are low [39].

3.6.2 Electrical resistivity

The range of resistivity values of ferrite and garnet material is wide, from 10^{-4} to 10^{9} Ω.m at room temperature [40].In Ferrites, the value of resistivity is associated with the simultaneous presence of Ferrous and ferric ions on equivalent lattice sites. The extra electron on a ferrous ion requires little energy to move to a similarly situated adjacent ferric ion. The valence states of the two ions are interchanged .Under the influence of an electric field, these extra electrons can be considered to constitute the conduction current, jumping or hoping from one iron ion to the next. Thus, mechanism of conduction in stoichiometric ferrites is due to thermally activated electron hopping. Since the materials are semiconductors, their resistivity ρ should decrease with increase in temperature according to a relation of the form

$$\rho = \rho_0 \exp (\Delta E/kT)$$

This relation is indeed often observed and the activation energy ΔE can then be interpreted as the energy required causing the electron jump referred above. The activation energy varies from several hundredths of eV for Fe^{2+} content to ~ 0.2 eV to 0.6 eV for stoichiometric ferrites. As would be expected with such a conduction mechanism, the high activation energy is associated

with a high resistivity at room temperature. It has been found that the pre - exponential factor ρ_0 is almost fully determined by the Fe^{2+} concentration [41].

In many ferrite systems it is observed that slope of Arrhenius curve changes to the Curie point. The activation energy increases on changing from ferrimagnetic to paramagnetic region. This anomaly strongly supports the influence of magnetic ordering upon the conductivity process in ferrites. Figure 27 shows resistivity versus temperature plot for pure YIG and Ho-and Ga- substituted YIG.

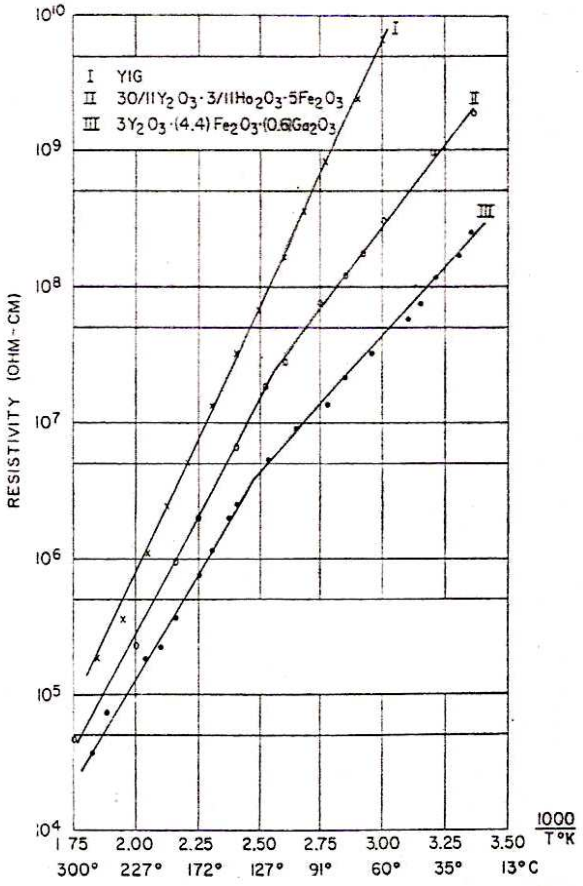

Fig.27 Resistivity versus temperature plot for pure YIG and Ho- and Ga-substituted YIG

Experimental details

The temperature dependence of dc electrical resistivity for all the garnet system has been studied at Department of Physics, Saurashtra

University, Rajkot. In the electrical resistivity measurement a typical sample holder shown in Figure 28. specially designed and fabricated for the resistivity measurement was used.

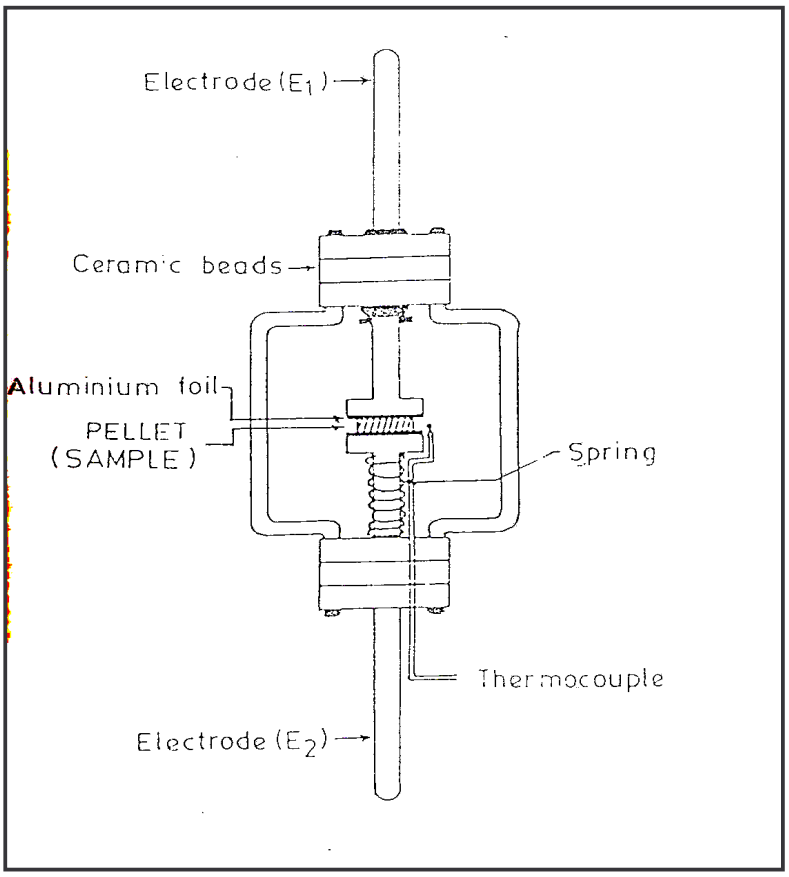

Fig.28 Typical sample holder for dc resistivity measurements

It consists of two ceramic beads with supporting metal rods. The electrodes E1 and E2 are also shown in this figure. The spring loaded brass electrode (E2) is introduced into the ceramic beads and it pressed hard against the surface of the pellets. The brass electrode E1 is fixed at the other end. The resistance of a pellet was measured by two terminal method using meg-ohm meter supplied by ARUN ELECTRONICS. The sample surfaces were rubbed by graphite and thin aluminium foils were placed between the

terminals of sample holder with the pellet was placed in a horizontal electric furnace to study the change in resistivity wit h temperature. The temperature of the furnace was controlled by maintaining the current passing through the heater with Cr-Al thermocouple. Experimental set-up is shown in the fig. The activation energy for the ferrimagnetic region (Ef) and paramagnetic region (Ep) in electron volt (eV) were determined from the slopes of log ρ versus $10^3/T$ plots.

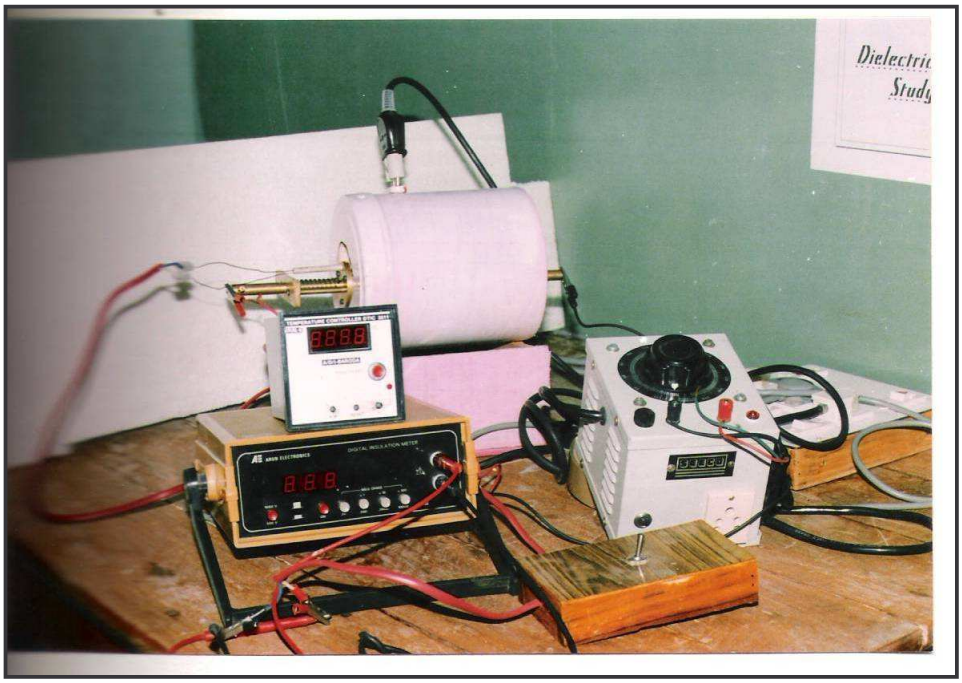

Fig.29 A Photograph of two probe dc resistivity measurement setup

3.6.3 Thermoelectric power

A temperature difference between the two ends of a semiconductor gives rise to an electromotive force (emf) known as thermo emf (ΔV). It is found that the generated thermo-emf is proportional to the temperature difference (ΔT) and is given by the relation;

$\Delta V = \alpha . \Delta T$

where α is the Seebeck coefficient also often known as the thermo –electric power.

The Hall effect and thermo-electric properties are widely used in the interpretation of the conduction mechanism in semiconductors. The interpretation of Hall effect is more straightforward, it also gives precise results. However, in the case of low mobility materials such as ferrites, it is difficult to measure the Hall effect; in these circumstances the thermo-electric power measurement is the only alternative. The sign of the thermo-electric emf gives vital information about the type of conduction in semiconductors whether it is p-type or n-type. Another important significance of thermo emf is that it enables one to calculate the values of the charge carrier concentration, which inturn used to calculate mobility of charge carriers.

The Fermi energy in the case of a semiconductor can be obtained from the relation: $\alpha T = (E_G - E_F) + 2kT$, for n- type semiconductors and

$\alpha T = E_F + 2kT$, for p-type semiconductors.

where, E_G; band gap energy of the ferrite semiconductor,

E_F;Height of the Fermi energy level from the top of the filled Valency band

and 2kT= the term which accounts for the transfer of kinetic energy of the carriers in moving from the hot region of the ferrite to a cold one.

While discussing the electrical properties of α-Fe_2O_3, for which the mobility of the charge carrier is low, Morin [42] assumed that the conduction is occurring in exceedingly narrow bands or in localized levels. This assumption leads to the result that the kinetic energy term in the Seebeck effect can be neglected, so that for electrons alone, $\alpha = E_G - E_F$

While for holes alone, $\alpha = E_F$

Plot of thermoelectric power (S) against inverse of temperature (T^{-1}) for rare-earth iron garnets is shown in Figure 30.

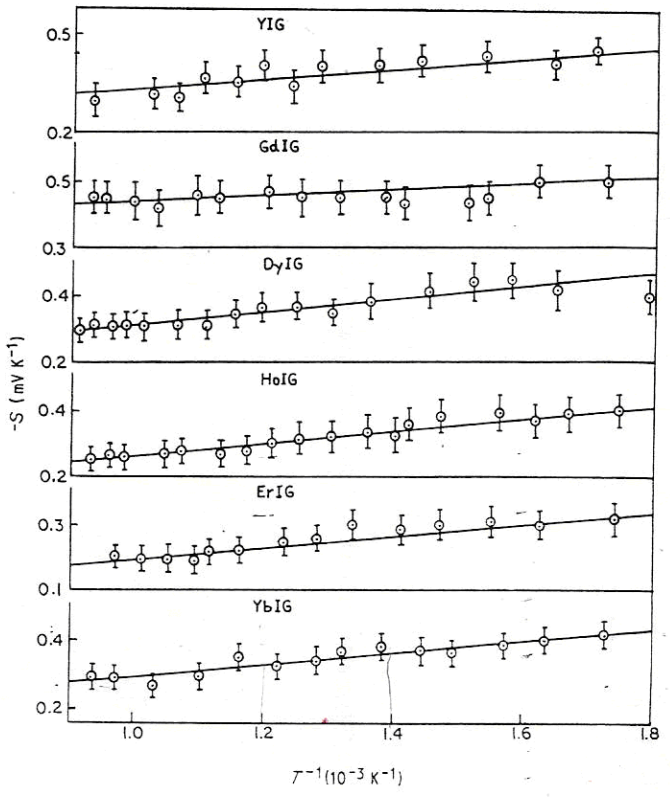

Fig.30 Plot of thermoelectric power (S) against inverse of temperature (T^{-1}) for rare-earth iron garnets

The values of seebeck coefficient (α), slope (η) and intercept of the curve (H) with α axis and mobility (μ) for some garnet are summarized in the Table 1.

Table 1 Values of seebeck coefficient (α), slope (η) and intercept of the curve (H) with α axis and mobility (μ) for some garnet

System	α (mV/K)	η(V) $\pm$0.05	H (mV/K)	μ x 10^{-10} m^2/V.sec
$Y_3Fe_5O_{12}$	0.34	0.10	0.28	6.93
$Gd_3Fe_5O_{12}$	0.34	0.12	0.26	9.33
$Dy_3Fe_5O_{12}$	0.31	0.16	0.18	9.22
$Ho_3Fe_5O_{12}$	0.34	0.17	0.10	6.96
$Er_3Fe_5O_{12}$	0.28	0.17	0.03	14.26
$Yb_3Fe_5O_{12}$	0.35	0.17	0.14	21.71

Experimental details

Seebeck coefficient for Fe^{3+}-subsituted yttrium iron garnet ($Y_{3-x}Fe_{5+x}O_{12}$; x=0.0, 0.1, 0.3 and 0.5) compositions have been determined as a function of composition and temperature by the two probe differential method at Department of Physics, Saurashtra university, Rajkot.

Thermo electric power measurement set-up is as shown in Figure 30. It consists of a point contact probe, which acts as a hot junction and a base which acts as a cold junction. Sample is placed between these two junctions. The temperature of the hot probe is raised to a maximum of about 673 K with the help of an electric heater, which is wound round the hot probe.

A pointed hot probe is used here since garnet samples are very good thermal conductors; if a pointed probe is not used to upper and the lower surfaces of the sample will attain almost the same temperature and no temperature gradient will be maintained between them . It was found that the value of α does not depend on the temperature when the temperature gradient between the two junctions is less than 10K. The hot probe and cold

base are connected to a digital microvolt meter (model:DMV001) supplied by Scientific Equipment & Services for measuring the thermo-emf. The error in the measurements of seebeck coefficient is about ±3%.

In the case of an n-type semi-conducting material, the hot surface becomes positively charged, as it loses some of its electrons. The cold surface of the semiconductor becomes negatively charged due to the diffusion of the free electrons from the hot portion. Conversely, in a p-type semi-conducting material, the hot surface becomes negative, and the cold one positive. Thus the type of conduction in a given semi-conducting material can readily be determined from the sign of the thermo-emf.

The values of the thermo-emf have been noted while cooling, because the samples will attain sufficient thermal stability while cooling rather than while heating. The sample is maintained at a given temperature for about 10minutes. The temperature of the two surfaces has been measured with the help of an alumel thermocouple which were kept very close to the chromel sample.

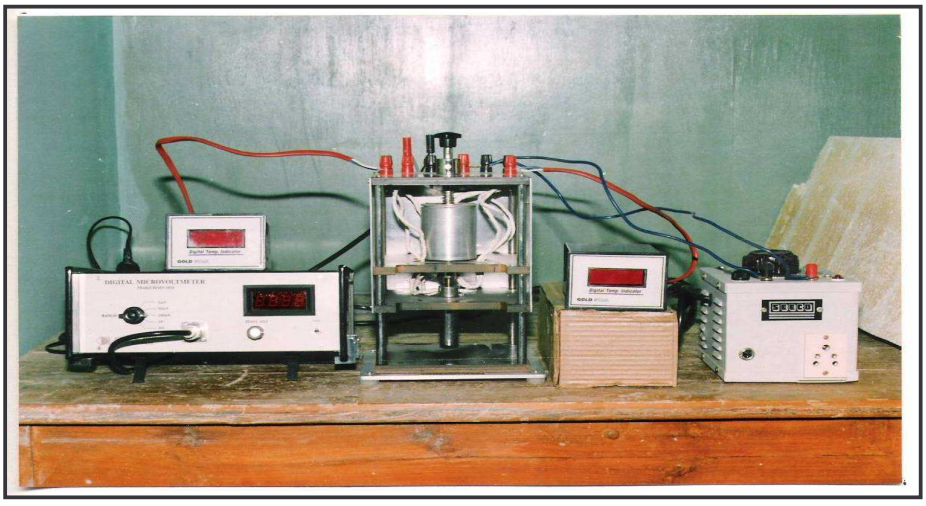

Fig.31 Thermoelectric power measurement setup

3.6.4 Dielectric constant and Loss Factor

The dielectric material reacts to an electric field differently from a free space because it contains charge carriers that can be displaced and the charge displacement within a dielectric can neutralize a part of applied field, which involve the bond charge neutralization by polarization of the dielectric. There are various possible mechanisms for polarization in a dielectric material. One process common to all materials is electronic polarization, the shift of center of the negative electron cloud in relation to the positive nucleus. The second mechanism is displacement of positive and negative ions in relation to one another called the ionic polarization. Then, there are orientational and space charge polarization. Thus, the total polarization of the dielectric can be represented as the sum of the contributions of these mechanisms,

$$\alpha_p = \alpha e + \alpha i + \alpha o + \alpha s$$

where αe = electronic polarizability

αi = ionic polarizability

αo = orientational polarizability

αs = space charge polarizability

In an ideal capacitor the electric charge adjusts itself instantaneously to any change in voltage. In practice however, there is an inertia-to-charge moment that shows up as a relaxation time for charge transport. The polycrystalline ferrites are very good dielectric materials. Ferrite materials possess high dielectric constant (~10^5) in low frequency region, which drastically reduces to quite low value (~10) in the microwave region thus showing dispersion. The very high dielectric constants often observed at low

frequencies have been ascribed to the effect of heterogeneity of the samples i.e. pores and/or surface layers on grains causing poor electrical contact between them. The higher value of dielectric is also explained on the basis of interfacial polarization [43], which causes the electrical charges to accommodate on the interfaces of heterogeneous dielectric material. The origin of interfacial polarization has been attributed to the distribution of the electrical resistivities caused by the non-uniform distribution of oxygen ions produced due to the sintering process [44]. In ferrites geometry an oxygen ion has the two extra electrons which are loosely bound to the nucleus and when a small electrical field is applied to the material, it distorts it to produce polarization.

Koops [45] gave a phenomenological theory of dispersion based on Maxwell- Wagner interfacial polarization model [46,47] for inhomogeneous dielectric structure. In this theory the solid is imagined to consist of well conducting grains separated by poorly conducting layers or grain boundaries, while the current is assumed to flow along parallel alignments of the grains. Such type of heterogeneous structure is understood to be formed at the time of sintering process of the material.

To understand the complex behaviour of ferrites, Koops [45] proposed the heterogeneous structure of the ferrite as equivalent to a series and parallel combination of resistances and capacitances. If R_1, R_2 and C_1, C_2 represents the resistances and capacitances of the grain boundaries and grains respectively, then according to the A.C. field theory and assuming that if same current flows through the grains and their grain boundaries then the circuit shown in Figure 32(a) can be represented as equivalent circuit of

another parallel R-C circuit given in Figure 32(b), a series-parallel combination of these components.

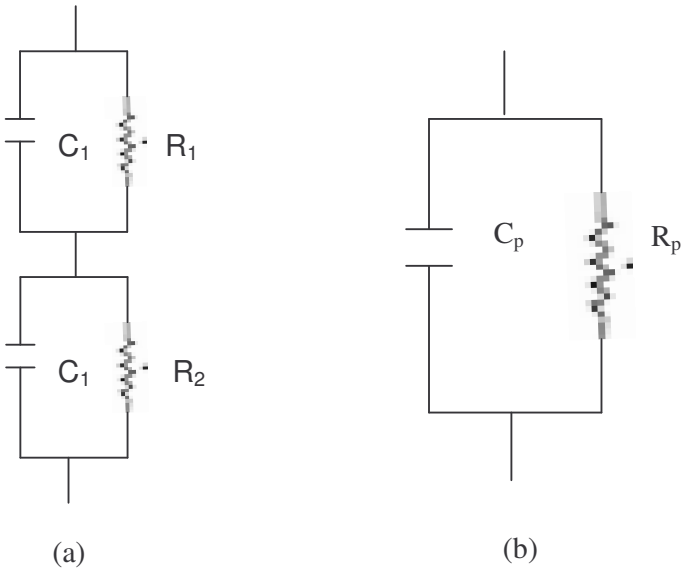

Fig.32 (a) Circuit diagram of ferrite material containing grains and grain boundaries. C_1, C_2 and R_1, R_2 represent capacitance and resistances of grains and grain boundaries respectively

Fig .32 (b) The equivalent circuit

The R_p and C_p represent the equivalent resistances and capacitances of grain boundaries and grains respectively. In these cases R_p and C_p do not remain constant with respect to the frequency but obey the dispersion phenomenon similar to those observed in ferrites. It is further assumed that the dielectric constant of grains and grain boundaries are equal. The model explains a strong dispersion phenomenon in ferrites [48,49]. The dielectric properties of ferrites are dependent upon several factors including the method of preparation, chemical composition and grain structure and size. The heterogeneous structure of ferrite is believed to form of during sintering

process. At high temperatures some of the Fe^{3+}may get reduced to Fe^{2+} ions, which increase the conductivity of the grains. On cooling the ferrites in a slightly oxidizing atmosphere, The Fe^{2+} ions present in the outer layer of the grains get oxidized to Fe^{3+} producing layers of lower conductivity. Presence of air gap also contributes to the formation of the heterogeneous structure in ferrites [45, 50].

Due to the loss factor in the dielectrics, the dielectric constant or permittivity ε', is represented as a complex quantity

$$\varepsilon = \varepsilon' - j\varepsilon''$$

where ε' represents the real or dispersive part and ε'' represents its imaginary part or dissipative part, which accounts for the losses. The absorption of electrical energy by the dielectric material that is subjected to an alternating electric field is termed as dielectric loss. The dielectric loss factor, tan □, is the ratio between imaginary and the real part of the dielectric constant and is given by the reciprocal of the quality factor, Q, of the circuit and can be given as

$$D = \tan\delta = \frac{\varepsilon''}{\varepsilon'} = \frac{1}{Q} = \frac{1}{\omega R_p C_p} = \frac{4\pi\sigma}{\omega\varepsilon'}$$

$$C_p = \frac{\varepsilon_0 \varepsilon A}{d}$$

and

$$R_p = \frac{d}{\sigma A}$$

where ε_0 is the free space permittivity (~$8.85*10^{-12}$ F/m), A is the area of the capacitor plates, d is the distance between plates completely filled with dielectric under investigation and σ is the conductivity (σ=1/ρ).

Sometimes some electronic polarization effect is supposed to be connected with the conduction hopping mechanism itself, which also could contribute to the low frequency dispersion of dielectric constant. At higher frequencies the measured values may be regarded as insensitive to both of these contributions and they are usually taken as actual intrinsic dielectric constants corresponding to normal ionic and electronic polarizations. In the frequency region of the lattice vibrations the ionic polarization becomes slow and damps out (infrared absorption) while the electronic polarization is fast enough to persist to the region of electronic excitations in near infrared and visible part of the spectrum (crystal field and charge transfer transitions). As far as the temperature dependence is concerned, dielectric constant usually increases with increasing temperature together with the electrical resistivity. The dielectric properties of ferrites are dependent upon several factors like the method of preparation, chemical composition and grain structure or size. When the ferrite powder is sintered under slightly reducing conditions, the valence state change, the individual cation formed in the sample leads to high conductivity and when such material is cooled in an oxygen atmosphere, it is possible to form films of high resistivity over the constituent grains. The ferrites behave as inhomogeneous dielectric material if the individual grains are separated by either air gap or low conducting layer. Therefore, the ferrites possess dielectric constant as high as 10^5 and are useful in designing microwave devices such as isolators, circulators, etc. Even at low frequency (10^2 Hz – 10^5Hz) this has aroused considerable interest**.** The prominent studies were carried out by Koops [45], Rezlescu [38], Brockman [51] and Josyulu [52]. In recent times, the polarization studies were further extended to

understand and interpret the earlier theories in a microscopic manner relevant to different materials. These theories were also extended to interpret the low frequency dielectric of ceramic materials including ferrites. Koops [45] gave a phenomenological theory of dispersion based on the Maxwell – Wagner interfacial polarization model for inhomogeneous dielectric structure. It was assumed that the solid consists of well conducting grains separated by poorly conducting layers. This model explains a strong dispersion in dielectric constant ε'' at low frequencies. Thus, it is known that the dielectric constant of polycrystalline ferrite is related to the average grain size of the specimens of the same compositions.

Experimental details

The Dielectric constant for the all samples was calculated by measuring the capacitance of the material. For better contacts the two sides of the pellet were painted with silver paste so that the two sides of the pellet act as the electrodes. The following relation was used for the calculation.

$$\varepsilon' = \frac{C}{C_0}$$

where ε' is the real part of the dielectric constant, C is the capacitance of the material inserted between the electrodes and C_0 is the capacitance of the medium as air or no medium between the electrodes. The C_0 for the parallel plate capacitor can be calculated using the following expression

$$C_0 = \frac{\varepsilon_0 A}{t}$$

The dielectric loss factor, tanδ was directly measured from LCR meter, δ being the loss angle. Since the loss factor is the ratio of the imaginary and the real

parts of the dielectric constant, the imaginary part ε'' can be calculated from the relation

$$\varepsilon'' = \varepsilon' \tan \delta.$$

using the values of ε' & ε'', ac resistivity (ρ_{ac}),real part of electric modulus(M') and imaginary part of electric modulus(M'') were calculated using following equations:

$$\rho_{ac} = \frac{2\pi f C D t}{A}$$

Where f= frequency, C=capacitance, D= dissipation factor, t=thickness of the sample and A=area of the sample.

$$M' = \frac{\varepsilon'}{\left(\varepsilon'^2 + \varepsilon''^2\right)}$$

and

$$M'' = \frac{\varepsilon''}{\left(\varepsilon'^2 + \varepsilon''^2\right)}$$

Frequency dependent Dielectric behaviour (at selected temperatures) of $Y_{3-x}Fe_{5+x}O_{12}$ (x=0.0, 0.1, 0.3 and 0.5) and $Y_3Fe_5O_{12}$ (Milling hours: 3hrs,6hrs, 9hrs and 12hrs) series were studied using the precision LCR meter (Model: 4284 A) in the frequency range 100Hz-1MHz at Department of Physics, Saurashtra University, Rajkot and all compositions of $Y_{3+x}Fe_{5-x}O_{12}$ (x=0.0, 0.2, 0.4, 0.6) series were characterized at different temperatures, before and after SHI-irradiation, using the impedance analyzer in the frequency range 100Hz-13MHz at UGC-DAE CSR (IUC), Indore.

Fig.33 A photograph of Impedance analyzer (4284 A) and sample holder used in present investigation

References

1. Elton N. Kaufmann, “Characterization of Materials”, John wiley & sons, Inc., Hoboken, New Jersey, Vol. 1(2003).
2. B. D. Culity, “X-Ray Diffraction”, Wesly Pub. Co. Inc. (1978).
3. C.Dong , J. Appl. Cryst. 32,838 (1999).
4. H. M. Rietveld, J. Appl. Cryst. 2, 65 (1969).
5. H. M. Rietveld ,Acta. Cryst. 22, 151(1967).
6. J. Rodriquez-Carvajal, Physica B, 192, 55 (1993).
7. L. B. McCusker, R. B. Von Dreele, D. E. Cox, D. Louer and P. Scardi, J. Appl. Cryst. 32, 36 (1999).
8. R. A. Young, “The Rietveld Method”, Oxford University Press Inc (1993).
9. Ian. M. Watt, “The principles & practice of Electron microscopy”, 2nd Ed., Cambridge University Press (1997) 89.
10. Elton. N. Kaffmann, “Characterization of materials “, John Wiley &sons, Inc., Hoboken, New Jersey, Vol.2 (2003).
11. Michael de Podesta, Understanding the properties of matter, 2nd Edition. Taylor & Francies, NY. 2002.
12. A.M. Hofmeister and K.R. Campbell, J. Appl. Phys. 72(2)(1992)638 and reference therein.
13. C.R.K. Murty, S.D. Likhite and P.Sahastrabude, Proc. Indian. Acad. Sci. 87A(1978)245.
14. N.N.Greenwood,and T.C.Gibbs,” Mossabauer Spectroscopy “,Chapman & Hall,London,(1971).
15. A.J.Watson and A.J.Freeman, Phys. Rev.123 , 2027,(1961).

16. A. J Stone, Appendix to: G. M Bancroft, A. G Maddock., W. K Ong,R. H., Prince and A.J Stone. J. Chem. Soc. (A), 1966 (1967).
17. J. R. Gabriel and S. L. Ruby Nucl. Instr. Methods, 36, 23 (1965).
18. B. L. Crisman and T.A. Tumolillo., “Computer Analysis of Mössbauer spectra”, Dept. of Physics Univ. of Illinos, Urbana, 111.
19. R. A. Brand, User manual for NORMOS software (1992).
20. F. Bloch,Z. Physik 74 (1932) 295.
21. S. Chiazumi, “Physics of magnetism”, John Wiley & sons Inc. New York (1964).
22. E.A. Sachwabe and D.A. Campbell, J.Appl. Phys. 34 (1963)1251.
23. A.Globus, C.R.Acad. Sci. 255 (1962)1709.
24. E.C. Snelling and A.D. Giles, ”Ferrites for inductors and transformers”, John Wiley & Sons Inc. New York (1983).
25. H. Igarashi and K. Okazaki, J. Am. Ceramic Soc. 60(1977) 51.
26. J. L. Snoek, Physica 14(1948)207.
27. J. L. Snoek, Nature 160 (1947) 90.
28. L.Landau and E.Lifshitz, Physik Z, Sowjetunion 8 (1935)153.
29. G. T. Rado, R. W. Wright and W. H. Emerson, Phys. Rev. 80 (1950) 273.
30. G. T. Rado, R. W. Wright, W. H. Emerson and A. Terris, Phys. Rev. 88 (1952)909.
31. G. T. Rado, Rev. Mod. Phys. 25 (1953)81.
32. A. Globus and M. Guyot,IEEE Trans. Magn, MAG-7,(1971)617.
33. A.Globus and P. Duplex,Phys. Stat. Solidi 31 (1961) 765.
34. J.P.Bouchand and P.G.Zrah, J. Appl. Phys. 67 (1990)5512.

35. Carl Heck, “Magnetic Materials and their Application”,Butter Worths, London,(1974).
36. Krupicka and P. Novak, In “Ferromagnetic materials” Vol. 3, Ed. E.P. Wohlfarth, Page 189, North Holland Publishiing Co., 1982.
37. P.W. Anderson, Phys. Rev., 109, 1492, (1958).
38. N. Rezlescu and E. Rezlescu ,Phys. Stat. Sol. (a) 23,575 (1974).
39. S.L.Kakani and C. Hemrajani, “A text book of solid state physics”,Sultan chand(1997).
40. K. J. Standly, “Oxide Magnetic Materials”, Oxford, (1962).
41. N. Miyata, J. Phys. Soc. Japan, 16, 206, (1961).
42. F. J. Morin, Phys. Rev., 93(1953)1195.
43. B. Tareev, “Physics of dielectric materials” Mir Publishers, Moscow, (1959)105.
44. K. Iwauchi, Jap. J.Appl. Phys. 10 (1971) 1520.
45. C. G. Koops, Phys. Rev. 83 (1951)121.
46. J. C. Maxwell, “Electricity and magnetism” Oxford University Press, London, 1(1954)328.
47. K. W. Wagner, Ann. De. Physik, 40(1913)817.
48. L.G. Van Uitert, J. Chem. Solid, 9 (1956)306.
49. G.H. Jonker, J. Phys. Chem. Solid, 9(1959)165.
50. G. Moltgen, Z. Physik 4(1952)216.
51. F.G. Brockman and K. E. Matterson, J. Amer. Ceramic Soc., 53, 517, (1970).
52. O. S. Josyulu, and J. Sobhanadri, Phys. Stat. Sol. (a) 59 , 323, (1980).

Chapter 4

Interaction of Ion with Matter

Swift Heavy Ion Irradiation (SHII)

4.1 Interactions of SHI with materials

When swift heavy ion (SHI) with energy E passes through a material medium it losses its energy in the medium. If the thickness of the target is less than the range of the projectile ion, then the projectile deposits an energy dE in the medium and comes out with an energy E-dE [1]. There are mainly two modes of energy deposition of an ion beam in the material medium.

4.1.1 Nuclear energy loss (S_n): Elastic collision with target atoms leading to displacements of atoms from their regular lattice sites. This mode of energy transfer is known as nuclear energy loss denoted by $(dE/dX)_n$ or S_n. It is well known mechanism of defect creation in the low energy range (i.e., KeV range) of the ion beam but at very high –energy regime it has negligible contribution. It introduces disorders near the projectile range in the form of clusters, vacancies, interstitial and cascade of atoms. This is also referred as nuclear stopping.

4.1.2 Electronic energy loss (S_e): Electronic energy loss is due to inelastic collisions (interactions) between the atomic electrons of material with the energetic ion beam. It is generally denoted by S_e (electronic stopping). It is responsible for reversible and irreversible excitation or ionization in the electronic subsystem of the material. This electronic stopping is dominant at high energies i.e., MeV energy range, where the displacement of atoms due to elastic collisions is insignificant.

The energetic ion creates damages along its path due to its large electronic energy deposition. The track diameter is a quantity of interest for

understanding of basic ion insulator interaction. Electronic excitation produced by swift heavy ions has vast potential in the field of modification of materials.

Swift heavy ions in MeV range under different conditions can produce additional defects; create phase transformations, gives rise to anisotropic growth in some materials. The energetic ion beam also suffers repeated coulomb scattering with less probability and these collisions are governed by the well-known Rutherford formula of scattering. The nuclear energy loss (S_n) is smaller in comparison to the electronic energy loss (S_e). The total energy loss is given by

$$\left(\frac{dE}{dx}\right)=\left(\frac{dE}{dx}\right)_e+\left(\frac{dE}{dx}\right)_n$$

There is certain threshold value of S_e for each material, above which it gets affected. It is well known that to create amorphization in a material, certain threshold value of electronic energy loss (S_{eth}) is required. If S_e is less than S_{eth}, only point/ clusters of defects will be generated in the materials [2]. It is well known that irradiation of solids with high-energy heavy ions lead to creation of wide variety of defects [3]. When an ion passes through a material, it is only towards the fag end of the range when its energy is low and elastic collision probability increases that the nuclear loss effects becomes predominant. This produces cascade of collisions and ion stops in the material, this process is termed as ion implantation. It is known that many insulators, semiconductors and even – metallic glasses [4] get modified by heavy ion implantation.

After the passage of SHI, the solid returns to its equilibrium state leaving behind bulk and surface modifications. The nature of modifications

depends on the electrical, thermal and structural properties of the target material, mass of the projectile ion etc. Since the beginning of 1950's, several theoretical models, e.g. Coulomb spike model [5, 6] Thermal spike [7, 8] or exciton model have been proposed to explain the formation of tracks due to slowing down of energetic ions in the electronic stopping power regime.

4.2 Theoretical models

4.2.1 Thermal Spike Model

This is a transient model, developed to explain the phase transformation after the SHI irradiation. The heavy ion irradiation may increase the lattice temperature that induces solid to liquid phase transformation in a localized zone of few nanometer (nm), which is followed by a rapid thermal quenching (10^{13}K/s) of a cylinder of molten liquid along the ion track. This results in the formation of amorphized latent tracks. The Threshold value for the creation of the latent tracks is associated with the energy needed to induce a liquid phase along the ion path [9, 10].

The incoming ion gives its energy to the electron gas in ~10^{-17}s which is calculated from the collision time of ion with electron. The local thermalization in electronic system will take 10^{-15} s to complete. Heat transfer from the electronic to atomic subsystem becomes substantial between 10^{-14} and 10^{-12} s depending on the magnitude of the coupling (electron –electron coupling, electron- phonon and phonon-phonon coupling) between the subsystems. The electron phonon coupling implies the ability of electrons to transfer their energy to the lattice that originates from phenomenon of local

polarization. The local polarization appears due to the displacement of atoms from their equilibrium positions.

4.2.2 Ionic Spike Model

In this model [11, 6] it is assumed that the incoming ions scatter the target electrons and create a column/cylinder of ionized atoms and the excited electrons are ejected by the Coulomb repulsion. The electron excitation energy rapidly shared with other electrons via electron-electron interaction. The mutual Coulomb repulsion of the ions produces atomic displacements leading to a dense cloud of interstitial atoms and vacancies along the original ion trajectory. The model seems to be well suited for insulating materials. In metals which has large electronic mean free path, the free electrons carry away the excitation energy so efficiently that the sample warms up as a whole without considerable atomic motion.

4.3 Irradiation of Ferrites

The fundamental understanding of solid state phenomena in magnetic ferrite materials motivate physicist to investigate the nature of irradiation induced defects and other resulting structural, magnetic, electrical aspects. The investigations are of interest in several fields e.g., in the nuclear industry to know the behaviour of ferrites near a reactor, to know the behaviour of ferrites in space radiation or some improved properties leading to the applications in science and technologies.

The term swift heavy ion (SHI) here refers to the energetic ions having energy in the range of a few tens of million electron volts (MeV) to giga

electron volts (GeV). In the past decade some research activities began to study the influence of SHI irradiation on various ferrite materials. Many experimental results have been reported on the properties of spinel and garnet ferrimagnetic oxides after irradiation by various kinds of particles like electrons, γ-photons, fast neutrons, protons, low energy ion and high energy ions. The effect of fast neutron irradiation for different ferrites on saturation magnetization [12, 13], Curie temperature [14] magneto crystalline anisotropy has been studied in detail. The resulting effects in the irradiated materials are well interpreted by redistribution of the cations over two crystallographic sites. The fast neutron irradiation of magnetite proves the material to be resistant to the irradiation [15]. The improved properties of the bubble ferrimagnetic garnets by low energy ion implantation have been established in 1971[16]. In 1984, Pascard [17] proposed a linear law for irradiated materials corresponding to a model based on the transformation of Fe^{3+} into Fe^{2+}. The garnet and spinel structure have been extensively studied in the field of irradiation effects induced by SHI. With the use of Heavy ions like Ar, Xe, Kr, Pb and U for irradiation [18, 19], study on the defect morphologies, variation of effective track radii, recrystallization etc have been deduced using high resolution electron microscopy (HRTEM), Mossbauer spectroscopy and magnetic measurements. In most of the materials, heavy ion irradiation induces specific anisotropy [20], a specific volume increase of the matter and orientation of the magnetization. The creation of ferrimagnetic behaviour in $ZnFe_2O_4$ [21] by SHI irradiation was also observed by a certain groups. Spinels like $NiFe_2O_4$, $MgFe_2O_4$ exhibit increase in magnetization after SHI

irradiation. These interesting results are correlated to the cation displacements induced by amorphization –recrystallization processes.

4.4 Track Morphology

The study of highly energetic ion effects in magnetic oxides has been carried out for several years. From the various studies on the latent track morphology evolution versus the electronic stopping power, dE/dx for different materials like $Y_3Fe_5O_{12}$, $BaFe_{12}O_{19}$ and $NiFe_2O_4$, the following description on defect evolution and defect morphology is proposed [22] :

(i) For 4.5 MeV/μm < dE/dx < 7 MeV/μm, the spherical defects appear with a radius of the order of 1.5nm.

(ii) For 7 MeV/μm < dE/dx < 14 MeV/μm, the spherical defects percolate and discontinuous cylindrical defects appear with radii of the order of 1.5 nm.

(iii) For 14 MeV/μm < dE/dx < 20 MeV/μm, the cylindrical defects percolate and the latent track radius starts to increase.

(iv) For dE/dx > 20 MeV/μm the latent track is long and cylindrical but after this the damage yield does not increase as rapidly as in the previous range and finally there is saturation in the damage efficiency.

4.5 Pelletron

The main building at Nuclear Science Center houses the Pelletron tower, beam hall and the laboratory. The 50 meter tall tower is made of heavy concrete for irradiation shielding. The 15 UD Pelletron [23], a versatile heavy

ion tandem electrostatic accelerators installed in a vertical configuration in an insulating tank of 26.5 meter height and 5.5 meter diameter. The accelerator tank is filled with an insulating gas sulphur hexafluoride (SF6) maintained at a pressure of 6-7 atmosphere.

A schematic showing the principal of acceleration of ions in Pelletron is shown in Figure 4.1.

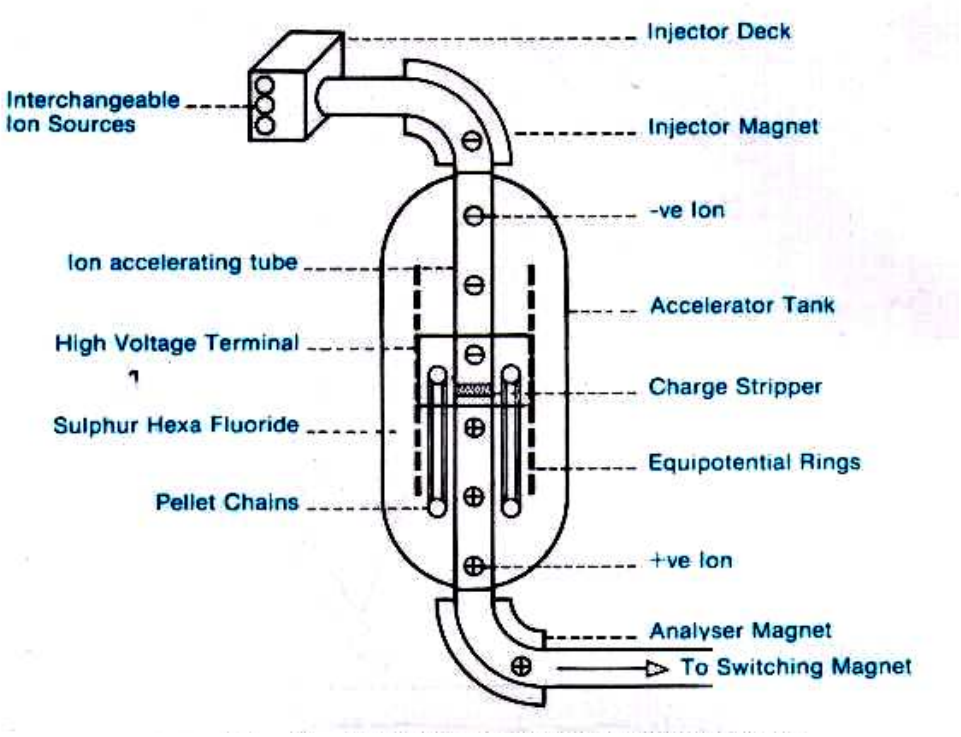

Fig. 4.1 A schematic figure showing the principle of acceleration of ions in Pelletron

In this machine the negative ions are produced and pre-accelerated to ~300 keV by the Cesium sputter ion source known as SNICS(source of Negative Ions by Cesium sputtering) (Now it has been replaced by MCSNICS (Multi-Cathode SNICS)). The ions are mass analyzed by a dipole magnet called injector magnet and are turned vertically downward direction. The ions

then enter the strong electric field inside the accelerator. A terminal shell, about 1.52 meters in diameter and 3.61 meter in height, located at the center of the tank which can be charged to a high voltage (~15MV) by a pellet charging system. The negative ions on transversing through the accelerating tubes from the column top of the tank to the positive terminal get accelerated. On reaching the terminal they pass through the stripper which removes some electrons from the negative ions thus transforming the negative ions into the positive ions. For very heavy ions (A>50), the lifetimes of the carbon foils used in stripper are limited to a few hours due to radiation damage. Therefore a gas filled canal or a combination of the gas stripper followed by a foil is used for heavy ions. The transformed positive ions are then repelled away from the positively charged terminal and are accelerated to the bottom of the tank. In this way same terminal potential is used twice to accelerate the ions. Therefore this accelerator is called a tandem Pelletron accelerator. The final energy of the emerging ions from the accelerator is given by

$$E_i = [E_{decpot} + (1+q_i)V]$$

where E_i is the energy of the ion having a charge state q_i after stripping. V is the terminal potential in MV and E_{decpot} is the deck potential of the SNICS source. On exiting from the tank, the ions are bent into horizontal plane by analyzing magnet diverts the high energy ion beam into desired beam line of the beam hall. The ion beam is kept centered and focused using steering magnets and quadrupole triplet magnets. The beam line of the accelerator is in ultra high vacuum condition (~10^{-10}mbar). The beam is monitored by beam profile meter (BPM) and the current is observed by means of Faraday cups. The entire machine is computer controlled and is operated from the control

room. The accelerator can accelerate an ion from proton to Uranium from few MeV to hundreds of MeV (200 MeV) depending on the ion.

4.5.1 Materials Science beam line

The accelerated beam from the Pelletron is brought to the beam hall and switched to anyone of the seven beam lines using the switching magnet.

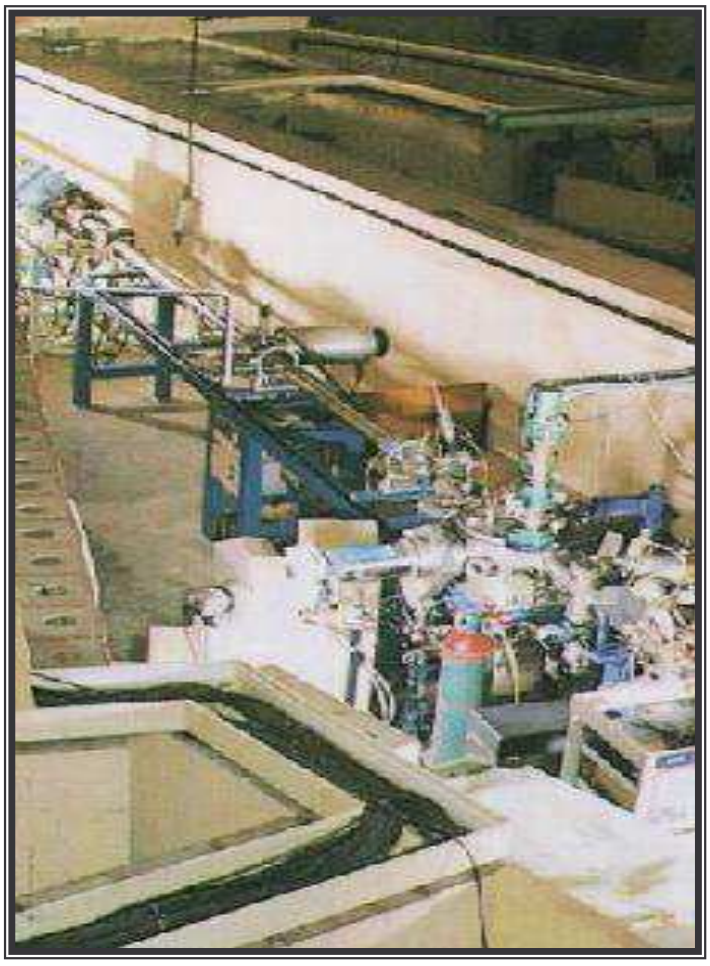

Fig. 4.2 Material science Beam line

The materials science beam line is at 15˚to the right with respect to the zero degree beam line. These beam line houses three chambers – high vacuum chamber, ultra high vacuum chamber and goniometer chamber. The

high vacuum chamber is a cylindrical shaped multiport stainless steel chamber. A view of the high vacuum chamber is shown in the Figure 4.2. Most of the irradiation experiments are performed in high vacuum chamber. A typical vacuum of $1*10^{-6}$mbar is generally maintained during irradiation. The samples to be irradiated are mounted on the four sides of the target ladder (on copper block). The whole of the ladder is made up of stainless steel and a perforated square copper block is brazed at the end of the ladder. The target ladder is mounted through a Wilson seal from the top flange of the chamber. This top flange is connected to the chamber through a flexible bellow that can expand up to 11 cm from its minimum position. A stepper motor in conjunction with a suitable mechanical assembly is used to control the up and down motion of the ladder. The beam on the ladder can be observed by observing the luminescence of the beam on the quartz crystal mounted on all sides of the ladder.

After the observation of the beam on the quartz, the sample to be irradiated is brought to the same position as that of the quartz by moving the ladder in the desirable position. A CCD camera is attached to one of the ports of the chamber for viewing the sample and the quartz position. The positions can be monitored using close circuit television (CCTV) in the data acquisition room. The magnetic scanner that can sweep the beam (25 mm in Y-direction and 10 mm in x-direction) ensures the uniform irradiation of the samples. A cylindrical enclosure of stainless steel surrounds the sample ladder, which is kept at a negative potential of 120V. This enclosure suppresses the secondary electrons coming out of the sample during irradiation. An opening in the suppressor allows the ion beam to fall on the sample. The total number

of the particle/charges falling on the sample can be estimated by a combination of the current integrator and the pulse counter (Faraday cup) from which the irradiation fluence can be measured.

4.6 Experimental details

The irradiation experiments were performed in high vacuum chamber, with a typical vacuum maintained at 1x 10^{-6} mbar. The reason for requiring vacuum is to avoid any collision of the particle (beam) with gas molecules. The samples to be irradiated were mounted on the four sides of the target ladder (on copper block), which were separated from each other by a distance of about 1 cm. the counts calculated for the desired ion fluence for each sample was calculated using the following relation

$$n(dose) = \frac{I(nA).t}{1.6\text{x}10^{-19}.q}$$

$$\text{Number of counts} = \frac{\text{dose.q. } 1.6\text{ x}10^{-19}}{\text{pulse height}}$$

For the present work, the bulk samples were irradiated with 50 MeV Li^{3+} (Lithium) ions with fluence of 5 x 10^{13} ions/cm^2 using 15 UD pelletron accelerators at IUAC, New Delhi. The targets for irradiation experiments in the form of thin layer of garnet material having thickness of about 20 mg/cm^2 were prepared by spreading fine ferrite powders in a aluminium ring of 1 cm diameter on a thin aluminium foil, and uniform thickness was achieved by fixing the powder using liquid GE varnish. The electronic energy loss (S_e) of 50MeV Li^{3+} ions in this compound calculated using the SRIM -98 code is around 12eV/Å which is less than the electronic energy loss threshold (S_{eth}) required to surmount for producing columnar amorphization that is of the

order of 10^3 eV/ Å. Therefore, it is expected that SHI –irradiation has generated points /cluster of defects.

References

1. G. Szenes, Phys. Rev. B 51, 13(1995) 8026, M. Toulmonde, Nucl. Instr. and Meth. B 156 (1999)1.
2. F. Studer and M. Toulemonde, Nucl. Instr. and Meth. B65 (1992)560.
3. M.W. Thompson, Defects and Radiation Damage in Metals, Cambridge University Press, Cambridge (1969).
4. S. Klaumunzer, M.D. Hou and G. Shumacher, Phys. Rev. Lett. 57(1986) 850.
5. R.E. Johnson and W.L. Brown, Nucl. Instr. and Meth. B198 (1982)103.
6. D. Lesueur and A. Dunlop, Radiat. Eff. Defects Solids 126 (1993)163.
7. G. Szenes, Phys. Rev. B51 (1995)8026.
8. M. Toulemonde, Ch. Dufour, Z. Wang and E. Paumier, Nucl. Instr. and Meth. B112 (1996)26.
9. M. Toulemonde, C. Dufour and E. Paumier, Phys. Rev. B 46,22(1992) 14362.
10. Z. G. Wang, Ch. Dufour, E. Paumier and M. Toulemonde, J. Phys. Condens. Matter 6 (1994)6733.
11. R. L. Fleischer, P. B. Price and R. M. Walker, Phys. Rev. 156, 2 (1967)353.
12. Yu. G. Chukalkin, B.N. Goshchitskii, S. F. Dubinin, S.K. Sidorov, V.V. Petrov, V.D. Parkhomenko and V.G. Vologin, Phys. Stat. Sol. (a0 28 (1975)345.
13. Yu. G. Chukalkin, V. V. Petrov and B. N. Goshchitskii, Phys. Stat. Sol. (a) 67 (1981)421.

14. P.J. Van der Zaag, A. Noordermer, M. J. Johnson and P.F. Bongers, Phys. Rev. Lett. 68 (1992)3112.
15. S. Mellion, F. Studer, M. Hervieu and H. Pascard, Nucl. Inst. And Meith. B. 107 (1996)363.
16. R. wolfe, J.C. North, R.L. Bams, M. Robinson and H. J. Levinstein, Appl. Phys. Lett. 19 (1971)298.
17. H. Pascard, Phys. Rev. B. 30,(1984)2299.
18. F. Studer, Ch. Houpert, D. Groult and M. Toulemonde, Radiat. Eff. Def. Sol. 110 (1989)55.
19. A. Meftah, F. Brisard, J. M. Constantini, M. Hage- Ali, J. P. Stoquert, F. Studer and M. Toulemonde, Phys. Rev. B 48 (1993)920.
20. M. Toulemonde, G. Fuchs, N. Nguyen, F. Studer and D. Groult, Phys. Rev. B 35 (1987)6560.
21. F. Studer Ch Houpert, D. Groult, J. Yun. Fan, A. Meftah and M. Toulemonde, Nucl. Instr. Meth. B 82 (1993)91.
22. M. Toulemonde, Nucl. Instr. Meth. B 156 (1999)1.
23. D. Kanjilal, S. Chopra, M.M. Narayannan, I.S. Iyer, V. Jha, R. Joshi and S. K. Datta, Nucl. Instr. Meth. A 238 (1993) 97.

Chapter 5

Studies of Structural, Magnetic, Electrical, Dielectric and Elastic Properties of Bulk Fe^{3+}-substituted Yttrium Iron Garnet: $Y_{3-x}Fe_{5+x}O_{12}$; Y(Fe)-Fe-O system

5(a) Structural, magnetic and elastic properties of $Y_{3-x}Fe_{5+x}O_{12}$ (x= 0.0, 0.1, 0.3 and 0.5) system

5a.1 EDAX and X-ray diffraction studies on $Y_{3-x}Fe_{5+x}O_{12}$ (Y (Fe)-Fe-O) system

The high temperature, prolong sintering may result in loss of ingredient which leads to non-stoichiometry in composition which in turn shows unexpected behaviour, that can not be explained on the basis of normal stoichiometry. Thus, it was essential to check the chemical stoichiometry of each composition. A representative energy dispersive analysis of x-rays (EDAX) pattern for typical composition x=0.3 is shown in Figure 5a.1.1. The results of EDAX (Table 5a.1.1) confirm the expected stoichiometry. No trace of any impurity was found indicating the purity of the samples. It is also clear that there is no loss of any ingredient after high temperature sintering. The EDAX results suggest that the precursors have fully undergone the chemical reaction to form the expected garnet material. The reason for making EDAX characterization was to ratify the purity and surety of the chemical composition.

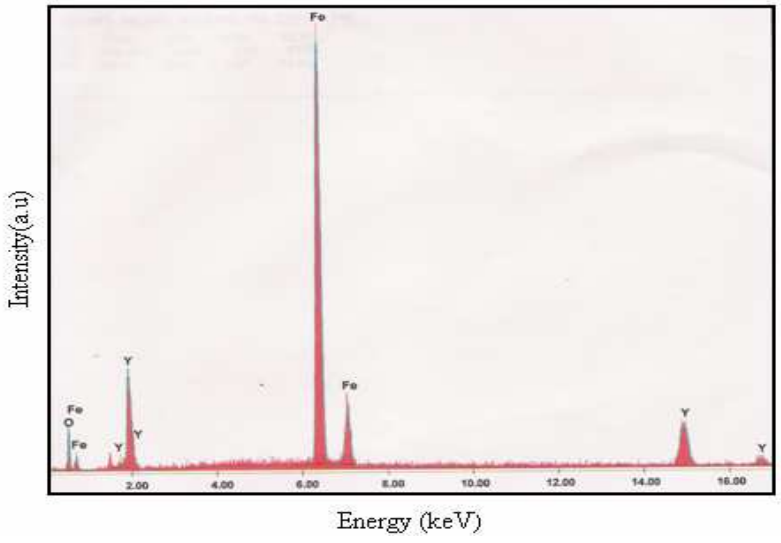

Fig. 5a.1.1 EDAX pattern of $Y_{2.7}Fe_{5.3}O_{12}$(x=0.3) composition

Table 5a.1.1 EDAX results for $Y_{2.7}Fe_{5.3}O_{12}$ composition

Element	EDAX wt (%)	Expected wt (%)
O	27.11±3%	26.37
Fe	39.91±2%	40.66
Y	32.98±2%	32.97

The room temperature (300K) X-ray diffraction patterns of the samples were obtained by powder X-ray diffractometer. The Rietveld method refines a crystal structure by comparing the measured diffraction pattern with that calculated from known crystal structure. A least square refinement is used to optimize the structural parameters. Indexing and Rietveld refinement using General scattering analysis software (GSAS) of XRD patterns of all the $Y_{3-x}Fe_{5+x}O_{12}$ (x=0.0-0.5) samples revealed that these are single phase compounds crystallizing in a bcc structure (space group-Ia3d). No peaks from impurity phases could be detected within the limits of X-ray detection, which is typically 5%. Figure 5a.1.2 displays a typical Rietveld fitted XRD patterns for all the studied compositions (x=0.0, 0.1, 0.3 and 0.5). The lattice constant and interionic distances, obtained from the above mentioned refinement, are given in Table 5a.1.2, from which it is seen that lattice constant and interionic distances decrease with increasing Fe^{3+}-content (x) in the system. Usually in a solid solution of garnets within the miscibility range, a linear change in the lattice constant with the concentration of the components is observed [1]. The linear decrease in lattice constant is due to the replacement of larger Y^{3+} ions (0.893 Å) by the smaller Fe^{3+} ions (0.64 Å) in the system. The observed reduction of interionic distances (Table 5a.1.2) can also be explained along similar lines of argument.

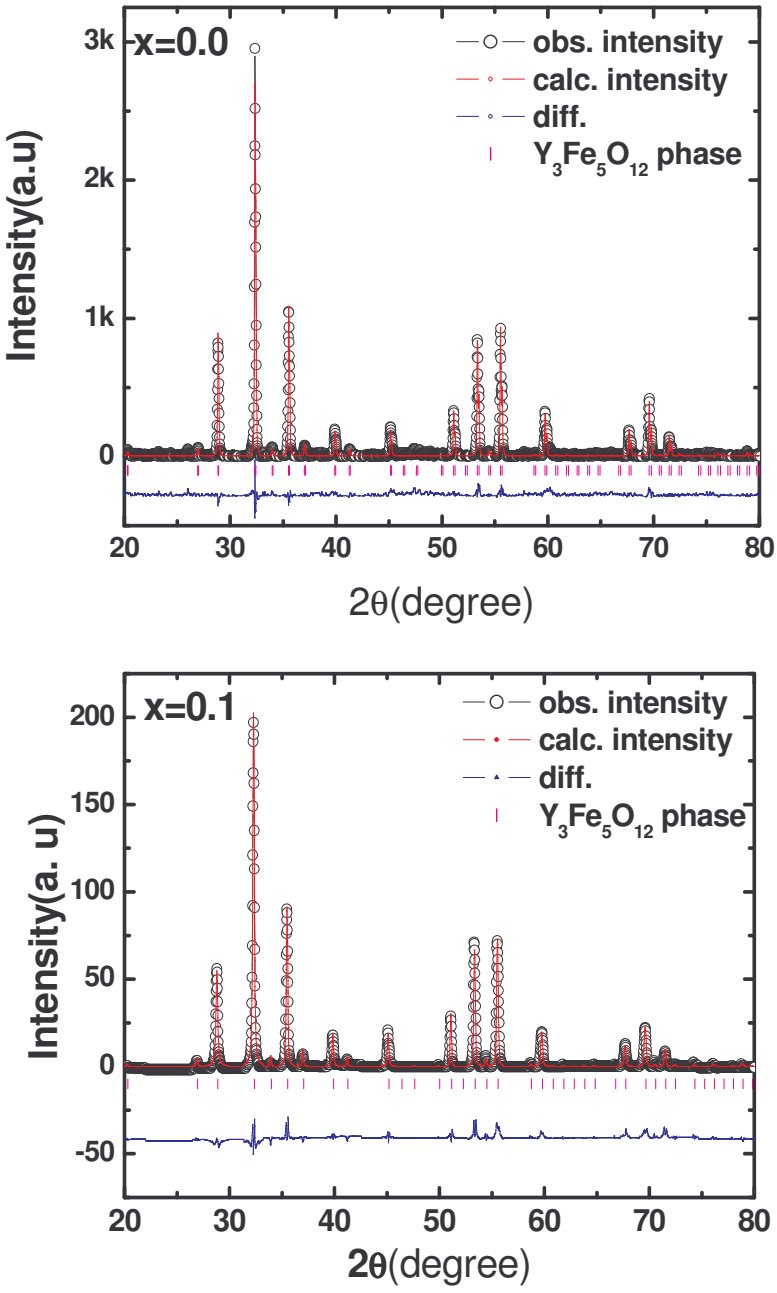

Fig. 5a.1.2 Rietveld fitted XRD patterns for Y (Fe)-Fe-O system

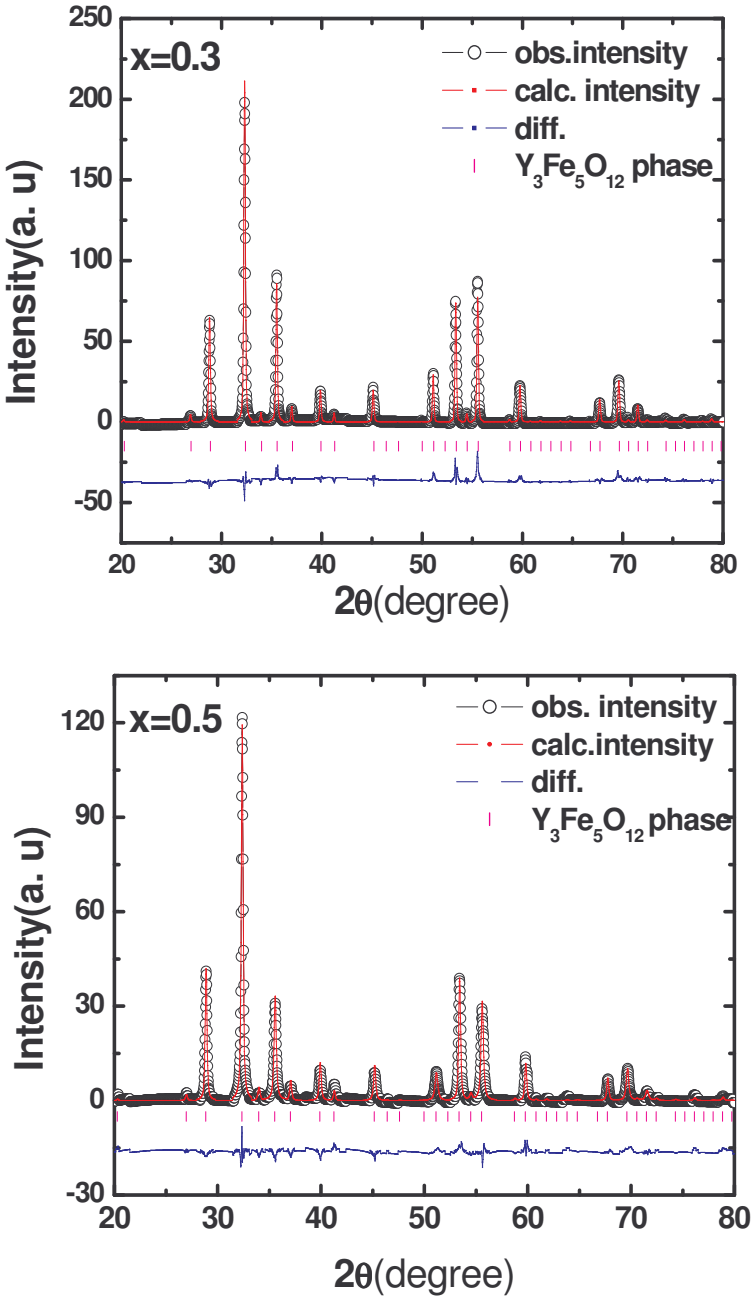

Fig.5a.1.2 Rietveld fitted XRD patterns for Y (Fe)-Fe-O system

Table 5a.1.2 Lattice constant and nearest-neighbour interionic distances in $Y_{3-x}Fe_{5+x}O_{12}$ compositions

	$Y_3Fe_5O_{12}$	$Y_{2.9}Fe_{5.1}O_{12}$	$Y_{2.7}Fe_{5.3}O_{12}$	$Y_{2.5}Fe_{5.5}O_{12}$
Lattice constant	12.379±0.002 Å	12.372±0.002 Å	12.363±0.002 Å	12.359±0.002 Å
Ion	Interionic distances(Å)	Interionic distances(Å)	Interionic distances(Å)	Interionic distances(Å)
Y^{3+}	$4Y^{3+}$ at 3.791 $4Fe^{3+}$(a) at 3.460 $2Fe^{3+}$(d) at 3.095(2),3.791(2) $8O^{2-}$ at 2.369(4), 2.430(4)	$4Y^{3+}$ at 3.789 $4Fe^{3+}$(a) at 3.459 $2Fe^{3+}$(d) at 3.094(2),3.789(2) $8O^{2-}$ at 2.368(4), 2.429(4)	$4Y^{3+}$ at 3.787 $4Fe^{3+}$(a) at 3.457 $2Fe^{3+}$(d) at 3.092(2),3.787(2) $8O^{2-}$ at 2.367(4), 2.427(4)	$4Y^{3+}$ at 3.786 $4Fe^{3+}$(a) at 3.456 $2Fe^{3+}$(d) at 3.091(2),3.786(2) $8O^{2-}$ at 2.366(4), 2.428(4)
Fe^{3+}(a)	$6Y^{3+}$ at 3.460 $6Fe^{3+}$(d) at 3.460 $6O^{2-}$ at 2.010	$6Y^{3+}$ at 3.459 $6Fe^{3+}$(d) at 3.459 $6O^{2-}$ at 2.010	$6Y^{3+}$ at 3.457 $6Fe^{3+}$(d) at 3.457 $6O^{2-}$ at 2.008	$6Y^{3+}$ at 3.456 $6Fe^{3+}$(d) at 3.456 $6O^{2-}$ at 2.006
Fe^{3+}(d)	$2Y^{3+}$ at 3.095(2),3.791(2) $4Fe^{3+}$(a) at 3.460 $4Fe^{3+}$(d) at 3.791 $4O^{2-}$ at 1.872	$2Y^{3+}$ at 3.094(2),3.789(2) $4Fe^{3+}$(a) at 3.459 $4Fe^{3+}$(d) at 3.789 $4O^{2-}$ at 1.872	$2Y^{3+}$ at 3.092(2),3.787(2) $4Fe^{3+}$(a) at 3.457 $4Fe^{3+}$(d) at 3.787 $4O^{2-}$ at 1.870	$2Y^{3+}$ at 3.091(2),3.786(2) $4Fe^{3+}$(a) at 3.456 $4Fe^{3+}$(d) at 3.786 $4O^{2-}$ at 1.871
O^{2-}	$2Y^{3+}$ at 2.369(1),2.430(1) $1Fe^{3+}$(a) at 2.010 $1Fe^{3+}$(d) at 1.872 $9O^{2-}$ at 2.684(2),2.957, 2.863,2.80,2.994(2), 3.151(2)	$2Y^{3+}$ at 2.368(1),2.429(1) $1Fe^{3+}$(a) at 2.010 $1Fe^{3+}$(d) at 1.872 $9O^{2-}$ at 2.683(2),2.956, 2.862,2.799,2.993(2), 3.149(2)	$2Y^{3+}$ at 2.367(1),2.427(1) $1Fe^{3+}$(a) at 2.008 $1Fe^{3+}$(d) at 1.870 $9O^{2-}$ at 2.682(2),2.954, 2.86,2.797,2.991(2), 3.147(2)	$2Y^{3+}$ at 2.366(1),2.428(1) $1Fe^{3+}$(a) at 2.006 $1Fe^{3+}$(d) at 1.871 $9O^{2-}$ at 2.678(2),2.956, 2.861,2.798,2.989(2), 3.149(2)

Finally, attempt has been made to calculate lattice constant value theoretically for different compositions using following relation [2]:

$a_{th}= b_1+b_2r_c+b_3r_d+b_4r_a+b_5r_cr_d+b_cr_cr_a$

with the coefficients, b_1=+7.068,b_2=+3.25001,b_3=+2.49398,b_4=+3.34124,

b_5 = -0.90158, b_6 = -1.42777.

Here, b_1-b_6 are exchange interactions in agreement with earlier report [3]. As the magnetic moments of c- and a-sites as well as c- and d-sites are antiparallel to each other [4], exchange constants, b_5 and b_6 are found to be negative.

For each composition the values of mean ionic radius per molecule of the d, a, and c- sites have been calculated by using the relations:

$$r_d = \frac{1}{3}\left[f_c(Fe^{3+}).r(Fe^{3+})\right]$$

$$r_a = \frac{1}{2}\left[f_c(Fe^{3+}).r(Fe^{3+}) + f_c(Y^{3+}).r(Y^{3+})\right]$$

$$r_c = \frac{1}{3}\left[f_c(Fe^{3+}).r(Fe^{3+}) + f_c(Y^{3+}).r(Y^{3+})\right]$$

where f_c and r represent concentration and ionic radii of the cations on the respective site. The distribution of cations among the available a, c and d-sites of garnet structure have been determined from Mossbauer spectral analysis. Using these formulae, the mean values of the tetrahedral, octahedral and dodecahedral ionic radii have been calculated and are listed in Table 5a.1.3. It is found that there is reasonable agreement between experimentally found and theoretically calculated lattice constant values.

Table 5a.1.3 X-ray density (ρ_x), bulk density (ρ), pore fraction (f), porosity(P), Theoretical lattice constant values for Y(Fe)-Fe-O system

Fe^{3+}-content (x)	ρ_x	ρ	f	P(%)	r_a	r_d	r_c	a_{th}
	$(kg/m^3)x10^3$				(Å)			
0.0	5.166	4.572	0.115	11.5	0.6837	0.64	0.8608	12.409
0.1	5.153	4.825	0.064	6.4	0.6862	0.64	0.8508	12.398
0.3	5.119	4.901	0.043	4.3	0.6675	0.64	0.8467	12.351
0.5	5.070	4.833	0.047	4.7	0.6837	0.64	0.8192	12.339

The X-ray density (ρ_x) decreases with ferric ion concentration, because the decrease in molecular weight overtakes the decrease in volume of the unit cell. The pore fraction (f) was calculated using the relation: $f = (1-\rho/\rho_x)$ and percentage porosity by the relation: ($P = f * 100\%$). The variation of porosity (P) with Fe^{3+}-content(x) is a result of the interplay between ρ and ρ_x.

5a.2 Infrared Spectral Analysis of $Y_{3-x}Fe_{5+x}O_{12}$(x=0.0, 0.1, 0.3 and 0.5) system

Synthetic garnets are important from technological point of view. Yttrium iron garnet ($Y_3Fe_5O_{12}$; YIG) is used in magnetic bubble memory where as yttrium aluminium garnet ($Y_3Al_5O_{12}$; YAG) is the host crystal for near-infrared lasers.

The studies on vibrational modes of these compounds are of interest as physical characteristics and are also useful in constraining inter-atomic potentials. The garnet structure in body centered cubic (bcc) and the space group $O_h^{10}(Ia3d)$ consists of a three dimensional network of alternate corner-linked regular octahedral and distorted tetrahedral, both of which share edges with interstices that are slightly distorted from triangular dodecahedral [5, 6]. According to Roberts et al. [7] and Bauman et al. [8], this structure has 17 triply degenerate T_{1u} modes that are active in the infrared region (100-700 cm^{-1}). If the vibrational motions of the tetrahedron are mildly perturbed by placing this unit in the garnet structure, then these 17 IR modes should consist of three asymmetric bands ϑ_4, one symmetric band ϑ_2, two rotations R of the tetrahedron, two translations T of the tetrahedron, two translations T_d of the dodecahedral cations and three translations T_o of the octahedral cations.

The room temperature (300K) infrared spectra for x=0.0, 0.1, 0.3 and 0.5 compositions are shown in Figure 5a.2.1. It can be seen that the IR spectra of Fe^{3+}- substituted Yttrium iron garnet are found to exhibit five bands in the wave number range 400-800 cm^{-1}.No absorption band were observed above 800 cm^{-1}. Bands can be associated with atomic motions through the

response of frequency to chemical substitution. A complete band assignment for YIG has been made by Hofmeister and Campbell [9]. Accordingly, the high frequency peaks (#13 and 14) are assigned to bending motions of the tetrahedral. The three high frequency peaks (#15-17) are associated with asymmetric stretching of the tetrahedron, as suggested by factor group analysis, spectra of solutions and as previously concluded for rare earth garnets [5, 6 and references therein].

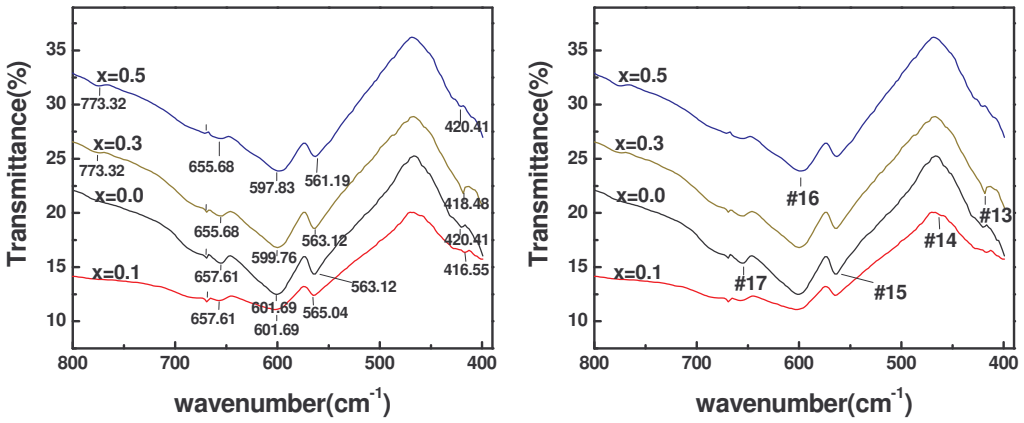

Fig. 5a.2.1 Powder transmission spectra for x=0.0, 0.1, 0.3 and 0.5 compositions of Y (Fe)-Fe-O system at 300 K

In addition to these five (# 13-17) well assigned bands, we have observed small kink (about peak # 17) for all the compositions and high frequency shoulder in vicinity of ~ 773 cm^{-1} for x=0.3 and 0.5 compositions. The high frequency kink/shoulder was observed earlier for Mg-Mn spinel ferrite system [10] and was assign to disparity of cationic masses present at tetrahedral site. In the present case, tetrahedral (d-site) is occupied by Fe^{3+}-ions only. Thus this probability is ruled out. The observed kink may be due to tetrahedral ion (Fe^{4+})-oxygen (O^{-2}) stretching vibration [11, 12]. The formation

of impurity centres (Fe^{4+}) due to native defects has been established by thermo-electric power measurement on the system. On the other hand, the distinct band (shoulder like) observed for x=0.3 and 0.5 compositions is assigned to the in- plane Fe-O bending vibrations. The intensity of this shoulder is very weak for x=0.0 and 0.1 compositions, while its intensity increases from x=0.3 to x=0.5 composition. It is important to note that for any of the composition, we have not observed characteristic band of Yttrium orthoferrite ($YFeO_3$), generally appeared at ~473 cm^{-1} [13], and this is consistent with the result of X-ray diffraction patterns analysis.

A careful examination of IR spectra reveals the fact that (i) The centre frequency of peaks (# 15-17) shifts towards lower frequency side (ii) the centre frequency of peak (# 13) shifts towards higher frequency side (iii) intensity of peaks (# 15-17) is maximum for x=0.0 composition, minimum for x=0.1 composition while intensity decreases with increasing Fe^{3+}-ion concentration(x) from x=0.3 to 0.5 composition. The observed shifting of centre frequency towards lower frequency side for peaks (# 15-17) of substituted compositions (x=0.1-0.5) suggests that asymmetric stretching of the tetrahedron hinders due to Fe^{3+}-substitution while shifting of centre frequency towards higher frequency side for peak (# 13) indicates enhancement of bending motions of the tetrahedra with Fe^{3+} substitution for Y^{3+} in the system.

It is known that intensity of infrared bands can give useful information concerning the change in electric dipole moment with interionic distances and the charge on each ion. It has been shown from infrared reflectivity data of zinc ferrite ($ZnFe_2O_4$) and nickel ferrite ($NiFe_2O_4$) that effective ionic charge on

Zn, Fe, Ni and O is different from the actual ionic valence, with different magnitude on A- and B- site. For example, effective ionic charge of Fe^{3+} is +2.86 for A-site and +2.88 for B-site in $NiFe_2O_4$ while it increases to +3.1 for B-site in $ZnFe_2O_4$ [14]. Of course, this ionic charge is always close to the ionic valence of respective ion, because of the residual spread of the electron orbital [15]. Based on above facts we feel that for x=0.1 composition relative displacement (d_i) and the effective charge on different ion (q_i) change in such a way that magnitude of electric dipole moment ($P_i = q_i.d_i$) decreases and as a result intensity of absorption bands. Observed variation of intensity for x=0.3 and 0.5 compositions may be explained on the similar lines of argument. For detailed understanding infrared reflectivity measurement alongwith available Rietveld refinement of X-ray data may be useful.

Finally, we have also recorded IR spectrum of YIG (x=0.0) in the wave number range of 250-400 cm^{-1}.The IR spectra of YIG, YAG and Yttrium gallium garnet ($Y_3Ga_5O_{12}$; YGG) [9], are also shown for comparison purpose. We are not able to observe peaks (# 1-6) due to non- availability of the data below 250 cm^{-1}, while peaks (# 7-12) were observed in the wave number range studied.

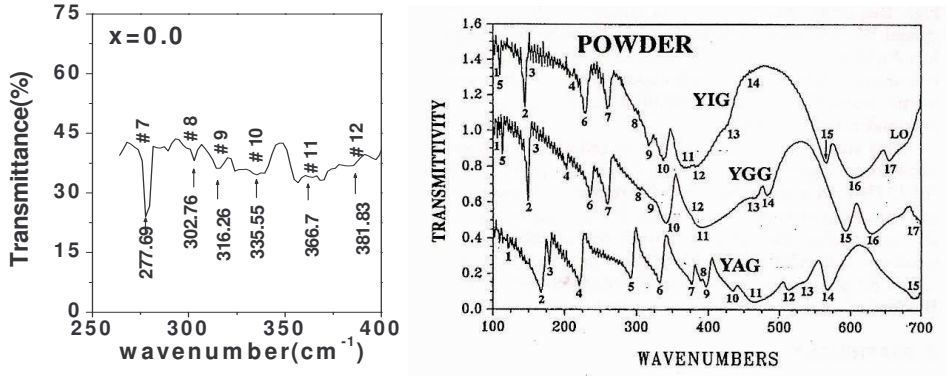

Fig. 5a.2.2 IR spectra of x=0.0 composition in wavenumber range of 250-400 cm^{-1} and IR spectra for YIG, YAG and YGG from Ref [9]

The peaks (# 7 and 9) are originated from the rotation of the tetrahedron, the peaks (# 8 and 10) are assign to translations of the octahedral cations, while peaks (# 11 and 12) are assigned to bending motion of the tetrahedral similar to that of peaks(# 13 and 14) (Figure 5a.2.1).

Studies on Magnetic Properties of $Y_{3-x}Fe_{5+x}O_{12}$ series (x=0.0, 0.1, 0.3 and 0.5)

5a.3 M-H loop characteristics of Y (Fe)-Fe-O system

Field dependence of magnetization M(H) data recorded at 300K for x=0.0, 0.1, 0.3 and 0.5 compositions are displayed in Figure 5a.3.1.The absence of high field slope exhibits strong evidence for collinear spin structure in the system.

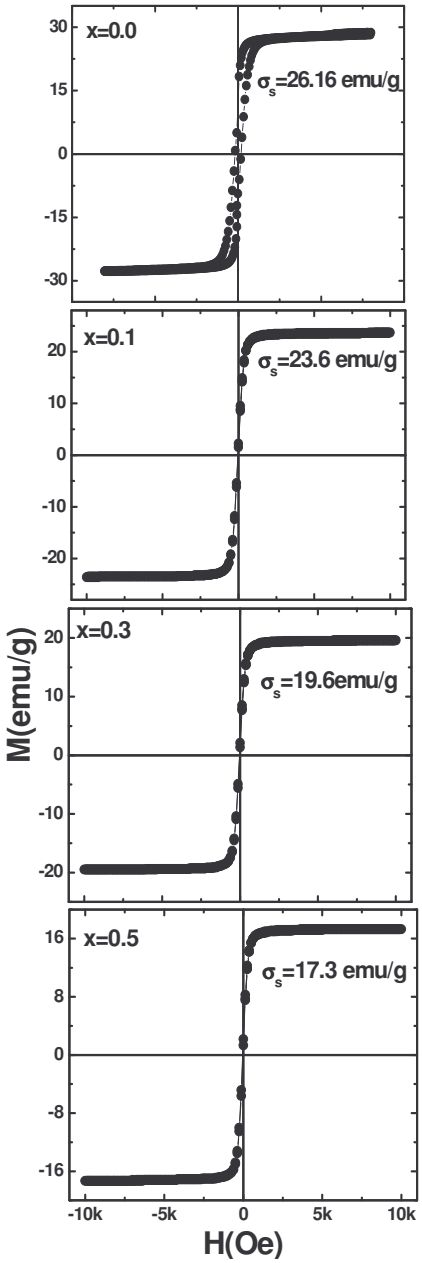

Fig 5a.3.1 Hysteresis loop patterns of $Y_{3-x}Fe_{5+x}O_{12}$ system at 300K

The saturation magnetization σ_s(emu/gm), 4πMs(Gauss) and magneton number n_B(saturation magnetization per formula unit in Bohr magneton) at 300K and 80K obtained from magnetization data for x=0.0-0.5 compositions are summarized in Table 5a.3.1. From field dependence of magnetization and observed magnetic moments it is clear that samples with x=0.0-0.5 show ferrimagnetic behaviour which decreases with increasing Fe^{3+} concentration (x). The compositional dependence of magneton number can be explained in the light of distribution of cations among the available tetrahedral (d-), octahedral (a-) and dodecahedral (c-) sites of garnet lattice.

Table 5a.3.1 Saturation magnetization (σ_s) and magneton number (n_B) for Y (Fe)-Fe-O system

Fe^{3+}-content (x)	σ_s (emu/g)	4πMs (Gauss)	n_B (μ_B)	σ_s (emu/g)	4πMs (Gauss)	n_B (μ_B)
	(300K)			(80K)		
0.0	26.2	1699.9	3.46	36.24	2351.4	4.79
0.1	23.6	1527.4	3.11	33.06	2139.7	4.35
0.3	19.6	1260.2	2.56	26.24	1687.1	3.42
0.5	17.3	1101.7	2.24	20.90	1334.9	2.70

5a.4 Mössbauer Spectroscopic study on $Y_{3-x}Fe_{5+x}O_{12}$ system at 300 K

The ^{57}Fe Mössbauer spectroscopy is an important probe for garnet and spinel ferrites to study the structural changes, hyperfine interaction, magnetic behaviour and to deduce unambiguously the distribution of Fe^{3+} ions among sublattices of garnet structure. We have earlier reported that substitution of Fe^{3+} ions changes the magnetic properties of the YIG system [16]. One therefore expects that the internal hyperfine magnetic field experienced by the Fe nucleus would also be affected by Fe^{3+}-substitution and such changes should be reflected in the ^{57}Fe Mössbauer spectra.

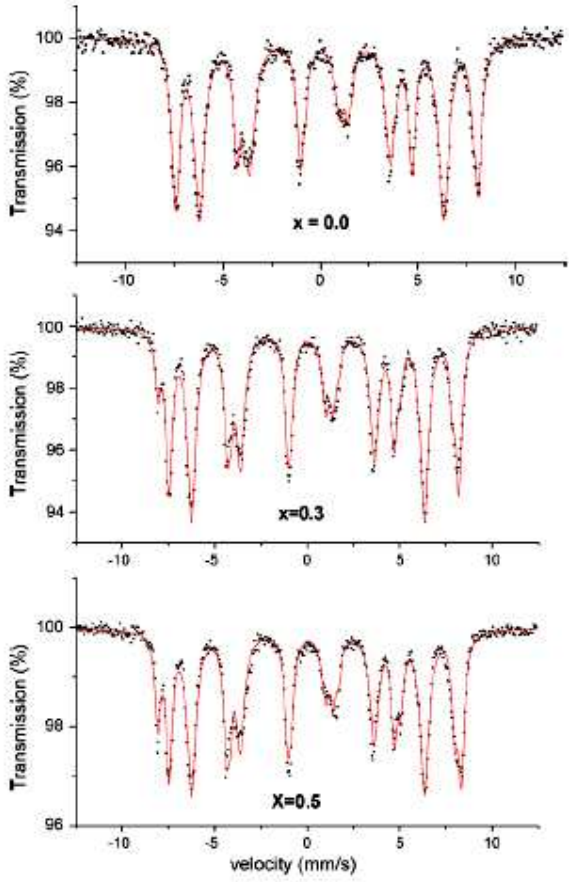

Fig. 5a.4.1 Mössbauer spectra of Y(Fe)–Fe–O system at 300 K

Mössbauer spectra recorded at 300 K for samples with x = 0.0, 0.3 and 0.5 are shown in Figure 5a.4.1.The Mössbauer spectra were analyzed and the hyperfine interaction parameters were refined by computer software using least squares method and assuming each spectrum to be a sum of Lorentzian functions.

The Mössbauer spectra of all the compositions exhibit three superimposed asymmetric Zeeman split sextets due to Fe^{3+} ions at tetrahedral (d), octahedral (a) and dodecahedral (c) sites. The three sextets for x = 0.0 composition is rather unexpected, because it is well established that Fe^{3+} ions occupy d- and a-sites in the ratio of 3:2, as a result two sextets may be expected.

Table 5a.4.1 Mössbauer parameters: isomer shift (I. S.), quadrupole shift (Q. S.), hyperfine field (H_f) and line width (W) for Y (Fe)–Fe–O system at 300 K

Fe^{3+}-content (x)	Site	I.S. (mm/s)* ± 0.02	Q.S. (mm/s) ± 0.02	H_f (kOe) ±1kOe	W (mm/s)	Area (%)
0.0	d	0.11	0.07	397	0.56	60
	a	0.35	0.13	478	0.37	33
	c	0.45	0.18	493	0.21	7
0.1	d	0.11	0.02	397.5	0.51	59
	a	0.30	0.20	485	0.32	32
	c	0.35	0.02	496	0.29	9
0.3	d	0.12	0.03	398	0.49	56.5
	a	0.27	0.6	494	0.28	33.9
	c	0.37	0.17	502	0.38	10
0.5	d	0.11	0.04	398	0.50	54.5
	a	0.29	0.50	500	0.31	30
	c	0.40	0.27	507	0.34	16

*With respect to Fe-metal.

The hyperfine parameters deduced through Mössbauer spectra are given in Table 5a.4.1. We note that the isomer shift for d-site shows no significant

variation with Fe^{3+}-substitution while that for a- and c-site shows considerable changes. This indicates that s-electron charge distribution of the Fe^{3+} ions on a- and c-site are influenced by Fe^{3+}-substitution. The value of isomer shift for a-site is well within the range of Fe^{3+} isomer shift values (0.2–0.3 mm/s), on the other hand for d-site and c-site values lying below and above the range. The isomer shifts for Fe^{3+} at different sites are different. The isomer shift for d-site is the smallest ~0.11 mm/s and is independent of Fe^{3+}-substitution. The isomer shift at c-site is greater than that at a-site and is influenced by the amount of Fe^{3+}-substitution. As all the iron ions are in the trivalent state, the change in isomer shift signifies that the 3s electron density at the nucleus of Fe^{3+} ion is governed by the kind of bonding it makes with the neighbouring oxygen ions. The difference in the neighbouring environment (tetrahedral, octahedral or dodecahedral) can cause different stretching of d-electrons and partial hybridization resulting in different distribution of 3s electron. The compositional variation of quadrupole shift in the magnetic sextets is given in Table 5a.4.1. It shows that the quadrupole shift of d-sites remains the same for all the samples and is around 0.1 mm/s which fall in the range corresponding to that produced in Fe^{3+} ion in such an environment. The quadrupole shifts of a- and c-sites show significant variation with increase in Fe^{3+}-substitution. The substitution of Fe^{3+} in the system creates an asymmetric displacement of oxygen ions surrounding a- and c-sites. Fe^{3+} is normally a spherically symmetric ion and therefore Q_{local} is expected to be zero, hence the quadrupolar interaction seen in our case for a- and c-sites must arise from the $Q_{lattice}$. This creates an asymmetry or distortion at the lattice site leading to significant quadrupole shift. The external substitution of

Fe^{3+} changes the amount of oxygen displacement resulting in corresponding change in quadrupole shift.

It is seen that (Table 5a.4.1) the nuclear hyperfine field for d-site is lower than that of the a- and c-sites, further Hc > Ha, for all the samples. This happens because the c-site Fe^{3+} ions experience a stronger average magnetic bonding with d- and a-sites Fe^{3+} ions compared to the d- and a-site Fe^{3+} ions for which some of the bonds are with diamagnetic Y^{3+} at c-sites. The magnetic hyperfine fields for pristine composition (x = 0.0) are found to be 478 kOe for a-sites and 397 kOe for d-sites (Table 5a.4.1), are in agreement with reported earlier [3].

The Zeeman lines from d-sites are more broadened than those from a- and c-sites. This can be related to the fact that the d-sites exhibit a strong magnetic interaction with a- and c-sites giving rise to a large distribution of magnetic hyperfine field (MHF) coming from a perturbation in the three sublattices.

From the results of Mössbauer spectra, we can consider the cation distribution as follows. It is known that YIG is a ferrimagnetic oxide with three cation sites and the formula is given by:

$$\{Y_3^{+3}\}^c (Fe_2^{+3})^a [Fe_3^{+3}]^d O_{12}^{-2}$$

Considering the peak area ratio determined through Mössbauer spectral analysis, the cation distribution for the compositions are deduced as:

$$x = 0.0, \{Y_{2.65} Fe_{0.35}\}^c (Fe_{1.65} Y_{0.35})^a [Fe_3]^d O_{12}^{-2}$$

$$x = 0.1, \{Y_{2.53} Fe_{0.47}\}^c (Fe_{1.63} Y_{0.37})^a [Fe_3]^d O_{12}^{-2}$$

$$x = 0.3, \{Y_{2.48} Fe_{0.52}\}^c (Fe_{1.78} Y_{0.22})^a [Fe_3]^d O_{12}^{-2}$$

$$x = 0.5, \{Y_{2.15}Fe_{0.85}\}^{c}(Fe_{1.65}Y_{0.35})^{a}[Fe_{3}]^{d}O_{12}^{-2}$$

According to the Neel's three sublattice, collinear spin model [14], the magnetic moment per formula unit at 0 K in units of μ_B is n_B^N which can be expressed as:

$$n_B^N = [M_d(x) - M_a(x)] - M_c(x)$$

where Md, Ma and Mc are the d-, a- and c-sublattice magnetic moment in units of μ_B calculated using cation distribution formula and magnetic moment of 5 μB for Fe^{3+} ions. The variation of magneton number (n_B) at 80 K obtained from magnetization data [Table 5a.3.1] and n_B^N values for all the compositions (Table 5a.4.2) are in good agreement, confirming the collinear spin ordering in the system. The small observed difference between n_B^N and n_B values may be due to thermal effects.

The higher value of n_B at 80K for x=0.5 composition, compared to n_B value at 0K, n_B^N, may be due to formation and presence of Fe^{2+}-ions (4μ_B, 0.74 Å) in the system. During the synthesis process under slightly reducing condition, the formation of Fe^{2+} is quite probable. These ferrous ions are statistically distributed throughout the system, but according to Torres et al [17] and Antomini et al [18] , Fe^{2+} ions prefer to occupy octahedral sites, Although occasionally minor contents of Fe^{2+} ions have been found in d-sites [17,18], which under steric aspects are supposed to have mainly occupied by the smaller Fe^{3+}-ions.

The presence of Fe^{2+} ions on a-site reduces site magnetic moment as Fe^{2+} has magnetic moment of 4 μ_B compared to 5 μB of Fe^{3+} ions. This results in

the increase of the net magnetic moment. The presence of Fe^{2+} ions helps to understand and explain two aspects:

(i) Small reduction in lattice constant value from x=0.3(12.363 Å) to x=0.5 (12.359 Å) composition, This may be due to larger ionic radius of Fe^{2+} ions (0.74 Å) as compared to ionic radius of 0.64 Å for Fe^{3+} ions in the system.

(ii) Formation of impurity centres Fe^{4+} due to native defects [19, 20]. These may be formed from divalent metal ions (Fe^{2+} ions) present at Fe^{3+} sites in the system [21].

Table 5a.4.2 Magneton number (n_B) and exchange integral (J) for Y (Fe)–Fe–O system

Fe^{3+}-Content (x)	n_B (μ_B) 80K	n_B^N (μ_B)	n_B^M (μ_B)	J_{ad} (cm^{-1})	J_{ac} (cm^{-1})	J_{dc} (cm^{-1})
0.0	4.79	5.0	5.0	14.91	5.09	3.78
0.1	4.35	4.5	4.44	15.13	5.99	4.42
0.3	3.42	3.5	3.29	14.75	6.14	4.73
0.5	2.70	2.5	2.11	15.37	8.18	6.07

A check for the presence of a canted spin (non-collinear) structure follows from the apparent proportionality between (H_f) and the average sublattice magnetization. By neglecting intra-site interactions (J_{dd}, J_{cc} and J_{aa}) between the ions on the same site, it can be shown that:

$$\mu(x) = \frac{H_d(x)}{H_d(0)} M_d(x) - \frac{H_a(x)}{Ha(0)} M_a(x) - \frac{H_c(x)}{H_c(0)} M_c(x)$$

where H_d, H_a and H_c are hyperfine field values (Table5a.4.1).

The values of magnetic moment per formula unit $n_B^M \approx \mu(x)$ as a function of Fe^{3+}-content (x) were determined from above equation the same are presented in Table 5a.4.2. There is reasonable agreement among the value of

$n_B^M(x)$ obtained from Mössbauer data, $n_B(x)$ from magnetization and $n_B^N(x)$ calculated from Neel's model, confirming a collinear magnetic structure.

In such garnet systems, formation of yttrium orthoferrite ($YFeO_3$) and α-Fe_2O_3 is quite probable [22, 23]. If it is so, it would have reflected in X-ray diffraction, magnetization and Mössbauer spectroscopic measurements. In X-ray diffraction pattern it appears as extra Bragg's reflections, which do not correspond to the bcc phase of YIG. The presence of weak ferromagnetic $YFeO_3$ and unreacted Fe_2O_3 lowers the saturation magnetization value [4]. There are reports showing the presence of an additional sextet in Mössbauer spectrum has been observed with hyperfine field value ≥510 kOe corresponding to $YFeO_3$ or α -Fe_2O_3 phase formation [4, 5]. In the present case, no such indications have been observed, ruling out any formation of unwanted phases in the system.

It is possible to estimate the value of the exchange integral J_{ad}, J_{ac} and J_{dc} from Neel temperature (T_N) by using the following equation [24]:

$$T_N = \frac{2s(s+1)}{3K}\sqrt{\frac{\lambda}{\mu}}Z_{ad}J_{ad}$$

where the value of S, spin for Fe^{3+} ions is 5/2; Z_{ad} the number of nearest neighbours to the a-site is 6; λ = [{2/(5 + x)} (2 - y)/2] the fraction of magnetic ions at the a-site, with y the amount of non-magnetic ions at the octahedral site;μ= [{3/ (5 + x)}(3 - z)/3] the fraction of magnetic ions at the d-site, z the amount of non-magnetic ions at the tetrahedral site; k the Boltzman constant and J_{ad} is the average exchange integral which is to be evaluated. In similar manner values of J_{ac} and J_{dc} have been calculated and presented in Table 5a.4.2. It can be seen that $J_{ad} > J_{ac} > J_{dc}$, i.e. the a–d exchange interaction is

the strongest interaction in a garnet irrespective of the presence of rare earth ion [4]. It is interesting to note that J_{ad} remains almost constant while J_{ac} and J_{dc} increase with increasing Fe^{3+}-substitution in the system. Now it is possible to explain compositional variation of hyperfine field in the light of the strength of exchange interactions. The observed compositional variation of H_d, H_a and H_c is similar to that of the variation of J_{ad}, J_{ac} and J_{dc}, respectively, suggesting that the hyperfine field of d-sites (H_d), octahedral sites (H_a) and dodecahedral sites (H_c) is governed by J_{ad}, J_{ac} and J_{dc} exchange interactions, respectively.

5a.5 Thermal variation of low field ac susceptibility study on Fe^{3+}-substituted $Y_3Fe_5O_{12}$ system

The temperature dependence of relative ac susceptibility χ_T/χ_{RT} for all the four compositions is shown in the Figure 5a.5.1. The results of the ac susceptibility exhibit normal ferrimagnetic behaviour. The magnetic transition temperature, i.e Neel temperature (T_N), at which magnetic susceptibility vanishes, is determined from thermal variation of ac susceptibility. The T_N determined from ac susceptibility measurements are listed in Table 5a.5.1.

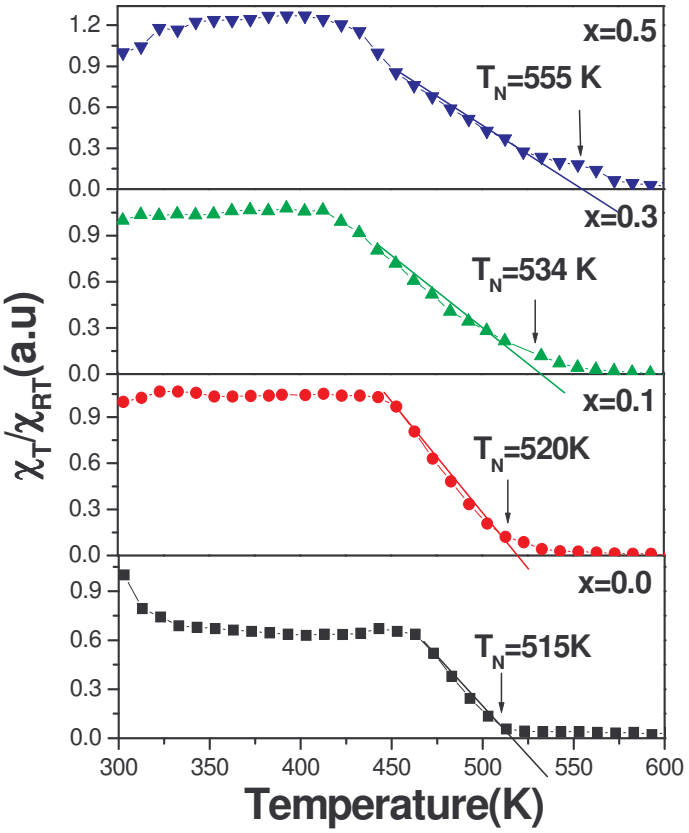

Fig.5a.5.1 Temperature dependence of ac susceptibility χ_T/χ_{RT} for different compositions of $Y_{3-x}Fe_{5+x}O_{12}$ system

It is evident from Table 5a.5.1 that T_N increases with increasing x for x=0.0 to 0.5. The T_N basically depends on the active magnetic linkages per magnetic ion per formula unit. The observed increase in T_N with x is due to replacement of non-magnetic Y^{3+}($0\mu_B$) by magnetic Fe^{3+}(5 μ_B) ions in the system, which enhances the strength of magnetic interactions responsible for change in T_N with content (x). The increase in T_N with x is found to be nearly linear for x=0.0-0.5 compositions which further supports the collinear ferrimagnetic ordering as confirmed by magnetization measurements.

It is possible to estimate the Neel temperature theoretically by applying the molecular field theory. The statistical model proposed by Gilleo and Geller [25] has been found to hold reasonably well for non-magnetic substitution on a- and d-sites. The calculations become more involved in case of magnetic substitution on a- and d- sites. When the magnetic substitution is made on c-site as in the present case, it becomes too complex to estimate Neel temperature. We have employed here the modified molecular field theory for garnets as suggested by Baldha et al [26], for spinel ferrites. This involves c-c, c-a and c-d sublattices interactions in addition to a-a, a-d, d-d interactions. The T_N(x) for a garnet doped with magnetic ion concentration (x) can be expressed in terms of the Neel temperature of the un-substituted garnet T_N(x=0.0), i. e $Y_3Fe_5O_{12}$ by equation;

$$T_N(x) = \frac{M(x=0.0)T_N(x=0.0)n(x)}{n(x=0.0)M(x)}$$

Here, M(x) is the relative weighted total magnetic ions per formula unit, calculated by considering the weighted magnetic ion concentration for substituted garnet to that of un-substituted one. Thus, M(x) for $Y_{3-x}Fe_{5+x}O_{12}$ system can be expressed as;

$$M(x) = \frac{5+x}{5}$$

n(x) is the number of interaction per formula unit expressed as;

$$n(x) = [a_f{}^2 \mu_a{}^2 + d_f{}^2 . \mu_d{}^2 + c_f{}^2 . \mu_c{}^2 + a_f d_f \mu_a \mu_d + a_f c_f \mu_a \mu_c + d_f c_f \mu_d \mu_c]$$

where a_f, d_f and c_f are the fraction of magnetic ions on the a, d and c-sites respectively while μ_a, μ_c and μ_d are the magnetic moments of corresponding magnetic ions. The Neel temperature estimated using the above equations are in good agreement with experimentally observed Neel temperature and are listed in Table 5a.5.1.

In the present case, lower value of T_N for un-substituted composition i.e pure$Y_3Fe_5O_{12}$ (T_N=515 K), when compared to literature value of 553 K [27], may be due the presence of non-magnetic Y^{3+} on a-site, that weakend a-d and a-a interactions. It is found that the number of interaction per formula unit n(x) for $Y_3Fe_5O_{12}$ with normal cationic distribution $\{Y_3\}^c(Fe_2)^a[Fe_3\}^dO_{12}$, having magnitude of 475 while it is 460.53 in the present case as observed (Table 5a.5.1), that supports our argument of weakening of magnetic interactions.

Illustrative calculations for n(x) and T_N(x) with x=0.3 composition:

$\{Y_{2.48}\ Fe_{0.52}\}^c\ (Fe_{1.78}Y_{0.22})^a\ [Fe_3]^d\ O_{12}^{-2}$

n(x=0.3)= $[(1.78)^2(5\mu_B)^2 + (0.52)2(5\ \mu_B)2+(1.78)(3)(5\ \mu_B.5\ \mu_B) + (1.78)$

$(0.52)\ (5\ \mu_B.5\ \mu_B)+ (0.52)(3)(5\ \mu_B.5\ \mu_B)]$

=506.61

$$T_N(x=0.3) = \frac{(1.0)(515K)(506.61)}{(460.53)(1.06)} = 534.57K$$

Table 5a.5.1 The Neel temperature (T_N) for Y (Fe)-Fe-O system

Fe^{3+}-content (x)	M(x)	n(x)	T_N(K) ± 2K	
			(susceptibility)	(Theoretical)
0.0	1.00	460.53	515	-
0.1	1.02	473.60	520	519.24
0.3	1.06	506.61	534	534.57
0.5	1.10	546.20	555	555.27

5a.6 Elastic properties of Fe^{3+}-substituted $Y_3Fe_5O_{12}$, by Ultrasonic pulse transmission technique

Ultrasonic wave is a strain wave, which produces longitudinal and transverse elastic waves, while propagating through a solid. The velocity of such waves is characteristic feature of a solid. The fundamental idea is that if there is distortion of the solid from equilibrium shape, the average separation of atoms within the solid is no longer optimal; some atoms will be too close to their neighbour and some too far apart. In either case there will be a restoring force, which will act to return the atoms to their equilibrium separations. The dynamics of the elastic wave will be affected by the way the solid responds to the restoring force. The restoring force per unit displacement, i.e. the natural "springiness" of the substance and density of the substance are most critical parameters that determine this response. On the other hand the restoring force on the small region of the solid depends on the type of distortion (strain) that has taken place during synthesis process. The parameters that describe restoring force per unit strain are known as elastic moduli of the substance. In the present work, we have employed ultrasonic pulse transmission technique as a tool to get an idea about such stress/strain ratio.

From fundamental research point of view knowledge of elastic moduli for any polycrystalline material elucidates the nature of binding forces and also helps to understand the thermal properties of the solids. When we think about the application of any polycrystalline material, in addition to the knowledge of its magnetic and electric/dielectric responses, the elastic moduli help to decide the suitability of the material for a specific application.

The yttrium iron garnet ($Y_3Fe_5O_{12}$) (YIG) is the most widely studied material. The studies on various cation substituted YIG and its effect on various physical properties are countless. Untill now mechanical property measurements for garnet material have not received a great deal of attention. To our knowledge very few reports are available in the literature on elastic properties of single crystal and polycrystalline YIG [28]. Since no work has been reported on elastic behaviour of any garnet system in general and $Y_{3-x}Fe_{5+x}O_{12}$ in particular, the present work is important from fundamental research point of view. The present work aims to study the effect of Fe^{3+}-substitution on elastic properties of yttrium iron garnet. Porosity effect is taken in to account using different models in a porous medium. The lattice energy determination and approximation of elastic parameters for single crystalline materials from its polycrystalline counterpart are the central purpose of the study.

The experimental values of longitudinal wave velocity (V_l), transverse wave velocity (V_s) determined through the UPT technique and the bulk density (ρ) for different compositions are used to calculate longitudinal modulus (L), rigidity modulus (G), bulk modulus (B), Poisson's ratio (σ), Young's modulus (E), mean sound velocity (V_m) and Debye temperature (θ) using the following formulae [29,30]:

Longitudinal modulus (L) = $\rho (v_l)^2$

Rigidity modulus (G) = $\rho (v_s)^2$

Bulk modulus (B) = L-(4/3) G

Poisson's ratio (σ) = $\frac{3B-2G}{6B+2G}$

Young's modulus (E) = (1+ σ) 2G

Mean sound velocity (V_m) = $\left[\frac{3(V_l^3 V_s^3)}{(V_s^3 + 2V_l^3)}\right]^{\frac{1}{3}}$

Debye temperature (θ) = $\frac{h}{k}\left[\frac{3N_A}{4\pi V_A}\right]^{\frac{1}{3}} V_m$,

Where h and k are Plank's and Boltzman's constants respectively, N_A is Avogadro's number and V_A is mean atomic volume given by (M/ ρ)/q , where M is the molecular weight and q is the number of atoms in the formula unit (in present case, q=20).

The polycrystalline ceramics under study can be treated as an isotropic elastic medium, because the grain size estimated from the SEM study for different compositions is much smaller than the ultrasonic wavelength. For example, a 1 MHz longitudinal ultrasonic wave traveling with a velocity of about 4500 ms^{-1}has a wavelength 4500 μm, which is much greater than the grain size of the samples. Knowledge of any two elastic moduli will suffice to give the values of the remaining elastic constants. Here, it should be noted that for solids, the adiabatic (ultrasonic) and isothermal moduli differ much less than that for gases, and thus generally it is not stated which value is presented. If the data are derived at high pressure then generally it is possible to determine only the isothermal modulus. If the data are determined by using speed of sound (as in the present case), the approximate modulus to use is the adiabatic modulus [31].

The velocity of transverse waves is approximately half as that of longitudinal waves (Table 5a. 6. 1).This is due to the reduction in the energy of the transverse waves, i.e when a wave travel through a material, due to transfer of energy, it makes the particle to vibrate and hence, the vibrating

particle incident on the neighbour one causes it to vibrate and so on. In case of transverse wave, the particle in medium vibrates perpendicular to the direction of the propagation of the wave motion and hence, it requires a larger energy to make the neighboring particle to vibrate. This result in the reduction in the energy of the ultrasonic waves and hence, velocity of the transverse waves is about half that of longitudinal waves. The value of Poisson's ratio (σ) is found in the range 0.25-0.30 for different compositions. These values lie in the range from -1 to 0.5, which are in conformity with the theory of isotropic elasticity. The acoustic Debye temperature (θ) at which nearly all modes of vibrations in a solid are excited, plays an important role in the study of a large number of solid state problems involving lattice vibrations. The observed decrease in θ with Fe^{3+}-content (x) suggests that lattice vibrations are enhanced due to Fe^{3+}- substitution.

Table 5a.6.1 Elastic wave velocity (V), Elastic constants and Debye temperature (θ) for Y (Fe)- Fe- O system

Fe^{3+}-content (x)	V_l	V_s	V_m	L	G	B	E	σ	θ(K)
	(m/s)			(GPa)					
0.0	6611	3677	4095	199.8	61.8	117.4	157.7	0.276	497
0.1	6000	3468	3849	173.7	58.0	96.3	144.9	0.249	491
0.3	5010	2812	3128	123.0	38.8	71.3	98.4	0.270	403
0.5	4652	2500	2790	104.6	30.2	64.3	78.3	0.296	359

At this juncture, it would be interesting to correlate variation of elastic constant values with porosity rather than with composition. The presence of pores is unavoidable and they enter into the material through fabrication routes. Pores are of different sizes and shapes. Their magnitudes and distributions are different .These parameters decide overall strength of a

material. In most of the solids, the velocity decreases linearly with increase in porosity and increase in porosity will decrease the density [29], which in turn reduces the magnitude of the elastic moduli and vice versa. It is found that (Table 5a.6.1) variation of elastic constant with porosity does not follow this general trend as discussed. The magnitude of elastic moduli decreases with decreasing porosity. This is rather unexpected.

Zero porosity correction to elastic moduli

It is fact that in real applications Young's modulus, rigidity modulus and Poisson's ratio of the real bulk porous material are important. The basic purpose behind zero porosity correction to elastic constants is that it gives an idea about the maximum strength of the material that can be achieved by controlling porosity. In compositional dependent study based on the magnitude of void free moduli one can have insight about relative change in the strength of the material as a function of substitution. Other important aspect of zero porosity correction is that one can also approximate the magnitude of elastic constants and other parameters for single crystalline material of the same composition [32], which is important from the applications point of view. Thus, it is a common practice for polycrystalline oxide material that certain parameters like resistivity [33, 34], permeability [35, 36], including elastic constants [37-39] are corrected for zero porosity.

The measured elastic moduli do not have much significance unless they are corrected to zero porosity. As the garnets under study are porous the values of elastic moduli have been corrected to zero porosity. The correction

methods commonly used are those developed for pores of cracked bodies, such as ceramics and rocks, or those for a composite with inclusions. Different methods based on distinct approaches that restrictively account for one or a few factors (porosity, dimensions, distribution, shape of the cracks etc.) can give different values for the corrected elastic moduli. If the specimen is at atmospheric pressure in air (as in the present case) or under vacuum, porosity is the only effective factor [38]. We have employed here three different approaches (i) Hasselman and Fulrath model [40] (ii) Ledbetter and Datta model [41] and (iii) elastic theory [42], for the determination of elastic constants in void-free state.

(i) Hasselman and Fulrath model

The basic assumption in their treatment is that pores are spherical and distributed in a material having homogeneous and isotropic elastic properties. According to the Hasselman and Fulrath model, elastic constants have been corrected to the void-free state using the empirical relations:

$$\frac{1}{E_0} = \frac{1}{E}\left[1 - \frac{3f(1-\sigma)(9+5\sigma)}{2(7-5\sigma)}\right]$$

$$\frac{1}{G_0} = \frac{1}{G}\left[1 - \frac{15f(1-\sigma)}{(7-5\sigma)}\right]$$

$$\sigma_0 = \left(\frac{E_0}{2G_0}\right) - 1$$

$$B_0 = \left(\frac{E_0 G_0}{3(3G_0 - E_0)}\right)$$

The corrected values of Young's modulus (E_0), rigidity modulus (G_0), Poisson's ratio (σ_0) and bulk modulus (B_0) for different compositions are given in Table 5a.6.2 (a).

(ii) Ledbetter and Datta model

Ledbetter and Datta assumed that the randomly distributed spherical voids posses zero resistance to both dilation and shear. The modified equations thus arrived, incorporating these assumptions are given by:

$$G_0 = \left(\frac{1}{2A_1}\right)\left[-A_2 + (A_2^2 - 4A_1A_3)^{\frac{1}{2}}\right]$$

$$B_0 = \frac{(4G_0B)}{[4(1-f)G_0 - 3fB)]}$$

$$E_0 = \frac{9B_0G_0}{3B_0 + G_0}$$

where,

$$A_1 = \left(\frac{8}{3}\right)(1-f)$$

$$A_2 = (3-2f)B - \left(\frac{8}{3} + 4f\right)G$$

$$A_3 = -3(1+f)BG$$

The void free values of Young's modulus (E_0), rigidity modulus (G_0) and bulk modulus (B_0) for all the compositions are summarized in Table 5a.6.2 (b).

(iii) Elastic Theory

Based on elastic theory, the linear relation between the elastic moduli as a function of porosity at lower range of porosity (f < 0.2) can be written as:

$$V_l = V_{l0}(1 - C_l f)$$

$$V_s = V_{s0}(1 - C_s f)$$

$$E = E_0(1 - C_E f)$$

$$G = G_0(1 - C_G f)$$

$$\sigma = \sigma_0 (1 - C_\sigma f)$$

where C_l, C_s, C_E, C_G and C_σ are constants of the material. The subscript '0' denotes non-porous elastic constant of the material. The exact expressions for the constants are as follows:

$$C_l = \frac{1}{2}\left\{\left|\frac{\left[C_E + 2C_\sigma \sigma_0^2 (2 - \sigma_0)\right]}{(1-\sigma_0)(1+\sigma_0)(1-2\sigma_0) - 1}\right|\right\}$$

$$C_s = \frac{1}{3}$$

$$C_E = \left(\frac{1}{18}\right)(29 + 11\sigma_0)$$

$$C_G = \frac{5}{3}$$

$$C_\sigma = \left(\frac{5}{9}\right) + \left(\frac{11\sigma}{18}\right) - \left(\frac{1}{18}\sigma\right)$$

The above relations are used to determine the elastic moduli for non-porous material and the results are shown in Table 5a.6.2 (c).

Table 5a.6.2 Elastic data corrected to zero porosity

(a) Longitudinal modulus (L_0), rigidity modulus (G_0), bulk modulus (B_0), Young's modulus (E_0) and Poisson's ratio (σ_0) (Hasselman and Fulrath model) for Y (Fe)-Fe-O system

Fe^{3+}-content (x)	L_0	G_0	B_0	E_0	σ_0
	(GPa)				
0.0	268.8	79.5	162.8	205.1	0.290
0.1	200.7	66.3	112.3	166.2	0.253
0.3	135.7	42.2	79.3	107.6	0.274
0.5	117.0	33.2	72.8	86.4	0.302

(b) Longitudinal modulus (L_0), rigidity modulus (G_0), bulk modulus (B_0), Young's modulus (E_0) and Poisson's ratio (σ_0) (Ledbetter and Datta model) for Y (Fe) -Fe-O system

Fe^{3+}-content (x)	L_0	G_0	B_0	E_0	σ_0	A_1	A_2	A_3
	(GPa)							
0.0	258.8	77.2	155.7	198.9	0.288	2.360	131.97	-24269.04
0.1	195.3	63.1	111.2	159.2	0.261	2.496	107.06	-17828.60
0.3	135.3	42.2	79.0	107.5	0.274	2.552	97.62	-8656.19
0.5	146.7	33.0	72.7	86.0	0.303	2.541	100.64	-6099.38

(c) Elastic wave velocity (V), rigidity modulus (G_0), Young's modulus (E_0) and Poisson's ratio (σ_0) (Elastic Theory) for Y (Fe)-Fe-O system

Fe^{3+}-content (x)	V_{l0}	V_{s0}	V_{m0}	E_0	G_0	σ_0	C_l	C_E	C_σ
	(m/s)			(GPa)					
0.0	8080	4494	5005	198.7	76.4	0.300	1.5809	1.794	0.7090
0.1	7417	3703	4155	163.5	64.9	0.260	1.6982	1.777	0.6939
0.3	5397	2853	3189	106.6	41.8	0.278	1.6676	1.781	0.7056
0.5	5021	2713	3028	85.5	32.8	0.306	1.5628	1798	0.7200

It can be seen from Tables 5a.6.2 (a) - (c) that the magnitude of elastic constants decreases with increasing Fe^{3+}concentration(x) in $Y_{3+x}Fe_{5-x}O_{12}$ for x=0.0-0.5, which suggests that the corresponding deformation of the solid is easy and the solid has weak tendency to spring (analogous to planes within a solid held together by atomic bond) back to its equilibrium position. Following the Wooster's work, the observed variation of elastic constants may be interpreted in terms of change in the strength of interionic bonding [43].

The strength of inter-ionic bonding is expected to change:

(I) if interionic distances get changed by the substitution of larger or smaller cations in the system [44-46].

In the present system, as discussed above (section 5a.1), lattice constant and interionic distances decrease with increasing Fe^{3+}-substitution (Table 5a.1.2). The observed reduction in the interionic distances enhanced strength of bonding and as a result the magnitude of the elastic moduli is expected to increase. On the other hand, the variation of elastic moduli with dopant's concentration may be explained on the basis of a model according to which the general relationship between elastic constant and interionic distance of a solid is given by;

$$C_{ij} = F_{ij}\left(\frac{(Ze)^2}{r^4}\right)$$

Where C_{ij} is the elastic constant, z is the valency, e is the electronic charge, r is the interionic distance and F_{ij} is a tensor which, however, has a constant value for a particular crystallographic structure. All the samples in the study are of bcc structure and as such F_{ij}, Z and e can be considered as a constant so that above relationship reduce to;

$$C_{ij} \propto \left(\frac{1}{r^4}\right)$$

As discussed, since the interionic distances decrease with increasing Fe^{3+}-content (x) in the system, the increase in the magnitude of the elastic moduli with increasing (x) is quite expected.

(II) change in the electronic configuration and as a result the nature of the bond formation between cations and cation –anion by cationic substitution in the structure [46-48].

It is well known that cations with completely filled outer most orbit is more stable as compared to cations with half filled outer most orbit or incomplete

outer most orbit. In the system under investigation, $Y_{3-x}Fe_{5+x}O_{12}$, Y^{3+}- have completely filled outermost orbit and is replaced by Fe^{3+}-ions having half filled ($3d^5$) outermost orbit, that contribute to the bond formation. Thus, on increasing Fe^{3+}-substitution for Y^{3+}, strength of bonding and magnitude of moduli are expected to enhance.

(III) the occupancy of the substituted cation along the grain boundary instead of interstitial structural position [49].

Here, from X-ray data refinement III-probability is ruled out, as there is systematic decrease in lattice parameters that suggest occupancy of Fe^{3+}-ions at interstitial structural position.

(IV) the grain size effect and the change in the microstructure with composition [10,46, 50].

In contrary to above facts, we have observed rapid decrease in magnitude of the elastic moduli with Fe^{3+}-substitution (Table 5a.6.2 (a)-(c)). This decrease in magnitude of the elastic constants may be due to the change in grain size and microstructure, which dominates the effect of reduction of length of interionic bonding and active bonds formation by Fe^{3+}- substitution. It is seen from SEM images that, the average grain size increases with increasing Fe^{3+}content (x) in the system.(Figure 5a.6.1)

The elastic moduli could be greatly influenced by the presence of pores, secondary phase and impurities, but not by the grain size in the micron range. As compared with the grain size, the geometry and distribution of pores also exert greater influence on the wave propagation in the polycrystalline YIG and thus the elastic properties thereof. A decrease of

elastic moduli values with decreased pore fraction just hints that the pore fraction might not be the dominant factor in determining the elastic moduli.

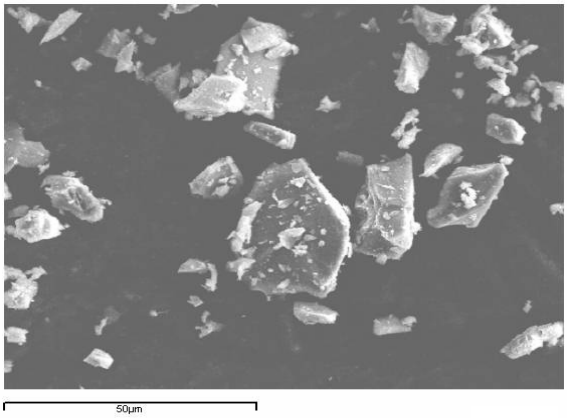

0.1

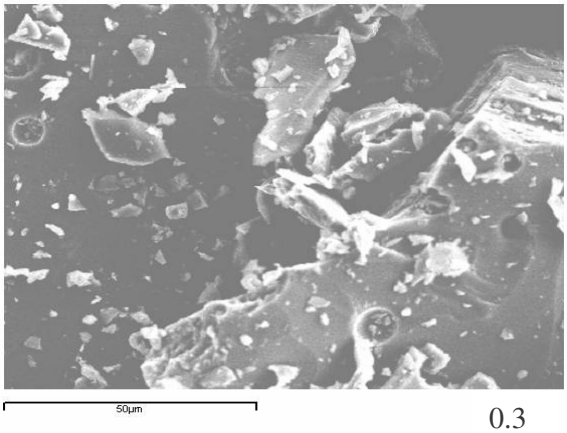

0.3

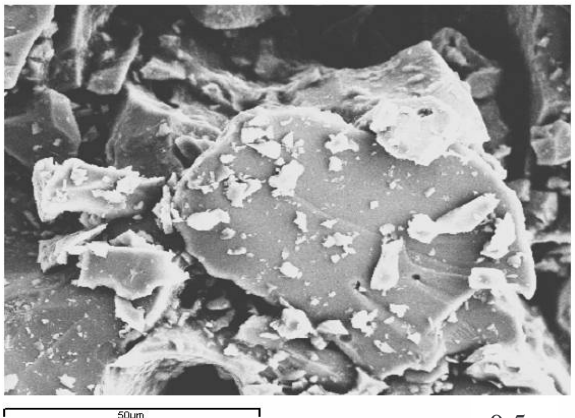

0.5

Fig.5a.6.1 Scanning electron micrographs for x=0.1, 0.3 and 0.5 compositions

The low apparent stiffness may result from oxygen vacancies, which soften interionic forces. This probability is ruled out based on EDAX results that have confirmed stoichiometry of compositions. Also, it may result from microcracks, which reduce elastic stiffness without lowering mass density. During synthesis process due to anisotropic thermal stresses, microcracks occur. This probability can not be neglected.

Relationship between M/q and V_l/ρ_x, V_s/ρ_x

In 1961, Brich [51] showed that the longitudinal velocity (V_l) is approximately a linear function of x-ray density ($\rho_{x)}$ in the case of silicates and oxides having same atomic weight (M/q) subsequently Simmons [52] confirmed this result and extended the applicability of such a linear relationship to transverse wave velocity (V_s) also. Anderson [53] further observed that whenever there is a variation in the values of V_l/ρ_x and V_s/ρ_x, a corresponding variation in the values of mean atomic weight is expected because the product of M/q with V_l/ρ_x and V_s/ρ_x should be constant. A similar relationship was arrived at by Reddy et al [54], Kumar et al [55] in the case of some mixed ferrites and by Buch et al [46] for manganite perovskites. As such, an attempt has been made to establish a relationship between V_l/ρ_x , V_s/ρ_x and M/q of the sample of present investigation and is given in Table 5a.6.3.It can be seen from Table 5 that the values of V_l/ρ_x and V_s/ρ_x decreases with decreasing mean atomic weight thus establishing the fact that these materials do not behave like other oxide materials described in the literature.

Table 5a.6.3 Experimental data of Fe^{3+}-substituted $Y_3Fe_5O_{12}$ garnets

Fe^{3+}-content (x)	M/q (kg)x10^{-3}	V_l/ρ_x	V_s/ρ_x ($m^4kg^{-1}s^{-1}$)x10^{-3}	$M/q.V_l/\rho_x$	$M/q.V_s/\rho_x$ ($m^4.s^{-1}$)x10^{-3}	M (kg)x10^{-3}
0.0	36.89	1273.7	711.8	47.2	26.3	737.8
0.1	36.73	1164.4	673.0	42.8	24.7	734.6
0.3	36.40	978.7	549.3	35.6	19.9	728.0
0.5	36.07	917.6	493.1	33.1	17.8	721.4

Lattice energy determination

The lattice energy of ionic solid is a measure of strength of the bonds in that compound. We have employed here Kudriavtsev's approach [56] according to that the velocity of sound waves (V) in liquids as well as in solids, assuming the addictivity of the internal energy, is a function of temperature (T (K)), molecular weight ((M (kg)) and potential energy (U_0 (eV)) of the substance, given by :

$$V^2 = -\frac{nm\gamma}{U_0} + \frac{\gamma RT}{M}$$

Where n and m are constants defining potential energy function and γ is the ratio of specific heats (C_p/C_v).

In the above equation, (i) for ionic solids, U_0 can be replaced by lattice energy of the solid, U_L, (ii) the contribution of the term (γRT/M) is negligible as compared to first term (iii) for majority of the ionic solid γ is nearly 1 (iv) the value of n=3 found suitable for many spinel ferrite, crystals with garnet structure and various ionic solids [57-59].

Based on the above considerations equation for lattice energy (U_L) in its simplified form is given by:

$U_L = -3.108(M.V_{m0}^2).10^{-5}$

where 'V' is replaced by zero porosity corrected mean sound velocity (V_{m0}) of the elastic wave (Table 5a.6.2 (c)).The lattice energy values of all the compositions is summarized in Table 5a.3.4. It is found that lattice energy, decreases with increasing Fe^{3+}-content(x) in the system, suggests weakening of strength of bonding, results in reduction of magnitude of elastic moduli; as observed.

The lattice energy is dependent on ionic charge and the ionic radius, as the charge of the ions increases the magnitude of the lattice energy increases (becomes more negative) and as the ionic radius decreases lattice energy increases. Attempt has been made to calculate the lattice energy (U_L) for all the compositions using Kapustinskii equation [60] for lattice energy determination for ionic crystals:

$$U_L = -1202.5\frac{\vartheta|Z^+|.|Z^-|}{r^+ + r^-}\left(1-\frac{0.345}{r^+ + r^-}\right)$$

In this formula ϑ is the number of ions in the empirical formula (i.e 20 in the present case), Z^- and Z^+ are the anionic and cationic charge, respectively and r^- and r^+ are the radius of the anion and cation respectively. It is important to remember that the units of the radii in this equation are in angstrom and the lattice energy is given by kJ/mole. For the calculation of Z^+ and r^+ we have taken weighted average of ionic charge and ionic radii while for Z^- and r-,ionic charge and ionic radius of the oxygen anion are taken to be (-2) and 1.32 Å respectively(Table 5a.6.4). The calculated value of Z^+, r^+ and U_L are given in Table 5a.6.4. For the sake of comparison lattice energy value for the related single crystalline compounds, yttrium orthoferrite ($YFeO_3$) and yttrium excess YIG ($Y_4Fe_4O_{12}$) based on weighted average of charge and radii

has been included in the Table 5a.6.4. It is found that there is fairly good agreement between the calculated values and those determined from Atomistic computer simulations [61], validates the present approach. The lattice energy value for parent composition (x=0.0) is consistent with lattice energy value of $Y_4Fe_4O_{12}$ composition. It is observed that in the present system lattice energy value increases with increasing Fe^{3+}-substitution.

The observed increase in lattice energy value with Fe^{3+}-substitution as well as magnitude of lattice energy value for substituted garnet compositions (x=0.1, 0.3 and 0.5) contradict with the trend observed and magnitude determined from Kudriavtsov's approach.

Table 5a.6.4 Lattice energy (U_L) for Y-Fe- O system

Fe^{3+}-content (x)	d(μm)	r^+ (Å)	r^- (Å)	Z^+	Z^-	U_L (Kudriavtsev et al) [33] (eV)	U_L (Kapustinskii et al) [39] (eV)	U_L(eV) Compound	present Work	
0.0	5.2	0.7349	1.32	3.0	2.0	574.42	605.28	$YFeO_3$	-149.82	-142.5 Ref.[61]
0.1	8.0	0.7317	1.32	3.0	2.0	394.16	606.10			
0.3	14.0	0.7254	1.32	3.0	2.0	230.10	607.60	$Y_4Fe_4O_{12}$	-599.27	-567.6 Ref.[41]
0.5	15.5	0.7191	1.32	3.0	2.0	205.57	609.10			

This leads to conclude that, for polycrystalline materials lattice energy is not only the function of ionic charge and radii as in the case of crystalline materials. The lower value of U_L for polycrystalline material can be explained as follows.

Polycrystalline materials are composed of a collection of many small crystals or grains. Adjacent grains having different crystallographic orientation are separated by grain boundary. Within the boundary region, which is probably just several atomic distances wide, there is some atomic mismatch in a transition from the crystalline orientation of one grain to that of an adjacent one. Various degrees of crystallographic misalignment between

adjacent grains are possible. The atoms are bonded less regularly along a grain boundary as bond angles are longer and consequently there is grain boundary energy. The magnitude of this energy is a function of the degree of mis-orientation, being larger for high angle boundaries [62]. These grain boundaries prevent long distance interactions as a result strength or lattice energy of polycrystalline material is smaller than its single crystalline counterpart. In the present case, grain growth due to Fe^{3+}-substitution further restrict these interactions and may have increase degree of mis-orientation at the grain boundary, these further reduces the lattice energy value for compositions with higher Fe^{3+}-concentration.

Single crystal approximation!

Single crystal of yttrium iron garnet (YIG) is widely used for magneto optical applications, in which magnetically saturated YIG rods rotate the polarization plane of light, known as the Faraday effect, which is used in optical isolators. Similarly, for microwave applications, YIG spheres with high Q-resonance over a broad frequency range makes its use attractive in a variety of products including magnetic resonance filters, tuned oscillators and tuned band reject and band pass filters.

The synthesis of various types of single crystalline material for such applications is not easy as well as it requires some expertise and becomes costly too. The zero porosity corrected values of elastic constants for polycrystalline yttrium iron garnet are comparable with single crystalline values. For example, for single crystal YIG, Young's modulus and Poisson's ratio is 200 GPa and 0.29 respectively [63] while it is 199-205.1 GPa and 0.29-0.30 respectively for polycrystalline YIG (Tables 5a.6.2 (a)-(c)).This has

prompted us to determine certain parameters important from application point of view, like anisotropy factor, magnetostriction constants, stiffness and compliance constants for single crystal material using various parameters of its polycrystalline counterpart.

The cubic crystal possesses symmetry elements and so the number of independent elastic constants is reduced to three only. The stiffness constants, C_{11} and C_{44} of single crystalline materials are equivalent to longitudinal modulus (L_0) and rigidity modulus (G_0) of the polycrystalline materials respectively [64]. These values of C_{11} and C_{44} are further used to calculate C_{12} using the formula: $C_{11} - 2\ C_{44}=C_{12}$. The elastic stiffness constants (C_{11}, C_{12} and C_{44}) are further used to calculate elastic compliances constants (S_{11}, S_{12} and S_{44}) using following relationships [64]:

$$S_{11} = \frac{C_{11} + C_{12}}{(C_{11} - C_{12})(C_{11} + 2C_{12})}$$

$$S_{12} = -\frac{C_{12}}{(C_{11} - C_{12})(C_{11} + 2C_{12})}$$

$$S_{44} = \frac{1}{C_{44}}$$

The term S_{11} measures the amount of tensile strain in x-direction produced by an x-axis tensile stress of unit magnitude and term S_{12} measures the amount of Y-axis (or Z-axis) strain which accompanies the x-axis tensile stress. The opposite sign of S_{12} clearly indicates the fact that a tensile strain is always accompanied by a compressive strain of opposite kind in all directions at right angles to the direction of the applied tensile stress. Since there is no distinction between X, Y and Z-axis in actual materials, we may also interpret S_{11} as measuring the Y-axis strain produced by a unit Y-axis tensile stress

and S_{12} as measuring the Z-axis (or X-axis) strain. With this understanding it is now clear that S_{11}^{-1} is equivalent to Young's modulus, $(-S_{12}/S_{11})$ equivalent to Poisson's ratio and S_{44}^{-1} equivalent to shear modulus. The calculated values of C_{11}, C_{12} and C_{44} for all the compositions are given in Table 5a.6.5. The values of S_{11}, S_{12} and S_{44} for parent composition are in fairly good agreement to those reported for single crystal YIG [32].The linear magnetostriction due to magnetic dipole- dipole interactions in cubic crystals is given by

$$\lambda_{100}=2U/ (C_{11}-C_{12}) \quad \text{and}$$

$$\lambda_{111}= -2U/3C_{44}$$

where λ_{100} and λ_{111} are the magnetostriction constants along the [100] and [111] directions and U is a quantity proportional to the square of the magnetization (Ms)(Table 5a.6.5). The calculated values of λ_{100} and λ_{111} for all the compositions are presented in Table 5a.6.5.It is seen that λ_{100} and λ_{111} decreases with increasing Fe^{3+}-substitution.The values of λ_{100} and λ_{111} for x=0.0 ($Y_3Fe_5O_{12}$) composition are in good agreement with the reported values for single crystal YIG. Finally, we have calculated the value of magnetostriction constant for polycrystalline YIG compositions based on the dipole – dipole approximation:

$$\lambda = \frac{1}{5}\left(2\lambda_{100} + 3\lambda_{111}\right)$$

We have seen that for all the compositions, λ is zero or having very small value, when compared with measured value, $(-3.7x10^{-7})$, for pure YIG [32]. Thus, it appears that the magnetic dipole-dipole interaction is not large enough to account for the magnetostriction in YIG.

The applicability of the procedure for lattice energy determination and single crystal approximation requires further investigation.

Table 5a.6.5 Elastic stiffness constants (C_{ij}), elastic compliance constants (S_{ij}), magnetostriction constant (λ) for $Y_{3-x}Fe_{5+x}O_{12}$ system

Fe^{3+}-content (x)	C_{11}	C_{12}	C_{44}	S_{11}	S_{12}	S_{44}	λ_{100}	λ_{111}	U
	(GPa)			10^{-11} (m^2/N)			(10^{-7})		(10^4)
0.0	268.8	109.8	79.5	0.487	1.26	-0.141	5.823	-3.882	4.63
0.1	200.7	68.1	66.3	0.602	1.51	-0.152	5.776	-3.851	3.83
0.3	135.7	51.3	42.2	0.930	1.95	-0.255	5.663	-3.775	2.39
0.5	117.1	50.7	33.2	1.157	1.97	-0.349	4.457	-2.971	1.48

References

1. C. G. Whinfrey, D. W. Eckart and A. Tauber, J. Am. Chem. Soc. 82 (1960) 2695.
2. R.D.Shannon and C.T. Orewitt, Acta Cryst. B. 25 (1969) B.20(1970)
3. Sung Ho lee, Kwang Pyo Chae, Seok Won Hong and Young Bae lee, Solid State Commun. 83 (2) (1992)97.
4. K.J. Standly, Oxide magnetic material, (Clarendo Press, Oxford)1972
5. F.Euler and J.A. Bruce, Acta Cryst. 19 (1965)971.
6. G.A. Novak and G.V. Gibbs, Am. Mineral, 56 (1971)791.
7. G.A.Slack, D.W. Oliver, R.M.Chrenko and S.Roberts, Phys. Rev. 177 (1969)1308.
8. J.P. Hurrell, S.P.S. Porto, I.F.Chang, S.S.Mitra and R.P.Bauman, Phys. Rev. 173 (1968) 851.
9. A.M.Hofmeister and K.R.Campbell, J. Appl. Phys. 72(2)(1992)638
10. T.K.Pathak, J.J.U Buch, U.N.Trivedi, H.H.Joshi and K.B.Modi, J.Nano Sci. Nanotech. 8(8) (2008)4181.
11. S.A.Mazen, Mat. Chem. Phys.62(2000)131
12. P. Tarte and J.Preudhomme, Acta. Crystallogr. 16(1963) 227.
13. Haitao Xu and Hua Yang Mat. Manu. Process. 23(2008)1.
14. T. Shimda, T.Tachibana, T.Nakagawa and T.A. Yamamoto, J.Alloys. Comps. 379 (2004)122.
15. T. Nakagawa Spectrochim. Acta 29 A(1973)1451.
16. K.B. Modi, H.J. Shah, U.N. Trivedi, R.P. Vara, M.C. Chhantbar and H.H.Joshi, Ind. J. Eng. Mater. Sci. 10 (2003) 502.

17. L.Torres, F. Walz, J. Iniguez and H. Kronmuller, Phys. Stat. (a) 15a (1997) 485.

18. B. Antonini, S. Geller, A. Paoletti, P. Paroli and T. Vicciarane, J. Magn. Magn. Matter. 22 (1981)203.

19. K. Shahi, H.B.Lal and S. Chandra, Ind. Pure and appl. Phys. 13 (1975)1.

20. G. V. Subbarao, B. M. Wanklyn and C.N.R. Rao J. Phys. Chem. Solids. 32 (1971) 340.

21. V.R. Yadav and H. B. Lal Jpn. J. Appl. Phys. 18 (12) (1979) 2229.

22. M. Ristic, I. Nowik, S. Popovic and I. Felner, Mater. Lett. 57 (2003) 2584.

23. R. Justin Joseyphus, et al. J. Magn. Magn. Mater. 272–276 (2004) 2257.

24. N. Miura, I. Oguro and S. Chicazumi, J. Phys. Soc. Jpn. 45 (1978) 5.

25. M.Gilleo and S.Geller, Phys. Rev. 110(1958)73

26. G.J.Baldha, R.V. Upadhyay and R.G. Kulkarni J. Mater. Sci. 3(1988)3357

27. Alex Goldman, Modern Ferrite Technology, 2nd edition, Springer, USA (2006) 68.

28. S. R. Murthy, J. Magn. Mater. 222(2000) 121 and references therein

29. R. Baldev, V. Rajendran and P. Palanichamy 2004, Science and Technology of Ultrasonics (New Delhi: Norosa publishing House) p.250.

30. V. Rajendran, N. Palanivelu, B. K. Chaidhuri and K. Goswami, 2002, J. Mater. Sci lett. 21 1699.

31. M de Podesta, 2002, Understanding the properties of matter 2002, 2nd edn.(London: Taylor and Francis) p.182.

32. A. E. Clark and R. E. Strakna, J. Appl. Phys. 32 (1961) 1172.

33. V. R. Yadav and H. B. Lal, Chem. J. Phys. 57 (1979) 1204.

34. M. P. Pandya, K. B. Modi and H. H. Joshi, J. Mater. Sci, 40 (2005) 5223.

35. A. D. P. Rao, B. Ramesh, P.R.M Rao and S. B. Raju, J. Alloys. Comp. 282(1999)268.

36. A. M. Sankpal, S.V. Kakatkar, V. D. Chaudahri, R. S. Patil, S. R. Swant and S. S. Suryavansi, J. Mater. Sci. 9 (1998) 173.

37. S.Yamanka, K.Kurosaki, T. Manekawa, T. Matsuda, S. Kubayashi and M. Uno, J. Nucl. Mater. 344 (2005) 61.

38. Q. Wang, G. A. Saunders, D. P. Almond, M. Cankurtaran and K. C. Goretta, Phy. Rev. B. 52 (1995) 3711.

39. K. Ganesh, R. J. Topare, S.S. Shah and P. V. Reddy, J. Alloys. Comp. 230(1995)23.

40. D. P. H. Hasselmann and R. M. Fulrath J. Am. Ceram. Soc. 47(1964) 52.

41. H. Ledbetter and S. Dutta, J. Am. Ceram. Soc. 79 (1986) 239.

42. R. W. Rice, Treatise on material science and technology ed. R. K. Mac Crane (Academic Press), New York, 11 (1977) p.199.

43. W. A. Wooster, Rep. Prog. Phys. 16(1953) 62.

44. M. B. Solunke, P. U. Sharma, M. P. Pandya, V. K. Lakhani, K. B. Modi, P. V. Reddy and S. S. Shah, Pramana-J. Phys. 65 (2005) 481.

45. M. B. Solunke, P. U. Sharma, V. K. Lakhani, M. P. Pandya, K. B. Modi, P. V. Reddy and S. S. Shah, Ceram. Int. 33(1) (2007) 21.

46. J. J. U. Buch, G. Lalitha, T. K. Pathak, N. H. Vasoya, V. K.Lakhani, P. V. Reddy, Ravi Kumar and K. B. Modi J. Phys. D: Appl. Phys. 41 (2) (2008)025406.

47. K. B. Modi, M. C. Chhantbar and H. H. Joshi, Ceram. Int. 32 (2006)111

48. S. S. Bhatu, V. K. Lakhani, A. R. Tanna, N. H. Vasoya, J. J. U. Buch, P. U. Sharma, U. N. Trivedi, H. H. Joshi and K. B. Modi, Ind. J. Pure. Appl. Phys. 45 (2007) 596.

49. M. B. Solunke, K. B. Modi, V. K. Lakhani, K. B. Zankat, P. U. Sharma, P. V. Reddy and S. S. Shah Ind. J. Pure Appl. Phys. 45 (2007)725.

50. K. B. Modi, U. N. Trivedi, P. U. Sharma, V. K. Lakhani, M. C. Chhantbar and H. H. Joshi, Ind. J. Pure Appl. Phys. 44 (2006) 165.

51. F. Brich, J.Geophys. Res. 66 (1961)2199.

52. G. Simmons, J. Geophys. Res. 69 (1964) 1117.

53. O. L. Anderson, Physical Acoustics vol. 3B ed. W. P. Mason (New York : Academic) (1965) p.43.

54. P. V. Reddy, M. B. Reddy, V. N. Mulay and Y. V. Rmana J. Mater. Sci. Letter 7 (1988)1243.

55. N. Kumar, Y. Purushottam, P. V. Reddy, Z. H. Zaidi and Pran Krishan, J. Magn. Magn. Mater. 92 (1999) 116.

56. B. B. Kudriavtsev, Sov. Phys. Acoust. 2(1956)172.

57. B. Komalamba, K. V. Sivakumar and V. R. K. Murthy Acoust. Letters 19 (1996)163.

58. B. Komalamba, K. V. Sivakumar and V. R. K. Murthy Acta Acoustica 85 (1999) 433.

59. M. Subrahmanyam, E. Rajagopal, N. Manohar Murthy and S. V. Subrahmanyam J. Acoust. Soc. India 14 (1986) 4.

60. A. F. Kapustinskii, Quart. Rev. Chem. Soc. 10 (1956) 283.

61. H. Donnerberg and C. R. A Catlow J. Phys. Condens. Matter. 5 (1993) 2947.

62. W. D. Callister, Material Science and Engineering: An Introduction (2000)(New York: Wiley)p. 166.

63. www. Deltronic Crystal.com

64. S. L. Kakani and C. Hemrajani A Text book of Solid State Physics, Sultan Chand & Sons, New Delhi, (1997) p.146.

5(b) Compositional and Thermal variation of electrical properties of $Y_{3-x}Fe_{5+x}O_{12}$ system

5b.1 Thermoelectric power study on Fe^{3+}-substituted YIG

The Thermoelectric voltage (ΔV) developed across each pellet of the garnet material does not significantly depend upon heating and cooling cycles and repeatable values (within ±10%) are obtained in successive observations. The results of variations in Seebeck coefficient $\alpha=\Delta V/\Delta T$ at different temperatures (T=300-650K) for the samples studied are shown in Figure 5b.1.1, as plots of α against T. No break in these plots is observed and α against T curves are nearly linear over the whole range of temperature.

Before presenting analysis of the data it must be made clear that we adopt the so called standard convention for the sign [1] of α which is opposite to sign used in the usual text books. According to this convention $\alpha=\Delta V/\Delta T$, and has negative sign for positive charge carrier and vice versa. The common feature for all the composition is that α is negative over whole temperature range indicating that the charge carriers are holes.

It is observed from Figure 5b.1.1 that α in the temperature range studied is not very dependent upon temperature. This small temperature dependent indicates that the number of Fe^{4+} centers does not remain constant over the entire temperature range but changes a little with temperature. On the basis of classification suggested by Bashikiriv and Liberman [2] these garnets are non-degenerate semiconductor as Seebeck coefficient 'α' is temperature independent.

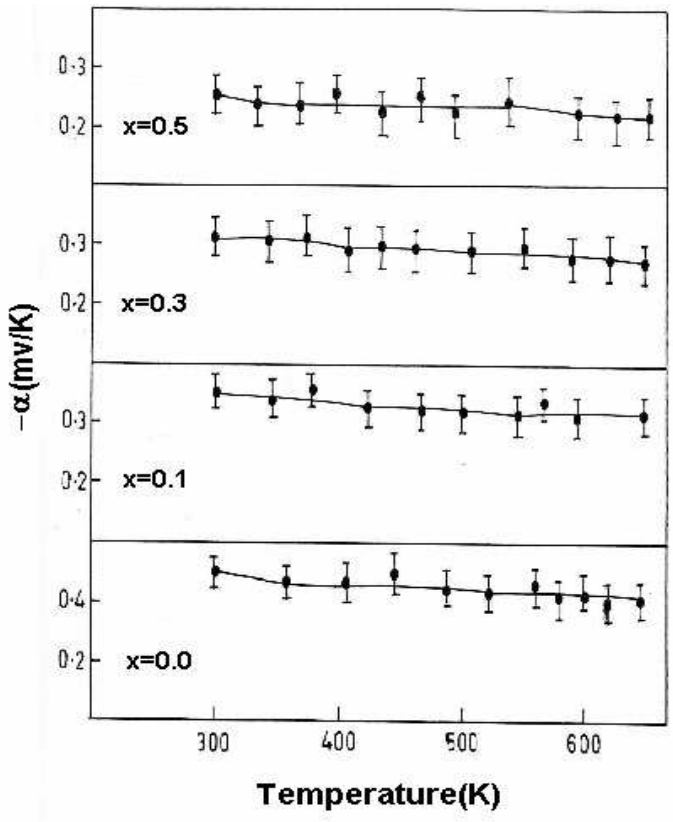

Fig. 5b1.1 Plot of thermoelectric power (α) against temperature (T) for different garnets.

Within experimental accuracy the variation of α with T can be represented by the following equation

$$\alpha = \eta\,(T^{-1}) + H$$

where T is the absolute temperature, η is the slope and H is the intercept of the curve with the α-axis. The experimental values of η and H for different garnets are given in Table 5b.1.1.

Table 5b.1.1 Experimental values of η and H

Fe^{3+}-content (x)	η (V)± 0.02V	H(mv/K)
0.0	0.082	0.40
0.1	0.037	0.31
0.3	0.054	0.27
0.5	0.074	0.22

The first step in the understanding of electrical transport in any solid is to know whether conductivity is ionic , electronic or mixed (partially ionic and electronic).There are several ways of determining this [3]. One of the ways is to carryout dc (ρ_{dc}) and ac (ρ_{ac}) resistivity study as a function of temperature. If ρ_{ac} values are higher than ρ_{dc} than conduction become ionic and if they coincide, the electrical resistivity due to free ions become negligible and it is entirely electronic. The simplest way is to measure ρ_{dc} as a function of time using electrodes which block ionic conduction. In the case of pure ionic conduction, ρ_{dc} increases with time and tends to become infinite after a sufficiently long time; whereas for an electronic conductor it is essentially independent of time. For mixed conduction it increases with time but tends to stabilize at some finite constant value, which is the electronic contribution [4].To check the type of conduction on the basis of above logic, ρ_{dc} for all the compositions was measured at constant temperature (400K) as a function of time using platinum foil electrodes [5,6]. The typical results for x=0.0 and 0.3 are shown in Figure 5b.1.2. It is observed that ρ_{dc} increases with time but becomes almost constant after 30 sec. The ratio of instantaneous, $\rho_{dc(0)}$, to steady state, $\rho_{dc(\infty)}$ electrical resistivity varies from 0.92 to 0.95 for different garnet pellets at different temperatures. This indicates that synthesized garnet samples are essentially electronic conductors and ionic conduction remains less than 9% at all temperatures.

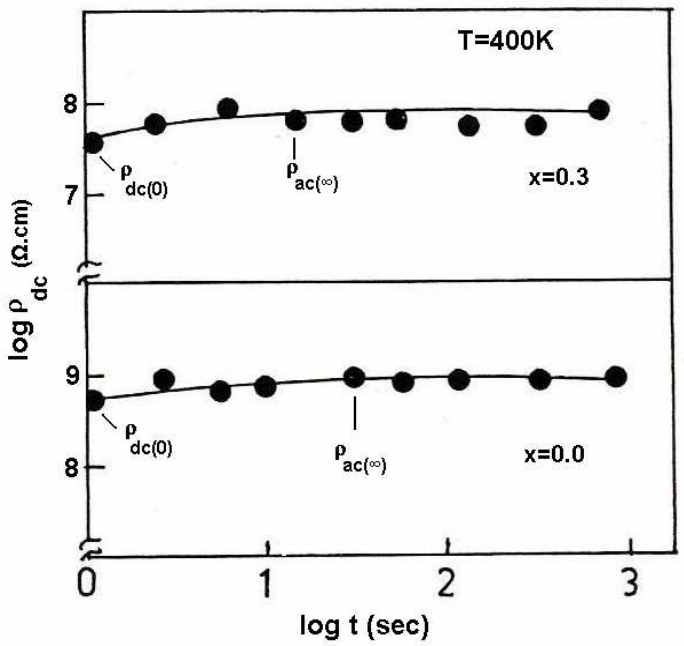

Fig. 5b.1.2 Plots of electrical resistivity (ρ_{dc}) of Y (Fe)-Fe-O pellets as a function of log time at fixed temperature

Now, probable conduction mechanism in garnet system can be explained on the basis of theory developed by Lal et al [4]:

According to that electronic conduction is broadly classified in two types (band or hopping types). It is customary to explain electronic conduction using the energy-band model and we shall first attempt to examine our results using this model.

The energy bands which may be relevant in the electrical conduction of yttrium and rare–earth iron garnets are filled O^{2-}: 2p band, RE^{3+}:4f degenerate level (or partially filled narrow band), partially filled Fe^{3+}:3d band, empty Fe^{2+}: 3d band, empty Fe^{3+}:4s band, empty RE^{2+} 4f degenerate level (or narrow band) and empty RE^{3+}: 5d band. Neither the detailed energy-band calculations are available for any of the garnets not the relevant optical data available for any of the garnets. The only alternative in such a situation is to

sketch a qualitative schematic energy band diagram based on some experimental results for some of the related compounds. For yttrium iron garnet (YIG; x=0.0) where 4f levels are absent, a a qualitative energy-band diagram has been sketched on the basis of various experimental results by Larsen and Metsellar [7].In the case of YIG, the energy difference between different bands has been indicated by the analysis of optical studies. It has been found that the difference between the top of the filled O^{2-}:2p band to the bottom of the Fe^{2+}: 3d band than 3eV. A difference of similar order between the O^{2-}:2p and Fe^{2+}:3d band has also been observed in the case of rare earth orthoferrites [8, 9]. Mizushima et al [10] have found a difference of 3 eV between degenerate Fe^{3+}: $3d^5$ levels and Fe^{2+}: $3d^6$ levels in Fe-doped TiO_2.

The striking feature of energy band diagram [Figure 5b.1.3] is that the partially filled Fe^{3+}: 3d band lies above the top of the uppermost completely filled O^{2-}:2p band. Thus, on simple band theory, these garnets should show high- metallic type conductivity. However, experimentally we have found that compositions studied are insulator (high value of resistivity) at room temperature and do not show metallic conduction (increase in resistivity on increasing temperature) even at high temperature (Figure 5b.2.1).This means that electrons in the Fe^{3+}: 3d bands are localized. This is quite possible due to a correlation effect between electrons. This fact prompts us to conclude that Fe^{3+}: 3d bands in garnet are narrow and do not support band conduction. The case for Fe^{2+}: 3d, RE^{3+}:4f and RE^{2+}:4f bands may be similar.

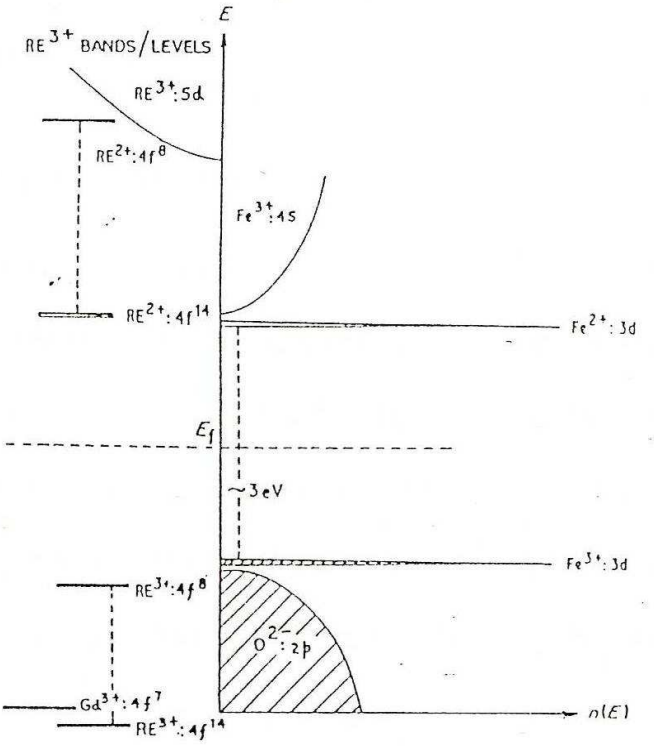

Fig. 5b.1.3 Schematic energy- band scheme for rare earth iron garnets, Crystal field splitting of bands is not considered [4].

Based on energy-band diagram, the intrinsic band conduction in substituted yttrium iron garnet can be suggested to occur by following processes:

(i) Electrons are excited from the O^{2-}: 2p to the Fe^{3+}:4s band creating holes in the former. The conduction in this process may be dominated by electrons in the latter band;

(ii) Electrons are excited from the O^{2-}: 2p to the Fe^{2+}: 3d band creating holes in the former band. The conduction in this process may be dominated by holes in the oxygen band;

(iii) Electrons are excited from the Fe^{3+}: 3d band to the Fe^{3+}: 4s band creating holes in the d-band. The conduction in this process will be dominated by electrons in the Fe^{3+}: 4s band;

(iv) Electrons are excited from a filled O^{2-}:2p band to an empty RE^{2+}: $4f^{n+1}$ level creating holes in the O^{2-}: 2p band. Holes will be the dominant charge carriers in this process;

(v) Besides the above, one can list processes which involve pairs of Fe^{3+}:3d, Fe^{2+}:3d, RE^{3+}:$4f^{n}$ and RE^{2+}: $4f^{n+1}$levels. However, they have been excluded here as these levels (or narrow bands) may not support band conduction. However, a hopping–type mobility, in which electrons will be the dominant charge carrier, may result if the above- mentioned bands are involved.

Thermoelectric power measurements indicate that in all the compositions and over the temperature range studied holes are dominant charge carriers in electrical conduction. This ruled out processes (i), (iii), and (v) suggested above for the electrical conduction. Processes (ii) and (iv), which give holes as the entity of the charge carriers, will need energy of more than 1.5 eV. The maximum activation energy observed in the electrical conduction of these garnets is 0.5 eV. Furthermore, the estimated values of mobility using normal relation for a conventional semiconductor (taking $m_e=m_h$ and $\mu_e=\mu_h$) are of the order of 10^{-10} cm^2 V^{-1} sec^{-1}, which are an order of magnitude less than the mobility one expects in band conduction. Hence it is concluded that the charge carriers taking part in electrical conduction in this solid are extrinsic and are related to impurities or defects. On the above considerations even processes (ii) and (iv) listed above ruled out as being effective in garnets, at least in the temperature range studied.

An alternative and interesting but less familiar way to understand the conduction mechanism, and particularly the charge carriers responsible, is to study the capacitance versus various bias voltage relationship for that composition [11-13]. Figure 5b.1.4 shows the plot of $1/c^2$ versus bias voltage for all the compositions at 323K and 373K. The positive slope of the curve for the present bias voltage range, indicating that conduction is only due to the holes, and electron conduction is negligible. These results are consistent with thermoelectric power measurements.

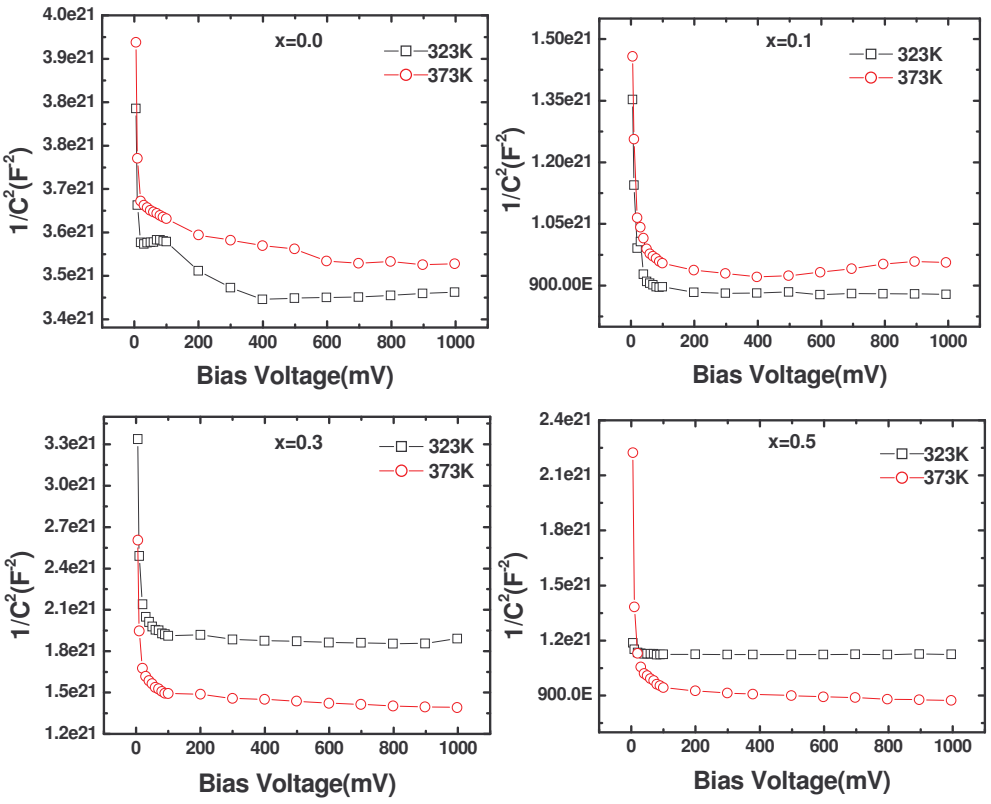

Fig. 5b.1.4 $1/c^2$ versus bias voltage plots for x=0.0, 0.1, 0.3 and 0.5 compositions at 323K and 373K

Electrical conduction in these solids is extrinsic in which holes localized on Fe^{3+} sites (Fe^{4+} centres created by native defects) conduct via a thermally activated hopping mechanism. For a hopping mechanism, the Seebeck

coefficient (α) is independent of temperature and its magnitude primarily depends upon the density of the charge carriers. It is expressed in the form of the Hiekes formula [14]:

$$\alpha = -\frac{k}{e}\left[\frac{S_T}{k} + \ln\frac{1-c}{c}\right]$$

where S_T is the effective entropy of the lattice which is temperature independent and S_T/k is very small and thus neglected, c is given by n/N, where n is the number of carriers in the states and N is the total number available states. Neglecting the term S_T/k from the relation gives:

$$\alpha = -\frac{k}{e}\left[\ln\frac{1-c}{c}\right]$$

Few years back J P Doumero [15] has derived a more general formula for systems containing mixed valency cations $M^{n+}/M^{(n+1)+}$, accordingly:

$$\alpha = -\frac{k}{e}\ln\left(\frac{1-c}{c}\right) = +\frac{k}{e}\ln\left(\frac{1-c_h}{c_h}\right)$$

where c_h, the hole concentration (number of holes per active transport site). c_h = 1-c = p/N (p-number of holes).

Assuming that N is equal to the total number of Fe^{3+} and Fe^{4+} ions on B- sites, and n to the number of Fe^{3+} ions on these sites we obtain:

$$\alpha = -\frac{k}{e}\ln\left(\frac{\left[Fe_B^{4+}\right]}{\left[Fe_B^{3+}\right]}\right) = +\frac{k}{e}\ln\left(\frac{\left[Fe_B^{3+}\right]}{\left[Fe_B^{4+}\right]}\right)$$

where, k is the Boltzmann constant and e is the electronic charge. Above equation contains no adjustable parameter and can be used to test various distribution models. This has been shown to be suitable way for some spinels, such as ferrites [16, 17], magnetite [18] and hausmannite [19] and mangnite

perovskites [20]. The square bracket denotes the ionic concentration per lattice molecule.

Based on the above equation and the thermoelectric power data shown in Table 5b.1.2 the ratio of Fe^{4+} to that of Fe^{3+} ions, $[Fe^{4+}]/[Fe^{3+}]$, was calculated and is listed in Table 5b.1.2. The ratio $[Fe^{4+}]/ [Fe^{3+}]$, increased from 1.3×10^{-3} to 12.5×10^{-3} with increasing Fe^{3+}-concentration (x). Although the ratio $[Fe^{4+}]/ [Fe^{3+}]$ can be obtained from the thermoelectric power measurements, the estimation of Fe^{4+} ion concentration from the measurement is not straightforward. The absolute concentration is typically obtained by wet-chemical analysis Iodometry titration, thermo gravitymetric analysis (TGA) etc. In our present study however, we have estimated the absolute concentration of Fe^{4+} ion by following the procedure suggested by Byeon et al [21]. The calculated concentration of Fe^{4+} increases form 0.07 wt % for x = 0.0 to 0.70 wt % for x = 0.5 composition at 400K.

Table 5b.1.2 Seebeck coefficient (α), ratio of Fe^{4+} to Fe^{3+}, absolute value of Fe^{4+}, charge carrier concentration(n_c) and mobility of charge carriers for Y (Fe)- Fe- O system

Fe^{3+}-content(x)	α (mv/K) (400K)	Fe^{4+}/Fe^{3+} $*10^{-2}$	Fe^{4+}(wt%)	n_c(ions/cm^3)$*10^{19}$ (400 K)	μ_d(10^{-10} cm^2/v.sec) (400K)
0.0	0.570	0.13	0.073	6.54	5.13
0.1	0.393	1.05	0.59	93.2	0.949
0.3	0.387	1.13	0.63	99.0	1.62
0.5	0.376	1.25	0.70	109.4	0.827

Charge Carrier concentration, mobility and Fermi energy determination:

The Hiekes formula used may be re-written as :

$$n_e = \frac{N}{V}\left[\frac{1}{1+\exp\left(\frac{\alpha}{k/e}\right)}\right]$$

The value of charge carrier concentration (n_c) per unit volume have been calculated for all the compositions at 300 K and 400K by using the values of the Seebeck coefficient (α). Here, V is the volume of the sample under study and N is the density of states. In the case of low mobility semiconductors like spinel ferrites and garnets having exceedingly narrow bands or localized levels, the value of 'N' can be taken as $10^{22}/m^3$ [22, 23]. Here it should be noted that for the determination of n_c, only magnitude of α should be taken into consideration, because positive or negative sign just indicates whether charge carriers are holes or electrons, it has nothing to do with its value. It is found that n_c increases with increasing Fe^{3+}- concentration(x) (Table 5b.1.2)

The mobility of the charge carriers was calculated from the experimental values of the electrical resistivity (ρ_{dc}) and charge carrier concentration (n_c) at mid temperature 400 K, by the formula;

$$\mu_d = \frac{1}{\rho_{dc} n_c e}$$

where e is the charge of carrier. The calculated values are listed in Table 5b.1.2.The magnitude of mobility is much smaller than those suggested for electrons (10^{-4} cm^2/v.sec) and for holes (10^{-8} cm^2/v.sec) [24]. The estimated values of mobilities are of the order of 10^{-10} cm^2/v.sec which is also very small in comparison to mobilities one expects in band conduction (1 - 100 cm^2/v.sec) [5]. Therefore intrinsic conduction for these solids is completely

ruled out in the studied temperature range. The order of mobility is quite appropriate for hopping type conductivity.

In the region where conduction is due to one kind of charge carriers (electrons and holes; not both), the relation between the Seebeck coefficient (α) and Fermi energy (E_F) is given by [25,26]:

$$E_F = e\,\alpha T - Akt$$

where A is the term connected with the kinetic energy of charge of carrier, e, k and T are charge of carrier, Boltzmann constant (8.6 *10^{-5} eV) and absolute temperature, respectively. The calculated values of E_F as a function of temperature for two values of A (A=0 and 2) are shown in Figure 5b.1.5.

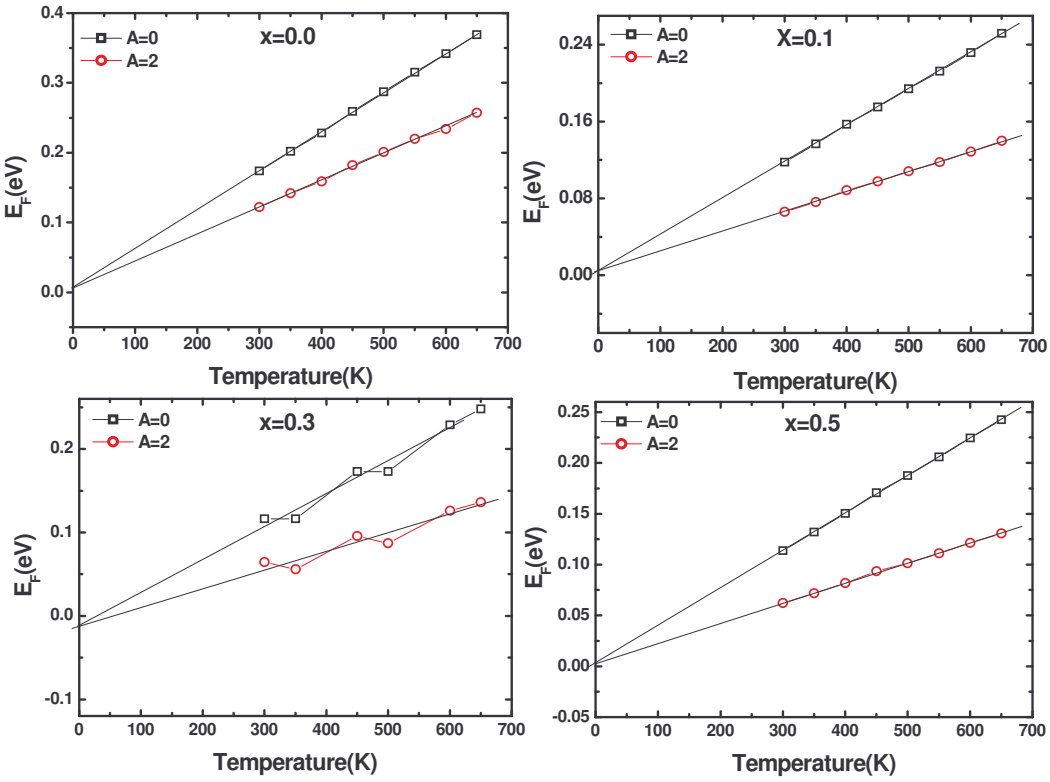

Fig. 5b.1.5 Temperature dependence of Fermi energy (E_F) for x=0.0, 0.1, 0.3 and 0.5 compositions of Y (Fe)-Fe-O system

The extrapolated value of E_F at T=0 K yields the value of E_F (0).Comparing the activation energies of the ferrimagnetic region (E_f) with E_F(0),it is seen that E_f»E_F(0). The difference between the two values can be attributed to the activation energy associated with hopping of charge carriers. Thus activation energy consists of two components; one that is associated with generation of charge carriers (holes/electrons) and the other associated with the hopping of the carriers between crystallographically equivalent sites.

5b.2 Thermal variation of dc resistivity study on Fe^{3+}-substituted YIG

The compositional dependence of dc resistivity (ρ_{dc}) at 400K is presented in Table 5b.2.1. It was observed from Table 5a.1.3, that the highest observed value of the bulk density (ρ) remains less than the x-ray density (ρ_x) of the material. This indicates that even highly pressed and sintered pellets contain pores. Therefore, a correction for pore fraction has to be applied to obtain the crystalline value of electrical resistivity. This has been done using the relation [27]:

$$\rho_{dc} = \rho_p [1 + f(1 + f^{2/3})^{-1}]^{-1}$$

where ρ_{dc} is the corrected value, ρ_p is measured value of dc resistivity and f is pore fraction (Table 5a.1.3). Above equation seems to hold good for f<0.4. The resistivity (ρ_{dc}) decreases with increase in Fe^{3+}-content(x). This happens because the replacement of non-magnetic Y^{3+} ions by magnetic Fe^{3+} ions in the system enhances the conduction through different lattice sites. The incorporation of Fe^{3+}- ions which do participate in the conduction process, prompts the degree of $Fe^{3+} + e^{+} \rightarrow Fe^{4+}$ conduction that occurs. Thus, the efficient method of enhancing the conduction process is the replacement of less effective ion (Y^{3+}) by the effective ones (Fe^{3+}).

Our results on thermoelectric power measurements suggest the formation of impurity centres Fe^{4+} in the system, though they remain nearly independent of temperature but one can expect increase in Fe^{4+}-centers with increasing Fe^{3+}-concentration(x). Thus observed reduction in dc resistivity value with increasing x may be attributed to more and more formation of Fe^{4+}centers.

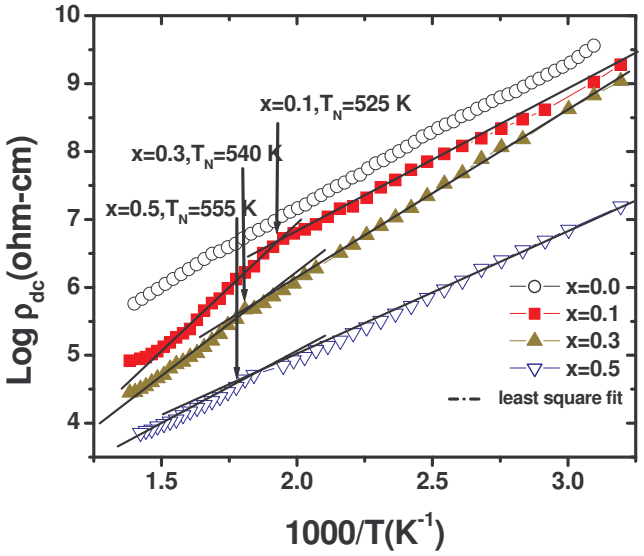

Fig. 5b.2.1 Electrical resistivity (ρ_{dc}) versus reciprocal of temperature for x=0.0-0.5 compositions of Y (Fe)-Fe-O system

The dc electrical resistivity of pellets of each sample made at pressure ≈2*10^7 kg/m^2 and sintered at 1500 ℃ for 24 hours have been measured as a function of temperature (300-700K). The resistivity values for a particular garnet do not differ much from sample to sample. Furthermore for each pellet no significant difference has been observed in resistivity values during the heating and cooling cycles. The ρ_{dc} values for a series of garnets lie between 10^7-10^{10} Ω.cm near room temperature, obviously they will be good insulators at room temperature. The ρ_{dc} variation with temperature for compositions x=0.0, 0.1, 0.3 and 0.5 are presented in Figure 5b.2.1 as plots of $\log_{10}\rho_{dc}$ against 10^3/T. As shown in figure, the curve consists of two straight line portions (except for x=0.0); hence there are two activation energies for the two different regions. A change in the slope may be due to the Neel temperature [28] or to the change in the conduction mechanism [29]. This anomaly strongly supports the influence of magnetic ordering upon the conduction

process. The Neel temperatures (T_N) deduced for x=0.1, 0.3 and 0.5 compositions (Table 5b.2.1) are in good agreement to those found experimentally from ac susceptibility measurements and calculated theoretically based on modified molecular field theory.

The temperature dependence of resistivity is given by the Arrhenious equation

$$\rho = \rho_0 \exp(\Delta E/kT)$$

$$\Delta E = 8.6 \times 10^{-5} \times 2.303 \times 10^{3} \times \text{slope}$$

$$\Delta E = 0.1981 \times \text{slope}$$

where k is Boltzmann constant (8.6×10^{-5} eV), ΔE is the activation energy and T is the absolute temperature.

Table 5b.2.1 Dc resistivity (ρ_{dc}), Neel temperature (T_N) and activation energy values for Y (Fe)-Fe-O system

Fe^{3+}- content(x)	ρ_{dc} (Ω. cm) (400 K)	T_N(K) (Resistivity) ± 2K	E_f (eV)	E_p (eV)
0.0	$1.86*10^8$	-	0.43	-
0.1	$7.1*10^7$	525	0.40	0.63
0.3	$3.9*10^7$	540	0.39	0.58
0.5	$6.9*10^5$	555	0.38	0.44

The activation energies for conduction are computed from log ρ_{dc} versus $10^3/T$ plots and are presented in Table 5b.2.1. The activation energy increases in changing from ferrimagnetic (E_f) ($T<T_N$) to paramagnetic (E_p) ($T>T_N$) region. According to the theory of magnetic semiconductors, one expects such a reduction on activation energy as the system undergoes the transition form paramagnetic to ferrimagnetic state. This is due to the fact that the ferrimagnetic state is an ordered state while the paramagnetic state is

disordered, thus charge carriers required more energy for the conduction. The high value of the activation energy in the paramagnetic state as compared to ferrimagnetic state is due to the volume expansion of the samples during the magnetic transition [30, 31]. The activation energies in the ferrimagnetic region are much higher than the ionization energies (E_i=0.1 eV) of donor or accepters and hence the possibility of band type conduction is ruled out. These values are also higher than the electron transition energy of Fe^{2+} and Fe^{3+} (Ee=0.2 eV) and smaller than energy needed for holes as the entity of charge carriers (~1.5 eV) but comparable with the small polaron hopping energy (~0.5eV).

The activation energy calculated from α against T curve is of the order of 0.1 eV, against activation energy of the order of 0.3 - 0.4 eV determined from $\log_{10} \rho_{dc}$ versus 10^3/T plots, suggests that the mobility of charge carriers is thermally activated. Near constancy of α with T indicates that the number of charge carriers is almost constant. Thus conduction can be attributed to localized charged impurities: p-type conduction with thermally activated hopping can result owing to the presence of Fe^{4+} centers. These centres may result from native defects. This is not strange as conduction in orthoferrites, orhotchromites and orthomagnetites is believed to occur by formation of impurity centers Fe^{4+}, Cr^{4+} and Mn^{4+} due to native defects [8,32]. These may be formed from divalent metal ions (M^{2+} ions) present at Fe^{3+} sites. The presence of M^{2+} ions cannot be ruled out in this solid [5].

Based on model [33,34] the electrical resistivity (ρ), for the present system is given by:

$$\sigma_{dc} = \frac{1}{\rho_{dc}} = const * [Fe^{3+}][Fe^{4+}] \exp \frac{\left(-\frac{E}{kT}\right)}{T}$$

where E is the activation energy ,k the Boltzmann constant and T the absolute temperature. As shown in equation, not the total Fe^{4+}-concentration but the product of Fe^{3+} and Fe^{4+} ion concentration is of importance for electrical conductivity. Our aim is to correlate resistivity data with the $[Fe^{3+}][Fe^{4+}]$ion concentration. Here, it is evident that the variation in the value of $[Fe^{3+}][Fe^{4+}]$ is about one order of magnitude for the compositional range of x=0.0-0.5. This result means that the variation in electrical resistivity cannot exceed by one order of magnitude, if the variation originates from the change in Fe^{4+} concentration. However, at 400K resistivity data for x=0.0-0.5 showed a variation close to three orders of magnitude (Table 5b.2.1). Thus it is clear that the $[Fe^{3+}][Fe^{4+}]$ ion concentration is not the only factor that governs conduction in garnets. Other factor such as oxygen content, grain, grain boundary resistivity, pores must also be taken into the consideration.

The observed decrease in activation energy with increasing Fe^{3+}-substitution (x), can be explained on the basis of changes in ionic distances in the ferrite crystal structure. The decrease in the value of 'a' manifests itself as decrease in the inter-ionic distances (Table 5a.1.2) and consequently in decrease in barrier height encountered by the hopping charge carriers. The activation energy is, therefore, expected to decrease with increasing Fe^{3+}-content(x).

The activation energy is also influenced by the grain size. Bigger grain size implies increased grain-to-grain contact area for the charge carrier to flow, and therefore, a lower barrier height. Since in present system grain size

is found to increase with Fe^{3+}-concentration (x) (Fig. 5a.6.1), the activation energy is expected to decrease. This explains the decrease in activation energy on Fe^{3+}-substitution.

References

1. S.M. Grivin, J.Solid State Chem. 25 (1978)65
2. S.S. Bashikiriv, A.B. Liberman and V.V. Parfenov, Inorg. Mater. 15 (1979)404.
3. L.Heyne, “Electrochemistry of mixed ion electronic conductors in solid electrolyte” edited by S.Geller (Springer- Verlag, N.Y. 1977) p. 169.
4. H.B. Lal, B. K. Verma and V.R. Yadav, J.Mater. Sci 17 (1982)3317.
5. V.R. Yadav and H.B. Lal, Canad. J. Phys. 57(1979)1204.
6. V.R. Yadav, Ph.D. Thesis, Gorakhpur University, India (1980).
7. P.K. Larsen and R. Metsellar, J. Solid State Chem. 12 (1975) 253.
8. G. V. Subbarao, B.M. Wanklyn and C.N.R Rao, J. Phys. Chem. Solids. 32 (1971)340.
9. J.B. Goodenough , J. Appl. Phys. (USA) (1966) 1415.
10. K. Mizushima, M. Tanaka, A. Asai and J. B. Goodenough, J. Phys. Chem.. solid. 40 (1979)1129.
11. J.G.Na, M.C.Kim, T.D.Lee and S.J.Park IEEE Trans. Magn. 29 (1993) 3520.
12. N.Ponpandian and A. Narayansamy, J.Appl. Phys. 92 (2002) 2770.
13. N.Ponpandian and A.Narayansamy, J.Phys. Condens. Matter 14 (2002) 3221.
14. R.R. Heikes and R.W. Ure, Thermoelectricity (New York: Wiley Interscience) 45(1961).
15. J.P. Doumera, J. Solid State chem. 109 (1994) 419.
16. B. Gillot, Phys. Status, Solidi 69 (1982)719.

17. J. Topfer, A. Feltz, P. Dorder and J.P. Doumero, Mater. Res. Bull. 29 (1994)225.

18. C.C. Wu and T.O. Mason, J.Am. Ceram. Soc. 64 (1981) 520.

19. S.E. Dorris and T.O. Mason, J.Am. Ceram. Soc. 71(1988)379.

20. J.J.U. Buch, T.K. Pathak, V.K. Lakhani, N.H. vasoya and K.B. Modi, J.Phys. D: Appl. Phys. 40 (2007) 5307.

21. S.C. Byeon, K.S. Hang, J.G. Park and W. N. Kang, J. Appl. Phys. 81(1997)7835.

22. A.A. Samokhavalov and A.G. Rustamov Soviet Phys. –solid state 6 (1953)749.

23. F.J. Morin, Phys. Rev. 93 (1953) 1195.

24. M.A. Ahmed, M.K.El. Nimr, A. Tawfik and A.M.El. Hasab, Phys. Stat. Sol. (a) 123 (1991)501.

25. A.J. Bosman and C. Crevecoeur, J.Phys. Chem. Solids. 30 (1969)1151.

26. Idem, Phys. Rev. 144 (1966) 763.

27. H.W. Russel, J. Am. Ceram. Soc.18 (1935).

28. A.P.Kumar, Bull. Acad. Sci. USSR Ser. Phys. 18 (1954)122.

29. K.R.Krishna Murthy, Ph.D. Thesis, IIT Madras, India, 1975.

30. J.B.Goodenough, Mater. Res. Bull. 8(1973)423.

31. M.W.Zemansky, 'Heat and thermodynamics' (Mc Graw Hill, New York, 1968) p 460.

32. A.K. Tripathi, Ph.D thesis, Gorakhpur Uni. Gorakhpur, India (1981).

33. M.I. Klinger and A.A. Samokhvalov, Phys. Status Solidi (b) 79(1977) 9.

34. H.L. Tuller and A.S. Nowick, J. Phys. Chem. Solids. 38 (1977) 859.

5(c) Temperature and frequency dependent dielectric properties of $Y_{3-x}Fe_{5+x}O_{12}$ system

5c.1 Variation of AC resistivity (log ρ_{ac}) with frequency

Figure 5c.1.1 shows the variation of ac resistivity (log ρ_{ac}) with frequency measured at different temperatures.

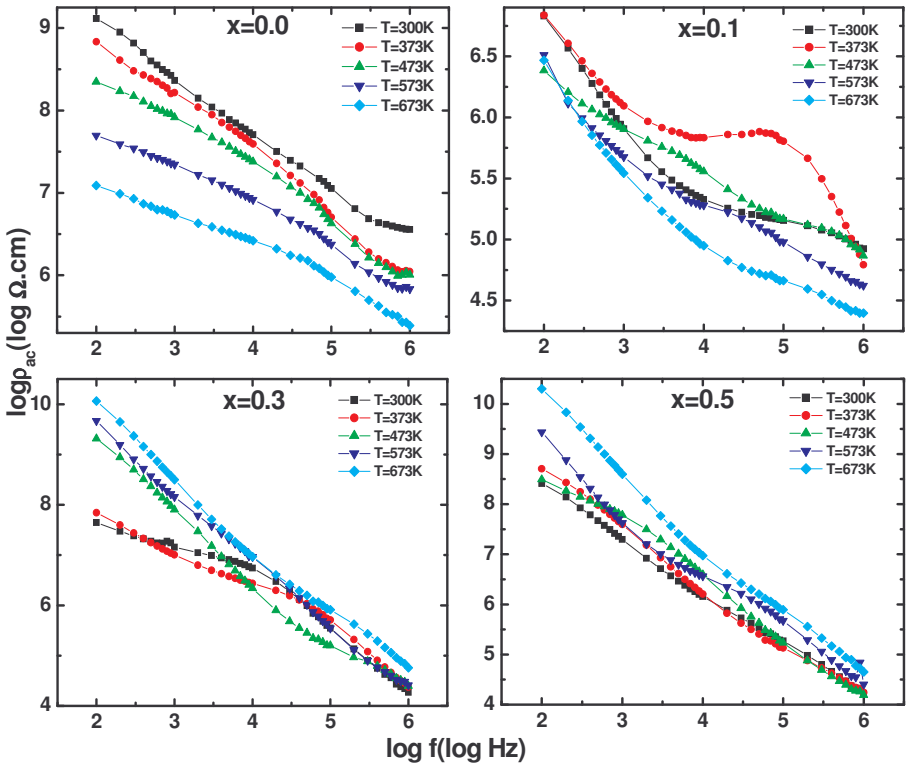

Fig. 5c.1.1 Frequency dependent ac resistivity behaviour of x= 0.0, 0.1, 0.3 and 0.5 compositions at different temperatures

All the samples show decrease in ρ_{ac} with increase in frequency from 100Hz to 1 MHz, which is the normal behaviour of ferrites. The conduction mechanism in the ferrites can be explained on the basis of hopping of charge carriers between Fe^{3+}-Fe^{4+} ions on respective sites. The increase in frequency of the applied field enhances the hopping of charge carriers resulting in an

increase in the conduction process thereby decreasing the resistivity. It has been observed that for x=0.0 and 0.1 compositions the variation of ρ_{ac} is sensitively dependent on the frequency and temperature. This indicates that grain boundary effects are not sufficiently minimized for highly pressed pellets even at high temperature. It is found that for x=0.3 and x=0.5 compositions, the ρ_{ac} is frequency dependent but having less effect of temperature. This suggests that for these compositions grain boundary contributions are negligible at least at high temperature.

Variation of AC resistivity (log ρ_{ac}) with temperature

Generally, the electrically resistivity of ferrites decreases with increase of the temperature. This type of conventional behaviour is observed for the compositions with x=0.0 and 0.1.

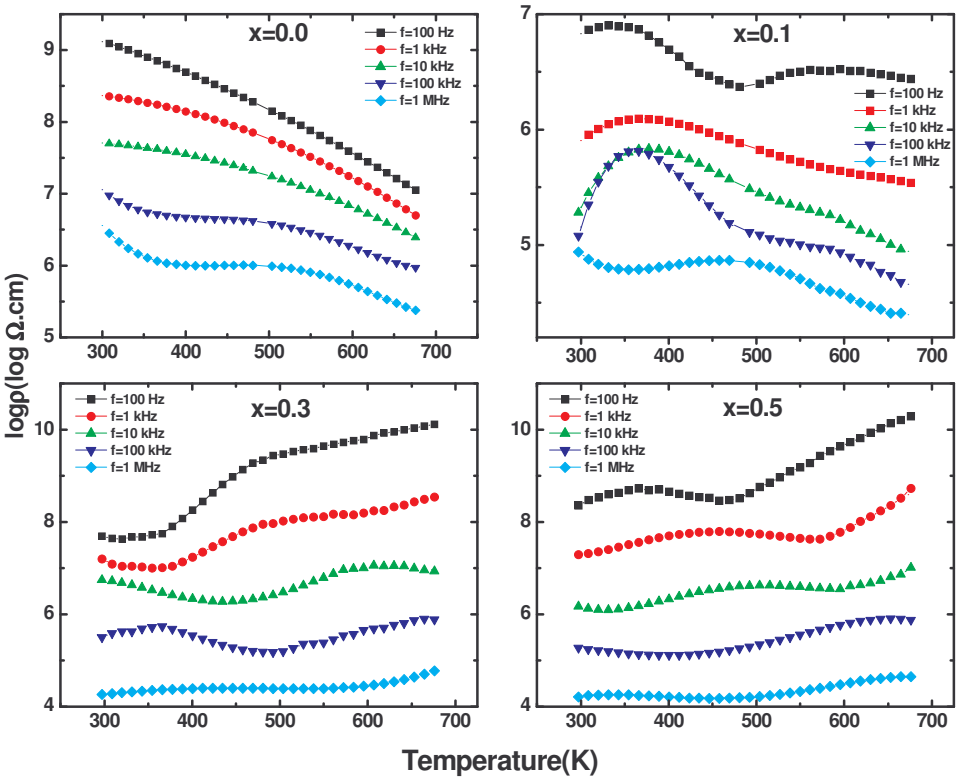

Fig. 5c.1.2 Temperature dependent ac resistivity behaviour of x=0.0, 0.1, 0.3 and 0.5 compositions at different frequencies

It is important to note the differences in $\log_{10}\rho_{ac}$ versus T (K) curves, with increasing Fe^{3+}- content(x). For the compositions with x=0.3 and 0.5, the resistivity increases with increasing temperature. The anomalous electrical behaviour of dc resistivity as a function of temperature for Sn^{4+} and Zn^{2+} substituted $NiFe_2O_4$ has been explained on the basis of electron hopping and current, due to electrons in the conduction band [1]. The metal-like unusual characteristic observed in the vanadium spinels, LiV_2O_4, has been explained in terms of the distance between two neighbouring B-site vanadium ions [2]. Along with the same lines, it may be assumed that the sufficient ($x \geq 0.3$) replacement of larger Y^{3+}(0.893 Å) ions by smaller Fe^{3+}(0.64 Å) ions in the $Y_{3-x}Fe_{5+x}O_{12}$ system, decreases the Fe – Fe separation distance below a certain critical value where, besides hopping of charge carriers, a nearly band like conductivity may occur. This is characterized by metallic conductivity in the temperature range studied.

5c.2 Compositional, Temperature and frequency dependent dielectric behaviour of Y (Fe)-Fe-O system

From the compositional variation of the dielectric constant (ε'), it is observed that the ε' increases rapidly for x=0.0 to 0.1 composition and then suddenly drops for x=0.3 composition while for x=0.5 composition it shows further small reduction in the magnitude at different frequencies and temperatures.

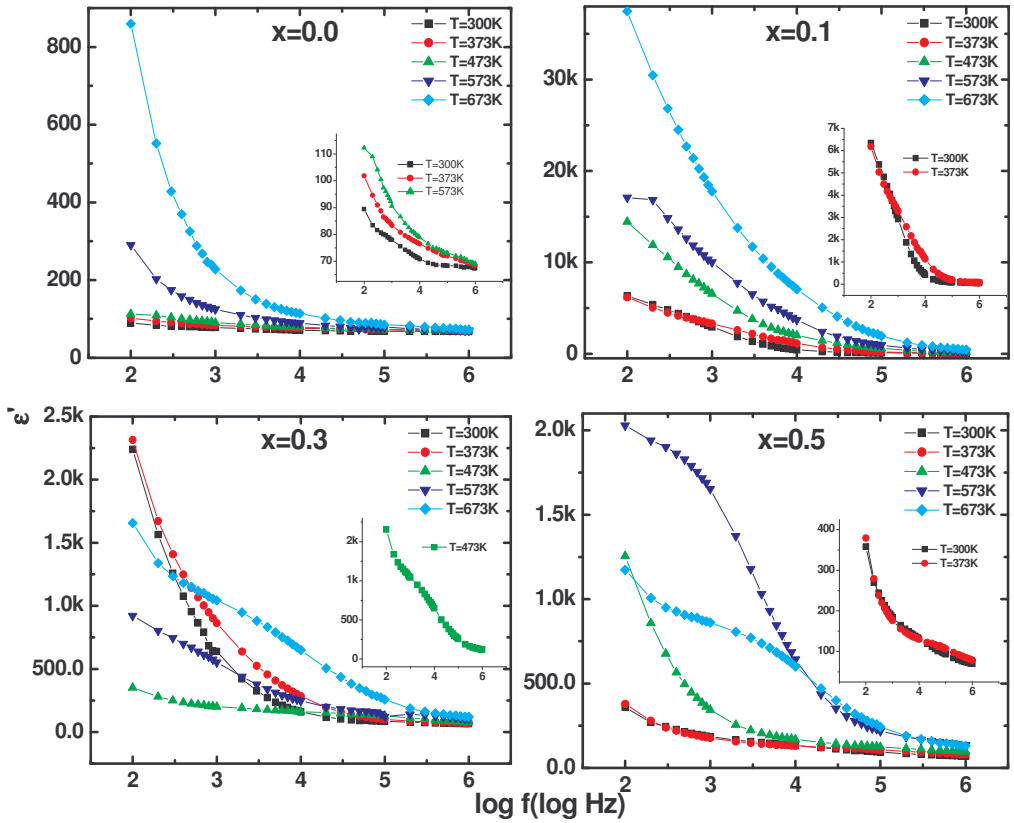

Fig 5c.2.1 Variation of dielectric constant (ε') with frequency at different temperatures for x=0.0, 0.1, 0.3 and 0.5 compositions.

It follows that addition of Fe^{3+} form Fe^{4+} centers, thereby decreasing the resistance of the grain, by thermally activated hopping of holes between Fe^{3+} and Fe^{4+} in the system. This decreases the probability of charge carriers reaching the grain boundary. As a result, the polarization and hence the

dielectric constant increases. The sudden drop in value for higher Fe^{3+}-concentration(x=0.3 and 0.5) is rather unexpected. It seems that for these compositions holes get localized on Fe^{3+}-sites. This decreases the probability of charge carriers reaching the grain boundary and as a result the polarization and hence the dielectric constant decreases.

The frequency (f) dependence plots of the real (ε') and imaginary (ε'') parts of the complex dielectric permittivity (ε*) and the dielectric loss tangent ($\tan\delta$) for different compositions of Y(Fe)-Fe-O system at several temperatures are plotted in Figures 5c.2.1-5c.2.3.

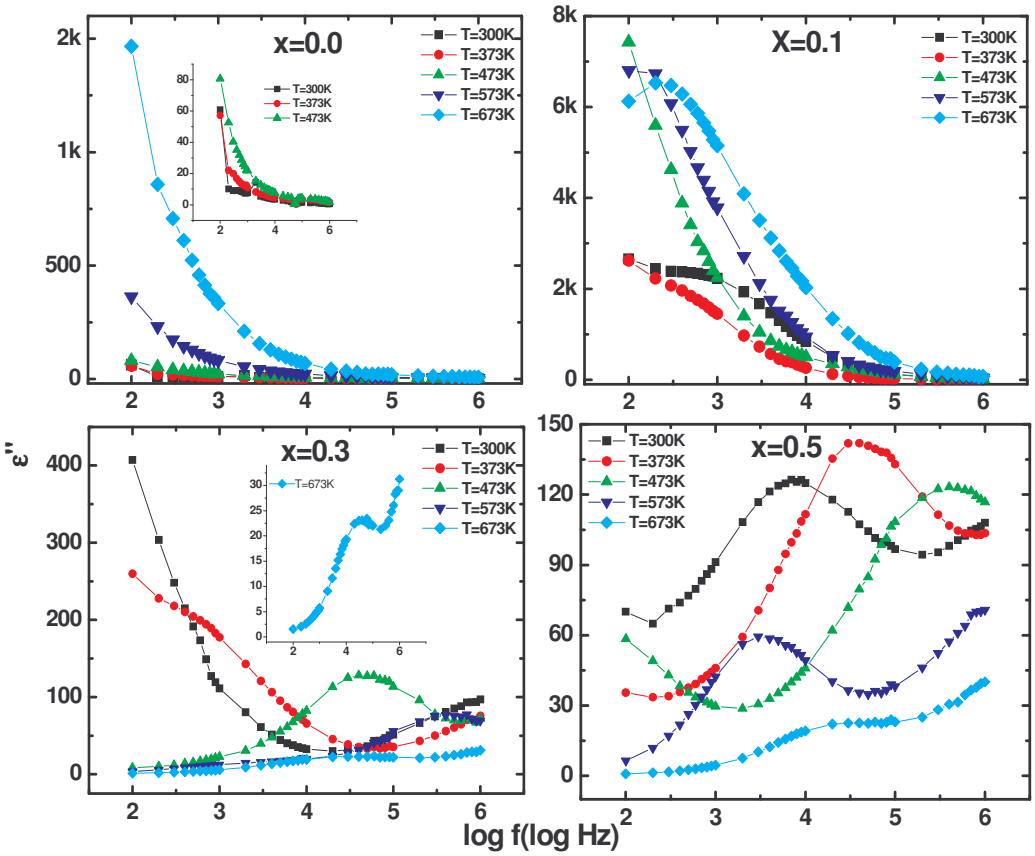

Fig. 5c.2.2 Frequency dependent behaviour of imaginary part (ε'') of complex dielectric permittivity (ε*) for x=0.0, 0.1, 0.3 and 0.5

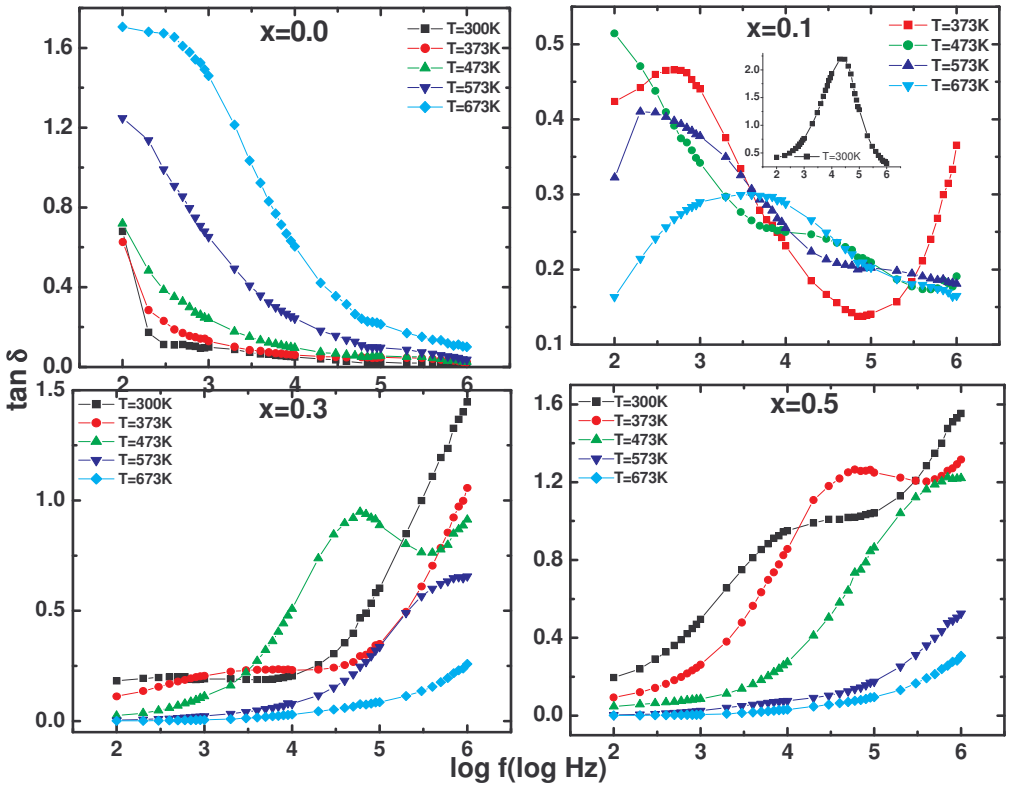

Fig. 5c.2.3 Variation of dielectric loss tangent with frequency at different temperatures for x=0.0,0.1,0.3 and 0.5 compositions

The bird eye –view of Figures 5c.2.1- 5c.2.3, show following main features: (i) the ε' and ε'' decrease as the frequency increases from 100 Hz-1MHz for x=0.0-0.5 and x=0.0-0.1 compositions respectively. (ii) The dielectric constant decreases rapidly in low frequency region and the rate of decrease is slow in high frequency region, the behaviour almost approaches to frequency independent behaviour.(iii) The ε'' is found to decrease faster than ε' in the low frequency region and the variation is same as ε' in higher frequency region. The phenomenon of dielectric dispersion in ferrites may be attributed to "free" charge buildup at interfaces within the bulk of the samples, (interfacial Maxwell-Wagner-Sillars (MWS) polarization [3]) and the interface between the sample and the electrodes (space charge polarization [4]). The polarization in garnets is through a mechanism similar to conduction process. In this model the exchange of electrons or holes between respective cations

results in local displacement of charge carriers in the direction or in opposite direction of applied field, which causes polarization. The polarization decreases with increase in frequency and then reaches a constant value due to the fact that beyond a certain frequency of external field the hole exchange cannot follow the alternating field.

The higher values of dielectric constant (ε') observed at lower frequencies are also explained on the basis of Maxwell- Wagners two layer model [5, 6] and Koop's phenomenological theory of dielectrics [7]. In ferrites, it is well known that that the samples consist of well conducting grains separated by poorly conducting grain boundaries [7]. In ferrites the permittivity is directly proportional to the square root of conductivity [8], therefore grains have high values of permittivity and grain boundaries have smaller values of permittivity. At lower frequencies the grain boundaries are more effective than grain in electrical conduction. Thinner the grain boundary, higher is the value of dielectric constant.

The loss tangent or tan δ is defined as the ratio of the imaginary part of the dielectric constant or the loss factor (ε") to the real part (ε').The variation of dielectric loss tangent (tan δ) with the frequency at different temperatures for the x=0.0-0.5 compositions is studied. The tan δ decreases with increasing frequency for =0.0 composition and can be explained on the basis of Koop's phenomenological model [7]. The appearance of resonance peak for x=0.1, 0.3 and 0.5 compositions can be explained as follows. Suppose an ion has two equilibrium positions say A and B, of equal potential energies, separated by a potential barrier. Then jumping probability of ions from A to B and from B to A will be the same. Depending upon this probability, the ion exchanges

position between the two states with same frequency, called the natural frequency of jump. When an external alternating field of the same frequency is applied, maximum electrical energy is transferred to the oscillating ions and power loss shoots up, thereby resulting in resonance.

It is evident from Figure 5c.2.3 that the position of loss peak shifts to lower frequency for x=0.1 and 0.3 compositions with increasing temperature from 300K to 473K while for temperature T> 473K it shifts to higher frequency. It is also seen that for x=0.5 composition loss peak shifts to higher frequency with increasing temperature. We have also observed same trend for frequency dependence dielectric loss (ε") behaviour at different temperatures (Figure 5c.2.2). It is interesting to note that for x=0.5 composition at 300K, 373K and 473K single loss peak is observed while at 573K and 673K low frequency loss peak as well as indication of another high frequency loss peak is observed. Therefore, it is understood that there are two different dielectric mechanisms. Namely, the crystal may also have two kinds of relaxation sites associated with two different characteristic relaxation times.

The shifting of $f_{\max}$ towards low frequency side can be explained as follows: It is an established fact that the condition for observing a maximum in the dielectric loss of a dielectric material is given by the relation: $\omega\tau = 1$, where $\omega = 2\pi f_{\max}$ and τ is the relaxation time. Now, the relaxation time τ is related to jumping probability per unit time "J_p" by an equation $\tau = \frac{1}{2}J_p$ or $f_{\max} = \left(\frac{J_p}{\pi}\right)$. This equation suggests that $f_{\max}$ is proportional to hopping probability. Now observed shifting of $f_{\max}$ towards higher frequency side with increase in temperature is due to the fact that at higher temperature, since the

energy available to the ions is more, the jumping probability between the two sites increases. This results in the increase in the jump frequency. One would, therefore, expect a shift in the resonance peak towards higher frequency. This further suggested by the fact that on increasing temperature the concentration of Fe^{4+} ions which are responsible for polarization in these ferrites, increases as evident by TEP measurements and as a result hopping probability per unit time increases continuously. The shifting of $f_{\max}$ towards low frequency side for x=0.1 and 0.3 composition for the temperatures T≤473K is rather difficult to explain. We feel that in this temperature range, expansion of unit cell increases the jump length as a result the jumping probability per unit time decreases. This effect overcomes the effect of energy acquired by the ions as well as formation and availability of Fe^{4+} ions, on increasing temperature.

The observed shifting of loss peak for x=0.1 and 0.3 compositions can also be explained as follows. In the temperature range 300K≤T<573K, material is in magnetically ordered ferrimagnetic state as Neel temperature (T_N) for x=0.1 composition is 520 K and 534 K for x=0.3 composition. Internally generated magnetic field affects ac conductivity to a greater extent due to magnetically linked network. This hinders the motion of charge carriers and as a result jumping frequency of charge carriers decreases. For the temperature T≥573K material is in magnetically disordered paramagnetic state with the absence of magnetic linkages. This gives rise to the free movement of traveling charge carriers. Therefore, the motion of charge carriers can easily follow the alternating applied electric field with increase in frequency. This also explains the increase in the resonant frequency at higher sample temperature.

Variation of dielectric constant (ε') with temperature

The variation of dielectric constant (ε') with temperature (T) for x=0.0, 0.1 and 0.5 compositions is given in figure 5c.2.4.

As can be seen, the ε' increases with temperature at all frequencies, the increase being quite significant at lower frequencies. As seen in Figure 5c.2.4, for x=0.5 composition, the dielectric constant gradually increases with the temperature at first and decrease beyond a certain temperature. This decrease, however, is not seen for x=0.0 and 0.1 compositions, in the temperature range investigated, although a similar trend is visible.

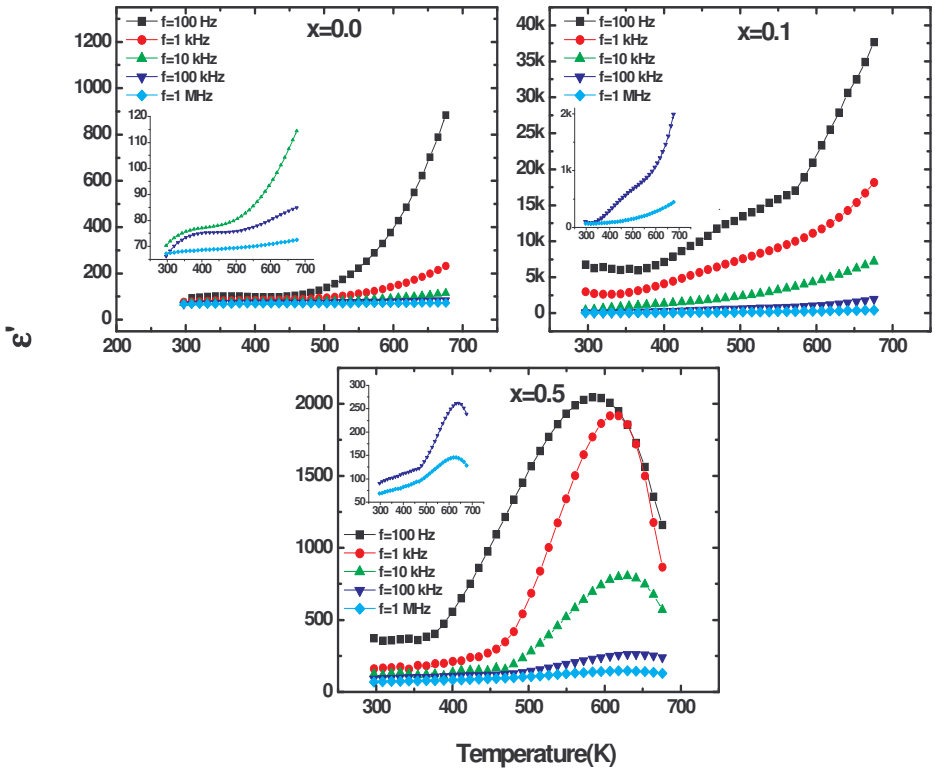

Fig. 5c.2.4 Temperature dependent variation of dielectric constant (ε') for x=0.0, 0.1 and 0.5 compositions

The thermal variation of ε' at different frequencies for all the compositions is consistent with the Debye- type of dispersion [9]. These curves can be understood on the basis of Debye equation:

$$\varepsilon' = \varepsilon_\omega - \left(\frac{\varepsilon_s - \varepsilon_\omega}{1 + \omega^2 \tau^2} \right)$$

where of ε_s and of ε_ω are the static and high frequency dielectric constants respectively, τ is the relaxation time equal to the reciprocal of jump frequency in the absence of external electric field, and ω is the angular frequency of the applied field.

At low temperatures, very high values of relaxation time results in value of ε' close to ε_ω [10]. At high temperatures, the thermal energy provided to the sample increases that decrease the relaxation time. The decrease in relaxation time consequently increases the dielectric constant. At still higher temperature, $\omega\tau$ becomes very much smaller than unity and a maximum value in dielectric constant equal to ε_s is observed at a certain temperature. The decrease in dielectric constant for x=0.5 for temperature T≥573K is due to the expected decrease in ε_s with further increase in temperature [10].

The dielectric maximums observed for x=0.5 composition is found to shift towards higher temperature with increase in the applied frequency. As the frequency of the applied field is increased the charge carriers reverse their direction of motion more often. This decreases the probability of charge carriers reaching the grain boundary and as a result the polarization decreases. Consequently, higher energies are required to restore polarization which is provided by increasing the temperature. This suggests that at higher

applied frequency, high temperature is required and thus the dielectric maximum shifts towards higher temperatures.

The occurrence of the peak in ε' versus T curves at different frequencies may be attributed to (i) transition from magnetically ordered ferrimagnetic state to magnetically disordered paramagnetic state of the system i.e Neel temperature (T_N) of the system [11]. The decrease in ε' above certain temperature is attributed to decrease in internal viscosity of the system giving rise to more degree of freedom to the dipoles with the result of increasing the disorder in the system and hence decrease in ε'. If it is so, such transition should be demonstrated by all the composition, as T_N for x=0.0, 0.1 and 0.3 compositions also lie in the measuring temperature range (Table 5a.5.1). (ii) the behaviour observed in x=0.5 composition is due to collective contributions of two type of charge carriers, "p" (holes) and "e" (electrons) to polarization and depend on temperature. Since the influence of temperature on the electronic exchange is more pronounced than that of the displacements of p-carriers, ε' will increase rapidly with increasing temperature. But above certain temperature, which normally depends on Fe^{3+}-content, the p-transitions become important and thus ε' will begin to decrease as a result of the contributions with opposite signs [12]. We feel that, in our case second possibility is more probable.

The thermal variation of ε' can further be explained as follows. In ferrites dielectric constant is attributed to interfacial, dipolar, atomic and electronic polarizations [13]. At lower frequencies at which all four types of polarizations contribute, the rapid increase in ε' with temperature is mainly

due to interfacial and dipolar polarization, which are strongly temperature dependent [14]. With increase in temperature more and more charges accumulated at the grain boundary as a result interfacial polarization enhances. The charges acquire adequate thermal energy beyond a certain temperature and able to overcome the resistive barrier at the grain boundary and conduction takes place resulting in decrease in polarization. The interfacial polarization occurs up to frequencies of around 1 kHz, with some contribution from the dipolar polarization also as the temperature increase. We have observed small rise to ε' value for all the compositions at 10 kHz of the frequency in the temperature range studied. This suggests there is a small contribution of dipolar polarization at this frequency. At higher frequencies, it is found that variation of ε' with temperature is relatively insignificant. This behaviour is ascribable to atomic and electronic polarizations, which are essentially frequency and temperature independent.

The rapid increase in ε' with temperature is observed to begin at a relatively lower and lower temperature with Fe^{3+}-substitution for Y^{3+} in the system. This observation is commensurate with the activation energies that decrease with increasing Fe^{3+}- concentration (x), (Table 5b.2.1). The lower activation energy, supports the lower energy barrier that results from structural perfection, as the probability of localized energy states arising out of structural imperfections would be low [15]. Thereby, the probability of charge hopping increases and consequently the polarization also increases. Furthermore, the polarizability of the individual metal ions also contributes to the dielectric constant. The polarizability of the metal ions depends on the number of electrons in their outer electronic shell as well as their Goldscmidt

radii [16, 9]. Greater the number of electrons in their outer electronic shells and greater the Goldscmidt radius, greater the polarization expected. From these considerations, the polarizability of the cations in the ferrites would be in the order $Y^{3+}>Fe^{3+}>Fe^{4+}$. Y^{3+} and Fe^{3+} ions would not lend themselves to polarization easily on account of their stable completely filled 4-p and half filled 3-d shells, respectively. Thus observed variation of dielectric constant is the overall result of the effect of the sum of the contribution of all these factors.

5c.3 Dielectric modulus

The effect of conductivity can be highly suppressed when the data are presented in the modulus representation. Williams et al [17] were the first to discuss the reciprocal of complex permittivity as an electrical analogue to the mechanical shear modulus. The dielectric modulus (M*) corresponds to the relaxation of the electric field in the material when the electrical displacement remains constant. Therefore, the modulus represents the real dielectric relaxation process [18]. The complex modulus M*(ω) was introduced to describe the dielectric response of non-conducting materials. The usefulness of the modulus representation in the analysis of relaxation phenomenon was demonstrated both for vitreous ionic conductors and polycrystalline ceramics [19].

The starting point for further consideration is the definition of the dielectric modulus: $$M^*(\omega) = \frac{1}{\varepsilon^*(\omega)} = M'(\omega) + iM''(\omega)$$

The real (M') and imaginary (M'') parts of the complex electrical modulus were obtained from ε'(ω) and ε''(ω) values using the relation:

$$M'(\omega) = \frac{\varepsilon'(\omega)}{\varepsilon'^2(\omega) + \varepsilon''^2(\omega)} = \frac{\omega a \varepsilon_0 z''}{t}$$

$$M''(\omega) = \frac{\varepsilon''(\omega)}{\varepsilon'^2(\omega) + \varepsilon''^2(\omega)} = \frac{\omega a \varepsilon_0 z'}{t}$$

where $\omega = 2\pi f$ is the angular frequency, ε_0 is the permittivity of free space, 'a' and 't' are the area and thickness of the pellet.

Based on the above equations, we have changed the form of presentation of the dielectric data, from ε'(ω) and ε''(ω) to M'(ω) and M''(ω). The obtained modulus spectra M'(f) and M''(f) are depicted in Figure 5c.3.1 and 5c.3.2 respectively. This pattern, M''(f),provides wider information relating charge transport process such as mechanism of electrical transport, conductivity relaxation and ion dynamics as a function of frequency and temperature. Figure 5c.3.1 and 5c.3.2 represents respectively the real and imaginary modulus at different temperatures for different garnet compositions.

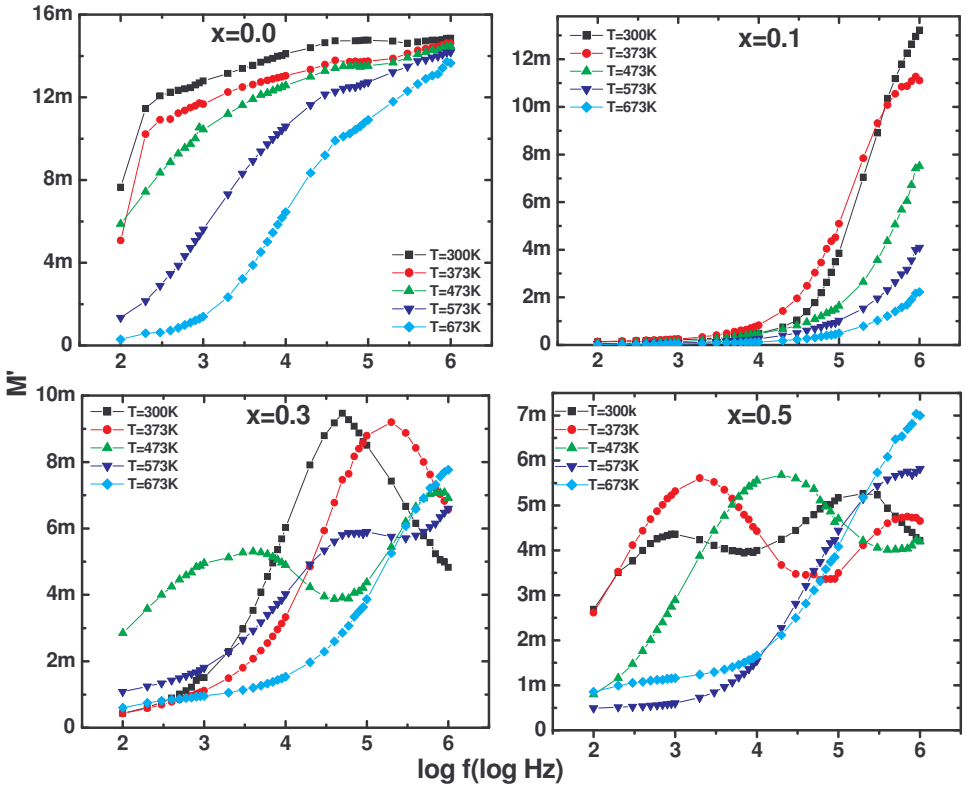

Fig.5c.3.1 Frequency dependent behaviour of real part of electric modulus (M') at different temperatures for x=0.0, 0.1, 0.3 and 0.5 compositions

We note in Figure 5c.3.1, that the real modulus M' for x=0.0 and 0.1 compositions, shows dispersion as the frequency is increased and tends to saturate at higher frequencies. We have observed relaxation hump for x=0.0 composition at 573K and 673K, for x=0.1 composition at 300K and for x=0.3

and 0.5 compositions, within the temperature range studied no such hump was observed in M''(f) curves. It seems that it may appear well above 1 MHz frequency of applied electric field frequency. The modulus patterns suggest the possibility of thermally activated long range mobility of charge carriers for x=0.1 (except for 300K), x=0.3 and x=0.5 compositions in the temperature range 300K to 673K.

The frequency region below the modulus peak determines the range in which charge carriers are mobile over long distances, whereas the region to the right of the peak maximum, where the charge carriers are spatially confined in their potential wells, being mobile on short distances.

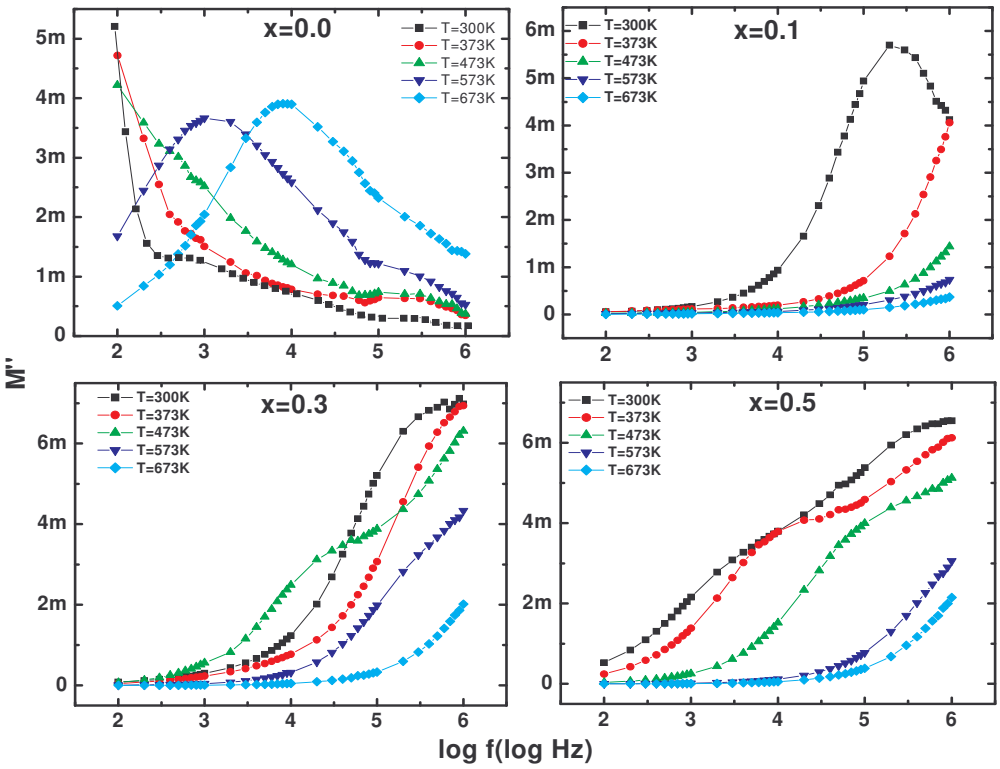

Fig.5c.3.2 Frequency dependent variation of imaginary part (M'') of electric modulus at different temperatures for x=0.0, 0.1, 0.3 and 0.5 compositions

A careful examination of M''(f,T) curves for x=0.0 composition reveals that : (i) The M''(f) peak shifts to higher frequencies with increasing temperature. This suggests that the relaxation rate for this process increases with increasing temperature, because of the thermal activation of the charge carriers.(ii) The magnitude of the peak decreases with increasing temperature, as one approaches the Neel temperature, which is a direct indication of increase in the dielectric constant and thereafter the magnitude goes up with further increase in temperature.

The asymmetric M'' is immediately suggestive of stretched exponent parameter (β) [20]. The value of β helps to decide whether the relaxation present in the material is Debye or non-Debye type. The value of β is equal to unity for an ideal dielectric for which the dipole-dipole interaction is negligible, but the β value is always less than unity for a system in which the dipole-dipole interaction is significant.

We have used the peak relaxation frequency f_{max} and the normalized width w_n; w_n is the full width at the half maximum (W) divided by the Debye width (W_D = 1.142 decades): $w_n=W/W_D$. The stretched –exponent parameters f_{SE} and β can be obtained from the peak position and width. To a very good approximation over the range $0.4<w_n^{-1}<1.0$, it is found that [21]:

$$\log_{10}(f_{SE}) = \log_{10}(f_{SE}) = 0.272(1-w_n^{-1})$$

and

$$(1-\beta) = 1.047\,(1-w_n^{-1})$$

In more simplified form equation for β can be written as:

$$\beta = \frac{1.196}{W} - 0.047$$

In present case for x=0.0 composition at 573K and 673K, the β value turned out to be less than unity (β=0.598 at 573K and β=0.794 at 673K), similarly β is found to be 0.802 for x=0.1 composition at 300K, showing the presence of the non-Debye nature of the dielectric relaxation. The observed change in β value as a function of temperature and composition suggests considerable change in average grain size with composition (as evident from SEM analysis) and temperature. The observed broad relaxation process can be explained on the basis of the fact that (i) it arises from two overlapping peaks and (ii) it could be single peak originating from a broad distribution of relaxation time due to a variety of energy barriers resulting from local defects.

It is known that β quantify that the asymmetric broadening of the relaxation time distributions. Their change shows that the relaxation time distribution becomes narrower with increasing temperature and composition. The reason is that dipoles taking part in the dielectric relaxation have almost same relaxation times.

Real, M' and imaginary, M'' part of the electric modulus versus log f obtained at different temperatures for x=0.0, 0.1, 0.3 and 0.5 compositions are shown in the Figure 5c.3.3. On the basis of assumption that the relaxation process at low frequency has a simple Debye behaviour, one can determine its characteristic relaxation time (τ_{dc}) [19]. In general, the value of τ_{dc} is defined by the frequency of the maximum dc- peak position, f_{max}:

$$\tau_{dc} = \frac{1}{2\pi f_{max}} \approx \frac{1}{2\pi f_{cross}}$$

Thus, an approximate but effective way of estimating τ_{dc} has been obtained. The logarithm of dc conductivity relaxation times (τ_{dc}) versus reciprocal temperature (1000/T) dependence has approximately linear characteristics. Thus, the Arrhenius law can be used to describe these data satisfactorily: $\left(\tau_{dc} = \tau_{0,dc} \exp\left[\frac{-E_{dc}}{kT}\right]\right)$, with the activation energy equal to $E_{dc} \approx 0.48$eV and $\tau_{0,dc} = 24.4$ nS.

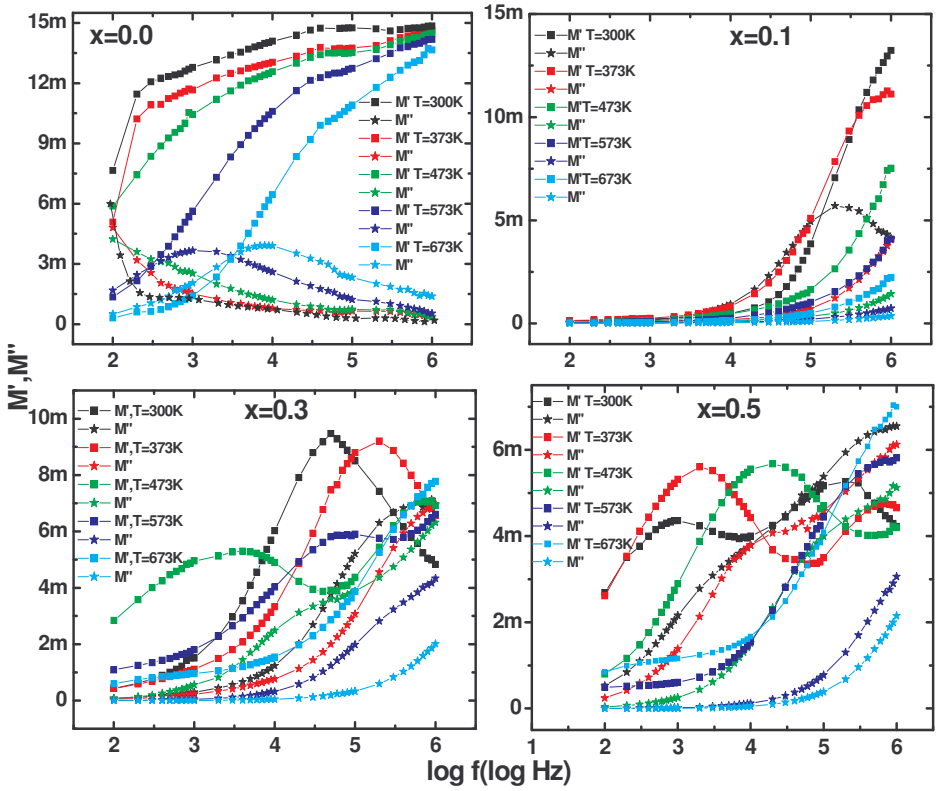

Fig.5c.3.3 Real and imaginary parts of the dielectric modulus versus frequency for x=0.0-0.5 compositions

5c.4 The Cole- Cole plots

In order to have a first insight into the solid under study almost new method has been suggested by Saafan et al. [22], to be used by experimentalists.

Accordingly (i) draw the Cole-Cole diagrams of the electric modulus M*(ω) i.e M''(ω) versus M'(ω) and those of the permittivity ε*(i.e ε''(ω) versus ε'(ω)) at different temperatures. (ii) then find out which one of the two groups of data has given one master curve, i.e. at all temperatures, the points have been collected in one curve with out performing any scaling process (dividing or multiplying by a constant or a function). (iiii) if the M* data gave the master curve, this will show that the solid belongs to a category having a property that we suggested to be "electric stiffness" is dominating. Whilst, if the ε* data gave that master curve, this will show that the solid belongs to a category having the reciprocal property dominating and suggested to be called "electric compliance".

The M* and ε* Cole-Cole plots for x=0.0-0.5 compositions at different temperatures are shown in the Figure 5c.4.1 and 5c.4.2. It is seen that only for x=0.0 composition M''(f) versus M'(f) data displayed master curve. The parabolic fitting relation, $M^*=a+bf+cf^2$, f being applied signal frequency, is satisfactorily valid and the parameters are found to be a=0.00128, b=0.69801, c= -53.5481.

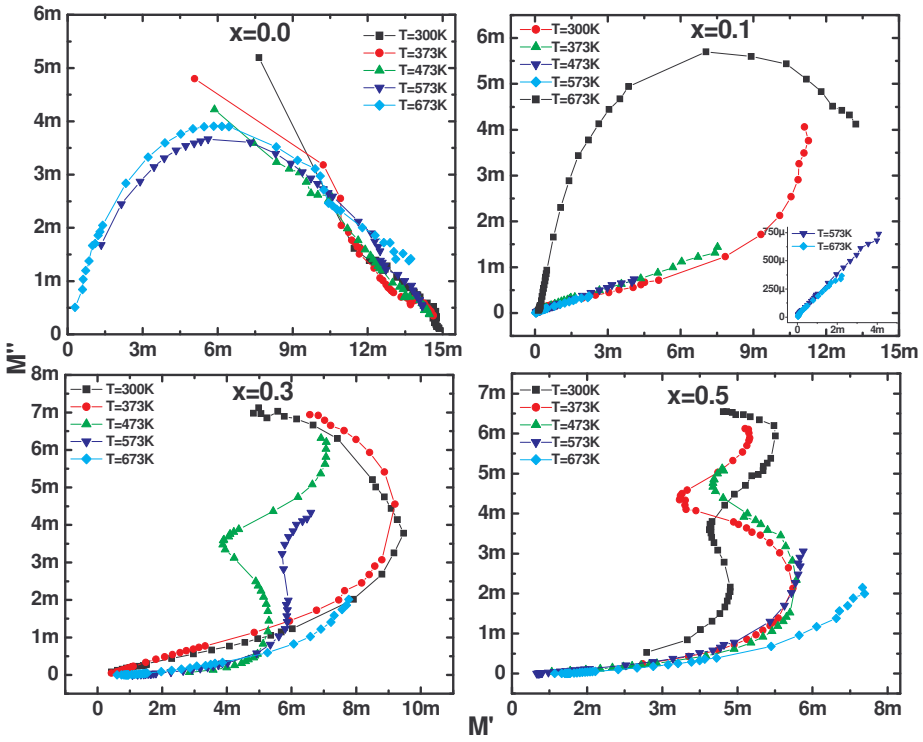

Fig.5c.4.1 M* Cole-Cole representation for x=0.0-0.5 compositions at different temperatures

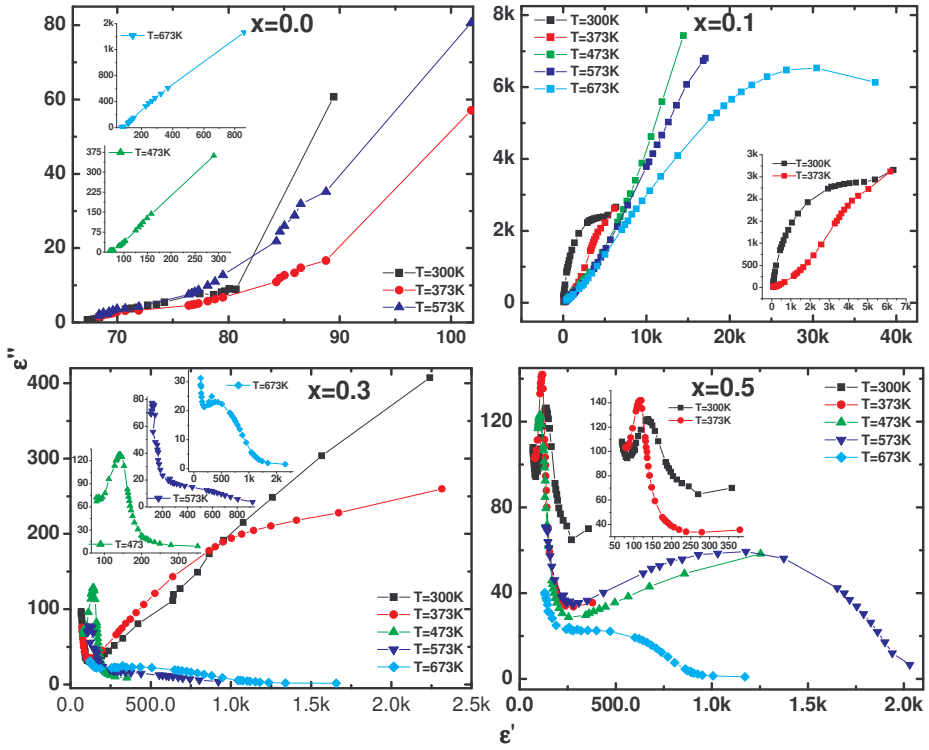

Fig.5c.4.2 ε* Cole-Cole representation for x=0.0-0.5 compositions at different temperatures

It is found that for this composition M''(f) versus M'(f) is the preferred representation and this composition having a dominating property which can be referred to as an “electric stiffness”. On the other hand M*(f) presentation for x=0.1, 0.3 and 0.5 compositions and ε*(f) presentation for all the compositions fail to give master curve. This also indicates that these three compositions can not be classified into the above mentioned categories of solids.

5c.5 Complex impedance spectroscopy

The complex impedance Z can be represented as Z*=Z'-iZ''= IZI Cosθ – i IZI sinθ, where Z' and Z'' are the real and imaginary parts of complex impedance and IZI and θ are the modulus and complex angle of the complex impedance, respectively. The complex impedance helps in determining inter-particle interactions like grain, grain boundary effects, etc.

The frequency dependent variation of the real (Z') and imaginary (Z'') part of the impedance at different temperatures are shown in Figure 5a.5.1 and 5a.5.2.

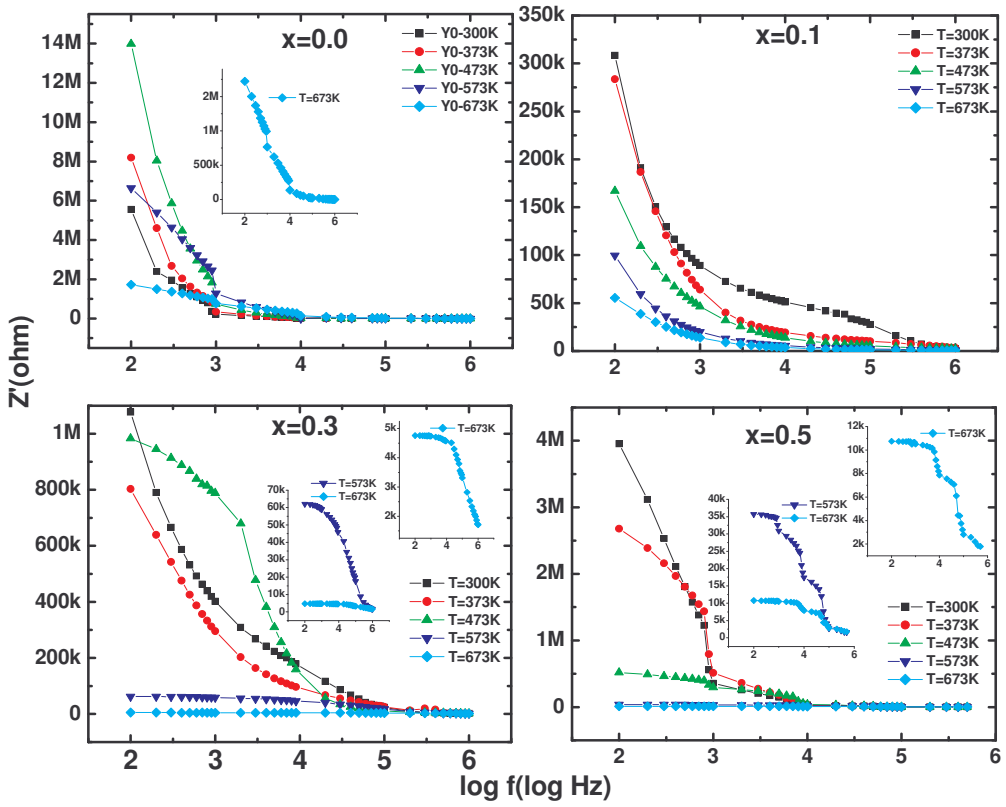

Fig. 5c.5.1 Frequency dependent variation of the real (Z') part of the impedance at different temperatures

It is observed that the magnitude of Z' decrease with increase in both the frequency as well as temperature. The Z' values for temperature range studied merge above 30 kHz. This may be due to release of space charges. This also indicates decrease in ac resistivity with temperature and frequency.

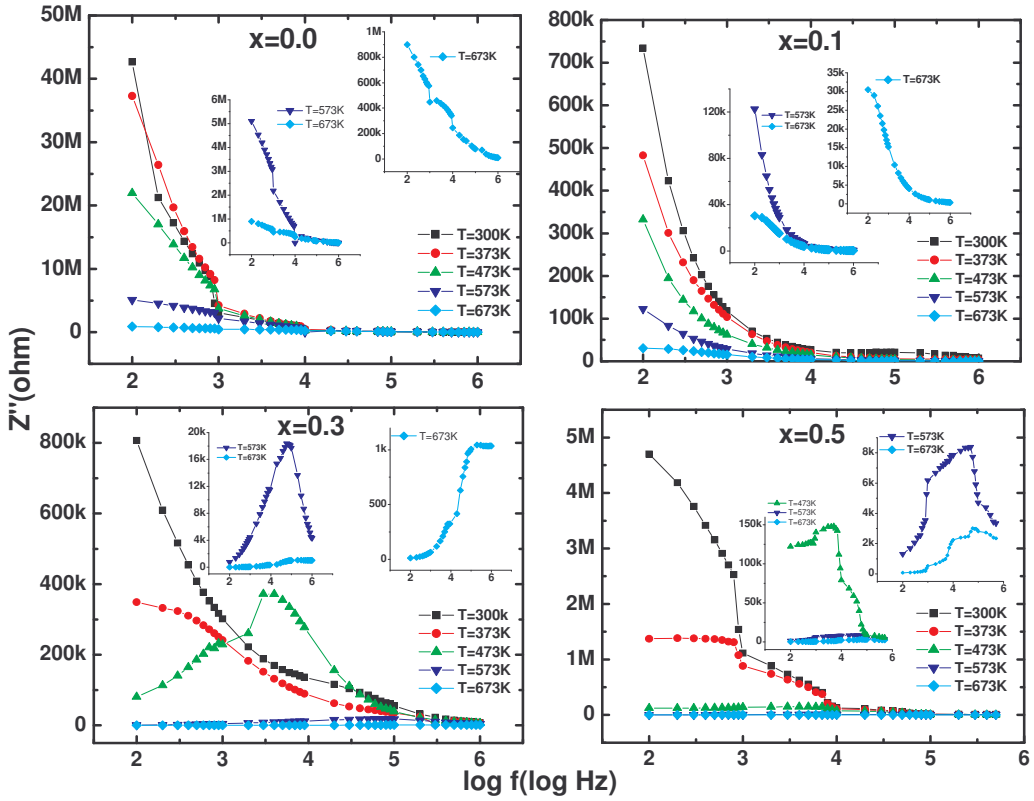

Fig. 5c.5.2 frequency dependent variation of imaginary (Z'') part of the impedance at different temperature

The variation of Z'' with frequency at several temperatures for x=0.0 and x=0.1 compositions is similar to that of Z'. The observations based on Z'' versus log f spectra for x=0.3 and x=0.5 compositions can be summarized as : (i) composition with x=0.3 at temperatures T≥473K and x=0.5 composition at temperatures T≥373K exhibit a peak with a slightly asymmetric degree, it seems that high temperature and increase in Fe^{3+}-concentration (x) in YIG trigger another relaxation process (ii) the curves show that Z'' exhibits the

maximum value for given temperature of measurement at a particular frequency (Z''_{max}) and then decreases continuously with further increase in frequency and temperature. (iii) the peak intensity decreases and the value of Z_{max} shifts to higher frequency with increasing temperature, indicating the increasing loss in the sample.

According to Van Hipple et at [23], in Z'' versus frequency plots, the peak heights are proportional to the grain resistance (R_g), based on the equation

$$Z'' = R_g \left[\frac{w\tau}{1 + w^2\tau^2} \right]$$

The relaxation time (τ_m) at peak frequency (w_m) is defined as $w_m \tau_m = 1$.

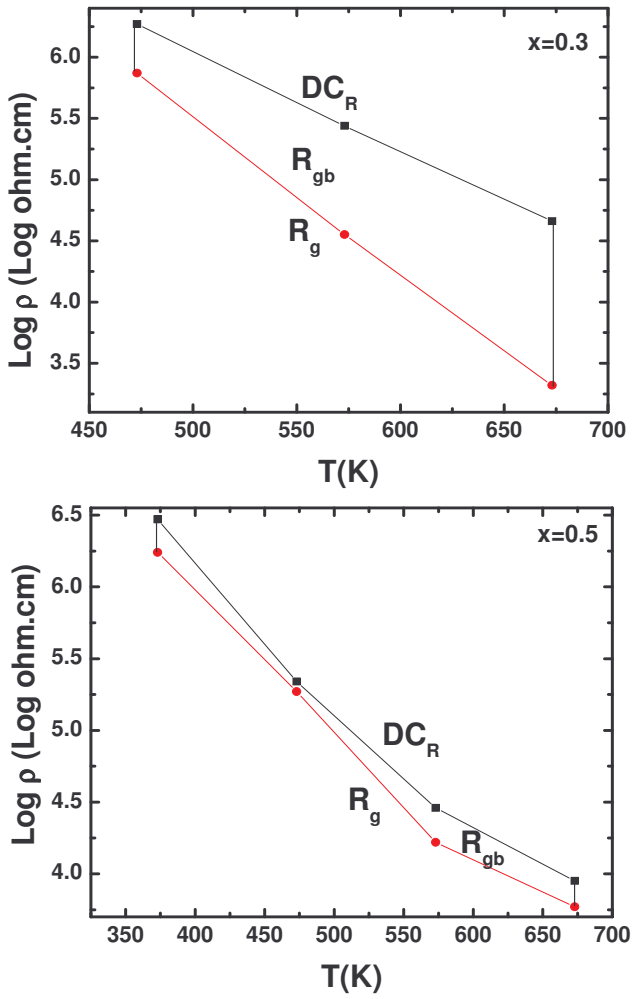

Fig. 5c.5.3 Variation of grain and grain boundary resistance with temperature

The value of grain resistance (R_g) calculated form the Z'' versus f plots and dc resistance observed at different temperatures is plotted in Figure 5c.5.3. In the absence of grain boundary resistance (R_{gb}), the bulk resistance from dc measurements (DC_R) and that from impedance plots should match ($DC_R \sim R_g$). The plot shows a difference in the values indicating the contribution of grain boundary resistance, which is not evident in the complex plane plot which seems to be prominent at still lower frequency range. This result is consistent with the conclusion drawn from the ρ_{ac} (f,t) variation (Figure 5c.1.1).To study the contribution due to different effects, cole-cole analysis has been done at different temperatures. These also provide information about the nature of the dielectric relaxation.

Figure 5c.5.4 shows the imaginary part (Z'';reactive part) of the impedance versus the real part (resistive part) of the impedance (Z') plotted over a wide range of frequency range at several temperatures, for all the compositions. It is seen that at 300K, the impedance data do not take the shape of a semicircle, but rather present a straight line with large slope, suggesting the insulating behaviour of garnet compositions at room temperature, supported by resistivity measurements. It is observed that with increase in temperature the slope of the lines decreases and they curve towards the real (Z') axis. We have observed signature of a semicircle formation for x=0.0 and 0.1 compositions about temperature T=673 K. For x=0.3 composition, at 473 K single semicircles while at 573 K two partially overlapping loops could be traced. On the other hand for x=0.5 composition two semicircles could be traced at 473 K and 573K. It is found that at 673K for

both the compositions only portion of semicircle is observed, it seems that second semicircle may appear at much higher frequency (f > 1 MHz), thus not observed in present frequency range studied. At higher temperature two semicircles could be obtained with different values of resistance for grains and grain boundaries. Thus, the grain and grain boundary contributions could be separated at these temperatures. The intercept of the semicircle with the real axis (Z') at low frequency represents the sum of the resistance of grains and grain boundaries, while the intercept at high frequency represents the resistance of the grains only. We have not observed third semicircle at the low frequency end suggests absence of electrode effect [24, 25]. This experimental finding (more than one semi-circle contributes to the plot (Figure 5c.5.4)) suggests that the monitoring conduction mechanism is of complex nature. More than one mechanism contributes to the measured dielectric response. Therefore, when an attempt has been made to scale the data (looking for a master curve) and to fit the data with the macroscopic theoretical models [24], the results were found to be unsatisfactory in the present case.

The complex impedance (Z*) measured by an impedance analyzer can be expressed as the following function of the R_{gb}, R_g, C_{gb} and C_g of the specimen.

$$Z' = \frac{R_g}{1 + w^2 R_g^2 C_g^2} + \frac{R_{gb}}{1 + w^2 R_{gb}^2 C_{gb}^2} \qquad Z'' = \frac{w R_g^2 C_g}{1 + w^2 R_g^2 C_g^2} + \frac{w R_{gb}^2 C_{gb}}{1 + w^2 R_{gb}^2 C_{gb}^2}$$

where $w = 2\pi f$ and 'f' is the frequency, R_g and C_g are the resistance and capacitance of the grain while R_{gb} and C_{gb} are that of grain boundary.

Depending upon the relative rate of decrease of R_g and R_{gb} and at the same time the relative rate of increase of C_g and C_{gb}, with w as the variable, the complex impedance curves gradually and successively change from one shape to the other [26], at different temperature.

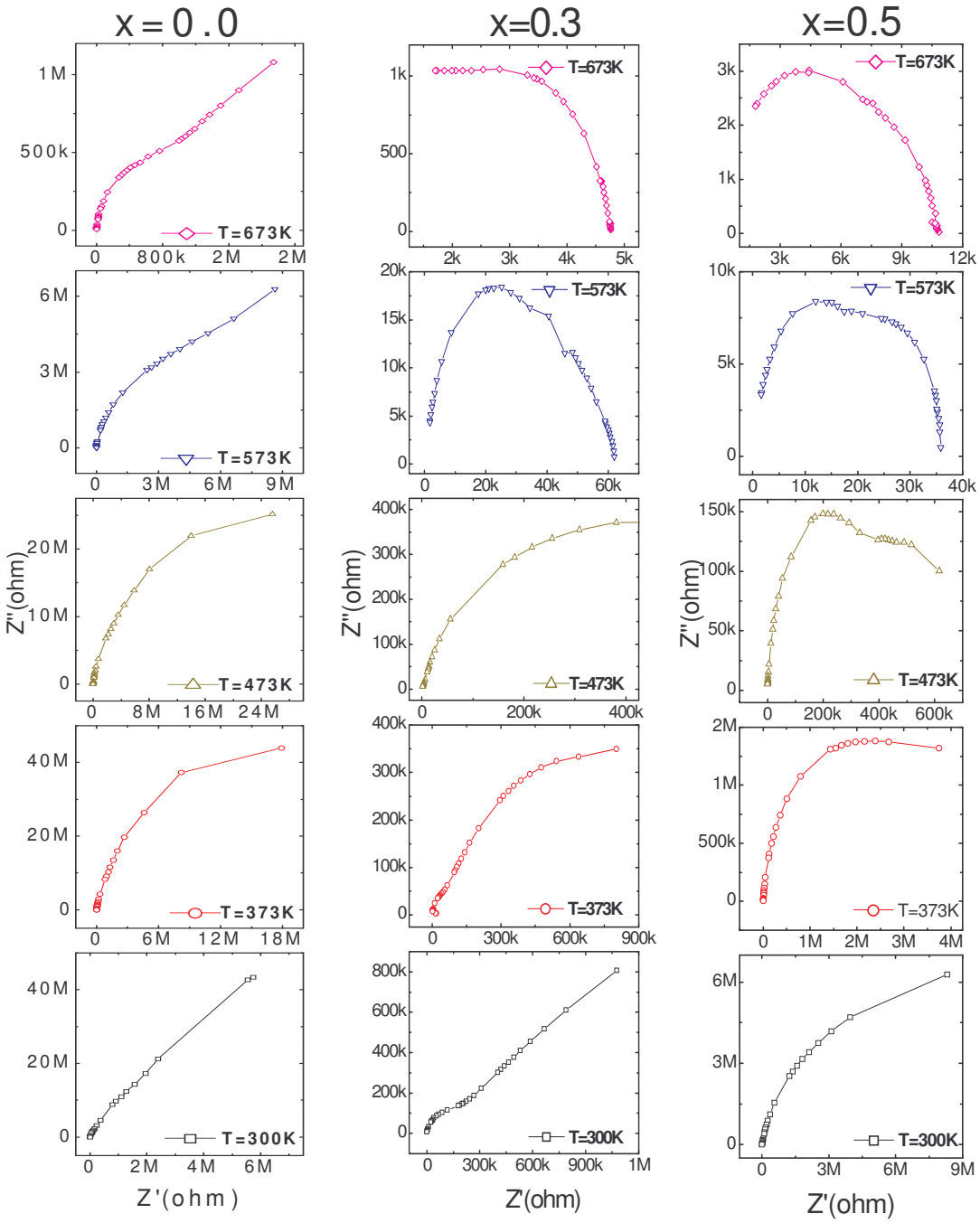

Fig. 5c.5.4 Nyquist diagram (cole-cole plots) for x=0.0, 0.3 and 0.5 compositions at different temperatures

References

1. U. Varshney, R. J. Churchill, R. K. Puri and R. G. Mendiratta in proceeding of the 5th Int. conf. on ferrite" Vol.1,edited by C. M. Srivastava, Bombay (1989) p.255.
2. D. B. Rogers, J. L. Gilsa and T. G. Gier, Solid State Commun. 5 (1967)143.
3. P. Hedvig, Dielectric Spectroscopy, edited by I.R. Macdonald (Wiley, New York) (1987) chap.2.
4. A. Kyritsis, P. Pissis and J. Grammatikakis, J. Polym. Sci. Polym. Phys. 33(1995)1737.
5. J.C. Maxwell, Electricity and magnetism, vol. 1, oxford University press, (1973) pp.328.
6. K. Wagner, Ann. Phys. 40(1993)817.
7. C.G.Coops, Phys. Rev. 83(1951)121.
8. P.V. Bradley, Materials for magnetic functions, Hayden Book company Inc., New York (1971) p.66.
9. L.L. Hench and J. K. West , Principles of Electronic Ceramics, John-Wiley and Sons. New York (1990)202,346.
10. A. Verma, O.P. Thakur, C. Prakash, T.C. Goel and R.G. Mendiratta, Mat. Sci. Engg. B 116 (2005)1.
11. M.C.Chhantbar, K.B.Modi and H.H.Joshi, J. Mater. Sci. 42(2007)6989.
12. N. Rezlescu and E. Rezlescu Phys. Stat. Sol. (a) 23(1974) 575.
13. W.D. Callister, Materials Science and Engineering –an Introduction, 5th Edition, John-Wiley and sons. Inc.(2000) p. 646.

14. L.L. Hench and J.K. West, Principles of electronic ceramics, John Wiley and Sons, New York (1990)205.

15. L.V. Azaroff, Introduction to solids , Tata McGraw- Hill Publishing Company Ltd. New Delhi (1992)321.

16. C.P. Smyth, Dielectric Behaviour and structure, McGraw- Hill Book Company Inc. (1995)p.132(chapter V).

17. N.G.McCrum, B.E. Read and G. Williams "An elastic and dielectric effects in polymeric Solids(New York : Wiley)1967.

18. M.J. Buerger, J. Crystal Structure Analysis (New York: Wiley)1960.

19. A. Molak, M. Palunch, S. Pawlus, J. Klimontko, Z. Ujama and I. Gruszka J. Phys. D:Appl. Phys. 38(2005)1450.

20. M. Harish Bhat, Munia Ganguli and K.J.Rao, Bull. Mater. Sci. 26(4)(2003)407.

21. P. K. Dickson, Phys. Rev. B. 42(13) (1990) 8179.

22. S.A. Saafan, A.S. Seoud and R.E.El. Shatter, Physica B 365(2005) 27.

23. Von Hipple R. Dielectric and waves (New York: Wiley) 1954.

24. M.H. Abdullah and A.N. Yusuff, J.Mater. Sci. 32(1997)5817

25. N.V. Prasad, G. Prasad, T. Bhimasankaram, S.V. Suryanarayana and G.S. Kumar, Bull. Mater. Sci. 24(2001)487.

26. J. Wang, F.Q Wu, G. Song, N. Wu and J.P Wang, Ferroelectrics 323 (2005)71.

Conclusions

The structural, infrared spectral, magnetic, electrical, dielectric and elastic properties studies on $Y_{3-x}Fe_{5+x}O_{12}$ (x=0.0, 0.1, 0.3 and 0.5) system as a function of composition, frequency and temperature lead to conclude that:

(a) Single phase stoichimetric garnet compositions have been synthesized successfully by usual double sintering ceramic technique. All the samples possess bcc structure as confirmed by Rietveld fitted powder X-ray diffraction patterns analysis.

(b) The interionic distances and as a result lattice constant value are found to decrease with Fe^{3+}-substitution, due to replacement of larger Y^{3+} ions by smaller Fe^{3+} ions in the system. The lattice constant values calculated theoretically are not in agreement with measured values, suggesting that practically Fe^{3+}-ion substitution does not affect the lattice constant.

(c) The infrared spectral evolution has been explained on the basis of change in interionic distances, site radii, and effective charge on the cation with Fe^{3+} -substitution.

(d) Field dependence of magnetization (M-H) study suggests collinear spin structure in the system and all the samples show ferrimagnetic behaviour which decreases with increasing Fe^{3+}-concentration.

(e) Mössbauer spectral analysis reveals 13% Y^{3+}-ions occupy to octahedral sites. The magnetic ion concentration, isomer shift, quadrupole shift and hyperfine field for d-site remain unaffected while those for a- and c- sites and show significant change with Fe-substitution. It is found that relative magnitude of hyperfine field is

$H_c > H_a > H_d$ while strength of exchange integral becomes $J_{ad} > J_{ac} > J_{dc}$. Mössbauer data also support Neel's type of collinear spin ordering in the system.

(f) The thermal variation of ac susceptibility exhibits normal ferrimagnetic behaviour. The Neel temperature increases with increasing x due to replacement of non-magnetic Y^{3+} by magnetic Fe^{3+} which enhances the strength of magnetic interactions in the system. The Neel temperature values deduced experimentally are in good agreement to those calculated theoretically using modified molecular field theory, indirectly supports cation distribution determined from magnetization and Mössbauer spectral analysis.

(g) The zero porosity corrected values of elastic moduli are found to decrease with increase in Fe^{3+}-substitution. This is mainly due to micro-cracks occurred during synthesis process. The lower value of lattice energy for polycrystalline materials as compared to its single crystalline counterparts is due to grain and grain boundary contribution to polycrystalline materials. It is possible to estimate single crystalline parameters from void free elastic constants values.

(h) All the compositions are p-type semiconductors and hopping of small polaron is responsible for conduction mechanism in the system.

(i) The observed increase in ac resistivity value with temperature for x=0.3 and 0.5 compositions is due to occurrence of nearly band like conduction besides hopping of charge carriers in the system.

(j) The frequency variation of dielectric parameters can be explained in the light of Maxwell- Wagner interfacial polarization. The dielectric maximums observed for x=0.5 composition in $\varepsilon'(T)$ curves is due to collective contributions of two types of charge carriers.

(k) The analysis of electrical and dielectric data through complex-plane impedance(Z^*) and dielectric modulus(M^*) provide more insights into the behaviour of the materials and information regarding the relaxation time, grain and grain boundary contribution to the resistance and Debye/ non-Debye nature of dielectric relaxation. It is found that relaxation time is of the order of microseconds, which is the general behaviour of ferrite systems. The magnitude of stretched exponent parameters indicates departure from the Debye behaviour. It is also found that the grain boundary contribution to the resistance is considerable in the frequency and temperature range studied.

Chapter 6

On the Effect of Thermal History and Swift Heavy Ion (SHI) - Irradiation on Physical Properties of Y^{3+}-substituted Yttrium Iron Garnet: $Y_{3+x}Fe_{5-x}O_{12}$; Y-Fe(Y)-O system

Study of SHI-induced ion beam mixing in Y^{3+}: YIG

It is well known that when magnetic insulators are subjected to swift heavy ion irradiation (SHII), it leads to the creation of a wide variety of defect states such as point/cluster and columnar defects in the materials [1] resulting to the modifications on their physical properties.

The yttrium iron garnet: $Y_3Fe_5O_{12}$ (YIG) has been found to be a relevant material for the purpose of irradiation because of its stability, well known magnetic properties and the possibility to find it in polycrystalline, single crystal or thin epitaxial film form [2]. However, majority of the work available in the literature deals with irradiation effect on various properties of single crystal and thin films of YIG [2-4]. Some facts to be mentioned are (i) to obtain pure garnet phase, temperatures of the order of 1400^{o}C are required (at 1300^{o}C, even for a prolong heat treatment the materials contain only 90% of the garnet phase [5]), (ii) in yttrium substituted yttrium iron garnets excess yttrium may be accommodated by formation of the perovskite $YFeO_3$ rather than non- stoichiometric phases, as there is very little difference in the lattice energies of the two phases [6]. In view of these facts, we have studied physical properties of polycrystalline Y^{3+} substituted for Fe^{3+} in yttrium iron garnet system with general formula : Y_{3+x} Fe_{5-x} O_{12} ,before and after SHI irradiation.

Two set of Y^{3+}- substituted yttrium iron garnet were prepared by usual double sintering ceramic technique. One set ($Y_{3+x}Fe_{5-x}O_{12}$; x=0.0, 0.2 and 0.4) of samples was sintered at 1300^{o}C and other set ($Y_{3+x}Fe_{5-x}O_{12}$; x=0.0, 0.2, 0.4 and

0.6) of samples was sintered at 1500°C. The specimens of the first set were irradiated in vacuum with 50 MeV Li^{3+} ions with fluence of 5 x 10^{13} ions/cm^2 using a 15 UD pelletron accelerator at IUAC, New Delhi. The targets for irradiation experiments in the form of thin layer of garnet material having thickness of about 20 mg/cm^2 were prepared by spreading fine ferrite powders in a aluminium ring of 1 cm diameter on a thin aluminium foil, and uniform thickness was achieved by fixing the powder using liquid GE varnish.

The X-ray diffraction analysis revealed that un-substituted yttrium iron garnet, $Y_3Fe_5O_{12}$ (x=0.0),sintered at 1300 ºC , 1500 ºC as well as irradiated by swift heavy ion, could be indexed for the bcc garnet structure.

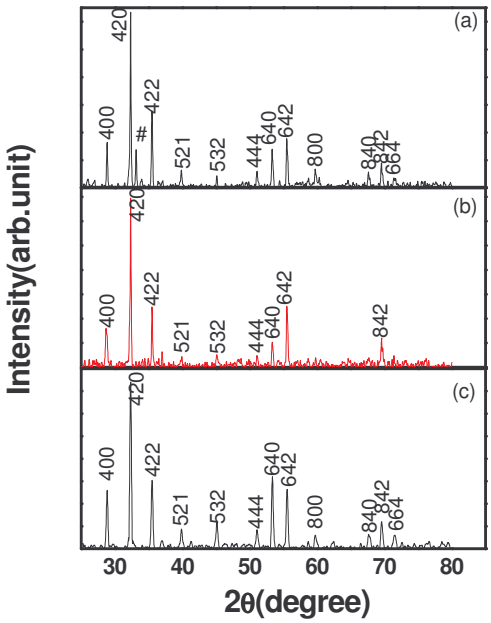

Fig.1. X-ray diffraction patterns of the x=0.2 compositions. (a) Un-irradiated (1300 ºC)(b) Irradiated (1300 ºC) (c) Un-irradiated (1500 ºC)

The behaviour of x=0.2 composition is particularly interesting. It has been shown that along with major bcc garnet phase, small indication of Yttrium ortho

ferrite ($YFeO_3$) phase (marked as #) occurs in 1300 ºC sintered composition. According to Catlow et al [6], based on atomistic computer simulation studies on energetically favorable intrinsic point defect structures in YIG, yttrium excess may be accommodated by formation of the perovskite $YFeO_3$ rather than non-stoichiometric phases as there is very little difference in the lattice energies of the two phases, -141.1 eV and -141.7 eV, for $YFeO_3$ and ¼($Y_4Fe_4O_{12}$) phase respectively. It is interesting to note that, this phase completely disappeared for x=0.2 composition, when irradiated by SHI and also when sintered at 1500 ºC (Figure 1).

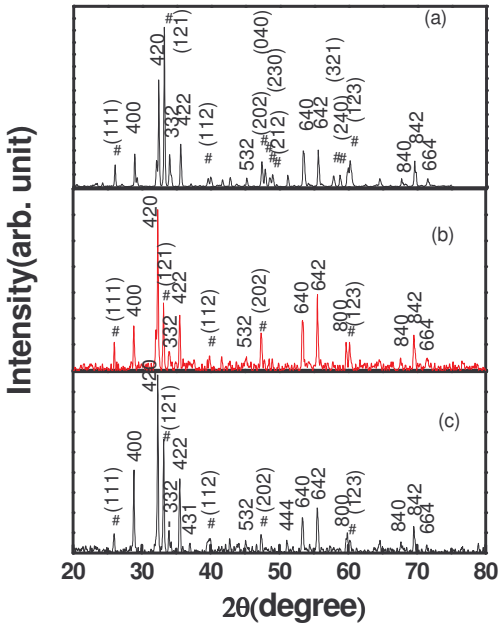

Fig. 2. X-ray diffraction patterns of the x=0.4 compositions. (a) Un-irradiated (1300 ºC) (b) Irradiated (1300 ºC) (c) Un-irradiated (1500 ºC)

For x=0.4 composition, formation of orthoferrite phase is quite high, but reduces considerably after irradiation and for 1500 ºC sintered samples (Figure 2). Furthermore, this reduction is prominent for irradiated as compared to 1500

ºC sintered composition. Thus, it is confirmed that the SHI-induced ion beam mixing delivers the garnet phase which is usually obtained at higher sintering temperature of 1500^{o}C.

^{57}Fe Mössbauer spectroscopy is an important tool to study structural changes, hyperfine interactions, and magnetic behaviour of garnet and spinel ferrites to deduce unambiguously the distribution of Fe^{3+} ions among sub-lattices of garnet structure. We have recently reported that substitution of Fe^{3+} ions changes the magnetic properties of YIG system [7,8]. One therefore expects that the hyperfine magnetic field experienced by the Fe-nucleus would also be affected by Y^{3+}- substitution and SHI irradiation, and that such changes should be reflected in ^{57}Fe Mössbauer spectra.

Mössbauer spectra recorded at 300K for the samples with x= 0.0, 0.2 and 0.4 are shown in Figure 3.

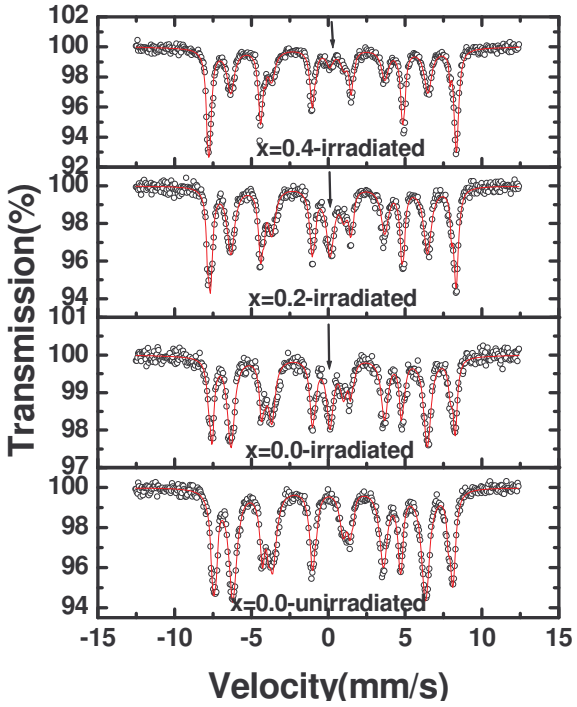

Fig. 3. Mössbauer Spectra at 300K for x=0.0(unirr & irr), x=0.2(irr) and x=0.4 (irr) of $Y_{3+x}Fe_{5-x}O_{12}$ system sintered at 1300 ºC

Table1: hyperfine field (H_f), Isomer shift (I.S.) and Quadrupole shifting (Q.S.) values for x=0.2 and x=0.4 compositions sintered at 1300 ºC (unirr &irr).

sample		Site	H_f(kOe) ± 1(kOe)		Area (%) ± 1(%)		Width(mm/s) ± 0.03(mm/s)		I.S(mm/s) ± 0.01(mm/s)		Q.S(mm/s) ± 0.01(mm/s)	
			unirr	irr	unirr	irr	Unirr	irr	unirr	irr	unirr	irr
x=0.2	Sextet	a	497	494	41	36	0.34	0.32	0.33	0.35	0.10	0.12
		d	396	395	49	41	0.57	0.53	0.11	0.12	0.07	0.06
		$YFeO_3$	481	490	10	6	0.25	0.15	0.4	0.31	-0.17	-0.31
	Singlet					17		0.60		0.21		
x=0.4	Sextet	a	499	508	45	54	0.30	0.32	0.32	0.35	0.085	0.07
		d	395	405	37	37	0.55	0.53	0.11	0.12	0.06	0.07
		$YFeO_3$	485	499	18	4	0.33	0.11	0.45	0.33	-0.10	-0.44
	Singlet					5		0.56		0.19		

The Mössbauer spectra were analyzed and the hyperfine interaction parameters were refined by computer software using least square method and assuming each spectrum to be a sum of Lorentzian functions. The Mössbauer spectra for all the three irradiated samples (Figure 3) exhibit a paramagnetic singlet or central enhancement superimposed on the magnetic sextets. The electronic energy loss (Se) of 50MeV Li^{3+} ions in this compound calculated using the SRIM -98 code is around 12eV/Å which is less than the electronic energy loss threshold (Se_{th}) required to surmount for producing columnar amorphization that is of the order of 10^3 eV/ Å. This suggests that the SHI –irradiation has generated points /cluster of defects. The generation of point/clusters of defects in these compounds inhibits the long range ferrimagnetic order through redistribution of cation in the localized defected region leading to the formation of paramagnetic centres. These paramagnetic centres resulted from breaking of magnetic ordering. The central paramagnetic enhancement in Mössbauer spectra can be explained on the basis of paramagnetic centres. In present case paramagnetic centres may be thought of created by redistribution of cations

induced by SHI-irradiation as observed earlier in Ti- substituted Li-ferrite [9].The population of the central singlet has been interpreted as due to some Fe^{3+} ions being isolated from other Fe^{3+} ions by non-magnetic Y^{3+} ions giving rise to varying sizes of clusters which have little magnetic interaction with the surrounding. Furthermore, magnetic ordering within the cluster is accompanied by much faster relaxation, especially for smaller clusters and gives rise to the paramagnetic components [10].Thus, the central singlet in the Mössbauer spectra of the irradiated samples originates from the SHI induced paramagnetic centres, not due to an amorphous phase.

Mössbauer spectra of x=0.0 composition exhibits two superimposed asymmetric Zeeman sextets due to Fe^{3+} ions at tetrahedral (d) and octahedral (a) sites of the crystal lattice. For x=0.2 and x=0.4 compositions in addition to these magnetic components, a third magnetic sextet has been observed. It is found that the third component corresponds to $YFeO_3$ phase as confirmed by X-ray diffraction pattern analysis.

The hyperfine interaction parameters for unirradiated (Unirr) and irradiated (Irr) x=0.2 and x=0.4 compositions, deduced through Mössbauer spectra are given in Table 1. It is seen that the nuclear hyperfine field for d-site is lower than that of the a-site for all the compositions before and after irradiation. This happens because the a-site Fe^{3+} ions experience a stronger average magnetic coupling than d-site ions due to more covalent nature of the Fe^{3+}-O^{2-} bond. The magnetic hyperfine fields for pristine composition(x=0.0) are found to be 478 kOe for a-site and 397 kOe for d-site in agreement with those reported earlier [8, 11].

It is evident from Table 1 that Isomer shift I.S.(d) and I.S. (a) values show very little change with Y^{3+}-substitution and after irradiation by SHI indicating that the s-electron charge distribution of Fe^{3+} is not much influenced by Y^{3+} substitution as well as by irradiation. As expected, the I.S. (a) is more positive than that for I.S. (d) because of larger Fe^{3+}-O^{2-} bond separation in the former. No quadrupole splitting for d- and a-sites have been observed (within the experimental error) for unirradiated and irradiated samples; this suggests that the coexistence of chemical disorder and overall cubic symmetry causes no net quadrupole splitting in Zeeman sextets.

The hyperfine field, isomer shift and quadrupole splitting values for third sextet are in agreement with those reported by Treves et al [12] for $YFeO_3$. It is seen from the Table 1 that the area corresponding to $YFeO_3$ phase decreases after the SHII for both the compositions. The decrease in area corresponds to $YFeO_3$ after the SHII, accompanied by evolution of singlet due to induced paramagnetic centres. This explains the transformation of $YFeO_3$ phase into the garnet phase after SHII having paramagnetic centres. It is well known that a swift heavy ion on passing through the materials loses its energy by electronic energy loss Se (inelastic process). This energy is being deposited in the form of electronic excitation or ionization, responsible for generating defect states. In fact, in the present study, Se not only dissolves the unreacted $YFeO_3$ phase but also participates in modifying the properties of main system, without any contamination. It is clear from Table that Mössbauer parameters of the garnet phase are not affected by the SHII. In contrast, the hyperfine interaction

parameters are much affected by SHII for $YFeO_3$ except for nuclear hyperfine field. The Mössbauer spectroscopic results reveal that SHII leads to the required garnet phase formation leaving behind the defected $YFeO_3$ phase. This is reflected in the reduce value of IS and Q.S suggesting drastic changes in chemical environment and charge symmetry of Fe^{3+} ion in $YFeO_3$.The magnetic nuclear hyperfine fields for both the compositions appear to be less sensitive to SHII (Table 1).

We conclude that the formation of $YFeO_3$ phase for higher Y^{3+} concentration compositions can effectively be reversed by swift heavy ion irradiation. This phenomenon of SHI induced ion beam mixing in Y^{3+} substituted YIG has been revealed through X-ray diffraction and Mössbauer spectral analysis. The electronic energy loss not only dissolves the unreacted $YFeO_3$ phase but also participates in modifying materials properties. The central enhancement observed in the Mössbauer spectra of the irradiated samples is not due to amorphization but its origin lies in the formation of localized paramagnetic centres.

Based on above findings it was decided to study effect of SHI-irradiation on various physical properties of Y^{3+}-substituted YIG: $Y_{3+x}Fe_{5-x}O_{12}$ (x=0.0-0.6) system sintered at 1500 ºC.

References

1. M.W. Thompson, Defects and radiation damage in metals, Cambridge University press, Cambridge, 1969.
2. F.Studer, C.Houpert, D.Groult and M. Toulemonde, Effects and defects in solids 110(1989)55.
3. M.Toulemonde, G.Fuchs, N.Nguyen, F.Studer and D.Groult, Phys.Rev. B, 35(13)(1987)6560 and references therein.
4. C.Houpert, M.Hervieu,D.Groult, F.Studer and M.Toulmonde, NIM B 22(1988)393.
5. P. Grosseau, A. Bachiorrini and B. Guilhot, Powder technology, 93(1997)247-251.
6. H. Donnerberg and C.R.A. Catlow J. Phys. Condens. Matter, 5(1993) 2947-2960.
7. K.B.Modi H.J.Shah, U.N. Trivedi, R.P.Vara, M.C. Chhantbar and H.H. Joshi, Ind. J. Eng. Mater. Sci. 10(2003)502.
8. P.U.Sharma, K.B.Modi, V.K.Lakhani,K.B. Zankat and H.H Joshi, Ceram. Int. 33(2007)1543.
9. M.C. Chhantbar, K.B.Modi, G.J. Baldha, H.H. Joshi R.V. Upadhyay and Ravi Kumar, NIM B 244(2006)124.
10. R.D. Shannon and C.T. Orewit, Acta. Crst. B 25(1969)
11. Sung Ho Lee, Kwang Pyo Chae, Seok Won Hong, Young Bae Lee, Solid State Commun. 83(2)(1992)97.
12. M. Eibschutz, S. Shitrikman and D.Treves, Phy. Rev. 156(2)(1967)562.

6a.1 Powder X-ray diffraction patterns analysis

The X-ray powder diffraction (XRD) patterns recorded at 300K are shown in Figure 6a.1.1 for the compositions with x=0.0, 0.2, 0.4 and 0.6 before and after SHI irradiation.

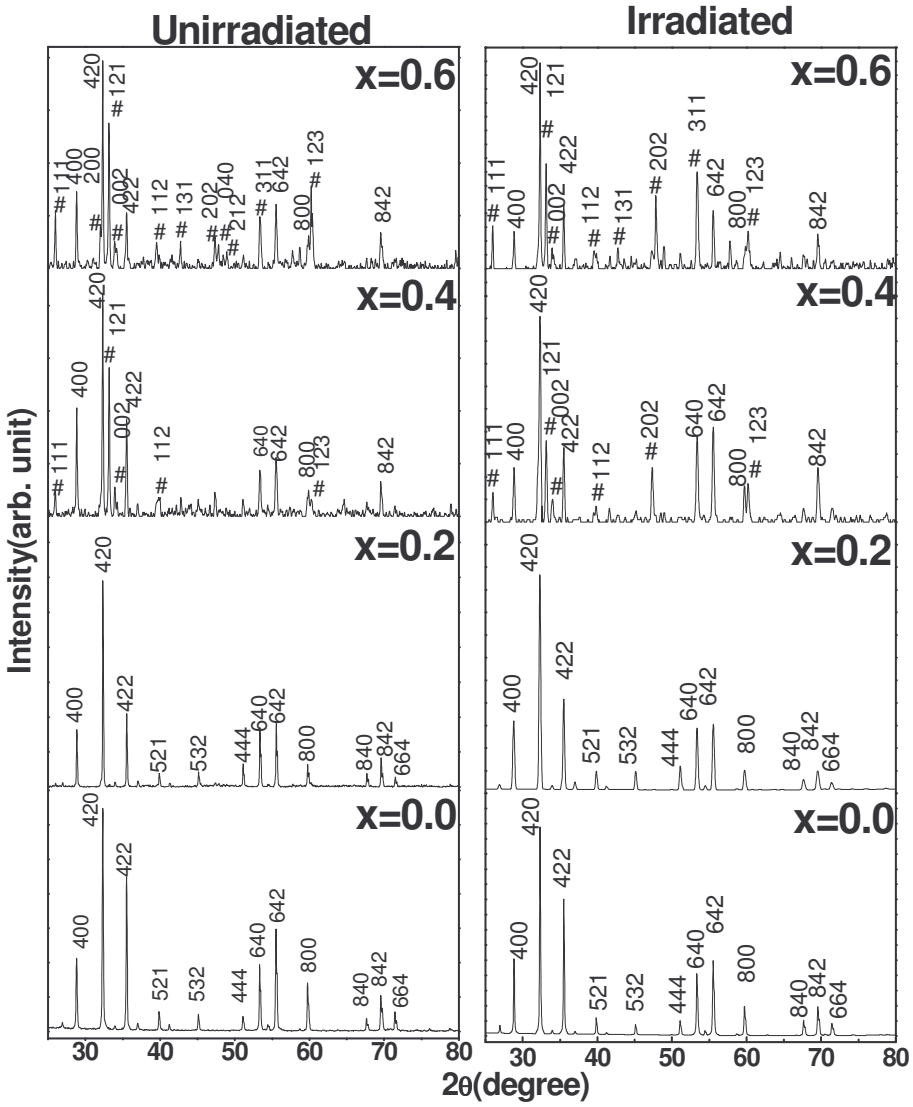

Fig.6a.1.1 X-ray diffraction patterns for all the compositions of Y-Fe(Y)-O system at 300K

The XRD patterns for all the samples were indexed for bcc-garnet phase (Space group: O_h^{10}- Ia3d) and orthorhombic phase of $YFeO_3$ (Space group: Pnma), using standard structural data files obtained from PCPDFWIN

program (PDF card No: 83-1027 & 86-0171 respectively) and the corresponding Bragg planes are shown in the patterns.

The XRD pattern analysis revealed that x=0.0 and x=0.2 compositions of $Y_{3+x}Fe_{5-x}O_{12}$ system, could be indexed for bcc garnet phase, before and after irradiation, with no extra lines corresponding to any other crystallographic phase or un-reacted ingredient. It is observed that along with major garnet phase, minor orthorhombic phase of $YFeO_3$ grows in intensity for compositions with x≥0.4. It is found that after irradiation this unwanted phase suppressed considerably for x=0.4 and x=0.6 compositions.

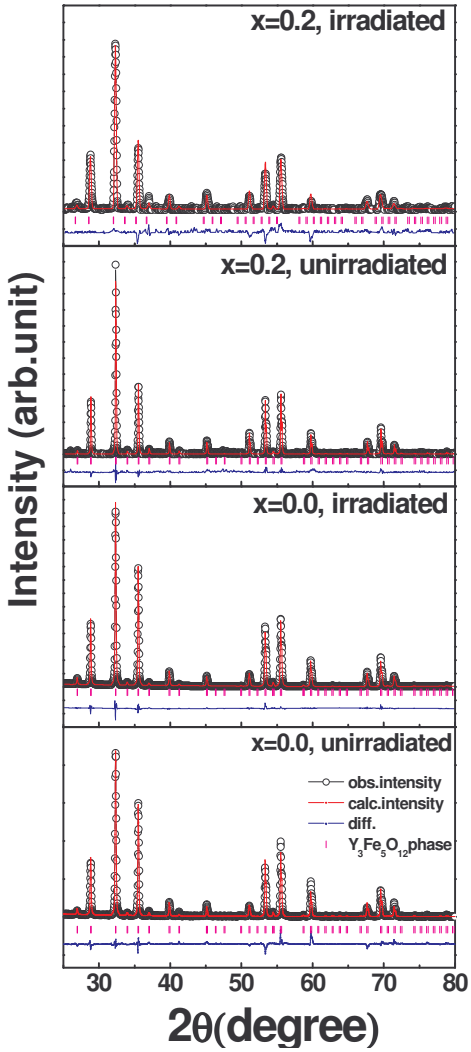

Fig 6a.1.2 Rietveld refined XRD patterns of x=0.0and 0.2 compositions, before and after irradiation at 300 K

Single phase nature of x=0.0and 0.2 compositions, before and after irradiation, is confirmed using rietveld analysis using General scattering analysis software(GSAS), which is as shown in Figure 6a.1.2.

The values of lattice constants, for both the phases, determined using detailed analysis of powder X-ray data are as given in Table 6a.1.1.

Table 6a.1.1 Lattice constant values for garnet and orthoferrite phase for all the compositions of Y-Fe(Y)-O system

Sample	Lattice parameters (Å)±0.002 Å							
	YIG phase		$YFeO_3$ phase					
	unirradiated	irradiated	unirradiated			irradiated		
			a	b	c	a	b	c
x=0.0	12.380	12.380	-	-		-		-
x=0.2	12.384	12.373	-	-		-		-
x=0.4	12.374	12.378	5.587	7.600	5.270	5.587	7.593	5.269
x=0.6	12.375	12.379	5.590	7.603	5.279	5.601	7.596	5.269

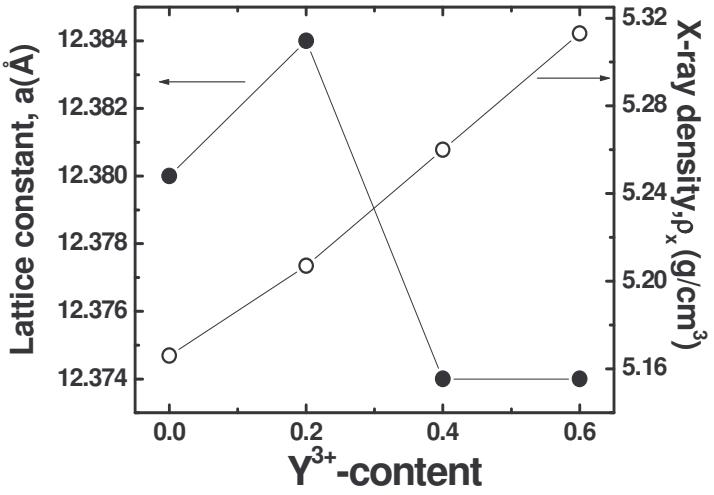

Fig. 6a.1.3 Variation of lattice constant and X-ray density with Y^{3+}-content for garnet phase, (unirradiated compositions) at 300K.

The variation of lattice constant of garnet phase as a function of Y^{3+}-content (x) is depicted in Figure 6a.1.3.

In the single phase region ($x \leq 0.2$),the lattice constant increases linearly with increase in Y^{3+}-content (x) and then starts leveling off for further increase in $x \geq 0.4$. The Y^{3+} ions, having the larger ionic radius (0.89Å), when substituted for Fe^{3+} (0.64 Å) , this causes linear rise in the lattice constant with x, following the Vegard's law [1], for $x \leq 0.2$.

The additional orthorhombic phase appears to grow in intensity with increase in Y^{3+}-concentration (x). All the Bragg reflection due to orthorhombic plane were indexed by generating inter-planner spacing (d) values using a computer programme and the lattice constants (cell-edge parameters) were calculated. It is found that the observed lattice constants for the orthorhombic phase remain uninfluenced by Y^{3+}-content and are exactly same as those of pure Yttrium orthoferrite (a=5.587 Å, b=7.595 Å, c=5.274 Å) [2]. The percentage formation of YIG phase and $YFeO_3$ phase for x=0.0, 0.2, 0.4 and 0.6 compositions are given in Table 6a.1.2.

Table 6a1.2 Percentage formation of YIG and $YFeO_3$ phase for Y-Fe(Y)-O system, before and after irradiation determined from XRD pattern analysis.

Y^{3+}-content (x)	YIG-phase (%)		$YFeO_3$-phase (%)	
	Unirradiated	Irradiated	Unirradiated	Irradiated
0.0	100.00	100.00	0.0	0.0
0.2	100.00	100.00	0.0	0.0
0.4	58.26	73.05	41.74	26.95
0.6	56.03	61.23	43.97	38.77

It is found that after irradiation by swift heavy ion, unwanted $YFeO_3$ phase reduces considerably from x=0.4 and x=0.6 compositions and at the same time percentage formation of YIG phase increases. This leads to conclude that irradiation may help to enhance substitution limit of larger cations like Y^{3+}, in the system. The small increase in lattice constant value of

the YIG phase for x=0.4 and 0.6 compositions after irradiation is also due to increase in diffusivity of larger Y^{3+} ions in the system. The lattice parameters of $YFeO_3$ phase for x=0.4 and 0.6 compositions remain unaffected after irradiation while lattice constant value of YIG phase for x=0.0-0.6 compositions show change after irradiation. This suggests that YIG phase is irradiation soft and $YFeO_3$ phase is irradiation hard phase.

The values of X-ray density (ρ_x) were calculated using the molecular weights and volume of the unit cell of garnet phase. The variation of ρ_x, for garnet phase, with Y^{3+}- content is shown in Figure 6a.1.2.In the present case, X-ray density of garnet phase, increases inspite of increase in lattice constant with increasing x (x=0.0 to 0.2). This is due to the fact that, increase in mass overtakes the increase in volume of the unit cell in the system. For higher concentration (i.e x> 0.2), variation in X-ray density (ρ_x) is consistent with variation of lattice constant.

6a.2 Scanning electron microscopic studies on Y-Fe(Y)-O system

The scanning electron micrographs (SEM) for x=0.0, 0.2, 0.4 and 0.6 compositions of $Y_{3+x}Fe_{5-x}O_{12}$ system are shown in figure 6a.2.1.

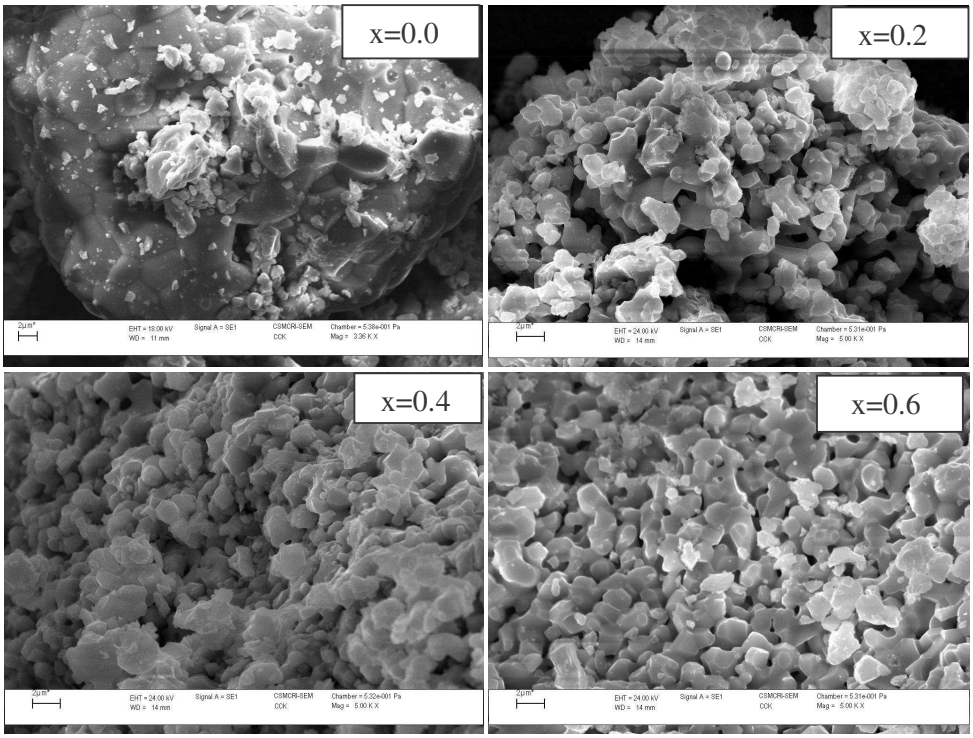

Fig. 6a.2.1 Scanning electron micrographs for x=0.0, 0.2, 0.4 and 0.6 compositions of Y-Fe(Y)-O system

It is seen that grain morphology: grain size, uniformity, homogeneity are highly influenced by Y^{3+}-substitution. We have observed exaggerated grain growth for pure YIG (x=0.0).When the grain growth rate is very high, pores may be left behind by rapidly moving grain boundaries, resulting in pores that are trapped inside the grains. The intragranular porosity is practically impossible to eliminate, leading to poor magnetic and mechanical properties. Samples with giant grains and included porosity, owing to exaggerated grain growth, still has good magnetic and mechanical properties

than those with normally grown grains, provided the distances between pores were the same. We feel that in our case same mechanism is responsible for excellent magnetic properties of pure YIG. For x=0.2 composition agglomeration of small grains is observed while for x=0.4 composition multilayer type grain growth is observed. The sample with x=0.6 shows small grains stuck to each other in a regular and uniform manner to form a network-like structure. In general with Y^{3+}-substitution, average grain size reduces from about 6 μm for x=0.0 composition to about 2.0 μm for x=0.6 composition, as well as uniformity and homogeneity of grains also found to increase. The decease in grain size with Y^{3+}-substitution is attributed to smaller solid solubility of Y^{3+}-ion in the garnet structure that hampers the grain growth [3].

6a.3 Pre and post effect of SHI- irradiation on IR spectra of Y-Fe(Y)-O system.

Infrared spectroscopy is one of the most powerful analytical techniques, which offers the possibility of chemical identification, vibration modes present for organic and inorganic substances. The technique is based upon the simple fact that a chemical substance shows marked selective absorption in the infrared region. After the absorption of infrared radiations, the molecules of a chemical substance vibrate at many rates of vibrations, giving rise to closed packed absorption bands, called IR absorption spectrum, which may be extended over a wide wavelength range. Various bands present in IR spectrum are corresponding to the characteristics functional group and bonds present in chemical substance.

IR absorption spectra of $Y_{3+x}Fe_{5-x}O_{12}$ (x=0.0, 0.2, 0.4, 0.6, 0.8 and 1.0) system were recorded at 300K in the wavenumber range 400-800 cm^{-1} are shown in figure 6a.3.1. No absorption bands were observed above 675 cm^{-1}. The IR spectra of x=0.0-0.6 compositions before and after irradiation show three bands and can be assigned to asymmetric stretching of tetrahedron in the YIG [4]. They are characteristic bands of the garnet ferrite. IR spectra of 0.8 and 1.0 compositions (included to study IR spectral evolution with Y^{3+}-substitution) are characterized by two absorption bands, identical with IR spectra of rare earth orthoferrites [5]. It is seen that for x=0.2 composition all the three bands shift towards lower frequency side as well as intensity of bands also increases. The observed shifting of bands is due to lattice expansion by larger Y^{3+}-substitution for smaller Fe^{3+}- ions in the system. It is

known that increase in site radius, hinders the fundamental frequency and therefore the centre frequency should shift towards lower frequency side. With further increase in Y^{3+}-content (x), intensity of absorption bands starts reducing as well as three distinct bands on higher frequency side getting merged in to an absorption band with centre frequency about 567 cm^{-1}. The presence of IR band about 500 cm^{-1} and 420 cm^{-1} can be attributed to the $YFeO_3$ phase associated to the YIG phase in x=0.4 and 0.6 compositions. The substitution of Y^{3+}-ions for Fe^{3+}-ions in the system will give rise to a microstructural distortion produced due to coexistence of $YFeO_3$ phase. The Fe-O bond lengths and angle show a variation because of the distortion. The Fe-O bond becomes strong and Fe-O-Fe superexchange interaction becomes weak so the intensity of bands decreases alongwith increasing Y^{3+}- content (x) (Figure 6a.3.1).

It is also interesting to note that after irradiation intensity of absorption bands for x=0.0-0.4 compositions is found to increase, while for x=0.6-1.0 compositions no effect of SHI irradiation on intensity has been observed. It is known that SHI- irradiation leads to the creation of a wide variety of defect states in materials. These defects restricts vibration rates of molecules and as a result intensity increases after irradiation for x=0.0-0.4 compositions. For x=0.4 composition partial removal of unwanted $YFeO_3$ after irradiation as evident from X-ray diffraction pattern analysis resulting in reduction of distortion and intensity increases. The compositions with x=0.6, 0.8 and 1.0 are dominated by $YFeO_3$ phase, as discussed earlier this phase is irradiation hard phase and thus no effect has been observed on intensity of absorption

bands. In other words, change in intensity after irradiation can be correlated with change in electric dipole moment [5].

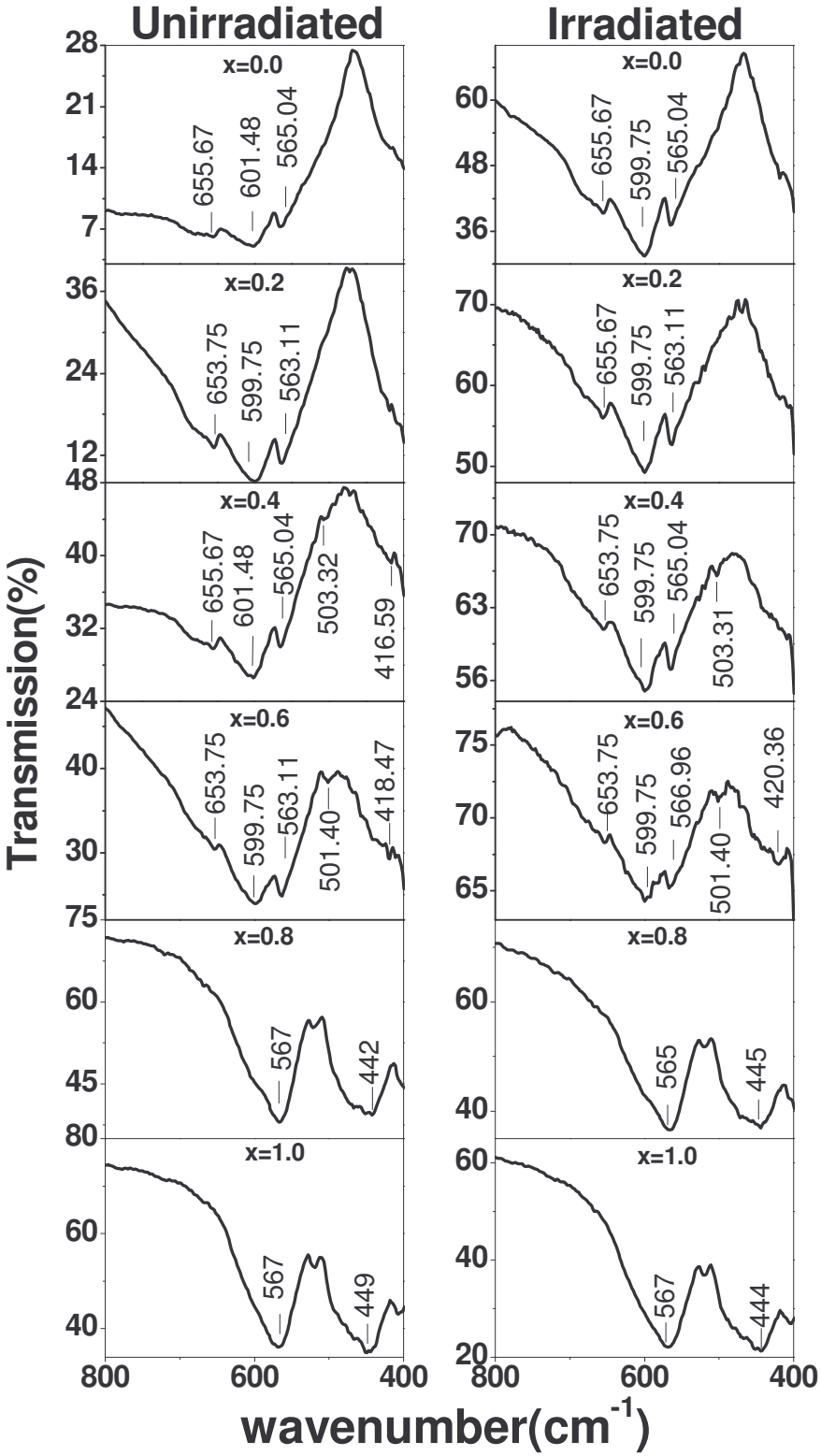

Fig.6a.3.1 Infrared spectra for different compositions for Y-Fe(Y)-O system before and after irradiation at 300K

6b.1 Effects on SHII on M-H loop characteristics of Y-Fe(Y)-O system

Room temperature (300K) field dependence of magnetization (M-H) curves recorded for x=0.0-0.6 compositions before and after SHI-irradiation are shown in Figure 6b.1.1.

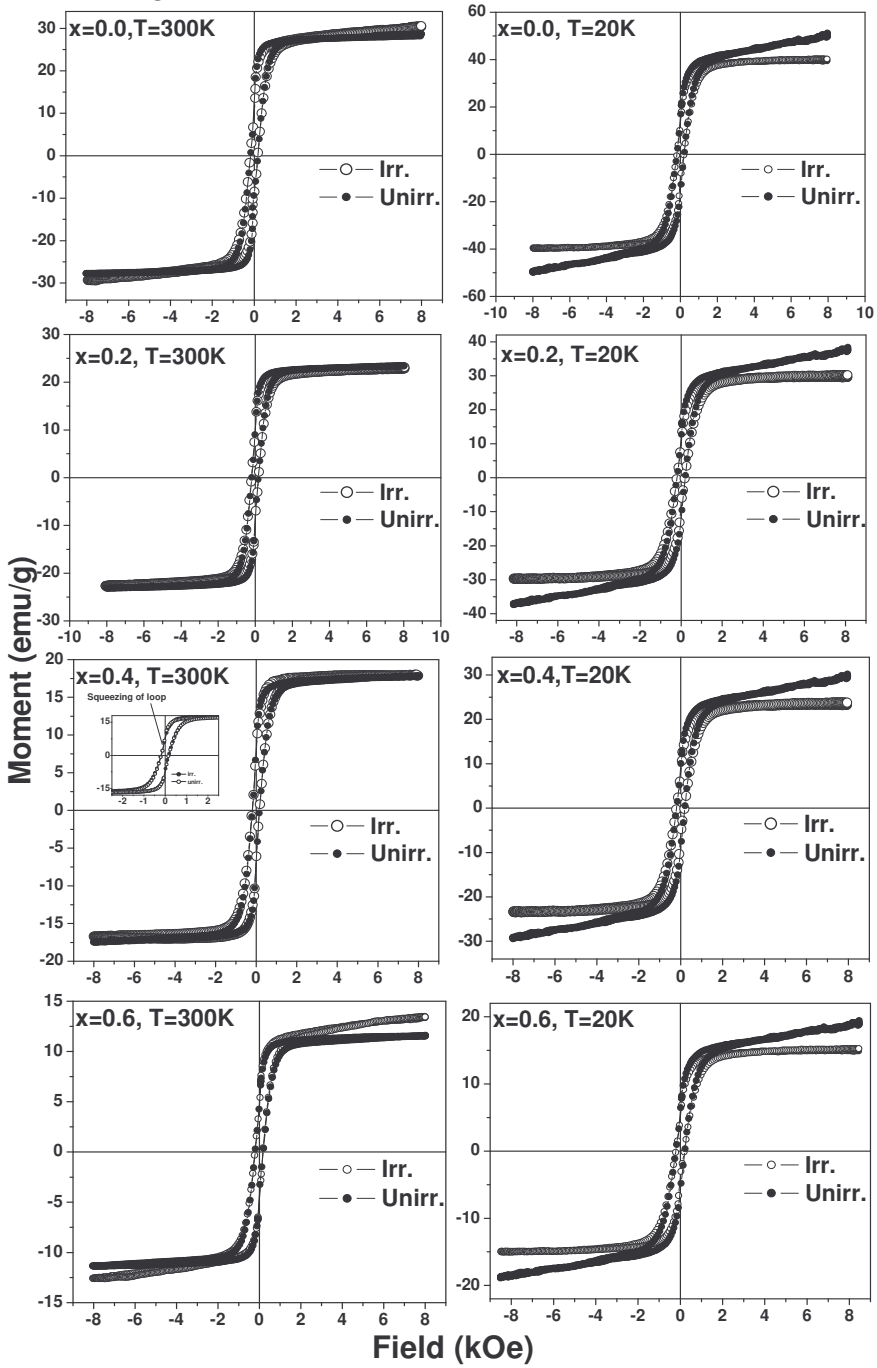

Fig. 6b.1.1 Hysteresis loop patterns of Y-Fe(Y)-O system at 300K and 20K before and after irradiation

The samples with x=0.0, 0.2, 0.4 show high field saturation and no effect of irradiation. The unirradiated, x=0.6 composition shows high field saturation while after irradiation it shows high field slope, may be due to fractional formation of paramagnetic centres resulting from SHI- irradiation.

Field dependence of magnetization (M-H) curves recorded at 20K for x=0.0, 0.2, 0.4 and 0.6 compositions before and after irradiation are shown in Figure 6b.1.1. It is observed that for all the unirradiated compositions, M-H curve show a linear decrease starting from the maximum magnetic field (9 kOe) and down to H= 0 kOe. There could be two probabilities either presence of ferrous (Fe^{2+}) ion or formation of Yttrium orthoferrite ($YFeO_3$) component along with major bcc phase of yttrium iron garnet ($Y_3Fe_5O_{12}$). First probability could be ruled out from Mössbauer spectral analysis. Presence of Fe^{2+}- ions would have been reflected clearly on isomer shift value in Mössbauer spectral analysis, as ferrous ions have larger positive isomer shift than ferric (Fe^{3+}) ions. Hence, unsaturated M-H curve may be due to $YFeO_3$ phase which manifest itself at low temperature. The magnetic structure of $YFeO_3$ can be described as composed by two Fe- magnetic sublattices that display weak ferromagnetic (WFM) ordering which results due to slightly canted alignment of Fe-moments. Moreover, squeezing of the loops (inset figure) near the origin or the difference between the ascending and descending branches of the hysteresis cycle for all the compositions is also due to the presence of two magnetic phases i.e ferrimagnetic component of garnet phase and weak ferromagnetic component of $YFeO_3$ phase, that do not allow spin moment to get align in the direction of applied magnetic field even at the field of 9 kOe.

Thus, we obtain saturation magnetizations and coercive fields due to both the magnetic phases.

A simple model has been proposed by Schmool et al [6] to aid the analysis of hysteresis loops for samples of more than one magnetic phase. Figure 6b.1.2 shows schematic diagram of hysteresis loops for two magnetic phases A and B of saturation magnetization M_A and M_B, respectively and coercive field H_{cA} and H_{cB} respectively.

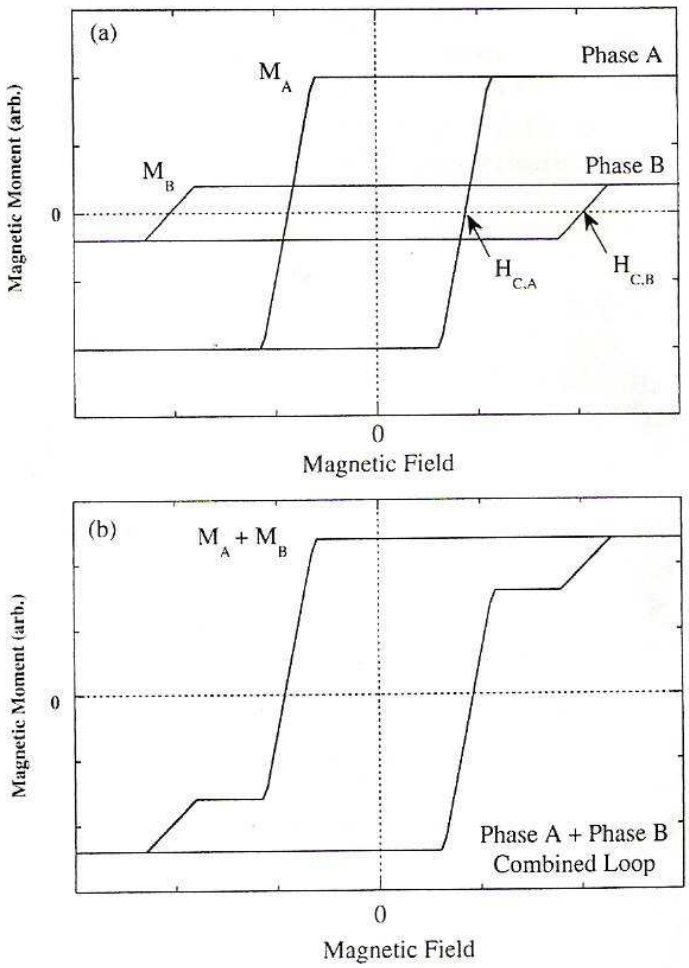

Fig. 6b.1.2 Schematic diagram of hysteresis loops for two magnetic phases A and B of saturation magnetization M_A and M_B

For a sample with a mixture of phases A and B we expect a hysteresis loop which will be an addition of those shown in Figure 6b.1.2 (a), this

illustrated in Figure 6b.1.2 (b), where we assume an equal content of the two phases. In our case x=0.4 and 0.6 compositions of $Y_{3+x}Fe_{5-x}O_{12}$ system possess two magnetic phases, magnetically soft primary phase $Y_3Fe_5O_{12}$ (A-phase) and magnetically hard secondary phase $YFeO_3$ (B-phase).

The M-H curve for irradiated compositions shows high field saturation. This also supports our findings derived from X-ray diffraction and Mössbauer spectral analysis that, the formation of $YFeO_3$ phase for higher Y^{3+}-concentration containing compositions can effectively suppressed by swift heavy ion irradiation.

The hysterisis parameters for all the compositions at 300K and 20K, determined from M-H loop analysis are presented in Table 6b.1.1.

Table 6b.1.1 hysterisis parameters for all the compositions at 300K and 20K

Y^{3+}-content (x)	σ_s (emu/gm)		Coercive field (H_c)(Oe)		Remainance (emu/g)	
	300K	20K				
	Unirr.	Unirr.	300K	20K	300K	20K
0.0	26.60	40.00	181	189	7.81	9.52
0.2	22.24	29.82	201	190	7.54	8.91
0.3	16.95	23.22	192	202	5.88	6.69
0.4	10.99	15.18	218	210	3.69	3.84

The value of saturation magnetization (σ_s emu/gm) decreases with increasing Y^{3+}- content (x) for both the sets of samples. This may be due to replacement of magnetic Fe^{3+} ions (5 μ_B) by non-magnetic Y^{3+}(0 μ_B) ions in the system and corresponding change in cation distribution among the available tetrahedral (d-), octahedral(a-) and dodecahedral (c-) sites. It may also be due to the presence and increasing percentage of weak ferromagnetic $YFeO_3$ phase (σ_s= 1.23 emu/gm) [7, 8] with Y^{3+}- substitution in the system. On

the other hand lower value of σ_s at 20 K for irradiated compositions as compared to unirradiated counterpart can be understood on the basis of SHI induced formation of the paramagnetic centres and the redistribution of the cations [9] that suppress expected enhancement of the magnetic moment by removal of $YFeO_3$ phase after irradiation.

In the present system due to replacement of magnetic anisotropic cation, Fe^{3+}, by non-magnetic Y^{3+}, one can expect decrease in coercive field (Hc) with increase in Y^{3+}-substitution (x). In contrary to expectation H_c is found to increase slowly with (x). The coercive field (H_c) at 300 K and 20K is found to increase slightly with increasing Y^{3+}-concentration (x). The observed small increase in value of H_c may be due to the presence of magnetically hard secondary phase of $YFeO_3$ in the system. The coercive field value of 24.6 kOe at 250K has been reported for $YFeO_3$ by Mathur et. al.[7].

6b.2 Effect of SHII on Mössbauer spectroscopy and hyperfine interaction parameters of Y-Fe(Y)-O system at 300K

The iron Mössbauer spectroscopy is an important microscopic probe for ferrites to study the hyperfine interaction parameters, coexisting magnetic phases and to deduce unambiguously the distribution of Fe^{3+} ions among the three antiferromagnetically coupled sublattices, tetrahedral (d-),octahedral(a-) and dodecahedral (c-) of garnet structure. It is well known that when magnetic insulators are subject to swift heavy ion irradiation (SHII), it leads to the creation of a wide variety of defect states in the materials [10] resulting to the modifications on their properties. Owing to the high sensitivity of superexchange interactions to any change in bond direction or length, the Mössbauer spectroscopy has been extensively used for the study of the SHI-induced modifications in the microstructure of spinel ferrites and garnets. The Yttrium iron garnet: $Y_3Fe_5O_{12}$ (YIG) has been found to be a relevant material for the purpose of irradiation because of its stability, well known magnetic properties and the possibility to find it in polycrystalline, single crystal or thin epitaxial film form [11]. However, majority of the work available in the literature deals with irradiation effect on various properties of single crystal and thin films of YIG [11-13].

We have recently reported that substitution of Fe^{3+}-ions changes the magnetic properties of YIG system [14]. One therefore expects that the hyperfine magnetic field experienced by the Fe-nucleus would also be affected by Y^{3+}-substitution and SHI irradiation and such changes should be reflected in ^{57} Fe Mössbauer spectra.

The Mössbauer spectra for pre and post SHI irradiated samples with x=0.0, 0.2, 0.4 and 0.6 of $Y_{3+x}Fe_{5-x}O_{12}$ system were recorded using a standard absorption method with ^{57}Co- in- Pd source placed on a constant acceleration spectrometer.

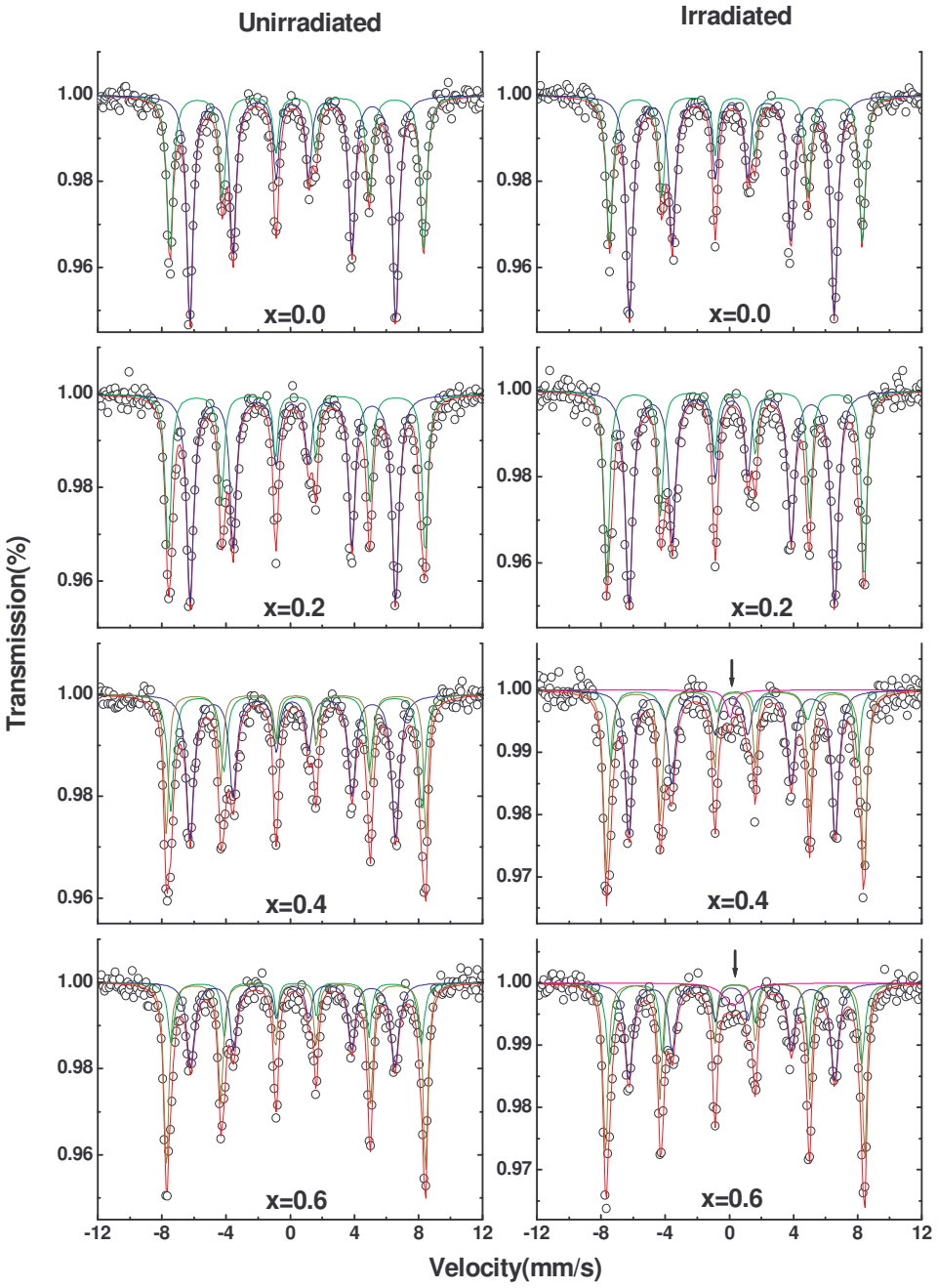

Fig.6b.2.1. Mössbauer spectra recorded at 300K for x=0.0, 0.2, 0.4 and 0.6 compositions of Y-Fe(Y)-O system, before and after irradiation

The Mössbauer spectra were analyzed and hyperfine interaction parameters were refined using NORMOS computer software using non-linear least square minimization [15].The solid lines through the data points are the results of computer fits of spectra obtained assuming equal line width for a- and d- sites. The Mössbauer spectra of x=0.0 and 0.2 compositions exhibit two normal Zeeman split sextets one due to the a-site Fe^{3+} ions and other due to d-site Fe^{3+} ions, before and after irradiation, which indicates ferrimagnetic behaviour the samples. For x=0.4 and 0.6 compositions before irradiation, in addition to these magnetic components, a third magnetic sextet has been observed. It is found that the third component corresponds to $YFeO_3$ phase as confirmed by X-ray diffraction pattern analysis. The Mössbauer spectra of x=0.4 and 0.6 compositions after irradiation exhibit a paramagnetic singlet or central enhancement superimposed on the magnetic sextets. The electronic energy loss (S_e) of 50 MeV Li^{3+} ions in this compound, calculated using the SRIM-98 code, is around 12 eV/Å which is less than electron energy loss threshold (S_{eth}) required to surmount the energy required for producing columnar amorphization that is of the order of 10^3 eV/ Å. This suggests that the SHI irradiation has generated points /cluster of defects. The generation of point/clusters of defects in these compounds inhibits the long range ferrimagnetic order through redistribution of cation in the localized defected region leading to the formation of paramagnetic centres. These paramagnetic centres resulted from breaking of magnetic ordering. The central paramagnetic enhancement in Mössbauer spectra can be explained on the basis of paramagnetic centres. In present case paramagnetic centres may thought of created by re-distribution of cations induced by SHI-irradiation as

observed earlier in Ti-substituted Al/Cr containing Li-ferrite systems [9]. The population of central singlet has been interpreted as due to same Fe^{3+} ions being isolated from other Fe^{3+} ions by non-magnetic Y^{3+} ions giving rise to varying sizes of clusters which have little magnetic interaction with the surrounding. Furthermore, magnetic ordering within the cluster in accompanied by much faster relaxation, especially for smaller cluster and giving rise to the central paramagnetic components [16]. Thus, the central singlet in the Mössbauer spectra of the irradiated samples originates from the SHI-induced paramagnetic centres, not due to an amorphous phase.

In contrast, the Mössbauer spectra of the x=0.0 and 0.2 compositions after irradiation do not show a slightest sign of central paramagnetic singlet. This suggests that the presence of magnetic ion Fe^{3+} (5 μ_B) in the lattice seems to play an important role of keeping the long range order intact inspite of SHI induced defected regions/rearrangement of the cations, while the coexistence of higher concentration of non-magnetic Y^{3+}(x>0.2) gives rise to SHI induced localized paramagnetic centres.

The hyperfine interaction parameters deduced through Mössbauer spectra are given in Table 6b.2.1.It is seen that the nuclear hyperfine field (H_f) for d-site is lower than that of the a-site for all the compositions before and after irradiation. This happens because the a-site Fe^{3+}-ions experience a stronger average magnetic coupling than d-site ions due to more covalent nature of the Fe^{3+}-O^{2-} bond. The variation in hyperfine field is due to the change in a-d, d-d and a-a interactions as the cation neighbours about given Fe^{3+} ion are changed. The magnetic hyperfine fields for pristine composition(x=0.0) are found to be 490.2 kOe for a-site and 397.3 kOe for d-

site in agreement with those reported earlier [17,18]. Because the non-magnetic Y^{3+} ions replace the magnetic Fe^{3+} ions at tetrahedral (d-) sites and due to the prominent a-d superexchange interaction, the supertransferred hyperfine field at a-site is influenced to a greater extent. Therefore, the a-site hyperfine field increases with Y^{3+}-substitution before and after irradiation for x=0.0-0.4. This can be related to the increase of covalancy. The average oxygen distance to 16(a) Fe^{3+} ion is about 2.01 Å while the tetrahedrally co-ordinate oxygen ions are at 1.87 Å from Fe^{3+} ion. Thus, the covalency character in the d-sites is inherently stronger than in the a-sites and the substitution of Y^{3+} ions with larger ionic radius will give rise to a microscopic structural distortion of the a- and d-sites to different degrees, even though they belong to a like coordination. The observed small difference in H_f value for a- and d-sites before and after irradiation suggests redistribution of cations after irradiation.

It is evident from Table 6b.2.1, that Isomer shift I.S.(d) and I.S. of $YFeO_3$ phase I.S.(Y) values show very little change but I.S. (a) shows considerable change with Y^{3+}-substitution before irradiation. It is found that I.S.(d), I.S.(a) and I.S.(Y) values change with Y^{3+}-substitution after irradiation, indicating in general, the s-electron charge distribution is influenced by Y^{3+}-substitution as well as by irradiation. As expected, the I.S. (a) is more positive then I.S. (d) because of larger Fe^{3+}-O^{2-} bond separation in the former. No quadrupole shifts for d-site and $YFeO_3$ phase have been observed (within the experimental error) for magnetically split spectra before irradiation. After irradiation Q.S. for a- and d-sites as well as Q.S for $YFeO_3$ phase changes considerably, suggests that the co-existence of chemical disorder and overall

cubic symmetry causes net quadrupole shifts in Zeeman sextets as well as contribute to change in the width with Y^{3+}-substitution before and after irradiation. The hyperfine field, isomer shift and quadrupole shift values of third sextet are in agreement with those reported by Eibschutz et al [19] for $YFeO_3$.

It is seen that the area corresponding to $YFeO_3$ phase decreases after the SHII for x=0.4 and x=0.6 compositions, accompanied by evolution of singlet due to induced paramagnetic centres. This explains the transformation of $YFeO_3$ phase into the garnet phase, after irradiation, having paramagnetic centres. It is well known that a swift heavy ion on passing through the materials loses its energy by electronic energy loss S_e (inelastic process). This energy is being deposited in the form of electronic excitation or ionization, responsible for generating defect states, in fact, in the present study; S_e not only dissolves the unreacted $YFeO_3$ phase but also participates in modifying the properties of main system, without any contamination.

It is clear from Table 6b.2.1 that, Mössbauer parameters of the garnet phase and $YFeO_3$ phase affected by SHII. The Mössbauer spectroscopic study results reveal that SHII leads to the formation of required garnet phase leaving behind the defected $YFeO_3$ phase. Furthermore, it is interesting to note that when all other parameters of $YFeO_3$ phase remain unaffected by SHII, nuclear hyperfine interaction parameters are highly influenced by SHII.

Table 6b.2.1 Mössbauer Hyperfine interaction parameters for unirradiated and irradiated samples of Y-Fe(Y)-O system at 300K.

sample	site	lines	H_f (kOe) ± 1 kOe		Width (mm/s) ±0.03 mm/s		Area % ±1%		I.S (mm/s)* ±0.02 mm/s		Q.S (mm/s) ±0.02 mm/s	
			Unirr.	Irr.	Unirr.	Irr.	Unirr.	Irr.	Unirr.	Irr.	Unirr.	Irr.
x=0.0	a	6	490.17	488.27	0.429	0.382	40.29	38.11	0.380	0.380	0.051	0.054
	d	6	397.34	395.42	0.443	0.452	59.71	61.89	0.152	0.147	0.022	0.018
x=0.2	a	6	492.46	493.99	0.362	0.394	48.75	46.41	0.372	0.374	0.048	0.022
	d	6	396.54	397.02	0.539	0.456	51.25	53.59	0.153	0.150	0.024	0.006
x=0.4	$YFeO_3$	6	485.30	476.71	0.419	0.466	30.67	16.13	0.387	0.368	-0.013	-0.126
	d	6	396.93	398.49	0.489	0.596	43.53	41.40	0.155	0.150	0.020	0.037
	a	6	501.49	497.75	0.305	0.315	25.80	40.32	0.356	0.358	0.023	0.008
	singlet	1	-	-	-	0.573	-	2.15	-	0.045	-	-
x=0.6	a	6	482.92	486.58	0.277	0.352	20.40	25.27	0.387	0.379	-0.033	0.010
	d	6	394.62	397.56	0.463	0.490	33.41	33.05	0.154	0.153	0.006	0.0002
	$YFeO_3$	6	500.30	500.49	0.354	0.328	46.19	36.71	0.353	0.360	0.012	0.005
	singlet	1	-	-	-	1.438	-	4.97	-	0.252	-	-

*with respect to iron metal

6b.3 Thermal variation of low field ac susceptibility study on $Y_{3+x}Fe_{5-x}O_{12}$ system

The temperature dependence of the normalized low field (0.5 Oe) ac susceptibility ($\chi_T/\chi_{RT;}$ $\chi(T)$) plots for x=0.0, 0.2, 0.4 and 0.6 compositions before and after irradiation are displayed in Figure 6b.3.1.

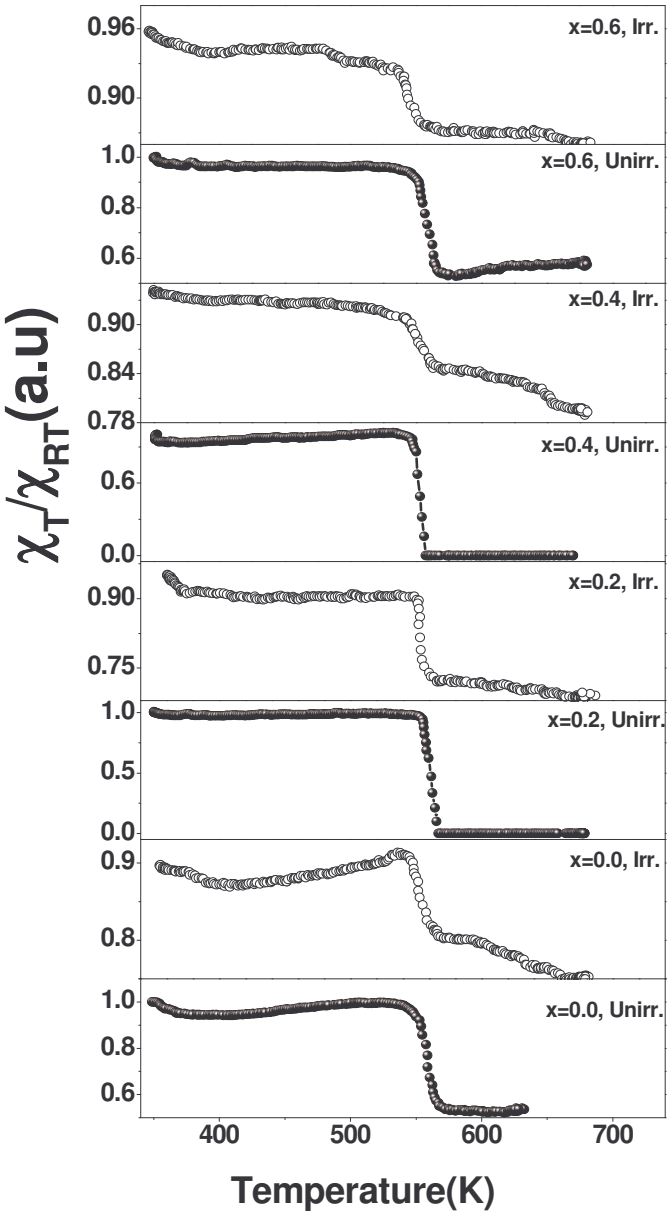

Fig. 6b.3.1 Temperature dependent low field (0.5Oe) ac susceptibility plots of unirradiated and irradiated samples of Y-Fe(Y)-O system

All the unirradiated samples exhibit normal ferrimagnetic behaviour with no indications of any magnetic phase transitions except at the transition temperature, (Neel temperature, T_N) for x=0.0, 0.2 and 0.4 compositions, while for x=0.6 composition first transition is relatively sharp and corresponds to garnet phase while second transition is blur, corresponding to T_N= 640K [19] of weak ferromagnetic $YFeO_3$ phase. A polycrystalline material consists of three types of domain state, viz. multi-domain (MD), single domain (SD) and super--paramagnetic (SP). It has been observed for MD ferrites that χ(T) does not change appreciably with temperature and drops of sharply at T_N. Therefore, in the light of our observations and what has been said above it can be concluded that samples under study contain MD states, as verified by permeability study.

It is interesting to note that all the irradiated samples exhibit tailing effect, indicating non-uniform effect of the irradiation.

Table 6b.3.1 Neel temperature (T_N) for Y-Fe(Y)-O system before and after irradiation

Y^{3+}-content (x)	T_N (K)±3K (ac susceptibitlity)	
	Unirradiated	Irradiated
0.0	564	555
0.2	558	550
0.4	552	-
0.6	567	-

The Neel temperature depends upon the active magnetic linkages per magnetic ion per formula unit [20]. It is expected to change due to the site magnetic dilutions, change in the unit cell volume, cation distribution, grain size, heat treatment, irradiation etc [21]. It is quite conspicuous that the T_N decreases with increasing Y^{3+}-content (x) from x=0.0 to 0.4, thereafter, it

increases with further increase in Y^{3+}-substitution. The observed reduction in T_N is attributed to the weakening of a-d interactions due to d-site magnetic dilution caused by non-magnetic Y^{3+}-substitution for magnetic Fe^{3+} in the system. For irradiated compositions it was not possible to determine T_N precisely due to blur transition for x=0.4 and 0.6 compositions, while for x=0.0 and 0.2 compositions T_N for the irradiated specimens are lower than their unirradiated counterparts. This may be due to cumulative effect of the redistribution of cations and fractional creation of localized paramagnetic centers resulting from SHI irradiation.

6b.4 Compositional, frequency and temperature dependence of permeability study

Permeability is one of the most important parameters used in evaluating magnetic materials. Not only is it a function of the chemical composition and crystal structure but it is strongly dependent on microstructure, temperature, stress, time after magnetization and several other factors [22].

The variation of real part of complex permeability henceforth referred to as initial permeability (μ') for pure $Y_3Fe_5O_{12}$ (x=0.0) composition sintered at 1200 ºC, 1300 ºC , 1400 ºC and 1500 ºC is as shown in Figure 6b.4.1(a).

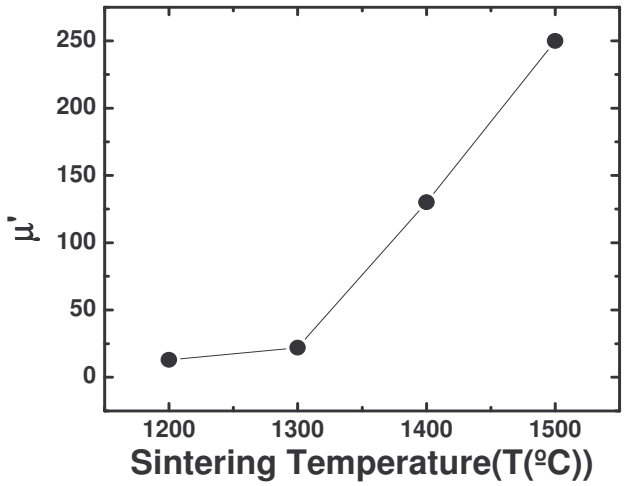

Fig.6b.4.1(a) Variation of initial permeability with sintering temperature for $Y_3Fe_5O_{12}$

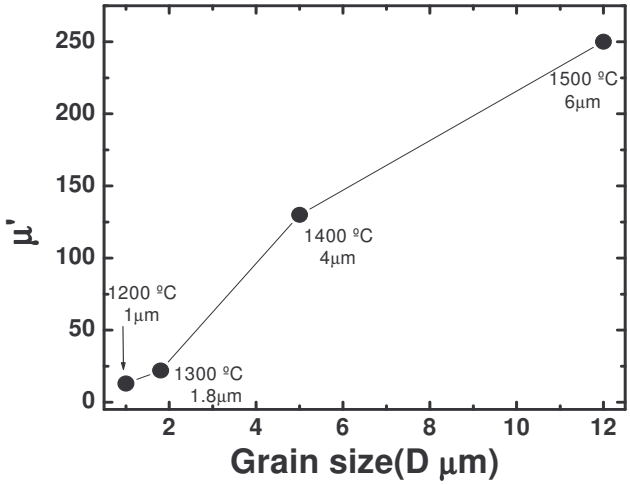

Fig.6b.4.1(b) Variation of initial permeability with Grain size for $Y_3Fe_5O_{12}$

It is found that μ' increases with increasing sintering temperature. This can be explained as follows:

(i)Increase in grain size was observed when the sintering temperature was raised from 1200 ºC to 1500 ºC (Figure 6b.4.1(b)). The larger the grains, the fewer the number of grain boundaries present. The domain walls normally remain pinned to the grain boundary. The presence of grain boundaries will act as impediment to domain wall motion. Based on above facts it is clear that on increasing sintering temperature impediments to domain wall motion reduces and hence permeability increases. (ii) Higher sintering temperature also results in the increase in density of the specimen which facilitates the movement of spins as the number of pores, which impede the wall motion, are reduced. (iii) The increase in sintering temperature also results in decrease in magnetic anisotropy by decreasing the internal stresses and crystal anisotropy which reduce the hindrance to the movement of the domain walls resulting thereby in the increased value of μ' [23].

Figure 6b.4.2 depicts the variation of μ' with Y^{3+}-concentration (x) at 300K, 400K and 500K at applied frequency of 10 kHz.

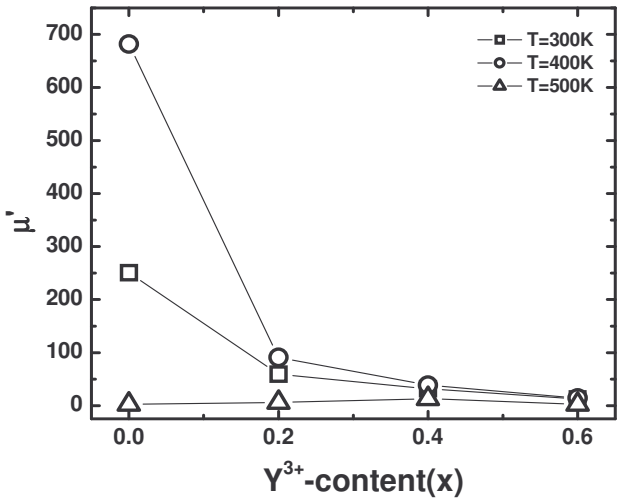

Fig.6b.4.2 Variation of μ' with Y^{3+}-concentration (x) at 300K, 400K and 500K

It is seen that μ' decreases with increasing Y^{3+}- concentration (x) in the system: $Y_{3+x}Fe_{5-x}O_{12}$. The observed reduction in μ' with Y^{3+}-substitution can be explained as follows: (i) According to Went and Wijn [24], the initial permeability is proportional to the square of saturation magnetization. Hence the variation of initial permeability with Y^{3+}-substitution follows a similar trend to that of saturation magnetization. (ii) According to Brion and Nemback [25], the soluble non-magnetic impurities inside the grain would hinder the reversible motion of domain walls, which can lower the initial permeability, therefore μ' decreases with Y^{3+}-substitution. (iii) The grain size reduction with Y^{3+}-substitution, results in increase in number of grain boundaries present, that impede the domain wall motion, and hence lowering of permeability is expected. In small grains, the formation of domain walls not being energetically favoured, the initial permeability will be lower.(iv) In addition to grain boundaries, ceramic imperfection impedes domain wall motion and thus reduces the permeability. Among these are pores, cracks, inclusions, second phases, as well as residual strains. Imperfections also act as energy wells that pin the domain walls and require higher activation energy to detach.

Permeability spectrum

At high frequencies, the permeability separates into two components μ' and μ''. The first, μ' represents the permeability with the magnetization in phase with the alternating magnetic field and the second, imaginary part of complex permeability, μ'', the permeability with the magnetization that is out of phase with alternating magnetic field. The two permeabilities are often plotted

on the same graph as a function of frequency. This is known as the permeability dispersion or permeability spectrum.

The permeability spectra for x=0.0, 0.2, 0.4 and 0.6 compositions of $Y_{3+x}Fe_{5-x}O_{12}$ system at 300K are shown in Figure 6b.4.3.

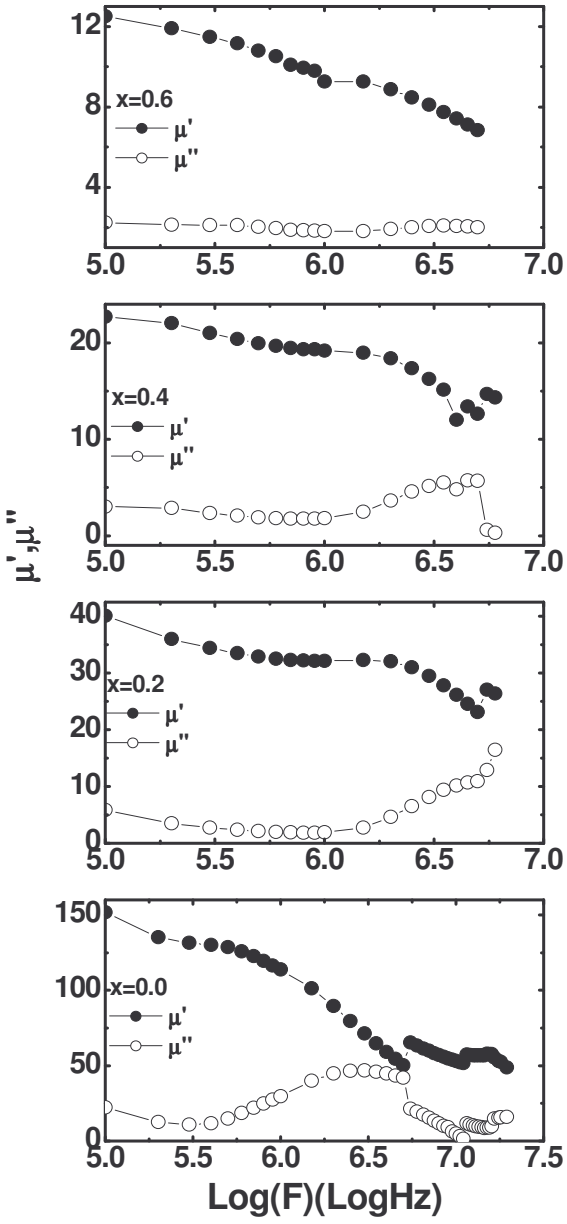

Fig.6b.4.3 Permeability (μ') spectra for x=0.0, 0.2, 0.4 and 0.6 compositions of $Y_{3+x}Fe_{5-x}O_{12}$ system at 300K

It is seen that μ' continuously decreases with increasing frequency. Such frequency dispersion in μ' is usually attributed to domain wall displacement [26]. The nature of permeability spectra is completely different when compared with permeability spectra of spinel ferrite systems [27-29], but quite consistent with permeability spectrum of YIG [30] . According to Globus [31-32] the shape of the permeability spectrum is relaxed for uniform and homogeneous grain size samples irrespective of the size of the grain and is the resonance type when the grain size is inhomogeneous. But according to Srivastava et al [30], the grain size is the predominant factor which controls the nature of permeability spectrum.

The spectra shown in Figure 6b.4.3, are of relaxed type. The relaxed spectra occur when for larger grains closure domains are present. It is found that for the same composition with constant magnetization on decreasing grain size permeability spectrum transfer from relaxed to mixed, to resonance, type behavior. For different compositions of garnet, range of grain size is very wide, for relaxed spectra it varies from 7.5-20 μm, for mixed spectra it changes from 4.6-15 μm while for resonance spectra grain size is varying from 1.4-6.5 μm [30]. In the present case average grain size for substituted garnets (x=0.2, 0.4 and 0.6) is much below than the lower limit of the grain size for relaxed type spectrum. Thus, one can expect mixed or resonance type nature of frequency dependent permeability spectrum. We have observed relaxed type nature of permeability spectrum for these compositions (Figure 6b.4.3). We feel that along with size of the grain, uniformity and homogeneity of the grain size play important role in deciding the nature permeability spectrum [31-32]. This argument is more clear based on SEM

image of x=0.6 composition, having average grain size of the order of 2.0 μm but with better homogeneity and uniformity. In figure 6b.4.4, is given the plot of the permeability spectrum of pure and Y^{3+}-substituted YIG sintered at 1200 ºC, which is of the resonance type.

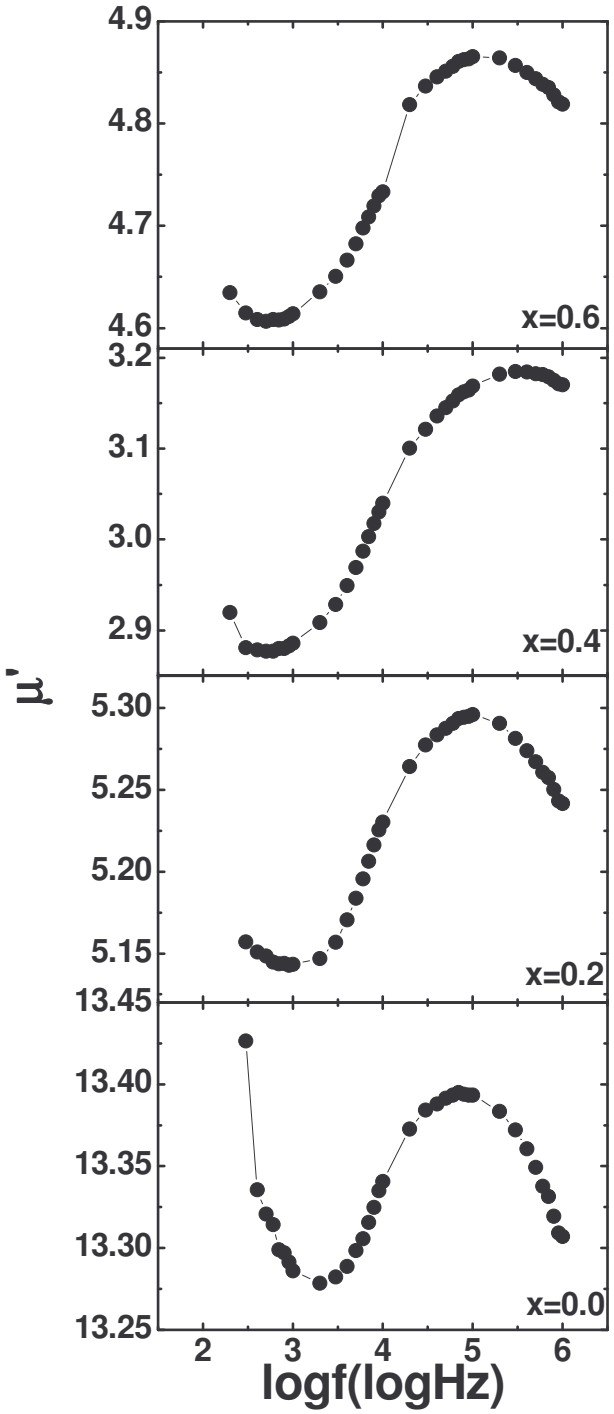

Fig.6b.4.4 Frequency variation of initial permeability for x=0.0, 0.2, 0.4 and 0.6 compositions of YIG sintered at 1200 ºC

The domain walls dynamics under external time varying fields has been studied by many workers [31, 33-35]. The equation of motion for domain walls is:

$$m_{\varpi}\ddot{z} + \beta_{\varpi}\dot{z} + \alpha_{\varpi} z = 2M_s H$$

where m_{ϖ} is the effective mass per unit area of the domain wall, β_{ϖ} is the damping constant and σ_{ϖ} is the stiffness constant. As discussed by Srivastava et al [30-35], the analysis of the relaxed spectrum can be carried out using above equation, if the term in m_{ϖ} or the term in α_{ϖ} is negligible. It has been shown that relaxed spectrum is obtained for increasing value of N (number of domain walls within a grain of polycrystalline garnet sample) with increase in M_s (saturation magnetization). In order to understand the result it is necessary to calculate the equilibrium number of domain walls which can exist within a grain of diameter D. This can be obtained by minimizing the total energy consisting of the wall energy and the magneto-static energy. If there are (2n+1) walls within a sphere of diameter D, the total energy is given by:

$$\varpi = \frac{\pi D^2}{4}\left[(2n+1) - \frac{n(2n+1)}{3(n+1)}\right]\sigma_{\varpi} + \frac{1}{2(n+1)}\frac{1}{2}\left(\frac{4}{3}\pi M_s\right)\left(\frac{1}{6}\pi D^3 M_s\right)$$

Minimizing ϖ with respect to n, the total number of domain walls, N within a grain become:

$$N = (2n+1) = 2\left[\frac{\pi}{6}\frac{M_s^2 D}{\sigma_{\varpi}} - \frac{1}{4}\right]^{\frac{1}{2}} - 1 \qquad (1)$$

The condition for the formation of one domain wall is given by N=1which leads to a critical grain diameter $D=D_c$ given by:

$$D_c = \frac{30}{4\pi}\frac{\sigma_\varpi}{M_s^2} = 2.39\frac{\sigma_\varpi}{M_s^2}$$

Equation (1) suggests that the equilibrium number N of domain walls reduces almost linearly with M_s for a constant grain diameter provided σ_ϖ is constant. Thus, it is clear that as the value of M_s is increased the number of domain walls within the grain increases, while for small values of M_s, N would tend to one which would mean that there will be one domain wall. In this case closure domains cannot be formed. The possibility of formation of closure domains increases as the number of walls increases.

For the relaxed spectrum one can expect the inertial term to be insignificant as discussed earlier. This can occur when closure domains are present so that the domain wall can move without any inertia and with a constant velocity as soon as it is subjected to as external force. In such cases the low frequency permeability will be large, as in the present observation. On the other hand, if the domain wall is anchored at the grain boundary, as will be the case without closure domains, the inertial term will be significant, leading to a resonance type spectrum and small low frequency permeability. From this we conclude that the relaxed spectrum is obtained when the closure domains are present and resonance spectrum when there are no closure domains. Drofenik [36, 37] has reported results that indicate that distances between pores account for variations in permeability. Samples with giant grains and included porosity owing to exaggerated grain growth still had higher permeabilities than those with normally grown grains provided the distance between pores were the same. Drofenik concludes that the large grained samples are less sensitive to grain boundary effects and thus the μ(T) curve is

more peaked (Figure 6b.4.5). The observed flatering of μ(T) curve for x>0.2 suggests reduction in grain size as evident from SEM analysis.

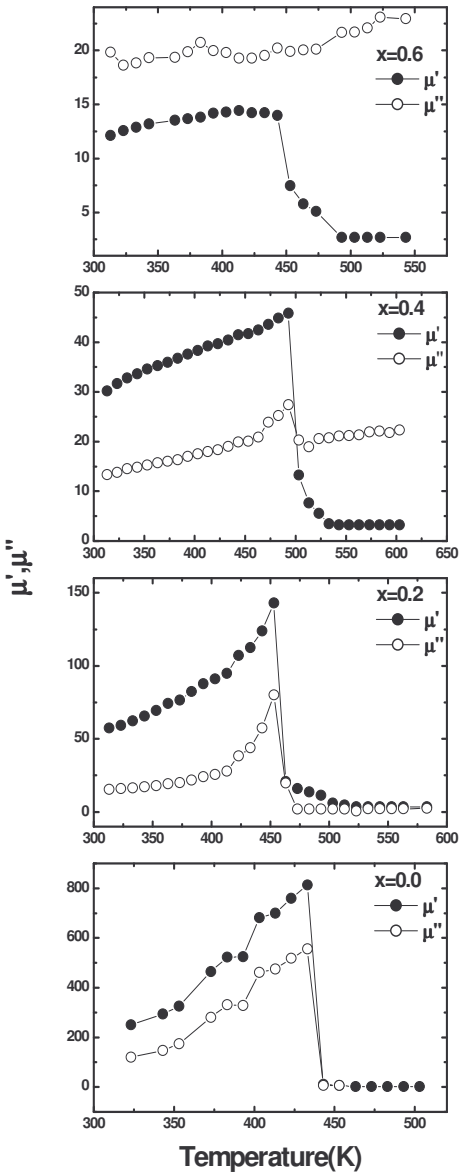

Fig.6b.4.5 Thermal variation of initial permeability for $Y_{3+x}Fe_{5-x}O_{12}$ system at applied frequency of 10 kHz.

Finally an attempt has been made to calculate the total number of domain walls, N within a grain and critical grain diameter D_c for which N reduces to 1, using following formulae [30]:

$$N = 2\left[\frac{\pi}{6}\frac{M_s^2.D}{\sigma_\varpi} - \frac{1}{4}\right]^{\frac{1}{2}} - 1$$

Here, the value of M_s=136 emu/cm^3 and D=6 μm for YIG sample sintered at 1500 ºC and $\sigma_\varpi = 0.11$ erg/cm^2 for the pure YIG are taken, therefore,

$$N = 2\left[\frac{3.14}{6}\frac{(136)^2(6x10^{-4}cm)}{0.11} - \frac{1}{4}\right]^{\frac{1}{2}} - 1$$

$$N = 2[52.80 - 0.25]^{\frac{1}{2}} - 1$$

$$N \sim 13.5$$

and $$Dc = 2.39\frac{\sigma_\varpi}{M_s^2}$$

$$Dc = 2.39\frac{0.11}{(136)^2} = 0.142\mu m$$

The value, N~13.5, is in excellent agreement to those reported for relaxed type of permeability spectrum [30].

Temperature variation of initial permeability μ', is shown in Figure 6b.4.5. Increase in temperature of the samples x=0.0 and 0.2, μ', initially increases gradually and then decreases rapidly. Near the transition temperature, T_p, μ' drops off sharply. The sharp drop in μ' during phase transition also suggests the single phase formation of the sample. This fact is confirmed by x-ray diffraction pattern analysis. For the samples with x=0.4 and 0.6 μ' increases slowly and drops off near T_p with tailing effect. Similar tailing effect due to paramagnetic contribution has been reported by Velenzulea et al [38]. The temperature at which μ' becomes zero is closed to Neel temperature (T_N) of that composition. Furthermore, the absence of an additional peak in

μ'→T curve suggests that there is no excess Fe^{2+} ion formation in the system [27].

In most of the magnetic materials, μ' increase with temperature upto the Neel/ Curie temperature T_N. This is because the anisotropy field usually decreases faster with temperature than Ms [39]. Both Enz [40] and Otha [41] have shown that the μ' is maximum at the temperature where the anisotropy constant K_1 changes sign. In our studies we have not observed any profound peaking in the μ'(T) variation for x=0.4 and 0.6 compositions. This may be because the rates of change of M_s and K_1 with temperature are nearly same. From the thermal variation of μ'' it is seen that with the increase of temperature μ'' increases, reaches a maximum near T_N and then falls sharply near to T_N. The loss becomes large near to T_N, which may be due to the damping effect on the domain walls [42].

Loss factor (LF) and Temperature factor (TF) determination:

The ratio of the imaginary part representing the losses in the material to the real pert of the permeability is a measure of the inefficiency of the magnetic system. It is called the magnetic loss tangent.

$$\tan \delta_m = \frac{\mu''}{\mu'}$$

If we normalize the loss tangent per unit permeability, we have a material property describing the loss characteristics per unit of permeability. This property is called the loss factor (L.F.).

$$LF = \frac{\tan \delta_m}{\mu'}$$

Obviously this parameter should be as low as possible.

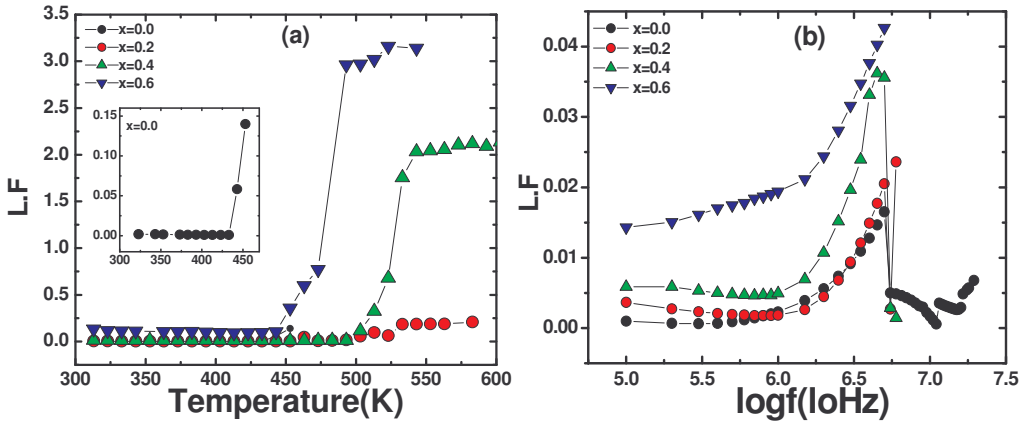

Fig.6b.4.6 (a) Thermal (f=10 kHz) (b) Frequency (T=300K) variation of loss factor for different compositions

It is seen that for all the compositions L.F tends to increase with the increase in temperature. The increase of L.F. is due to the thermal randomization of domains. The L.F. are found initially to increase with increase in frequency for all the compositions of $Y_{3+x}Fe_{5-x}O_{12}$ system. It is seen that L.F. increases with increase in x as a function of temperature and frequency. For x=0.0 and 0.2 compositions increase in L.F. is small but for x=0.4 and 0.6 compositions it jumps to relatively high values (Figure 6b.4.6). This is mainly due to the fact that x=0.0 and 0.2 compositions are single phase while x=0.4 and 0.6 compositions are of mixed phase. As discussed earlier ceramic imperfections like second phase leads to lower value of permeability and higher value of losses. At higher frequencies (f>1MHz), L.F. increases rapidly. The compositions with x=0.0, 0.2 and 0.4 show resonance peak while x=0.6 composition shows the tendency for a resonance loss peak, which occurs at frequencies higher than those used in this work. At the resonance maximum energy is transferred from the applied field to the lattice resulting in the rapid increase in L.F. Normally two resonance peaks are observed in ferrites, one at lower frequencies (10-100MHz) due to domain

wall displacement and the other due to domain rotation at high frequencies (~1GHz) [43,44]. As is evident from Figure 6b.4.6 (b), the observed peak corresponds to resonance frequency of domain wall displacement.

Of these two natural resonances, the resonance of rotation magnetization is caused by the action of the anisotropy field H_a, which is expressed in terms of the resonance frequency (f_r) as:

$$H_a = \frac{2\pi f_r}{\varsigma}$$

In the equation, ς is the gyromagnetic constant given by: ς = 8.791x10^6 g (Oe^{-1}.s^{-1}), where g is the gyromagnetic ratio. The resonance frequency due to domain rotation and the anisotropy field thus calculated with the assumption of g=2 Magnetocrystalline anisotropy (K_1) is related with saturation magnetization (M_s) and anisotropy field as:

$$H_a = \frac{K_1}{C.M_s}$$

where C is 1/2 for K_1>0 and -3/4 for K_1<0. In calculation of K_1, -3/4 was taken for C since K_1 for yttrium iron garnet is known to be negative, (K_1= - 6.7x10^3 erg/cm^3 at 300K) [45].

The value of anisotropy field, H_a, has been calculated using following formula, which inturn used to calculate anisotropy constant (K_1).

$$H_a = \frac{2}{3}(1 - f)4\pi M_s.\mu_{rk}^{-1}$$

where μ_{rk} is the rotational permeability and f is the pore fraction (1-ρ/ρ_x; ρ=bulk density and ρ_x= X-ray density) of the sample. On the other hand the value of μ_{rk} can be roughly described by the empirical relation:

$$\mu_{rk} = \frac{\mu'}{1+D} \approx \frac{d\mu'}{dD}$$ (slope from Figure6b.4.1(b))

where D is the grain diameter.

We have calculated these parameters for the pure YIG considering μ'=250, D=6 μm, f =0.11 and M_s =136 determined from other measurements. Accordingly, μ_{rk} is found to be 36 that gives, H_a= 28.4 Oe and K_1=-2.89x10^3 erg/cm^3. The value of H_a is further used to approximate the resonance frequency and in the present case it is found to be: f_r =79.5 MHz. That suggests resonance peak due to domain rotation occurs at this frequency, which well beyond upper frequency limit to which measurements are made in the present work.

The low frequency permeability is observed [31] to increase linearly with grain diameter. The contribution to permeability from domain wall translation is given by:

$$\mu'-1 = \frac{3\pi}{4} M_s^2 \frac{D}{\sigma_\omega \left(1 - \frac{\omega^2}{\omega_0^2}\right)}$$

where σ_ω is the wall energy per unit area, ω is the operating frequency, ω_0 is the domain wall resonance frequency, Neglecting $(\omega/\omega_0)^2$ compared to 1 as $\omega_0 >> \omega$, we obtain the value of σ_ω using the following formula, which is equal to 0.11 erg/cm^2.

$$\mu'-1 = \frac{3\pi}{4} M_s^2 \frac{D}{\sigma_\omega}$$

$$\sigma_\omega = 2.36 \frac{M_s^2 D}{\mu'-1}$$

Finally, we have calculated the wall permeability (μ_ω) and the spacing between domain walls (d_s) using the following formula [42, 46-47] just to get complete picture of permeability spectrum and grain structure.

$\mu_\omega = \mu' - (\mu_{rk} - 1)$ and

$$d_s = \frac{5M_s^2 D}{\pi K_1^2 \mu'}$$

The value of μ_ω is found to be 215.3. It is seen that the magnitude of wall permeability is greater than the magnitude of rotational permeability by a factor of almost 6. This suggests that the main contribution to initial permeability arises from domain wall motion. Magnetization in ferrites proceeds via two mechanisms, domain wall motion and domain rotation. The energy required for domain wall displacement being lower than that required for domain rotation, magnetization due to the former process is greater. The value of spacing between domain walls is found to be 0.45 μm.

The variation in the permeability with temperature is often very important consideration in magnetic component. If we plot permeability as the function of temperature, the slope over a specific temperature range of operation can be expressed as a material parameter called the temperature factor (T.F.) which is defined as:

$$T.F = \frac{\Delta\mu'}{\mu'^2.\Delta T}$$

where $\Delta\mu$=Difference in permeability (μ_2-μ_1) at T_2 and T_1 respectively and ΔT=change in temperature (T_2-T_1) and μ' is permeability at a standard temperature.

The temperature factor can be used to predict the variation in magnetic properties of magnetic component to those reported. Data on T.F. for the compositions of Y^{3+}-substituted YIG are given in Table 6b.4.1.

Table 6b.4.1 Temperature factor T.F. at 10 kHz

Y^{3+}-content (x)	T.F. $x10^{-6}$
0.0	79.4
0.2	136.78
0.4	80.36
0.6	103.16

References

1. C.G. Whinfrey, D.W. Eckort and A. Tauber, J Am. Chem. Soc. 82 (1960) 2695.
2. P. Coppens and M. Eibschuttz, Acta Crst. 19(1965)524.
3. C.M. Kanamadi, R.G. Kharabe, R.B. Pujar and B.K. Chougule, Ind. J. Phys. 79(3)(2005)257.
4. A. M. Hofmeister and K.R. Campbell, J. Appl. Phys. 72(2)(1992)638.
5. Osama Mohamed Hemeda, M.M. Barakat and D. M. Hemeda, Turk. J. Phys. 27(2003)537.
6. D.S. Schmool, N.Keller, M.Guyot, R. Krishnan and M. Tessier, J. Magn. Magn. Mater. 195(1999)291.
7. Sanjay Mathur, Michael Veith, Rasa Rapalaviciute, Hao Shem, G. F. Goya, W.L. Martins Filho and T.S. Berquo, Chem. Mater. 16(2004)1906.
8. G.F. Goya, T.S. Berquo, F.C. Fonseca, M.P. Morales, J. Appl. Phys. 94(2003)3520.
9. M.C. Chhantbar, Ali Yusuf, Ravi Kumar and H.H. Joshi, Hyperfine Interactions 184(2008)1.
10. M.W. Thompson: Defects and Radiation damage in metals. Cambridge University Press, Cambridge (1969).
11. F. Studer, C. Houpert, D. Groult, M. Toulemonde Radiat. Eff. Defects. Solids 110(1989)55.
12. M. Toulemonde, G. Fuchs, N. Nguyen, F. Studer and D. Groult, Phys. Rev. B. 35(13)(1987)6560.

13. C. Houpert, M. Hervieu, D. Groult, F. studer and M. Toulemonde, NIM B 32(1988)393.
14. P.U. Sharma, K.B. Modi, V.K. Lakhani, K.B. Zankat and H.H. Joshi Ceram. Int. 33(2007)1543.
15. R.A. Brand, NIM B 28(3)(1987)398.
16. R.D. Shannon, C.T. Prewitt, Acta Crystallogr. B. 25(1969)925.
17. S.H. Lee, K.P. Chae, S.W. Hong and Y.B. Lee Solid State Commun. 83(2)(1992)97.
18. Y.B. Lee, K.P. Chae and S.H. Lee, J. Phys. Chem. Solids. 62(2001)1335.
19. M. Eibschutz, S. Shitrikman and D.Treves, Phys. Rev. 156(2)(1967) 562.
20. M.A. Gilleo, J. Phys. Chem. Solids 13 (1957)33.
21. M.C. Chhantbar, K.B.Modi, G.J.Baldha, H.H. Joshi, R.V. Upadhyay and Ravi Kumar, NIM B 244 (2006)124.
22. Alex Goldman, “Modern ferrite technology”, 2nd edition Springer, USA (2006) p.30-31.
23. D. Polder, Inst. Electron Engrs. Part II 97(1950)246.
24. J.J. Went and H.P.J Wijn, Phys. Rev. 82 (1951) 269.
25. H.G.Brion and Nembark, Phys. Stat. sol. (a) 26 (1974) 559.
26. G.T.Rado and A.Terris, Phys.Rev. 83 (1951)177.
27. B.R.Karche, B.V.Khasbardar and A.S. vaingankar J. Magn. Magn, Mater. 168(1997)292.
28. R. Laishram and C. Prakash J. Magn. Magn. Mater. 305 (2006) 35.

29. A.K.Singh, T.C.Goel, R.G. Mendiratta, O.P.Thakur and C.Prakash, J. Appl. Phys. 92 (7)(2002)3872
30. Om Prakash, R.Aiyer and C.M.Srivastava Mater. Sci. Bull. 1(1) (1979) 49
31. A.Globus, Euro. Phys. Soc. Conf. on soft magnetic mater. (Cardiff)(1975)2.
32. A.Globus, Int. Conf. Ferrites 2, Bellevue, France, suppl. 70 J.Phys. c1-1(1976)
33. G.T.Rado, Rev.Mod. Phys. 25(1953)81
34. J.Smit and H.P.J. Wijn, Ferrites(NY: John Wiley) (1959) 27
35. C.M. Srivastava, S.N. Shringi, R.G. Srivastava and Nanadikar, Phys. Rev. B. 14 (1976)2032.
36. M. Drofenik, S.Besenicar and M.Limpel, Advances in ceramics 16(1985)229.
37. M.Drofenik, Am. Ceram. Soc. Bul. 65 (1986)656.
38. R. Velenzulea, J.Mater. Sci. Lett. 15 (1980) 3173
39. J.Smit, “Magntic properties of materials” (McGraw Hill Book Company, 1971)
40. U.Enz, Proc. IEEE 109(1962)246
41. K.Ohta, J.Phys. Soc. Jpn. 18(1963)685.
42. A.M. Sankpal, S.V.Kakatkar, N.D. Chaudari, R.S. Patil, S.R.Swant and S.S. Suryavanshi, J.Mat. Sci. 9(1998)173.
43. G.T.Rado, R.W.Wright and W.H. Emerson, Phys. Rev. 81(1950)273.
44. V.A.M. Brabers, Handbook of magetic materials, edited by K.H.J. Buschow(Elsevier Sci. Amsterdam 1995 p:189)

45. D.J. Craik, Magnetic oxides,John Wiley & Sons N.Y(1975) p.244.

46. R.B.Pujar, S.N.Kulkarni, C.B. Bellad and B.K. Chougale, J.Mat. Sci lett. 16(1997)1668.

47. M. Kernsten, Phys. Z. 44(1943)63.

6c.1 Effect of SHI irradiation on temperature dependent resistivity of Y-Fe(Y)-O system

Conductivity in ferrites is reported [1,2] to occur as a result of electron/hole hopping between ions of the same element existing in different valence states on equivalent lattice sites. Occurrence of ions in more than one valence state is caused by the preparation conditions especially the sintering temperature.

The variation of resistivity ($\log_{10} \rho_{dc}$) as a function of Y^{3+}-content (x) at 373K is represented in Table 6c.1.1.

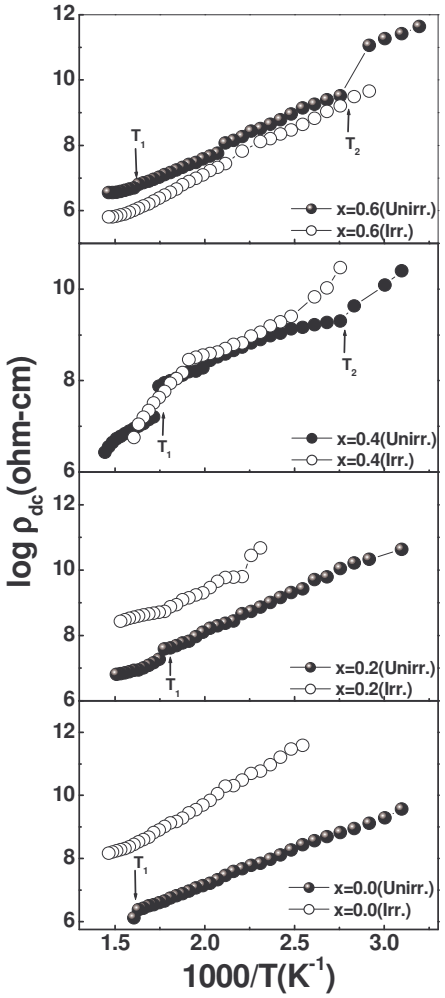

Fig. 6c.1.1 Thermal variation of dc resistivity for Y-Fe(Y)-O system, before and after irradiation

Table 6c.1.1 Compositional dependence of dc resistivity ($log_{10}\rho_{dc}$) for unirradiated samples at 373K

Y^{3+}-content (x)	$Log_{10}\ \rho_{dc}$ (log ohm-cm) (373K)
0.0	8.694
0.2	9.784
0.4	9.268
0.6	9.388

The resistivity in general, increases with increase in Y^{3+} concentration (x). This happens because the replacement of Fe^{3+} by Y^{3+} in $Y_{3+x}Fe_{5-x}O_{12}$ system reduces conduction through tetrahedral and octahedral sites. The incorporation of Y^{3+} ions which do not participate in the conduction process, limits the degree of $Fe^{3+} + Fe^{3+} \leftrightarrow Fe^{4+} + Fe^{2+}$ conduction that occurs. Thus, the efficient method of curtailing the conduction process is the replacement of the effective ion (Fe^{3+}) by less effective ones (Y^{3+}). The variation of dc resistivity as a function of temperature [log $_{10}\rho_{dc}$ versus 1000/T (K^{-1})] for x=0.0, 0.2, 0.4 and 0.6 compositions before and after SHI-irradiation is shown in Figure 6c.1.1. The behaviour is similar to that known in the case of ferrites with a change in the slope of the graphs at a certain temperature. It is interesting to note that the nature of the curve for the compositions with x=0.0 and 0.2 is different from that for x=0.4 and 0.6 compositions. For the former garnet compositions, curve consists of two slopes with single transition, while for x=0.4 and 0.6 have three distinct regions and two breaks. The change in the slope may be due to the Neel temperature [3] or to a change in the conduction mechanisms [4]. The transition temperature T_1 is nearly equal to the Neel temperature deduced from low field ac susceptibility measurements. Of course, such a change is less marked (except for x=0.4 composition) for

x=0.0-0.6 compositions. We have also observed low temperature transition marked as T_2~363K for x=0.4 and 0.6 compositions. In the case of Nd-substituted $LaFeO_3$ such a transition has been observed about 378-393 K [5], well below to the Neel temperature (T_N=738K, for $LaFeO_3$). Thus, low temperature transition may be due to presence of Yttrium orthoferrite, $YFeO_3$-phase, in the x=0.4 and 0.6 compositions.

The dc resistivity value for irradiated sample is much higher than its unirradiated counterpart of x=0.0 composition. On increasing Y^{3+}-concentration (x), this difference decreases for x=0.2 composition, for x=0.4 only for low temperature region difference is observed while for x=0.6 composition dc resistivity curve for unirradiated and irradiated sample, overlaps with each other.

The resistivity value of polycrystalline materials is expected to increase after irradiation. It has been shown through the study of swift heavy ion irradiation of magnetic insulators that irradiation of solids with the energetic particle beams leads to the creation of a wide variety of defect states (point defects, cluster of defects) that inhibits the long range ferromagnetic order through redistribution of cations in the localized defected region leading to the formation of paramagnetic centres. These, paramagnetic centres hinders the electron /hole conduction between $Fe^{2+}\leftrightarrow Fe^{3+}$ or $Fe^{3+}\leftrightarrow Fe^{4+}$ through equivalent cationic sites. Thus, resistivity increases after irradiation as observed for x=0.0 and 0.2 compositions. It is found that for x=0.4 and 0.6 compositions resistivity value at different temperatures before and after irradiation does not show much difference. This is consistent with the fact that compositions with x=0.4 and 0.6, contain yttrium orthoferrite phase, which is

irradiation hard phase and as a result no effect of SHI-irradiation on resistivity value has been observed. On the other hand from X-ray diffraction pattern analysis it is established that after irradiation $YFeO_3$ phase reduces considerably. This is also reflected in resistivity curves for x=0.4 and 0.6 compostitions where low temperature transition (T_2) belongs to $YFeO_3$ phase is not clearly observed, as in the case of unirradiated compositions.

6c.2 AC resistivity and dielectric properties of $Y_{3+x}Fe_{5-x}O_{12}$ system as a function of composition, frequency and temperature before and after irradiation

There are large controversies regarding the conduction mechanisms responsible for electrical and dielectric behaviour of pure and substituted garnet systems in single crystal and polycrystalline form.

From resistivity and thermoelectric power measurements on Hf^{4+}-doped yttrium iron garnet (YIG) in the temperature range 500-1000K, Elwell and Dixon [6] concluded that the conduction should be described by localized model rather than the band model. Studies on electrical conduction in Si^{4+}-doped YIG by Fontana and Epstein [7] in the temperature range 293-473K is interpreted as arising from localized hopping of electron amongst four Fe^{3+} cation- sites around Si^{4+} impurity sites. The dc resistivity and thermoelectric power measurements on Sn and Sb substituted Ho-Ca-Fe-O garnets [8], it is concluded that the conduction is due to thermally activated hopping p-type conduction owing to Fe^{4+} ions. Results of Lal et al. [9,10] and Petrov et al. [11] in high temperature range > 600K and activated hopping of p-type charge carriers in YIG. The conduction is proposed to be due to the formation of small polarons involving band-like conduction mechanism at low temperatures and by thermally activated hopping mechanism at high temperatures for electric and dielectric properties of single crystalline YIG [12]. The experimental results on the dc electrical conductivity and the seebeck coefficient of n-type and p-type singe crystals of YIG in the temperature range 600-1500K have been explained by Larsen and Metselaar [13]. According to

them the localized hopping model and small polaron do not give reasonable explanation of the experimental data. On the other hand large polaron model describes the data reasonably well but the estimated motilities and other parameters are not unambiguously determined and further experimental evidence is required.

Om Prakash and Bahadur [14] have explained the electrical properties of Ti-substituted YIG on the basis of electron hopping model. The treatment of conduction by polarons is discussed by several workers [15, 17]. Theoretical work by several workers over the years has provided same understanding of conduction in oxides and transition metal compounds [18]. For these materials, the interaction between electrons and optical phonons is strong and the conduction is explained on the basis of polarons.

In the present work our aim is to explain experimental results in best possible manner based on existing models and theory of conduction mechanism.

Small and large polaron

The object that results when an electron in the conduction band of a crystalline insulators or semiconductor polarizes or otherwise deforms the lattice in its vicinity is called polaron. The polaron comprises the electron plus its surrounding lattice deformation. Polarons can also form from holes in the valence band. If the deformation extends over many lattice sites, the polaron is ‘large’ and the lattice can be treated as a continuum. In this case of the system can be regarded as free electron plus a dielectric continuum representing quasi-particles (large polarons) having a mass which is somewhat larger than the bare-electron mass. Charge carriers inducing

strongly localized lattice distortions form 'small' polarons. In other words, the term small polaron refers to the unit comprising the severely localized (that is small) self trapped excess charge and the associated pattern of displaced atomic equilibrium positions.

The variation of ac resistivity ($\log_{10} \rho_{ac}$) with frequency at several temperatures ($\rho_{ac}(f,t)$) below and above magnetic phase transition is shown in the Figure 6c.2.1. The effect of SHI irradiation has been studied by performing same experiments on x=0.0, 0.2 .4 and 0.6 compositions of $Y_{3+x}Fe_{5-x}O_{12}$ system. Following observations can be drawn from $\rho_{ac}(f,t)$ curves of different compositions before and after irradiation. (i) ρ_{ac} decrease with increase in frequency and temperature. (ii) For x=0.0 and 0.2 compositions beyond particular frequency (> 1MHz) ρ_{ac} is found to increase, after irradiation this effect get pronounced but with increase in temperature observed rise in ρ_{ac} with frequency decreases. (iv) The frequency from which ρ_{ac} starts to increase shifts towards higher frequency side on increasing temperature.

The compositions under study show decrease in ρ_{ac} with temperature as well as with frequency upto 1MHz, before and after irradiation, which is the normal behaviour of ferrites. It has been observed that for all the samples the variation of ρ_{ac} is sensitively dependent on the frequency and temperature. This suggests that grain boundary contribution to the conductivity is not sufficiently minimized for highly pressed pellets even at high temperature. As discussed earlier for $Y_{3-x}Fe_{5+x}O_{12}$ system, on increasing frequency hopping of charge carrier also increases resulting in an increase in the conduction process thereby decreasing the resistivity. But, observed increase in ρ_{ac}

beyond certain frequency, can not be explained on the basis of hopping type conduction mechanism. For these materials the interactions between the charge carriers and optical phonon is strong and the conduction is explained on the basis of polarons. The small polaron conduct in band like manner upto a certain temperature, the resistivity showing a decrease with frequency. At higher temperature the conduction is by thermally activated hopping mechanism [16-17]. In the polaron model, the conductivity is by band mechanism at all temperatures and the ac resistivity increases with frequency. As the temperature is raised, number of large polarons decreases and that of small polaron increases. Finally the former becomes negligible and small polarons become the sole mobile charge carriers and thus, at high temperature T>573K for x=0.0 composition before and after irradiation, for x=0.2 composition (T>373K) before irradiation, for x=0.4 and 0.6 compositions (T>300K) before and after irradiation, decrease in ρ_{ac} with frequency is observed.

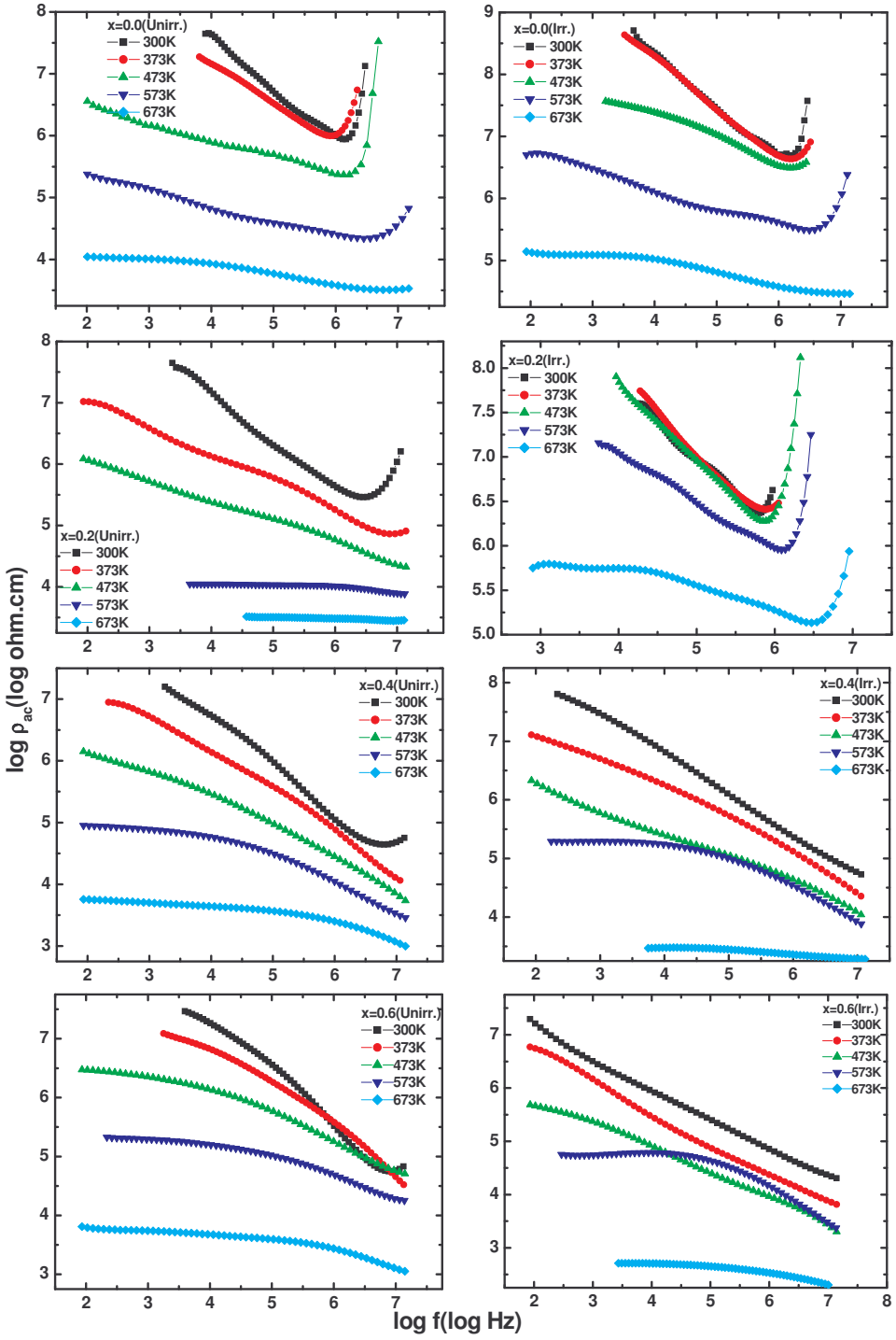

Fig.6c.2.1 Pellet electrical resistivity versus applied signal frequency for x=0.0, 0.2, 0.4 and 0.6 compositions at constant temperatures

As an evidence for small polaron conduction, we have examined the variation of conductivity with frequency on the basis of relaxation process, as applied to bound small polaron [18-19]. Adler and Feinleib [19] have shown that for conduction by small polarons the conduction increases with frequency and the following relation holds good:

$$\sigma_{\omega} - \sigma_{dc} = \frac{\omega^2 \tau^2}{1 + \omega^2 \tau^2}$$

where ω is the angular frequency and τ the staying time (~10^{-10}sec) for frequencies $\omega^2\tau^2 < 1$. Log (σ_ω-σ_{dc}) versus log ω^2 should be a straight line. Typical plot of log (σ_ω-σ_{dc}) as a function of ω^2 at 473 K for x=0.0 composition is shown in Figure 6c.2.2. It can be seen that the plot is straight line; this indicates that the conduction is due to small polarons.

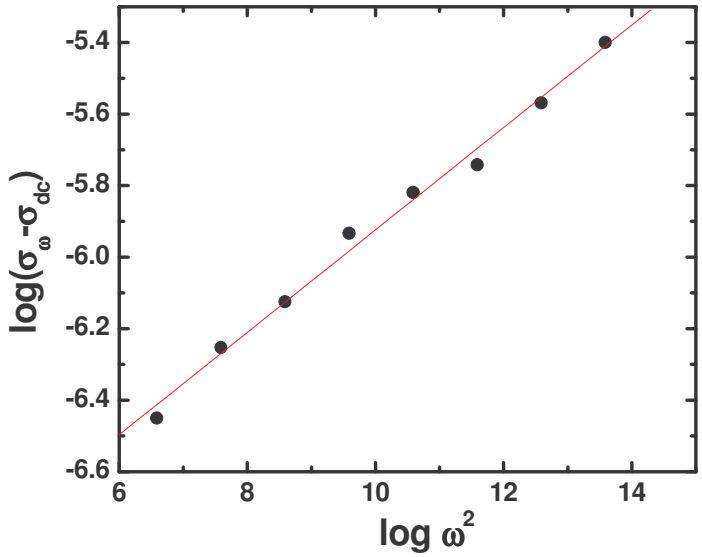

Fig.6c.2.2 Variation of Log (σ_ω-σ_{dc}) with log ω^2 at 473 K for x=0.0 composition

From our limited data it is difficult to decide the exact mechanism for conduction. In fact the contribution is not due to any single mechanism.

Determination of small polaron parameters for $Y_3Fe_5O_{12}$

The important parameters associated with polarons are polaron radius, r_p, polaron binding energy W_p, effective mass, m_p, and dimensionless electron phonon coupling constant, α. The polaron parameters were evaluated from the data on dielectric constant and other crystal parameters using the relations given by Austin and Mott [15].

The polaron radius, r_p, is given by $r_p = \frac{1}{2}\left(\frac{\pi}{6N}\right)^{\frac{1}{3}}$, where N is the number of sites per unit volume (=160/a^3, a= lattice constant= 12.380x10^{-8}cm). The polaron binding energy, W_p is given by $W_p=e^2/2\varepsilon_p r_p$, with $\varepsilon_p=(\varepsilon_\infty.\varepsilon_0)/ (\varepsilon_0-\varepsilon_\infty)$ where ε_∞ and ε_0 are the optical and static values of dielectric constant. The values ε_∞=4.84 and ε_0= 12.0 at I MHz of frequency at 300K for $Y_3Fe_5O_{12}$ composition are taken from the literature [20, 21]. The value of r_p turns out to be 0.919 Å and the value of W_p is found to be: 0.992 eV, that are in agreement to those reported for single crystalline YIG [12].

The two important parameters associated with polarons are the dimensionless coupling constant α and the effective mass of the polaron m_p. These can be calculated by the relations [22]:

$\alpha^2 = W_p/(0.1\hbar\omega_0)$

and m_p= 0.02 $m^*\alpha^4$

where $m^* = 20\varepsilon_p\hbar\omega_p / e^4 = 5.88x10^2 m_e$ [12], ω_0 is the frequency of polar optical mode and m* is the rigid band mass of the electron. The value of ω_0 was determined from the formula: $\omega_0=2\pi k\theta/h$, where θ= Debye temperature =600K zero porosity corrected value as compared to θ =497 K for porous medium,

Table 5a.6.1).The value of ω_0 is found to be 7.85 x 10^{13} Hz, α=13.86 and m_p= 1.3 x 10^5 m_e. For small polarons r_p should be less than the interionic distance (Table 5a.1.2), and coupling constant should be greater than 6 [18]. The values of the parameters are appropriate for small polarons.

6c.3 Dielectric Constant

The logarithmic frequency (f) dependence of dielectric constant (ε') and the loss tangent (tanδ) of dielectric permittivity and the real (M') and imaginary (M'') parts of the electric modulus are shown, respectively, in Figures 6c.3.1-6c.3.2 and 6c.4.1 - 6c.4.2 at temperatures varying from 300 to 673K before and after irradiation by swift heavy ions. The dielectric behaviour of the x=0.0, 0.2, 0.4 and 0.6 compositions of $Y_{3+x}Fe_{5-x}O_{12}$ system has been studied before and after irradiation over a range of frequency at different temperatures (Figure 6c.3.1). Initially, the value of ε' is very high, further, ε'decreases gradually with increasing frequency and showing dispersive behaviour at low frequencies. These are characteristic of dielectric material. The phenomenon of dielectric dispersion in ferrites has been explained on the basis of Maxwell-Wagner model and Koop's Phenomenological theory of dielectrics (section 5c).

The observed dispersion of the dielectric constant (ε') can be explained on the basis of hopping conduction between Fe^{2+} and Fe^{3+} (n-type conduction), Fe^{3+}-Fe^{4+} (p-type conduction) pairs of ions. In ferrites it is well known that the samples consist of well conducting grain boundaries. The charge carriers reach the grain boundary through hopping. If the grain boundary resistance is high enough, charge carriers pile up at the grain boundaries and produce polarization. However, as the frequency of the applied field increased, the charge carriers reverse their direction of motion more often. This decreases the probability of charge carrier reaching the grain boundary and as a result polarization decreases. Therefore, polarization decreases with increasing frequency of the applied field.

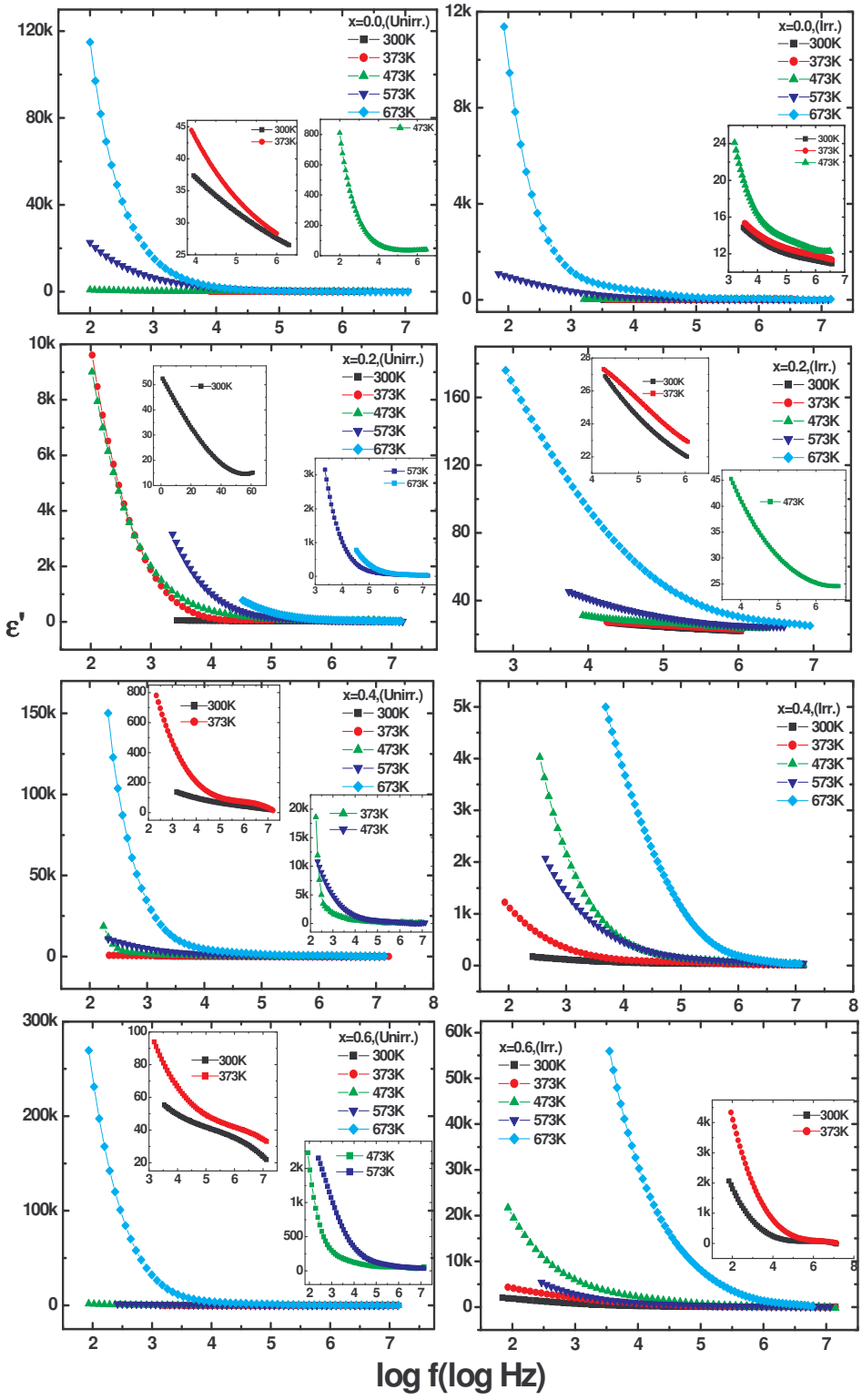

Fig.6c.3.1 Variation of real part of dielectric constant (ε') with frequency at different temperatures for Y-Fe(Y)-O system, before and after irradiation

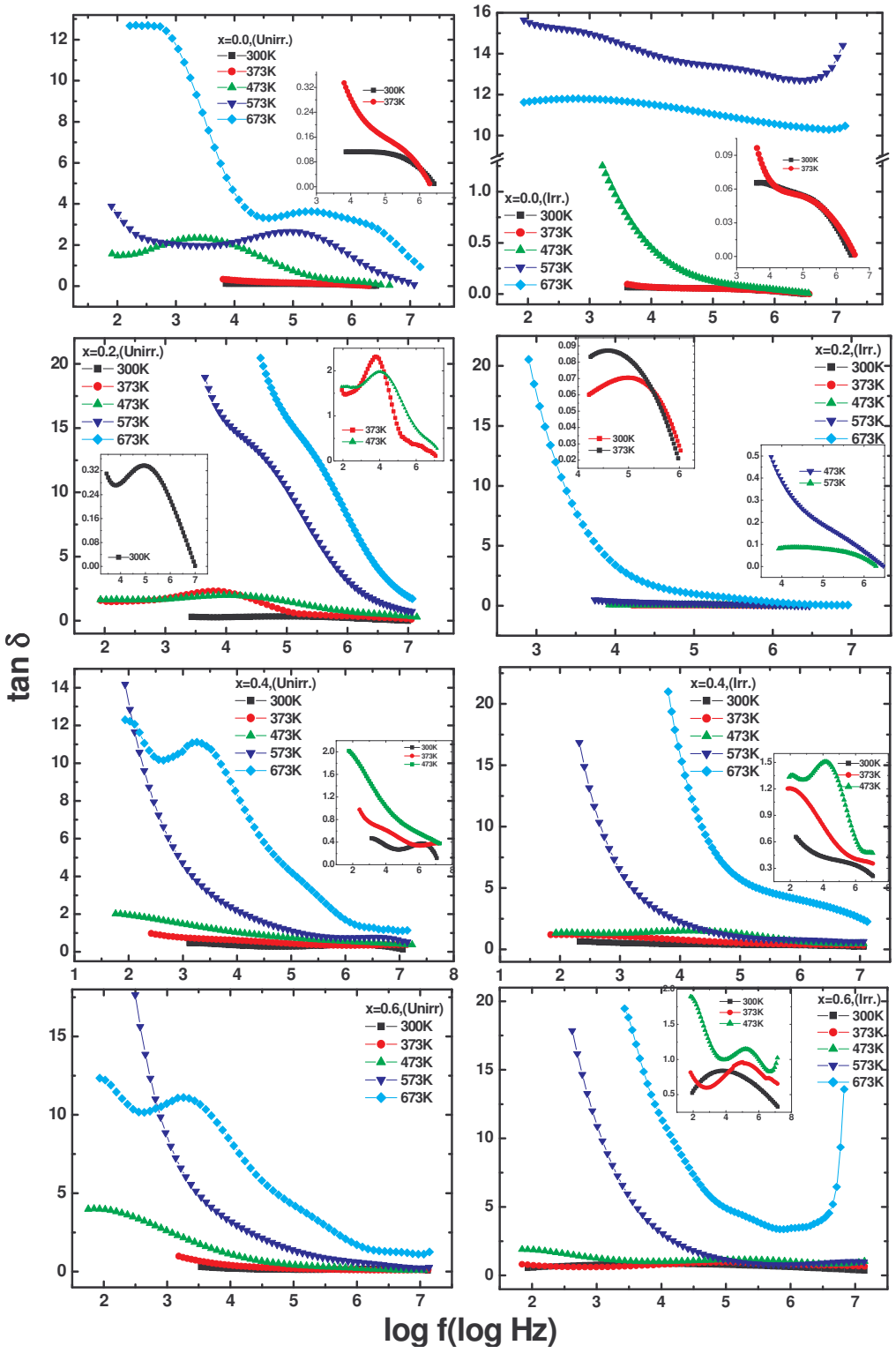

Fig.6c.3.2 Variation of loss tangent (tanδ) with frequency at different temperatures for Y-Fe(Y)-O system, before and after irradiation

Figure 6c.3.2 depicts the variation of loss tangent (tanδ) as a function of frequency at different temperature. The loss peaks are present in these graphs. The position of the peak shifts to higher frequency side with increasing temperature. This type of property indicates the relaxation behaviour in the materials [23].

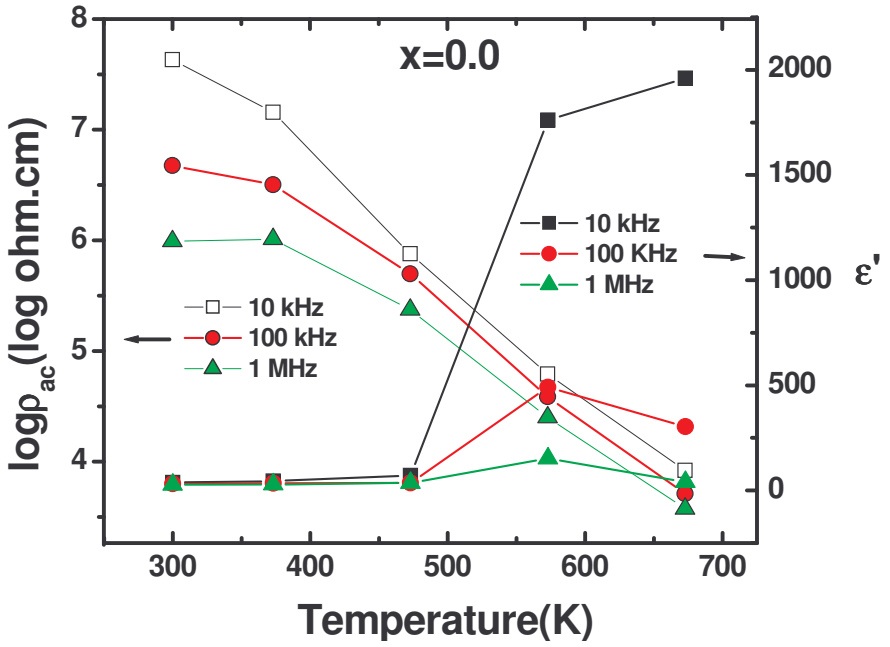

Fig.6c.3.3 Variation of ρ_{ac} and ε' with temperature for selected frequencies for x=0.0 composition of Y-Fe(Y)-O system

Figure 6c.3.3 shows the variation with temperature of the dielectric constant (ε') and ac resistivity (ρ_{ac}) measured at three different frequencies, ε' practically remains constant upto a temperature of 473K but then starts increasing. A slight increase in ε' with temperature is the usual trend in semi-conducting/ionic solids. This happens because the lattice expands and the polarizability of the ion is affected by changes in the temperature and the available volume. However this sharp increase in ε' may be due to an increase in conductivity (or decrease in resistivity). The trend of the increase

in ε' is very similar to the trend of decrease in resistivity. Like decrease in $\rho_{ac,}$ there is very little increase in ε' upto a temperature of 473 K; then there is an exponential increase in ε' with temperature and for $T \geq 573$ K the rate of increase becomes slow. At higher temperature ($T \geq 473$ K), there is a predominant formation of large polarons. This formation of polarons will greatly increase the polarization and hence ε'. The slow increase in ε' for $T > 573$ K may be showing the conversion of large polarons into small polarons.

6c.4 Electric Modulus

The 'electric modulus' formalism, first introduced by McCrum et al [24] and intensively used for the investigation of electrical relaxation phenomena by Macede and Moynihan [25,26], is defined as the inverse quantity of complex permittivity by the following equation:

$$M^* = \frac{1}{\varepsilon^*} = \frac{1}{\varepsilon' - j\varepsilon''} = \frac{\varepsilon'}{\varepsilon'^2 + \varepsilon''^2} + j\frac{\varepsilon''}{\varepsilon'^2 + \varepsilon''^2} = M' + jM'' \quad (1)$$

where M' is the real and M'' is the imaginary part of electric modulus ε' the real and ε'' the imaginary part of permittivity. The use of electric modulus offers some advantages in interpreting bulk relaxation processes since by its definition variation processes since by its definition variation in the large values of permittivity and conductivity at low frequencies are minimized. Thus, common difficulties like electrode nature and contact, space charge injection phenomena and absorbed impurity conduction effects, which appear to obscure relaxation in the permittivity, can be resolved or even ignored [27].

The recorded dielectric data were first expressed in terms of real and imaginary part of permittivity and then transformed, via equation (i) to the electric modulus formalism. Arguments for the resulting benefits of the electric modulus presentation have been exhibited and discussed elsewhere [28, 29]. The real part of electric modulus (M') versus frequency of the compositions with x=0.0, 0.2, 0.4 and 0.6 is shown in Figure 6c.4.1 at temperatures varying from 300K to 673K before and after irradiation.

It can be clearly seen that values of M' increase with frequency do not show saturation behaviour, while values of ε', as expected, decrease to an almost constant value. In the frequency range of this transition, peaks in the

values of M'', are developed, indicating a relaxation process, which is not clearly evident, in the values of tanδ. An increase in temperature, leads to a decrease in the frequency range studied.

For x=0.0 composition, in the electric modulus presentation, asymmetric peaks are formed, their maxima increase with increase of temperature and shift at the same time towards the right side of the frequency spectrum thus providing means for study of relaxation. The low frequency side of the peak in M'' versus f curves signifies the frequency range in which charge carriers can perform successful hopping from one site to the neighbouring site while high frequency side of the peak represents the range of frequencies in which charge carriers are spatially confined to their potential well [30]. The region where peak occurs is indicative of the transition from long range to short range mobility with increase in frequency. This type of behaviour of the modulus spectrum is suggestive of temperature dependent hopping type mechanism for electrical conduction in the system. After, irradiation, at a particular temperature peak shifts towards lower frequency side, peak intensity and peak broadening increases. The broadening of the peak points out the spread of relaxation with different mean time constant and non-Debye type of relaxation in the material.

On the other hand for x=0.2, 0.4 and 0.6 compositions, signature for two relaxation peaks in M'' versus f spectra is observed (Figure 6c.4.2). The existence of two relaxation peaks is clearly evident from Cole-Cole plots of M'' versus M' (Figure 6c.4.3). As first peak appears at much higher frequency it can not be ascribed to the dc conductivity originated process, for x=0.4 and x=0.6 compositions that suggests another relaxation process due to presence

of secondary, $YFeO_3$ phase. After irradiation M'(f) and M''(f) spectra are completely modified. Low frequency relaxation hump (x=0.2 and 0.4 compositions) and even high frequency peak observed for x=0.2, 0.4 and 0.6 composition are found to disappear in M''(f) and M'' versus M' curves. The presence of single circular arc for x=0.0 and 0.2 compositions and two semicircular arc for x=0.4 and 0.6 compositions confirm single –phase and mixed –phase character of the samples respectively. After irradiation two arc characteristics for x=0.4 and 0.6 compositions get converted into broad single arc suggests unwanted secondary $YFeO_3$ phase considerably reduces after irradiation as verified by X-ray diffraction pattern analysis. This also suggests that the dielectric properties and relaxation process can be modified by selecting appropriate swift heavy ion with different energy and fluence.

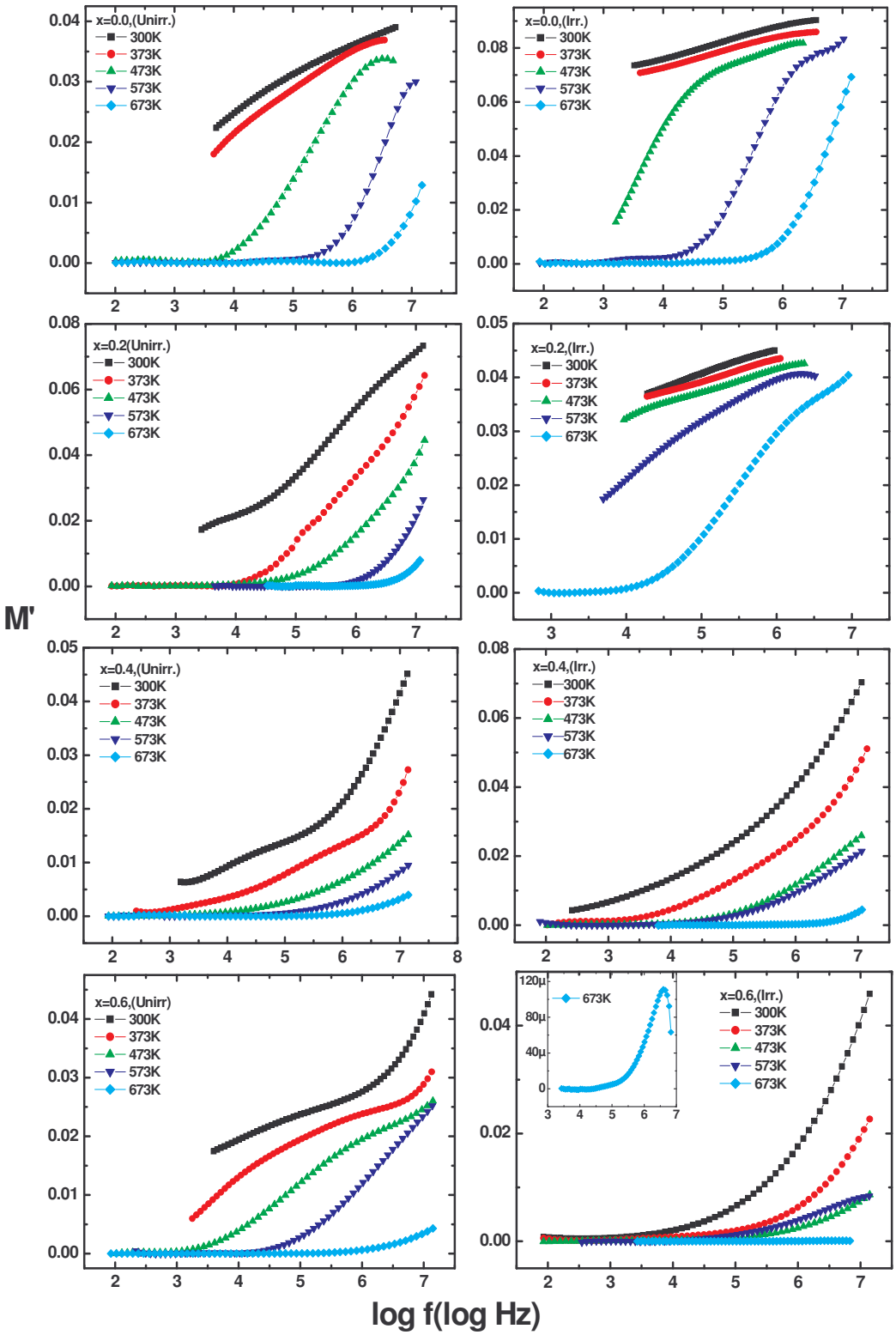

Fig.6c.4.1 Variation of real part of dielectric constant (ε') with frequency at different temperatures for Y-Fe(Y)-O system, before and after irradiation

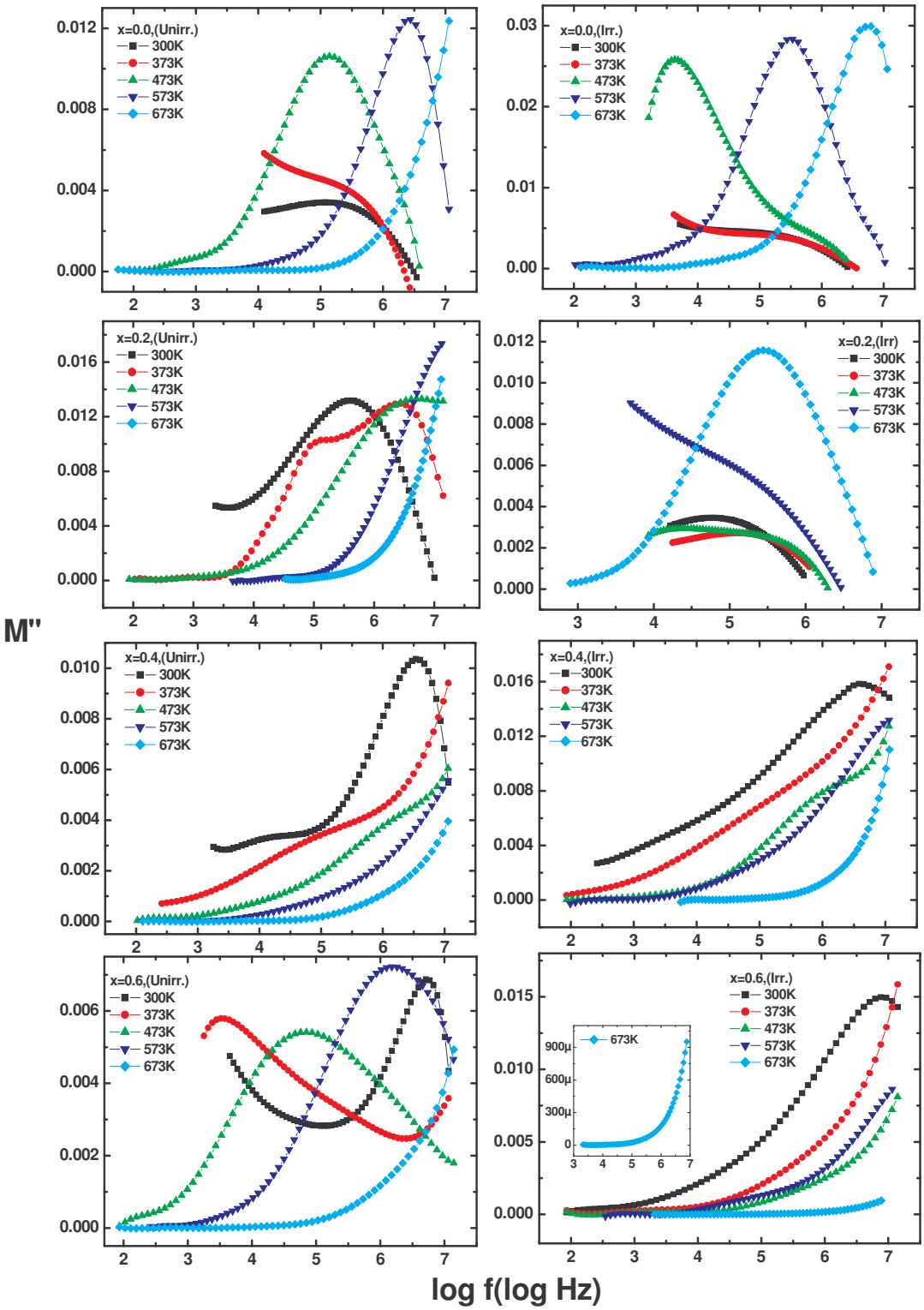

Fig.6c.4.2 Variation of real part of electric modulus (M') with frequency at different temperatures for Y-Fe(Y)-O system, before and after irradiation

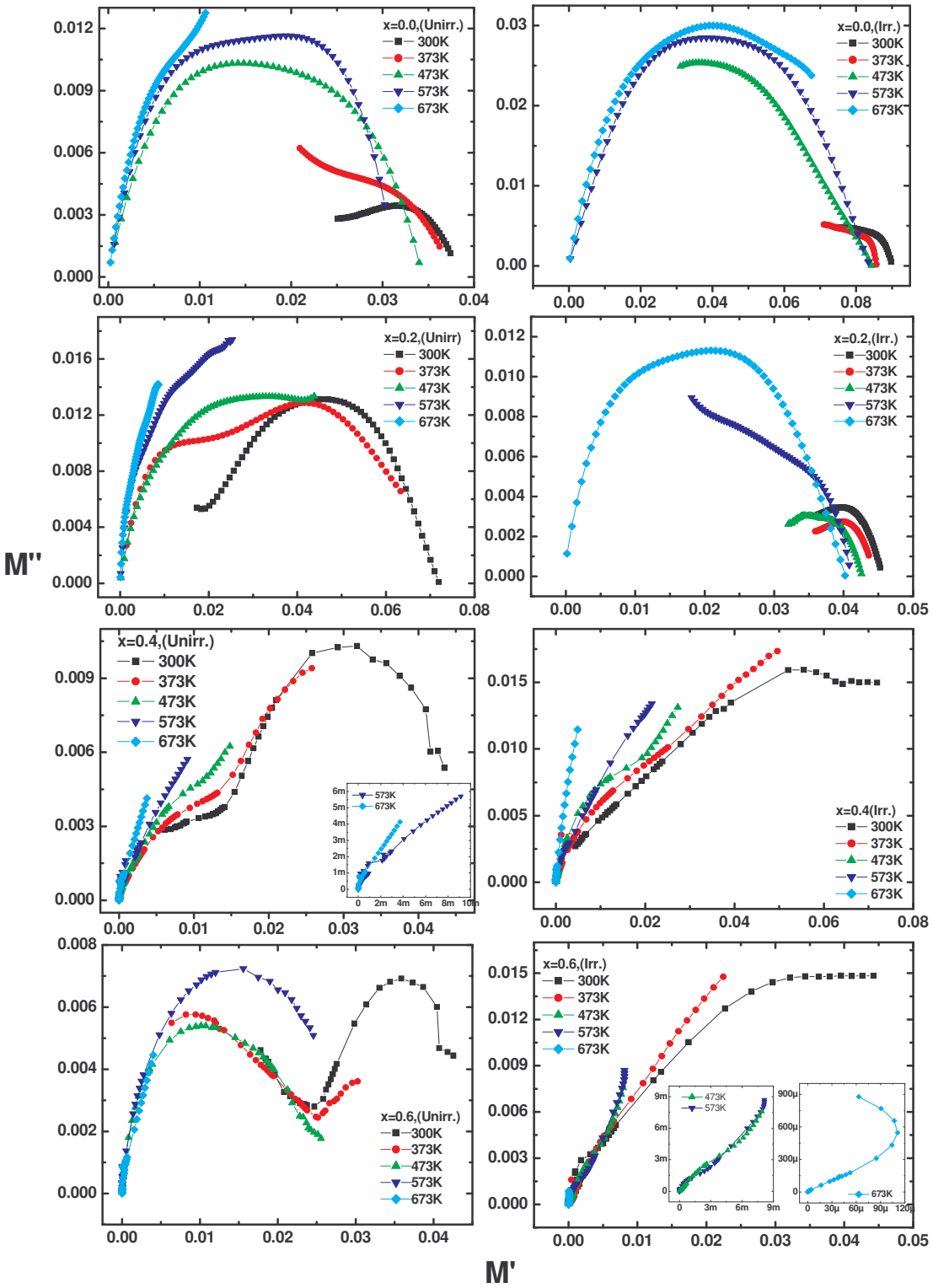

Fig.6c.4.3 Variation of imaginary part of electric modulus (M'') with frequency at different temperatures for Y-Fe(Y)-O system, before and after irradiation

6c.5 Impedance analysis

Figure 6c.5.1 shows the frequency dependence of impedance for x=0.0-0.6 compositions at various temperatures. The temperature affects strongly the magnitude of resistance. At lower temperatures, Z' decreases monotonically with increasing frequency upto some frequency and then becomes constant. At higher temperature, Z' is almost constant and for even higher frequencies it decreases sharply. The higher values of Z' at lower frequencies and low temperatures means the polarization is larger. This also means that the grain boundaries become conductive. This also shows that the grain boundaries are not relaxing even at very high frequencies, even at higher temperatures. The frequency dependence of Z'' is plotted for different temperatures in Figure 6c.5.2. At lower temperatures, Z'' decreases monotonically, suggesting that the relaxation is absent. This means that relaxation species are immobile defects and the orientation effects may be associated. As the temperature increases, the Z'' peak starts appearing in the spectra. As the temperature is increased, in addition to the expected decrease in magnitude of Z'', there is a shift in the peak frequencies towards the high frequency side. Also, it is evident that with increasing temperature, there is a broadening of the peaks and at higher temperatures; the curves appear almost flat. It is evident from figure that the position of the peak in Z'' (centered at the dispersion region of Z') shifts to higher frequencies with increasing temperature showing that the resistance of the bulk material is decreasing and that a strong dispersion of Z'' exists). The width of the peak in figure points towards the possibility of a distribution of relaxation times. This would imply that the relaxation is temperature dependent and there is

apparently not a single relaxation time and thereby relaxation process involved but different relaxations with their own discrete relaxation times depending on the temperature.

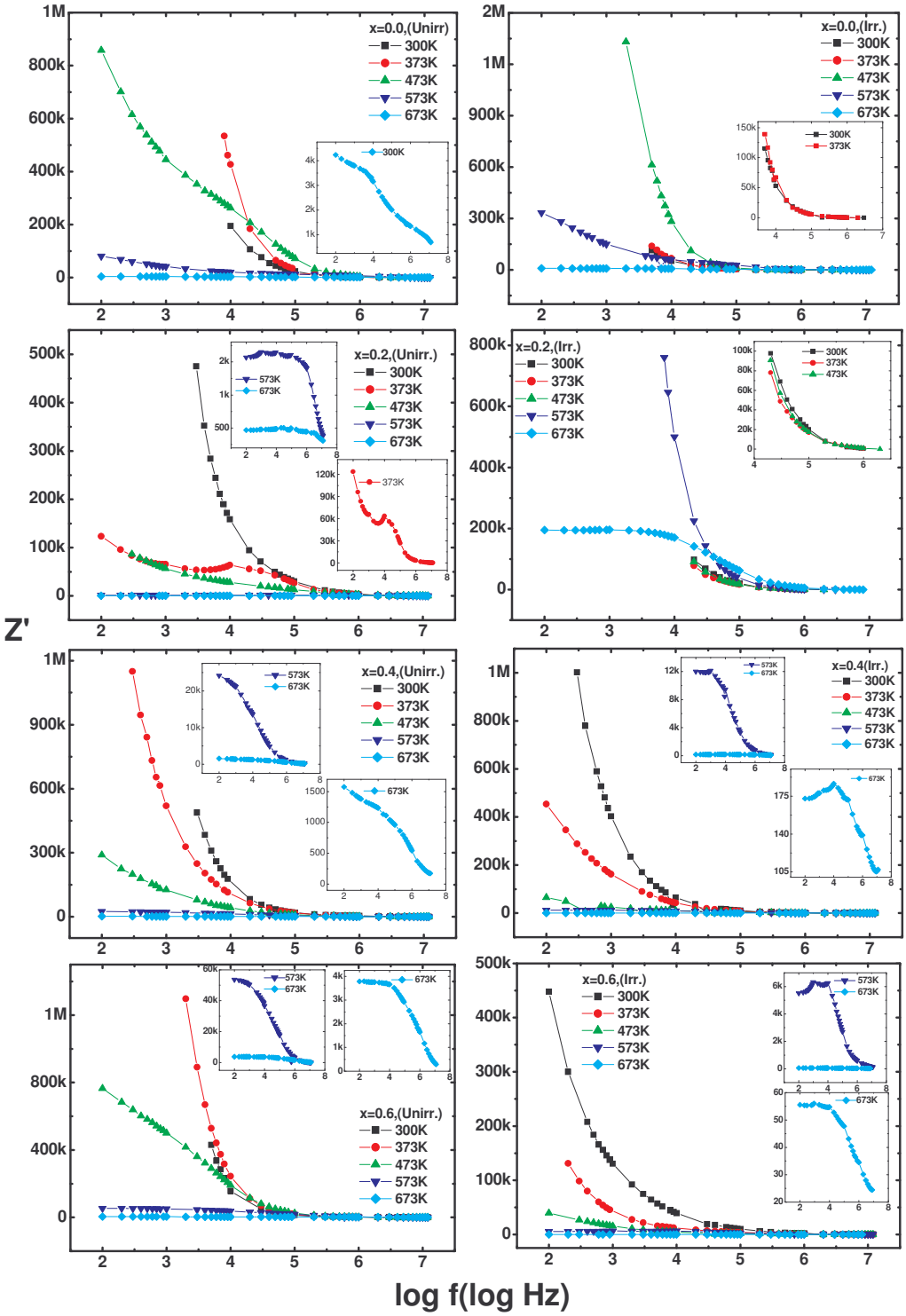

Fig.6c.5.1 Variation of real part of impedance (Z') with frequency at different temperatures for Y-Fe(Y)-O system, before and after irradiation

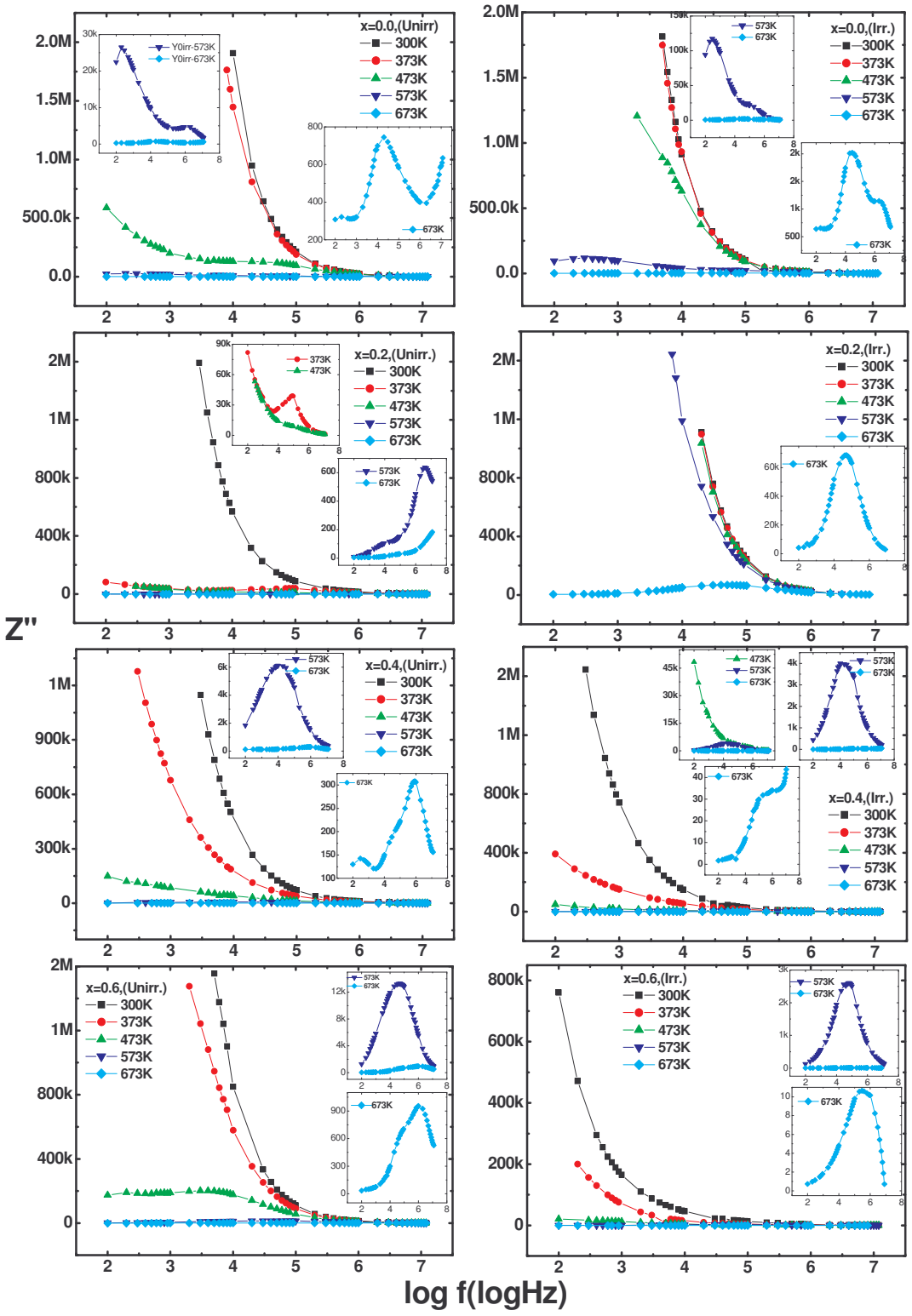

Fig.6c.5.2 Variation of imaginary part of Impedance (Z'') with frequency at different temperatures for Y-Fe(Y)-O system, before and after irradiation

Figure 6c.5.3 shows complex impedance spectrum (Nyquist plots i.e Z'' versus Z') at different temperatures. The plots could be interpreted in terms of single semicircle below 573K, which corresponds to grain contribution. Above 473K, there are mainly two overlapping semi-circles, which correspond to the grains (the semi-circle on the left hand side) and grain boundaries (the semi-circle at the right-hand side) in the material. The Z' values where the circular arc cuts real axis decreases sharply as the temperature increases. This shows that the conductivity increases sharply with increase in temperature.

It is found that after irradiation nature of ε' versus f curves do not change much for all the compositions at different temperatures, but magnitude of ε' decreases by the order of 10-100. The polarizability of the individual metal ions contributes to the dielectric constant. The polarizability of metal ions depends on the number of electrons in their outer electronic shells as well as their Goldscmidt radii [31, 32]. Greater the number f electrons in their outer electronic shells and greater the Goldscmidt radius, greater the polarizability expected. From these considerations, the polarizability of the cations in the garnet would be in the order; $Y^{3+}>Fe^{2+}>Fe^{3+}>Fe^{4+}$. Y^{3+} and Fe^{3+} ions would not lend themselves to polarization easily on the account of their stable completely filled and half filled outer most orbits, respectively. Thus the polarization and as a result magnitude of dielectric constant depends on the number of Fe^{4+}- ions in the system. It seems that after irradiation the number of Fe^{4+} centres reduces resulting in decrease in polarization and magnitude of dielectric constant.

Swift heavy ion (SHI) irradiation is known to generate controlled defects of various types such as point /cluster and columnar defects in the

materials [33] that lead to structural imperfection. On the other hand substitution of larger Y^{3+} smaller Fe^{3+} in the system also causes structural imperfection.

Structural imperfection would result in higher energy barriers as the probability of localized energy states arising out of structural imperfection would be low [34], decreasing the probability of charge carrier hopping and consequently the polarization and magnitude of dielectric constant.

The observed reduction in dielectric constant values is the overall result of the effect of the sum of the contribution of all these factors. Dielectric constant being inversely proportional to resistivity, an increase in resistivity after irradiation (Figures 6c.1.1 and 6c.2.1) would in lower dielectric constant. Here, it is interesting to note that dc resistivity (conduction mechanism) and loss tangent of mixed phase compositions (x=0.4,0.6) are not affect much by SHI- irradiation but dielectric constant values (i.e polarization phenomenon) are considerably affected by SHII.

Furthermore, dielectric constant presentation does not reveals presence of secondary $YFeO_3$-phase, electric modulus presentation (M''-M') demonstrates presence of secondary phase successfully. This is one of the important advantages of electric modulus presentation as compared to dielectric constant presentation.

The observed modifications in dielectric properties of garnet compositions after irradiation by swift heavy ion are mainly due to:

(i) The modification of the metal/insulator contacts due to the radiation damage induced disorder. That affects the space-charge polarization at the blocking metal/insulator contacts. [35].

(ii) Change in interfacial polarization due to swift heavy ion irradiation induced point/clusters of defects in the material and also compressive strain generated in the lattice structure [36].

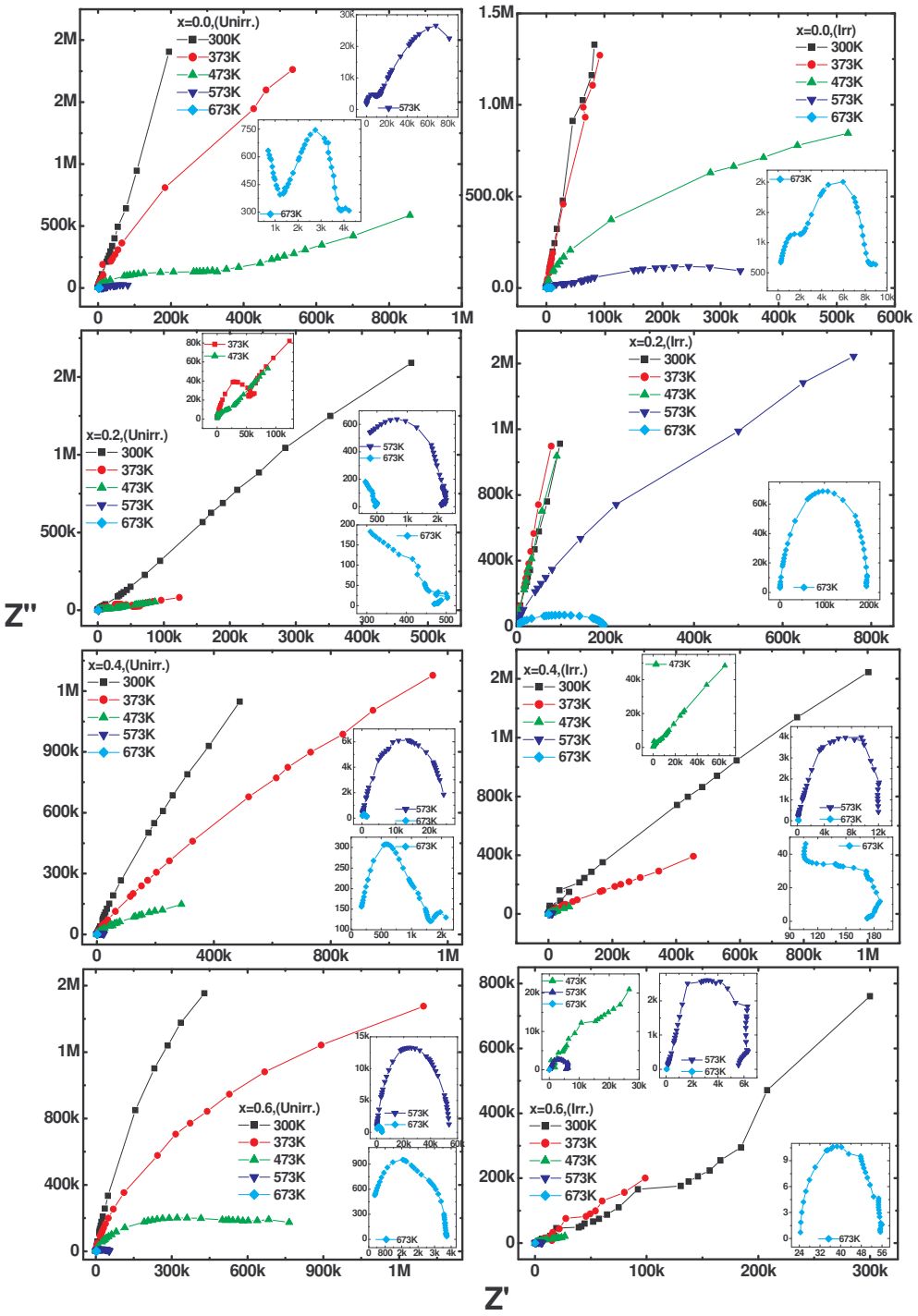

Fig.6c.5.3 Nyquist plots for Y-Fe(Y)-O system, before and after irradiation at different temperatures

References

1. E.J.W. Verwey and P.W. Haayman, Physica 8(1941)979.
2. L.G. Van Uitert, Proc. IRE 44 (1956)1294.
3. I.K. Kamilov, Sbnornik nauch n. Soobsbeh, Dagestan Univ. Ser. Fiz. 1(1977)55 (Russian).
4. K.R. Krishna Murthy, Ph.D Thesis, IIT Madras (1975).
5. O.M.Hemeda, M.M. Barkat and D.M. Hemeda, Turk. J. Phys. 27(2003)537.
6. D. Elwell and A. Dixon, Solid State Commun. 6(1968)585.
7. R.E. Fontana and D.J. Epstein, Mat. Res. Bull. 6(1971)959.
8. Milind Vaidya, V.A. Kale and P.H. Umadikar proc. Solid State Phys. Symp. 41 (1998) 427.
9. H.B.Lal, B.K. Verma, V.R. Yadav, J. Mater. Sci. 17(1982)3317.
10. V.R. Yadav and H.B.Lal, Jpn. J. Appl. Phys. 18 (12)2229.
11. A.N. Petrov, G.V. Denisov and U.M. Zhukovskii Inorg. Mater. (USA)22 (1986)579.
12. L.Sirdeshmukh , K.K.Kumar, S.R. Kaxman, A.R. Krishna and G. Sathaiah, Bull. Mater. Sci. 21 (3)(1998)219.
13. P.K.Larsen and R.Metselaar, Phys. Rev. B. 14(6)(1946)2520.
14. Om Prakash and D. Bahadur, J. Appl. Phys. 53 (1982)8228.
15. I.G.Austin and N.F.Mott, Adv. Phys. 18(1969)41.
16. J. Appel, Solid State Phys. (eds) F. Seitz, D. Turnbull and H. Ehrenreich (NY: Academic Press) 21 (1968)193.

17. N.F. Mott and E.A. Davis, Phonons and polarons in electronics processing in nanocrystalline materials (Oxford: Clarendon press) 1971.
18. A.J. Bosman and H.J. Van Dall, Adv. Phys. 19(1870)1.
19. D.Adler and Feinleib, Phys. Rev. B. 2(1970)3112.
20. E.E. Anderson, J.Appl. Phys. Suppl. 30(1959)2995.
21. A.M. Hofmeister and K.R. Campbell, J. Appl. Phys. 72(1992)638.
22. H.B.Lal, Naseeb Dar and Ashok Kumar, J. Phys. a 7(1974)4335.
23. S. Saha and T.P. Sinha, Phys. Rev. B 65(1-7)(2005)134103.
24. N.G. Mc Crum, B.E. Read and G. Williams Anelastic and dielectric effects in polymeric solids, London:Wiley;1967,p.108
25. P. B. Macedo, C.T. Moynihan and R. Bose. Phys. Chem. Glasses 13(1972)171.
26. F.S. Howell, R.A. Bose, P.B. Macedo and C.T. Moynihan, J. Phys. Chem. 78(1975)639.
27. A.A. Bakr and A.M. North, Eur. Polym. Sci. 13(1977)799.
28. G. M. Tsangaris, G.C. Psarras and N. Kouloumbi, J. Mater. Sci. 33(1998)2027.
29. G.C. Psarras, E. Manolakaki and G.M. Tsangaries, Appl. Sci Manufact. 33(2002)375.
30. K.P. Padmasree, D.K. Kanchan and A.R. Kulkarni, Solid State ionics 177(2006)475.
31. C.P. Smyth, Dielectric behaviour and structure, McGraw-Hill Book Company Inc. 1955, p. 132 (chapter V).

32. L.L. Hench, J.K. West, Principles of Electronic Ceramics, John Wiley and Sons. N.Y. (1990) p. 346.
33. M.W. Thompson, Defects and radiation damage in metals, Cambridge University Press, Cambridge (1969).
34. L.V. Azaroff, Introduction to Solids Tata McGraw- Hill lab. Company Ltd. New-Delhi (1992) p. 321.
35. J.M. Constantini, J.P. Salvetat and F. Brisard, J.Appl. Phys. 82(10) (1997)5073.
36. M. Singh, Anjan Dogra and Ravi Kumar, NIM B 196(2002)315.

Conclusions

The consequences of swift heavy ion (SHI) irradiation (Li^{3+}, 50 MeV, fluence= $5*10^{13}$ ions/ cm^2) on the structural, magnetic electrical and dielectric properties of Y^{3+}-substituted Yttrium iron garnet ($Y_{3+x}Fe_{5-x}O_{12}$; x=0.0, 0.2, 0.4 and 0.6) have been studied, it is found that:

(a) The formation of $YFeO_3$ phase for higher Y^{3+}-concentration compositions can effectively be reversed by swift heavy ion irradiation as revealed through X-ray diffraction and Mössbauer spectral analysis.

(b) The decrease in grain size as observed from SEM analysis with Y^{3+}-substituted is attributed to smaller solid solubility of Y^{3+}-ion in the garnet structure that hampers the grain growth.

(c) The squeezing of the M-H loop near the origin is due to the presence of two magnetic phases and week ferromagnetic component of $YFeO_3$ phase. The lower value of saturation magnetization for irradiated compositions as compared to unirradiated counterpart may be due to redistribution of cations and /or SHI induced formation of paramagnetic centers in the material.

(d) The central enhancement observed in the Mössbauer spectra of the irradiated samples is not due to amorphization but its origin lies in the formation of localize paramagnetic centres. The hyperfine interaction parameters of both phases are highly influenced by SHII.

(e) The tailing effect in $\chi(T)$ curves of irradiated samples indicating non-uniform effect of the irradiation while lower value of Neel temperature for irradiated samples as compared to unirradiated

counterparts is due to cumulative effect of the redistribution of cations and fractional creation of localized paramagnetic centres resulting from SHI irradiation.

(f) The permeability dispersion curve for different composition showing relaxed spectra due to presence of closure domains for large grains. The initial permeability , grain size and saturation magnetization values can be used to calculate many interesting parameters : Total number of domain walls, critical grain diameter for which number of domain walls reduces to 1, domain wall energy per unit area, spacing between domain walls, anisotropy field, resonance frequency, wall permeability and rotational permeability.

(g) The observed difference between dc resistivity values for irradiated and unirradiated samples (x=0.0 and 0.2) is due to SHI induced paramagnetic centres that hinders the conduction through equivalent cationic sites.

(h) The ρ_{ac} (f,t) curves before and after irradiation demonstrate polaron hopping mechanism.

(i) The observed modifications in dielectric properties of garnet compositions after SHI-irradiation are mainly due to: the modification of the metal/ insulator contacts due to the radiation damage induced disorder that affects the space charge polarization at the blocking metal/insulator contacts. Secondly change in interfacial polarization due to swift heavy ion irradiation induced point/cluster of defects in the material and also compressive strain generated in the lattice structure.

(j) The various parameters (except for hyperfine interaction parameters) of $YFeO_3$ phase remain unaffected by SHI-irradiation, suggests $YFeO_3$ is irradiation hard phase as compared to $Y_3Fe_5O_{12}$ phase.

This inherent property of $YFeO_3$ may find application in material suitable for pelletron and other radiation prone environment.

Chapter 7

Grain Size Dependent Structural, Infrared Spectral, Magnetic, Electrical and Dielectric Properties of Yttrium Iron Garnet

7a.1 X-Ray diffraction analysis

The X-ray powder diffraction (XRD) patterns for the unmilled, 3hrs, 6hrs, 9hrs and 12hrs milled samples of $Y_3Fe_5O_{12}$ recorded at 300K are shown in Figure 7a.1.1

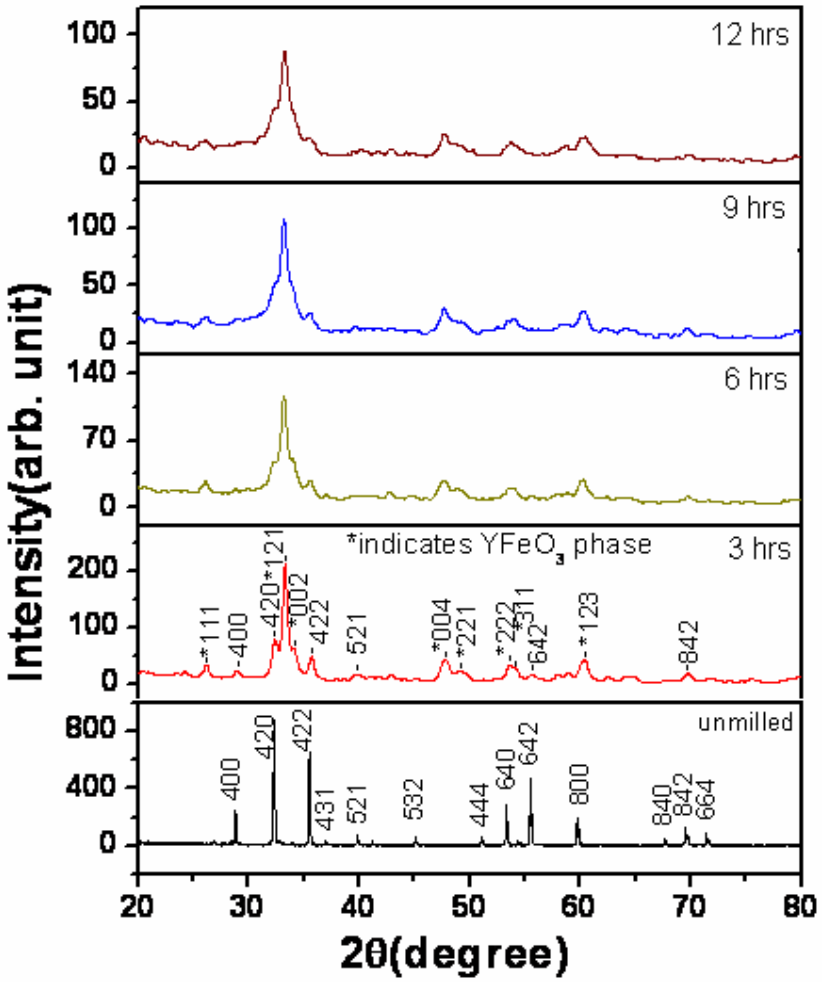

Fig. 7a.1.1 XRD patterns for unmilled, 3hrs, 6hrs, 9hrs and 12hrs milled samples of YIG

The XRD pattern confirms the formation of single phase bcc garnet structure for unmilled sample, with no extra lines corresponding to any other crystallographic phase or unreacted ingredient. It is found from the XRD patterns that the additional orthorhombic phase of yttrium orthoferrite ($YFeO_3$) (marked as *) grows in intensity for all the milled samples.

The XRD patterns for all the milled samples were indexed for bcc-garnet phase (Space Group: O_h^{10}-Ia3d) and orthorhombic phase of $YFeO_3$ (Space Group: Pnma) using standard structural data files obtained from PCPDFWIN program (PDF card No: 83-1027 & 86-0171 respectively) and the corresponding Bragg planes are shown in the patterns. The values of lattice constant were determined for both the phases for all the samples using powder-X analysis of X-ray diffraction data. The variation of lattice constants as a function of milling time is shown in Table 7a.1.1(a).

Table 7a.1.1(a) Percentage (%) of phase, Lattice constants, bulk density (ρ) and X-ray density (ρ_x) values for unmilled and milled samples of YIG

sample	(%) of phase		Lattice constant ± 0.002Å (from powder-x)				Bulk density(ρ)	X-Ray density(ρ_x)
$Y_3Fe_5O_{12}$	YIG	$YFeO_3$	YIG	$YFeO_3$				
			a=b=c	a	b	c	(g/cm^3)	(g/cm^3)
unmilled	100	-	12.377	-	-	-	4.572	5.170
3hrs	25.6	74.4	12.382	5.26	7.59	5.55	4.890	5.164
6hrs	21.1	78.9	12.435	5.25	7.57	5.58	4.586	5.098
9hrs	25.2	74.8	12.380	5.25	7.57	5.58	4.545	5.166
12hrs	26.9	73.1	12.371	5.25	7.58	5.58	4.527	5.177

Table 7a.1.1(b) Particle size ,Lattice strain, surface area (S) and Equivalent surface free energy values for milled and unmilled samples of YIG

sample	Particle size (nm)			Lattice strain (%)			Surface area (S) (cm^2/g)*10^4	Equivalent surface free energy (10^{-3} cal/g)
$Y_3Fe_5O_{12}$	YIG	$YFeO_3$	Average	YIG	$YFeO_3$	Average		
unmilled	1.8(μm)*	-	-		-	-	-	-
3hrs	24.8	26.2	25.5	-	-	-	48.11	11402.07
6hrs	16.2	15.6	15.9	0.981	0.732	0.856	82.29	19502.73
9hrs	13.2	13.4	13.3	0.910	0.910	0.910	99.27	23526.99
12hrs	9.4	11.4	10.4	1.083	1.042	1.062	127.44	30203.28

*from SEM Analysis.

It is found that the observed lattice constants for the orthorhombic phase remain uninfluenced by milling time and having values close to pure

yttrium orthoferrite [1] : (a=5.282Å, b= 7.605 Å and c=5.596 Å). On the other hand the lattice constant for the garnet phase increases linearly with increase in milling time upto 6hrs and then decreases with further increase in milling time (Table7a.1.1(a)).

Now, observed increase in lattice constant value for garnet phase from unmilled sample to 6hrs milled sample could be due to one or more of the following reasons.

(i) The strong internal strains introduces during mechanical milling treatment causing increase in plane spacing results in the unit cell expansions.

(ii) The formation and presence of Fe^{2+} ion with larger cationic radius of 0.74 Å, as compared to 0.64 Å of Fe^{3+} ions, may also be the reason for lattice expansion. The formation of ferrous ion is quite probable in such systems.

(iii) It follows that there would be un-paired electronic orbital at the outer surface dipoles would repelling each other and results in a larger value of equilibrium lattice constant than in the bulk crystal [2].

Here, the second probability is ruled out as presence of Fe^{+2} can be reflected clearly in Isomer shift value in Mössbauer spectral analysis, as ferrous ions have larger positive isomer shifts than ferric ions. So (i) and (iii) probabilities may be responsible for increase in lattice constant value for 3hrs and 6hrs milled samples.

The probable reason for reduction in lattice parameter for 9hrs and 12hrs milled samples could be the change in cation distribution taking place with higher milling hours [3]. The other probable reason could be the presence of

lattice defects and its influence on the nano-particles, especially on the surface. In nano particles; surface area and surface tension of the particles are high. This results in a tendency to shrink the lattice which causes reduction in lattice constant [3, 4]. The surface area and equivalent surface free energy of all the samples are given in Table 7a.1.1(b).

The percentage formation of the bcc garnet phase and the yttrium orthoferrite, $YFeO_3$ phase for these samples was determined taking intensity ratios of most intense peak of both the phases using the method described elsewhere (Table7a.1.1(a)).The percentage of Orthoferrite phase is:

$$\% \text{ orthoferrite phase} = \frac{100 * I_{ortho}}{I_{ortho} + I_{garnet}}$$

where I_{ortho} and I_{garnet} are the integrated highest band intensities of orthoferrite and garnet x-ray diffraction peaks, respectively. Accordingly the calculated orthoferrite phase percentage is ~75%.The maximum percentage of $YFeO_3$ formation is found for 6hrs milled sample.

Grain size determination

The average grain diameter (D) for the ball milled samples was calculated from the broadening of the respective high intensity (420) peak for YIG phase and (121) peak for $YFeO_3$ phase using the Debye Scherrer formula:

$$D = \frac{K\lambda}{B\cos\theta}$$

Here, λ is the wavelength of the CuK_α radiation (1.54059 Á), shape factor K=0.9, is related both to the crystalline shape and the way in which B and D are defined. B is the contribution to the XRD peak width (FWHM) due to the small size of crystallites in radians. The contribution must separate out from

the measured line width B_m which includes instrumental broadening B_{ins}, always present irrespective of the particle size. For this, one can record XRD pattern of a well crystallized, bulk standard material such as silicon powder under identical geometrical conditions and measure the peak width 'B_{ins}'. Usually, Instrumental broadening (B_{ins}) of a conventional powder X-Ray diffractometer is 0.1º. The broadening parameter B is obtained from the relation:

$$B = (B_m^2 - B_{ins}^2)^{\frac{1}{2}}$$

where B_{ins}=0.1º (=0.001744 radian).

Here, the particle size is calculated for both the phases, considering the B (FWHM) obtained by Gaussian fitting of most intense peak of both the phases. The average grain size reduces from ~26 nm for 3hrs. milled sample to ~10 nm for 12hrs (Table 7a.1.1(b)). The grain size decreases with increasing milling time because the kinetic energy generated by the series of collisions among balls is transformed to the system.

The grain size when calculated at different Bragg's angle (θ) values was at variance, indicating the presence of strain. Along with reduction in particle size, creation of non-uniform strain in the system also contributes in peak broadening, which is due to systematic shift of atoms from ideal positions, creation of point defects, plastic deformation or poor crystallinity produced in the system as a result of prolonged high energy ballmilling. Therefore, here, we have calculated strain (non-uniform) produced in the system as a result of milling. Here we have ruled out the probability of uniform strain as uniform strain contributes to shifting of d-spacing of the planes and hence the change in lattice constant values, but we have observed change in

d-spacing values of only YIG phase peak and not in the $YFeO_3$ phase peaks. It is found that the diffraction line (corresponding to Garnet phase) shifts to lower Bragg angle for 3hrs and 6hrs milled samples while it shifts to higher angle for 9 and 12 hrs milled samples with reference to peak positions for unmilled sample. The reduction in diffraction line intensity has been also observed (Figure 7a.1.1). These observations suggest non-uniform strain has been produced in the samples due to mechanical milling.

Strain determination

The average lattice strain of all the milled samples is calculated using the formula given by Stokes and Wilson (1944) who first observed that strained or imperfect crystals contain line broadening of a different sort, than the broadening that arises from small crystallite size. Accordingly, lattice strain value can be calculated from the relation:

$$\varepsilon_{str} = \beta/\{4 \tan\theta\}$$

where ε_{str} = weighted average strain and β = The integral breadth of a reflection located at 2θ (in radians).As milling time increases, value of lattice strain increases (Table 7a.1.1(b)).

Surface area and Surface energy determination

Attempt has been made to calculate surface area (S) and equivalent surface free energy for all the milled samples. Assuming all the particles be spherical, the specific surface area in centimeter square per gram is given by:

$$S = \frac{6000}{D.\rho}$$

where D is the particle diameter in nm and ρ is the density of the particle in g/cm^3. The specific surface area (Table 7a.1.1(b)) of the particle increases as the grain size decreases.

The surface free energy calculated assuming the grains to be spheres with a surface energy of 1000 erg/cm^2 [5], increases with decreasing grain size (Table 7a.1.1(b)) . In the case of nanoparticles, surface atoms are not bounded to the maximum number of nearest neighbours and are therefore in a higher energy state than the atoms at interior positions. The bonds of these surface atoms that are not satisfied give rise to a surface energy. In the field of nano-magnetism this surface energy plays very crucial role.

7a.2 Infrared Spectroscopy

Studies of relations between structure and the electromagnetic response of ferromagnetic semiconductors have been useful in understanding their properties.

The room temperature (300 K) infrared spectra in the wave number range 400 cm^{-1}-1000 cm^{-1} for all the samples are shown in Figure 7a.2.1.

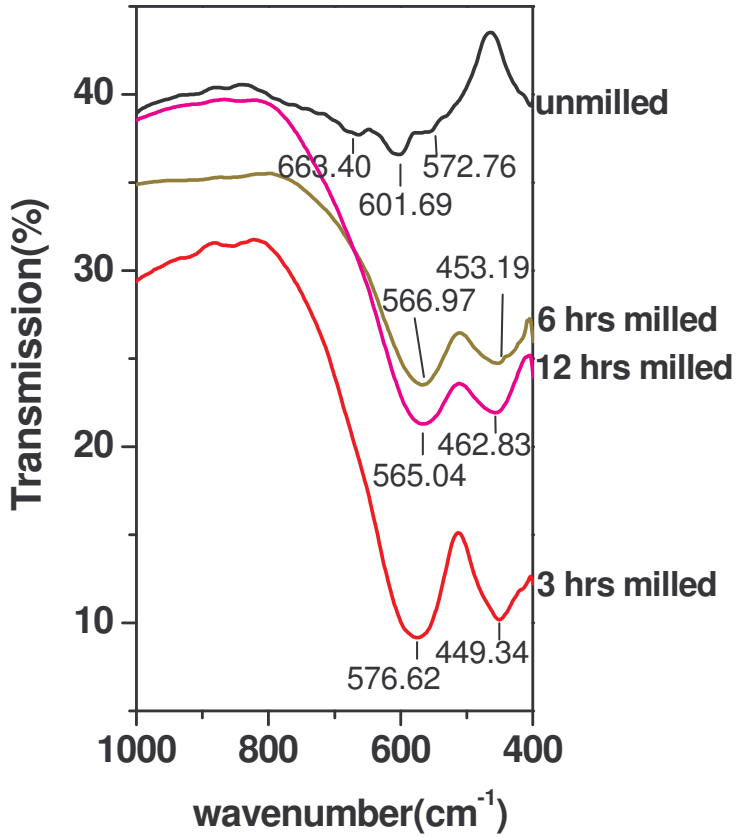

Fig. 7a.2.1 Room temperature (300 K) infrared spectra for unmilled, 3hrs, 6hrs and 12hrs milled samples of YIG

No absorption bands were observed above 700 cm^{-1}. The spectrum of unmilled sample shows three bands appear at 572.76 cm-1, 601.69 cm^{-1}, 663.40 cm^{-1} and can be assigned to asymmetric stretching of the tetrahedron in the YIG [6].They are characteristic bands of the garnet ferrite [6]. FT-IR

spectra of 3hrs, 6hrs, and 12hrs milled samples are characterized by absorption bands at 569±5 cm^{-1} and 456±7 cm^{-1}.

It has been reported by Mathur et al [7] that these two absorption bands are corresponding to the Y-O and Fe-O stretching frequencies of $YFeO_3$ compound. In contrary, it has been well establish by Venugopalan et al [8], that the absorption bands associated with the heavier Y^{3+} ions (88.9 amu) lie in the region below 300 cm^{-1}. On the other hand based on infrared and electronic spectral studies of rare earth perovskites, by Subbarao et al [9] it has been shown that IR spectra of the $LnZO_3$ (Ln is the rare earth ion or yttrium and Z=Cr, Mn or Fe) perovskites are comparable to the spectra of the corresponding transition metal sesquioxides, Z_2O_3. This implies that Ln ion does not affect IR spectra of perovskites compounds. We have also recorded IR spectra of constituent oxides: Y_2O_3 and Fe_2O_3, and are shown in Figure 7a.2.2.

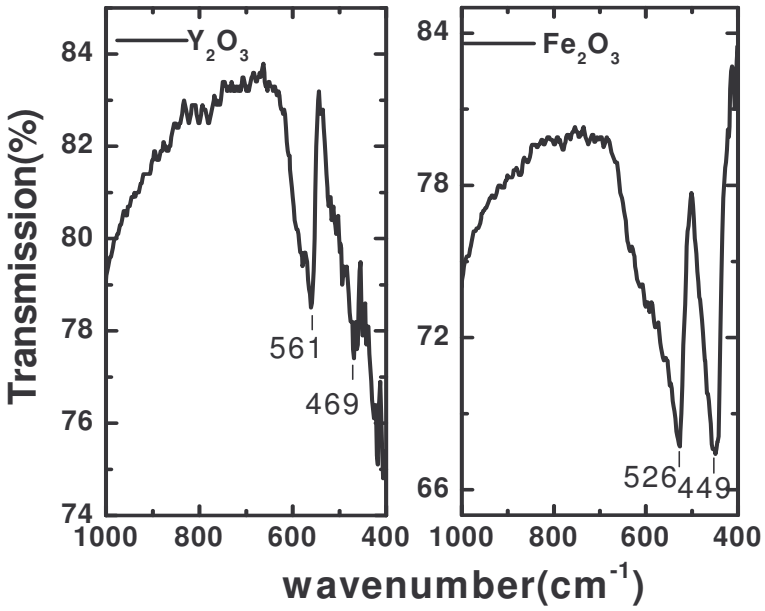

Fig. 7a.2.2 Infrared spectra of Y_2O_3 and Fe_2O_3 at 300 K

The spectra show identical nature with two absorption bands in wavenumber range studied. These spectra are also identical in nature with those observed for milled samples of YIG. In the present case the milled samples possesses mixed phase of bcc garnet phase and orthorhombic phase of $YFeO_3$. Based on the above facts it is clear that the two absorption bands observed for Y_2O_3 or milled samples of YIG cannot be due to Y-O vibrations.

It is concluded that high frequency absorption band at 569±5 cm^{-1} is due to combine effect of asymmetric stretching vibrations of the tetrahedron of the YIG- phase and the motion of the in-plane oxygen atoms of $YFeO_3$-phase. The low frequency absorption band at 456 ± 7 cm^{-1} involves bending motion of the tetrahedra of YIG – phase, which is not observed for un-milled sample of YIG but may be enhanced due to mechanical milling induced strain in milled samples, as well as the apical oxygen vibrations of $YFeO_3$- phase. These results are consistent with IR/Raman spectral analysis of materials with similar structure [8, 10].

A careful examination of IR spectra of milled samples reveal the facts that (i) high frequency absorption band shift towards lower frequency side (ii) low frequency band shift towards higher frequency side on milling (iii) intensity of absorption bands for 3hrs milled sample is maximum while for 6hrs and 12hrs milled samples intensity remains unaffected by milling time. Intensity of absorption bands for 12 hrs milled sample is slightly greater than absorption bands intensity for 6hrs milled sample.

The observed shifting of the bands may be due to micro-structural changes. The Fe-O bond lengths and angles show a variation because of the mechanical milling induced strain. The observed change in position of

absorption bands with milling time may also be due to milling induced oxygen vacancies [10, 11]. On the other hand, it is known that intensity of infrared absorption bands can give useful information concerning the change of electric dipole moment with inter-atomic distances and the charge on each ion.

Based on the above fact we feel that for 3hrs milled sample, relative displacement of atoms (d_i) and the effective charge on different ions (q_i) get changed in a such a way that the magnitude of electric dipole moment ($p_i = q_i . d_i$) increases and as a result intensity of absorption band. The observed change in intensity of absorption bands for 6 hrs and 12hrs milled samples may be explained in similar way. For a thorough understanding infrared reflectivity measurements and Rietveld refinement of X-ray data may be useful.

7a.3 Scanning electron microscopy (SEM)

The scanning electron micrographs of the YIG sample are shown in Figure 7a.3.1.

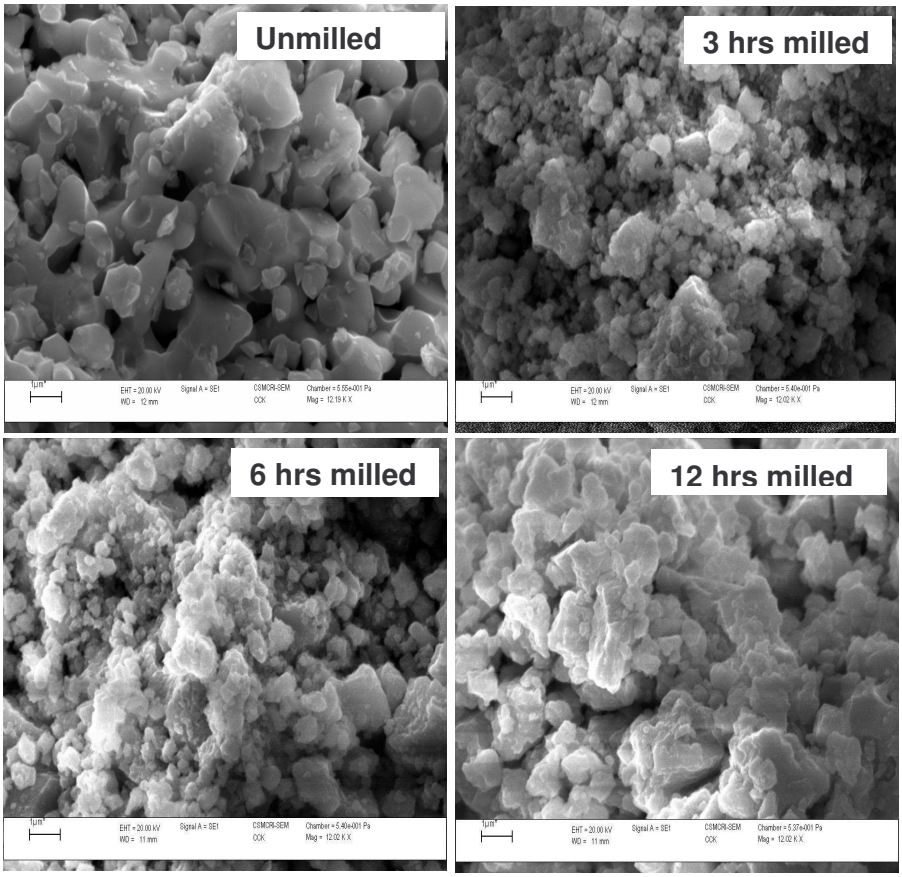

Fig.7a.3.1 SEM images for unmilled, 3hrs, 6hrs and 12 hrs milled composition of YIG

It is seen that the milling of YIG composition can be markedly enhances densification of the material. The average particle size can be estimated as 1.8 μm for un-milled sample. It is also observed that the particles were stuck to each other in a regular and uniform manner to the form a network- like structure. It is evident that morphology of milled samples deviate from unmilled sample 3hrs and 6hrs milled samples have grains with sizes that vary over a wide range and the small particles are getting agglomerated

due to generated heat in milling process. The 12hrs milled sample shows multi-layer type grain growth.

7a.4 Transmission Electron Microscopy (TEM)

Figure 7a.4.1 shows typical TEM photographs of 3hrs and 6 hrs milled samples of $Y_3Fe_5O_{12}$.

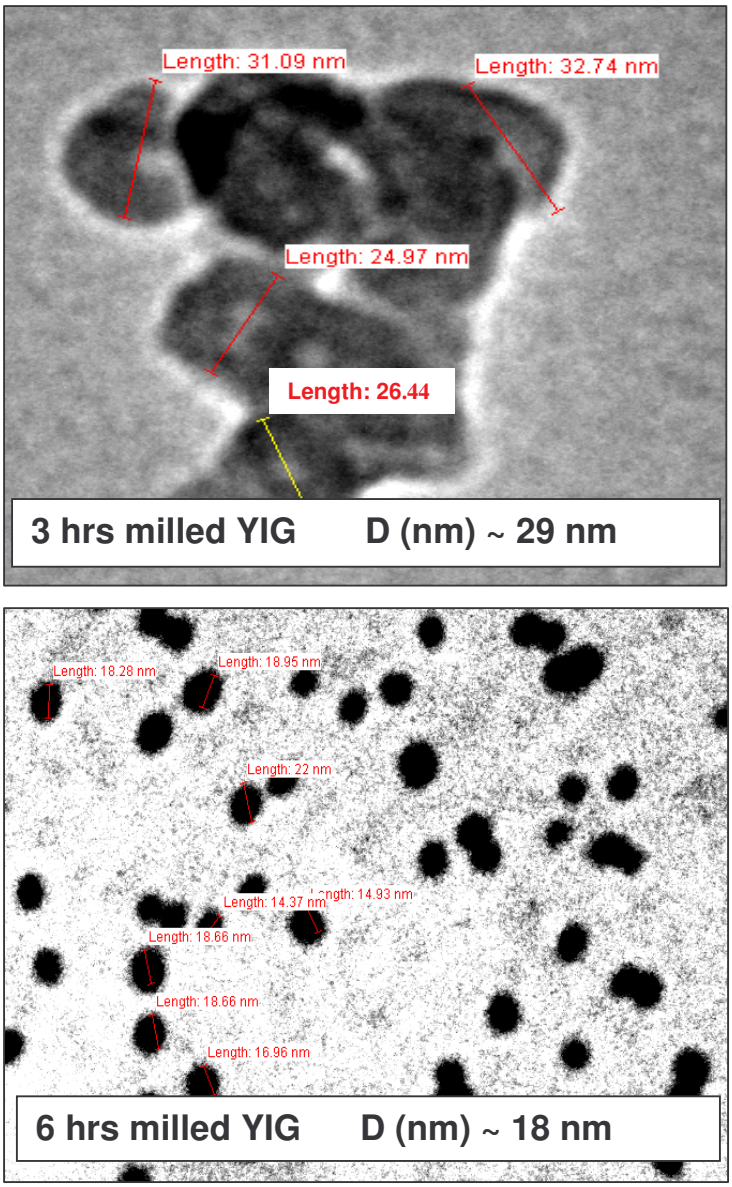

Fig.7a.4.1 TEM images of 3hrs and 6hrs milled samples of YIG

We see that the particles are quite well dispersed and are fairly uniform in size. The fact that the particle size decreases with increasing milling time, is very clear from the TEM photographs. Apart from that, the particle size distribution is quite narrow. From the photographs we see that the milled samples show nearly spherical shape which may be because of the reduced size of the particles.

The particle size and its distribution is one of the most basic parameter in nanoparticles research. X-ray diffraction pattern analysis gives the average crystallite size and no clue about its distribution. On the other hand, TEM can be used to measure the particle size of individual particles which can be used to quantitatively look at the particle size distribution in the sample. Normally, the particle size estimated from TEM is slightly greater than the particle size estimated from X-ray diffraction pattern analysis using Scherrer's formula, because X-ray diffraction gives information of the crystalline region only and the contribution from the amorphous grain surface does not contribute. On the other hand TEM gives the complete picture of the nano-particles [12].

7b.1 ^{57}Fe Mössbauer spectroscopic study on mechanically milled $Y_3Fe_5O_{12}$ (YIG)

The fundamental magnetic properties of iron garnets have their origin in the magnetic ions and their relationship to the surrounding oxygen ions. The oxygen ions influence the electronic configuration of the enclosed iron ions and provide the super-exchange between the iron ions in unlike sites.

Figure 7b.1.1 shows the Mössbauer spectrum of the un-milled and milled (duration: 3hrs,6hrs and 12hrs) YIG at 300K.The dots represents the experimental spectrum and the continuous curve results from the least square fitting of the experimental data, points with the Lorentzian function. The ratio of the intensities of the peaks in a sextet was fixed as 3:2:1::1:2:3 assuming random orientation of grains in polycrystalline samples. The relative intensities of the Mössbauer spectra of octahedral and tetrahedral sites of YIG are fixed to the ratio of their site population as 2:3.

The Mössbauer spectrum for unmilled sample exhibits two superimposed asymmetric Zeeman split sextets, one due to Fe^{3+} ions at the tetrahedral (d-) and other due to the Fe^{3+} ions at the octahedral (a-) sites of the garnet structure. The peak area ratio of the d- to a- sites $\Delta d/\Delta a$ is ≈1.5 which is typical value for YIG [13]. The magnetic hyperfine fields are 490 kOe and 397 kOe for the a- and d-sites respectively, and are in agreement with reported earlier [14, 15].

The Zeeman lines from the d-sites are broader than those from the a-sites, which suggest distribution of magnetic hyperfine fields resulting from a perturbation in the sub-lattice [16].

In order to gain more information regarding the complicated phase evolution of YIG during milling, Mössbauer measurements have been carried out for the samples with various milling times.

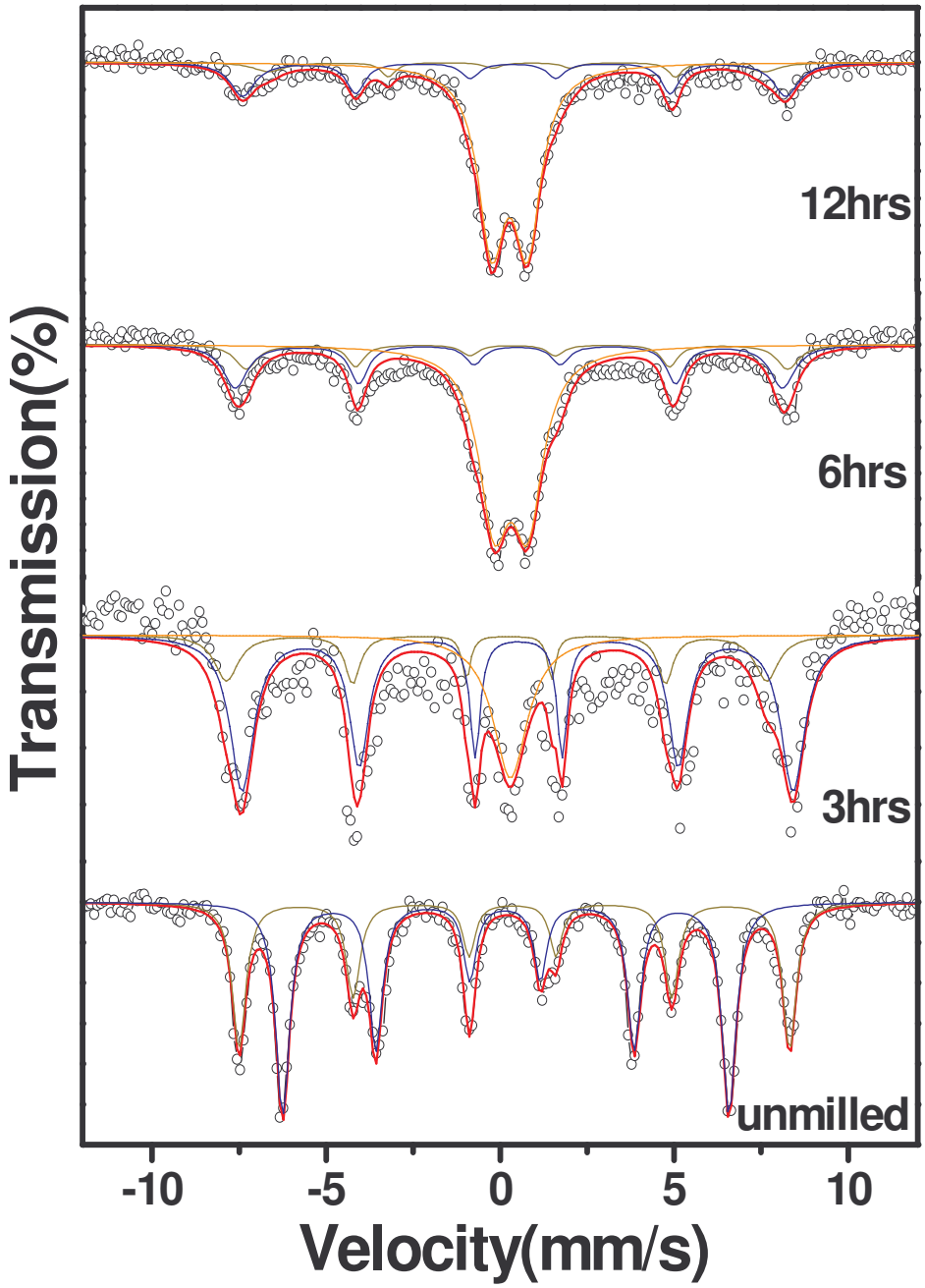

Fig. 7b.1.1 Mössbauer spectra at 300K for un-milled, 3hrs, 6hrs and 12hrs milled samples of YIG at 300K

Table 7b.1.1 Mössbauer parameters of unmilled, 3hrs, 6hrs and12hrs milled samples

Milling time	Hyperfine field (±1kOe)	Isomer shift* (±0.05mm/s)	Quadrupole shifting (±0.06mm/s)	line width (±0.05mm/s)	Relative intensity (± 1 %)	Phase (site)
unmilled	490.17	0.380	0.051	0.429	40.29	YIG(octa.)
	397.34	0.152	0.022	0.443	59.71	YIG(tetra.)
3hr	480.9	0.077	-0.359	0.282	17.95	YIG(octa.)
	490.6	0.516	-0.035	0.360	61.54	$YFeO_3$
	-	0.295	-	1.20	20.51	singlet
6hr	482.3	0.419	0.120	0.572	13.30	YIG(octa.)
	487.0	0.369	-0.242	0.631	26.02	$YFeO_3$
	-	0.309	0.963	1.05	60.67	doublet
12hr	441.0	0.699	-0.443	0.620	8.66	YIG(octa.)
	483.7	0.400	0.034	0.626	24.54	$YFeO_3$
	-	0.282	1.02	0.930	66.80	doublet
α-Fe_2O_3	518	0.40	-0.11	From Reference		
$YFeO_3$	495	0.52	0.010			

*with respect to Fe-metal

On milling as-prepared (unmilled) YIG for 3 hrs a super-paramagnetic singlet and for 6hrs and 12hrs, a super-paramagnetic doublet with a large line-width is obtained alongwith sextets arising from YIG and Yttrium ortho ferrite ($YFeO_3$) phases. On milling the tetrahedral site environment of garnet phase is disturbed in such a way that it is not resolved in Mossbauer spectra of all the milled compositions. It has been reported by Studer et al [17, 18] that when YIG is subjected to swift heavy ion irradiation, the tetrahedral sites are preferentially destroyed with respect to the octahedral ones. In the present case we feel that similar type of mechanism may have taken place by high energy ball-milling that has destroyed tetrahedral site completely. Two overlapped sextets includes the contribution from 'Fe^{3+} at octahedral site' of garnet phase and 'Fe^{3+} in octahedral environment' of the orthorhombic orthoferrite phase. These two 'Fe^{3+}-sites' in their respective phases have similar environment as both are surrounded by six oxygen ions. The co-existence of the doublet with the sextets is because of the distribution in

particle size and the small particles exhibiting super-paramagnetism at 300K. This also suggests that the measurement temperature is higher than the blocking temperature of the particles. The variation of hyperfine interaction parameters (Table 7b.1.1) with grain size/milling time may be summarized as follows: (i) Hyperfine field value for YIG and $YFeO_3$ phases decreases. (ii) Isomer shift values for YIG phase increase while I.S. value for $YFeO_3$ phase and paramagnetic doublet decrease (iii) Quadrupole shift/splitting show significance but not systematic variation (iv) line width of YIG and $YFeO_3$ phases are found to increase while it is found to decrease for paramagnetic doublet. (V) Area ratio for YIG and $YFeO_3$ phases decrease but for doublet area ratio increases with decreasing grain size or increasing milling time.

The reduction in the magnitude of the hyperfine fields on milling is due to the relaxation effects and also because of the surface spins of the small particles. Based on the results of the atomic –scale magnetic modeling of the oxide nanoparticles, Kodama et al [19] have proposed a model of the spin distribution within nanoscale ferrite particles consisting of ferrimagnetically aligned core spins and a spin glass like surface layer and this surface spin disorder in ferrimagnetic nano-particles is due to broken exchange bonds in the near surface layers.

7b.2 Low field ac susceptibility

The plots of thermal variation of low field (0.5 Oe) ac susceptibility are depicted in Figure 7b.2.1, which exhibit normal ferrimagnetic behaviour.

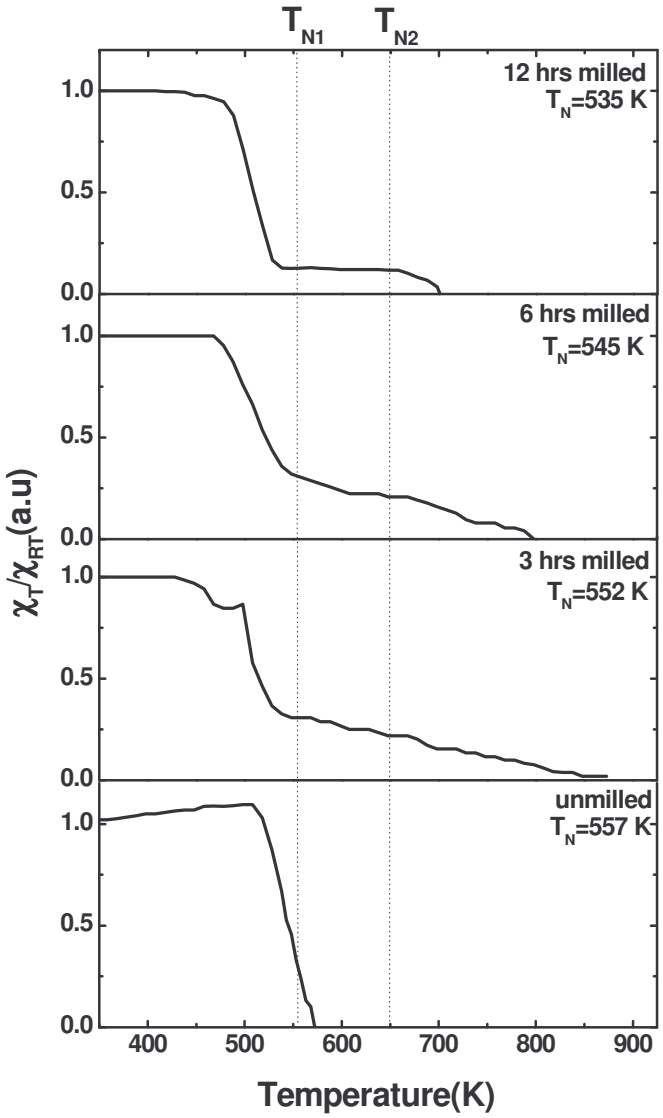

Fig.7b.2.1 Temperature dependence of ac susceptibility χ_T/χ_{RT} for unmilled and milled samples of YIG

It is seen that all the samples show (except for un-milled sample) two magnetic transitions. First transition is relatively sharp and it is in vicinity of the Neel temperature (T_{N1}) of unmilled YIG (~557 K) while second transition is blur, corresponding to Neel Temperature, T_{N2}=640 K [20] of weak ferromagnetic $YFeO_3$ phase. The plots exhibit the tailing effect for temperature $T>T_{N2}$. It is also important to note that transition temperatures and tailing effect decreases with increasing milling time. The breaking of the super-exchange bonds as a result of oxygen vacancies and the defects introduced upon mechanical milling weaken the super-exchange interactions and lower the Neel temperature. The decrease in T_N with the milling time suggests reduction in ferrimagnetic ordering and weakening of magnetic coupling. The tailing effect in the $\chi \rightarrow T$ plots is due to 'spin clusters'. The clusters are small groups of atoms with a kind of magnetic short-range order. These clusters of local spin order within a matrix of the spin disorder which constitutes a paramagnetic phase. The observed decrease in tailing effect with milling time may be due to increase in microstructural uniformity in the material.

The decrease in T_N with grain size for YIG could be explained on the basis of the finite size scaling theory [21]. This theory predicts that the shift in the transition temperature from that of the bulk should depend on a dimension of the system in the following manner:

$$\frac{T_N(\infty) - T_N(d)}{T_N(\infty)} = \left(\frac{d}{d_0}\right)^{\frac{-1}{\varsigma}} \qquad (1)$$

where $T_N(d)$ is the Neel temperature as a function of particle size (d), $T_N(\infty)$ is the bulk Neel temperature, d_0 is a constant, it should be of the order of the system and ς is the critical exponent of the correlation length. Depending on

the boundary conditions, geometry and interaction, the change in T_N may be positive or negative. According to Chen et al [22], it is possible that T_c decrease due to some unknown surface effect. For nano particles a significant fraction of atoms is on the surface, and it is reasonable to expect their magnetic interaction to be different hence a different average Neel Temperature. Since the ratio of surface to bulk atoms in a particle is proportional to 1/d, such an effect, if linearly dependent on the specific surface area, might yield a change in T_N proportional to 1/d which would be mathematically equivalent to above equation with ς=1.

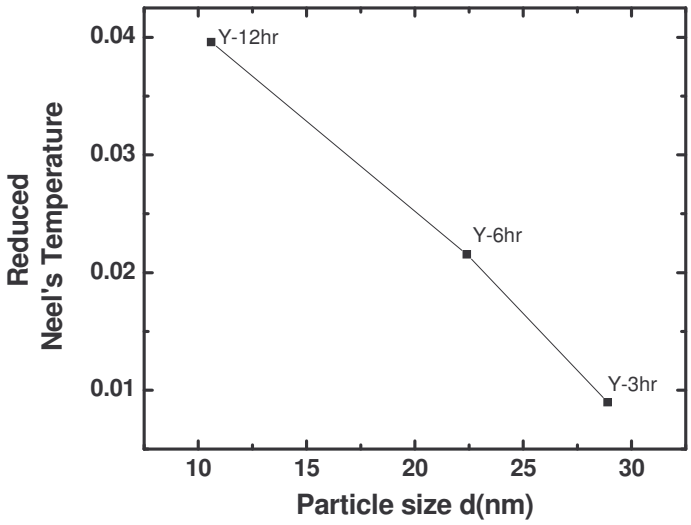

Fig.7b.2.2 Reduced Neel's temperature shift versus particle diameter

The straight line in figure 7b.2.2 is obtained as a result of fitting the experimental data using equation (1). The parameters obtained from the fit were, ς= 0.66±0.03and d_0= 14.845 ± 0.01 Á.

This value ς agrees well with those predicted by the isotropic three-dimensional Heisenberg model [23] which are in the range from ς=0.65±0.07 to 0.733±0.02. The value of d_0 is of the order of the lattice constant of YIG and

hence fulfills its identification as a microscopic length scale. Thus, we conclude finite size scaling describes the shift in T_N well.

7b.3 High field magnetization studies on mechanically milled $Y_3Fe_5O_{12}$ (YIG)

Figure 7b.3.1 shows magnetization hysteresis curves measured at 20 K for un-milled and 9hrs milled sample of $Y_3Fe_5O_{12}$.

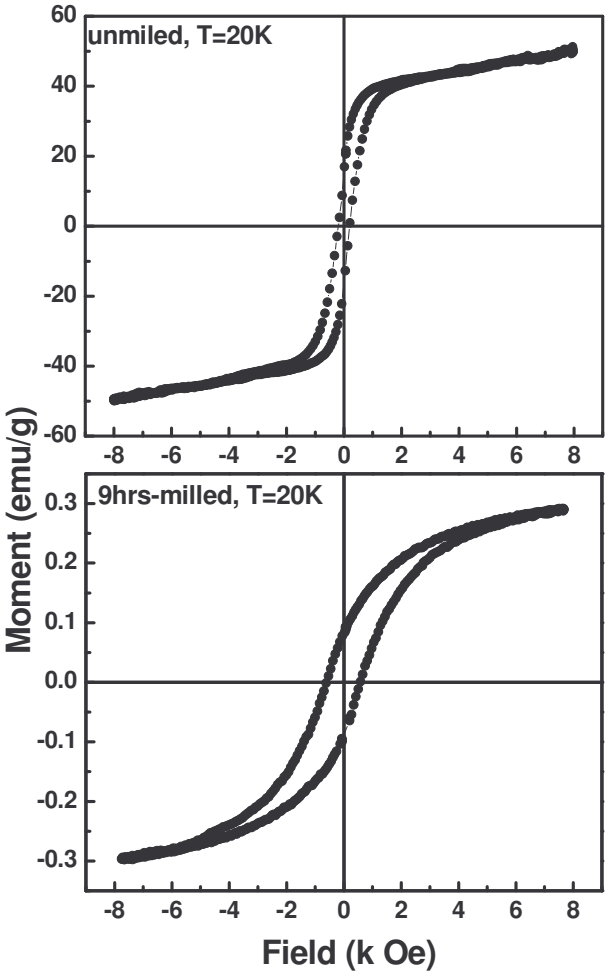

Fig. 7b.3.1 Magnetization hysterisis curves measured at 20K for unmilled and 9hrs milled samples of $Y_3Fe_5O_{12}$

The saturation magnetization (σ_s) is found to decrease from 40 emu/g for unmilled sample to 0.3 emu/g for 9hrs milled sample while coercivity is found to increase from 189 Oe for unmilled sample to 590 Oe for 9hrs milled samples. According to Greneche et al [24], the single domain size for the YIG

is 300 nm and it is found that for the 200 nm particles coercivity is maximum. Since the grain size of the 9hrs milled sample (13.3 nm) is below the single domain size the coercivity is expected to decrease with grain size reduction. In contrary to expectation we have observed 3 times increase in coercivity value for 9hrs milled sample when compared with coercivity value for unmilled sample. The observed increase in coercivity at 20K for 9hrs milled sample may be due to the increase in the surface anisotropy for smaller particles [25].Moreover, the observed increase in H_c for 9hrs milled sample, may also be due to presence of magnetically hard secondary phase of $YFeO_3$ in the sample. It has been reported that for Yttrium orthoferrite at 250 K, H_c=24.6 kOe.

The σ_s value is found to reduce by more than two order of magnitude for 9hrs milled sample. The much lower value of σ_s could be ascribed to one or more of the following reasons.

(i) Upon milling, the decomposition process accelerated so that the fraction of iron ions converted into the antiferromagnetic $YFeO_3$ which has very low saturation magnetization (1.23 emu/g) therefore the total saturation magnetization of the milled sample decreases with milling. The observed σ_s value (0.3 emu/g) for 9hrs milled sample is much lower than the σ_s value for $YFeO_3$. This suggests that beside formation of $YFeO_3$ other factors also contribute in lowering the σ_s value.

(ii) The second one is due to very small size of ferrite particles and defects and strain in the sample induced by ballmilling [26].

(iii) The non- saturation of the loop suggests the presence of the canted spin structure in the milled sample. The canted spin structure could arise due to weakening of the superexchange interaction on mechanical milling which causes structural damages and defects. The canted spin structure is linked to the effective anisotropy which increases because of the lattice strains introduced on milling [JMMM].

(iv) The surface structure disorder also contributes to the spin canting [Goya et al].

Figure 7b.3.2 shows the thermal variation of magnetization for 9hrs milled sample of YIG obtained with an applied field of 200 Oe after zero field cooling (ZFC) from 273 K to 20 K. The ZFC curve indicates that the milled sample exhibits a crystalline size distribution.

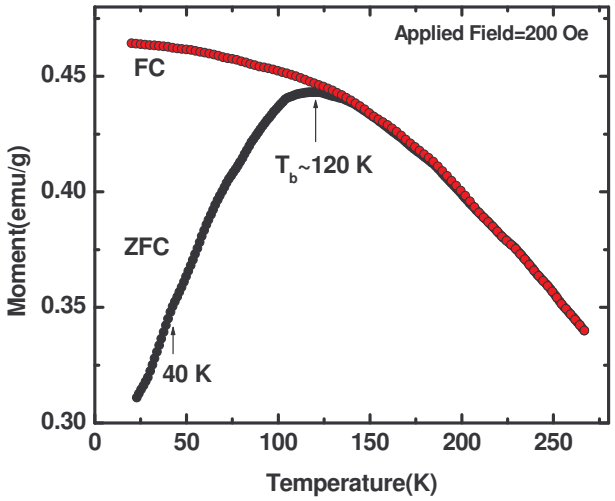

Fig. 7b.3.2 FC-ZFC curves for 9hrs milled sample

In an assembly of crystallites with different grain sizes, the variation of magnetization with temperature arising from contributions of both

ferrimagnetic and super-paramagnetic phases in the milled sample of YIG. The presence of ferrimagnetic phase given a decrease of magnetization with increasing temperature. Above 20 K, the increase with temperature of ZFC curve can be described to the presence of super-paramagnetic crystallites, which should give a maximum in the ZFC curve [27]. We have observed broad maximum in the temperature range between 100 and 130 K, indicating the blocking of most of the larger crystallites. The ZFC curve shows a shoulder (T~40 K), indicating the blocking of most of the smaller crystallites. As shown in the Figure 7b.3.2, the region of irreversibility disappears for T>140 K. Thus, the behaviour of the ZFC sample can be explained by the co-existence of both ferrimagnetic and super-paramagnetic phases. The contribution of the super-paramagnetic phase consists of two parts with different blocking temperatures due to crystallite sizes.

References

1. P.Coppens and M. Eibsschutz, Acta. Cryst. 19(1965)524.
2. Pushan Ayyub, V.R. Palker, Soma Chattopadhyay and Manu Multani, Phys. Rev. B 51(9)(1995)6135.
3. S. S. D. Shenoy , P. A. Joy and M.R. Anantharaman, J. Magn, Magn. Mater. 269(2004)217.
4. T. sato, IEEE, Trans. Magn. Magn. 6(1970)795.
5. E. Ryshkewitch, Oxide Ceramics, Physical Chemistry and Technology (NY:Academic Press)1960.
6. A.M. Hofmeister and K.R. Campbell , J.Appl. Phys. 72(12)(1992)638.
7. Sanjay Mathur et al , Chem. Mater. 16(2004)1906.
8. S. Venugopalan, Mitra Dutta, A.R. Ramdas and J. P. Remeika, Phys. Rev. B. 31 (3)(1985)1490.
9. G.V. SubbRao , C.N.R. Rao and J.R. Ferraro Applied Spect. 24 (4)(1970)436.
10. J. Fedorove et al , Phys. Rev. B. 60(17)(1991)11875.
11. N. Sivakumar, A. Narayansamy and N. Ponpandian, J. Appl. Phys. 101(2007) 084116.
12. C. Upadhyay, Ph.D thesis, IIT-Kanpur (2003)p.40.
13. R. Bauminger, S.G. Cohen, A. Manov and S. Ofer, Phys. Rev. 122 (1961)743.
14. Sung Ho Lee et al, Solid State Commun, 83(2)(1992)97.
15. Y.B. Lee, K.P. Chae and S.H. Lee J. phys. Chem. Solids 62(2001)1335.

16. P.U. Sharma, K.B. Modi, V. K. Lakhani, K. B. Zankat and H.H. Joshi, Ceram. Int. 33(2007)1543.
17. J.M. Constantini, J.P. Salvetat and F. Brisard, J. Appl. Phys. 82(10), 15(1997).
18. F. Studer,Ch. Houpert, M. Toulemonde and E. Dartyge, Solid State Chem. 91,238(1991).
19. R.H. Kodama, A. E. Berkowitz, E.J.McNiff Jr. and S. Foner, J. Appl. Phys. 81(1965)524.
20. M. Eibschutz, S. Shtrikman and D. Treves, Phys. Rev. 156(2)(1962) 562.
21. M.N.Barber, in phase transitions and critical phenomena, edited by C. Domb and J. L. Lebwitz(Academic, New York,(1983)Vol.8p.145.
22. J.P.Chen, C.M. Sorensen, K.J. Klabunde, G.C. Hadjipanayis, E. Devlin and A. Kostikas, Phys. Rev. B. 54(13)(1996)9288.
23. S. N. Kaul, J.Magn. Magn. Mater. 53(1985)5.
24. P. Vaqueiro, M.A. Lopez-Quintela, J.Rivas and J.M. Greneche, J.Magn. Mater. 169 (1997)56.
25. R.J. Joseyphus et al, J.Magn. Mater. 296(2006)57.
26. J.S. Jiang, L.Gao, X. L. Yang, J.K. Guo and H.L.Shen, J.Mater. Sci. lett. 18(1999)1781.
27. S.C. Yu, Y.Y. Song, L.F. Kiss and I.J. Vincze, J.Magn. Mater. 203 (1999)316.

7c.1 Thermal Variation of dc resistivity measurement

It is observed from Table (7a.1.1) that the highest observed value of bulk density (ρ) remains less than the X-ray density (ρ_x) of the material. This indicates that even highly pressed and sintered pellets contain pores. Therefore, a correction for pore fraction has to be applied to obtain the crystalline value of electrical conductivity. This has been done using the relation[a]:

$$\sigma_{dc} = \sigma_p \left[1 + f(1 + f^{2/3})^{-1} \right]$$

where σ_{dc} and σ_p are measured and corrected value of dc conductivity and f is pore fraction ($f = 1 - \frac{\rho}{\rho_x}$). Equation seems to hold well for f <0.4. The variation of σ with milling time at different temperature shows random nature (Figure 7c.1.1). The conductivity of ferrite materials is governed or influence by many factors: (i) change in charge carrier concentration (ii) change in cation distribution (iii) change in jump or hopping length (iv) anion or cationic vacancies creates by high temperature sintering or high energy ball milling (v) change in grain size.

The dc electrical conductivity of pellet of each garnet made at pressure (P_r) ≈ 2*107 kg/m^2 and sintered at 1300 ºC for 24 hours have been measured as a function of temperature (300-673K). The conductivity value for a particular garnet does not differ much from sample to sample. Furthermore, for each pellet, no significant difference has been observed in conductivity values during the heating and cooling cycles. The σ_{dc} values for a garnet milled for different duration lies between 10^{-8}-10^{-12} S.cm^{-1} at room temperature, obviously they are good insulators.

The $\sigma_{dc}T$ variation with reciprocal of temperature ($10^3/T$) for all the samples is shown in Figure 7c.1.1.

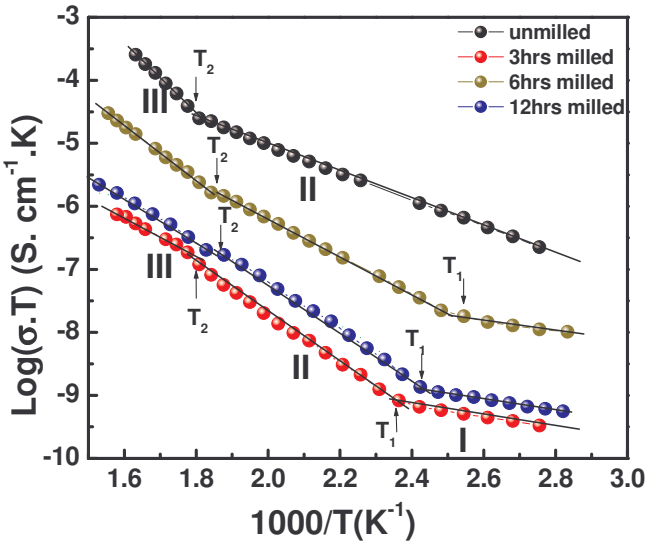

Fig.7c.1.1 ($\sigma_{dc}T$) variation with reciprocal of temperature ($10^3/T$) for all the samples

It is interesting to note that the nature and magnitude of $\sigma_{dc}(T)$ curve for un-milled sample is consistent with reported one [2], but in the present case clear magnetic phase transition has been observed about 555K. This temperature corresponds to magnetic phase transition, observed from thermal variation of ac susceptibility measurement. The nature of curve for the milled samples is different from that for unmilled sample. For the milled samples, we have observed three distinct regions and two breaks, the temperature T1 corresponds to transition from region I to II and temperature T2, from region II to III. The transition temperature T2 is nearly equal to the Neel temperature deduced from low field ac susceptibility measurements. The Neel temperature (T_N) determined is presented in Table, which is in good agreement to those determined from ac susceptibility measurements. We have also observed

another transition i.e change of slope for all the milled samples around 415K. Ghani et al [3] observed three regions in the temperature variation of resistivity for Cu-Ni ferrites. They attributed the conduction mechanism in the first region to the presence of impurities, in the second region to the phase transition and in the third region to the magnetic disorder. Earlier, similar transition has been observed in thermal variation of dc resistivity measurements of double rare- earth orthoferrite system: $La_{1-x}Nd_xFeO_3$ around 393 K [4].

This orthoferrite, $LaFeO_3$, possesses structure similar to that of $YFeO_3$ with Neel temperature, T_N= 738K. This leads to conclude that presence of yttrium orthoferrite phase in all the milled samples may be responsible for observed transition near to 415 K.

It is observed that throughout the temperature range σ_{dc} values for milled specimens are lower than the unmilled sample. The decrease in conductivity or increase in resistivity with grain size reduction may be attributed to the size effect and also due to increase in grain boundary volume and the associated impedance to the flow of charge carriers. If the crystallite size is smaller than the electron mean free path, grain boundary scattering dominates and hence the electrical conductivity as well as the temperature coefficient is expected to decrease.

We have co-related jump length (L) of the charge carriers between Fe^{3+} and Fe^{2+} ions (for n-type conduction) and Fe^{4+} and Fe^{3+} (for p-type conduction) on the respective cationic site to the electrical conductivity. It is well known that jump length or hoping length is directly proportional to the lattice constant (a).It is found that lattice constant increases from 12.377 Á for

unmilled sample to 12.435 Å for 6hrs milled sample. The resultant increase in 'L' with milling time suggests that charge carriers require more energy to jump from one cationic site to other which causes an increase in resistivity or decrease in conductivity for milled samples as compared to unmilled sample. The higher value of conductivity for 6hrs and 12hrs milled samples as compared to 3hrs milled samples may be due to oxygen vacancy conduction [5].Earlier, it has been reported by Goya et al [6] that during high energy ball milling, oxygen ions escape from the spinel structure, thereby creating anion vacancies. On the other hand Popandian et al [7] have reported that the oxygen vacancies created by high energy ball milling, contribute to electrical conductivity. In the present work, therefore, the increase in conductivity for higher milling time (6hrs and 12hrs milled samples) with the reduction in grain size can be attributed to oxygen vacancies created during high energy ball milling.

Table 7c.1.1 Activation energy (E) for unmilled and milled samples of YIG

sample	E_σ(eV)		
	I	II	III
unmilled	-	0.42	1.12
3hrs	0.20	0.57	0.60
6hrs	0.19	0.79	0.87
12hrs	0.19	0.72	0.68

The temperature dependence of the electrical conductivity in figure can be described well by the Arrhenius relation:

$$\sigma_{dc}T = \sigma_0 \exp(-E_\sigma/kT)$$

where σ_0 is the pre-exponential factor, E_σ is activation energy for charge carrier transfer and k is Boltzmann constant ($=8.6*10^{-5}$eV). The activation

energy calculated for different region is as shown in Table 7b.1.1. It is found that for milled samples activation energy in region I remains constant (i.e 0.2 eV), for region II activation energy is in the range 0.6-0.8 eV, while it is varying from 0.6-0.9 eV for region III for different milled samples. From the activation energies calculated and a high jump in conductivity for milled samples, it would appear that the conductivity is basically of mixed type corresponds to mixed phase system [8]. In general, the activation energy for conduction due to electron hopping is of the order of 0.2 eV and the energy needed for holes as the entity of charge carriers is of the order of ~1.5 eV. In the present work, the activation energy values for ferrimagnetic region (region II) are comparable with the small polaron hopping energy (0.5 eV). The anion vacancies are activated at higher activation energy (≈0.93 eV), which is characteristic of diffusion of oxygen vacancies [9]. The observed increase in activation energy value for unmilled, 6hrs milled sample and decrease for 12 hrs milled sample is commensurate with the change in Lattice constant/inter-ionic distances with milling time. The increase in value of 'a' manifests itself as increase in inter-ionic distances and consequently in an increase in the electrical energy barrier height encountered by the hopping charge carriers. The activation energy is, therefore expected to increase with increasing milling time.

Frequency dependent resistivity (ρ_{ac}) study at different temperature

Figure shows frequency dependence of ac resistivity plots at various temperatures.

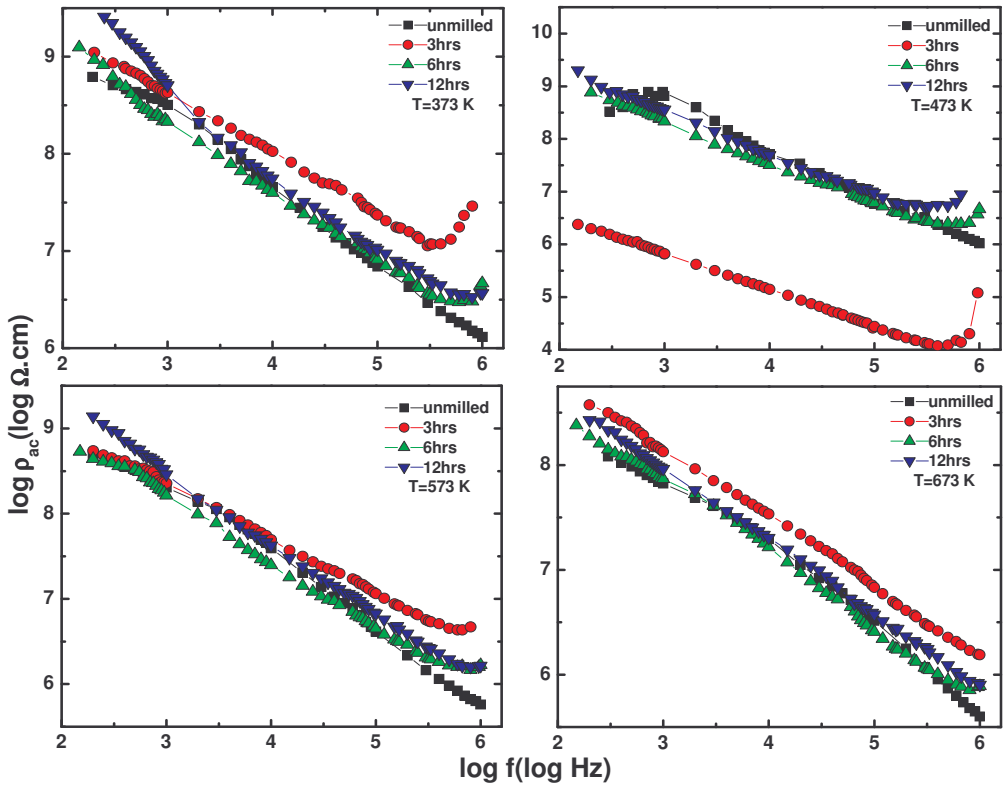

Fig. 7c.1.2 Frequency dependent ac resistivity (ρ_{ac}) at different temperature for unmilled, 3hrs, 6hrs and 12hrs milled sample of YIG

All the samples show decrease in ρ_{ac} with increase in frequency from 100Hz to 1MHz, which is the normal behaviour of ferrites. The conduction mechanism in the ferrites can be explained on the basis of hopping of charge carriers between $Fe^{2+} \leftrightarrow Fe^{3+}$ or $Fe^{3+} \leftrightarrow Fe^{4+}$ ions on respective cationic sites. The increase in frequency of applied field enhances the hopping of charge carriers resulting in an increase in conduction process and thereby decreasing resistivity. It has been observed that ρ_{ac} decreases continuously with increase in frequency with in the temperature range studied. This indicates that grain

boundary effects are not minimized for highly pressed pellets even at high temperatures. Extrapolation of this part towards lower frequency will give ρ_{dc}.

One can made following observations from log ρ_{ac} versus frequency curves recorded at different temperatures for unmilled and milled samples of YIG;

(i) ρ_{ac} increases with increasing frequency for 3hrs milled sample beyond frequency f ≥ 300 k Hz (T=300-573K).

(ii) On increasing milling time and temperature of measurement, rise in ρ_{ac} decreases.

(iii) With increase in measuring temperature, the value of frequency, from which ρ_{ac} starts to increase, increases.

Earlier, we have observed similar increase in ρ_{ac} with frequency for Y^{3+}-substituted YIG system (Figure 6c.2.1). In present case for unmilled sample no such rise in ρ_{ac} value has been observed, this may be due to limiting frequency range (upto 1 MHz) employed for the present investigation. In former the frequency range covered was upto 13 MHz.

As discussed earlier, on increasing temperature and in the present case on increasing milling time number of large polarons decreases and that of small polaron increases. Finally the large polarons becomes negligible and small polarons become the sole mobile charge carriers and thus at high temperature (T > 573 K) and for higher milling time ρ_{ac} decreases with increase in frequency.

7c.2 Frequency dependent dielectric properties and electric modulus study

The existence of Fe^{3+} ions and the minority Fe^{2+}/Fe^{4+} ions have rendered garnet materials dipolar. Rotational displacements of the dipoles results in orientational polarization. In the case of garnets, the rotation of Fe^{2+}-Fe^{3+} or Fe^{3+}-Fe^{4+} dipoles may be visualized as the exchange of electrons or holes between the ions so that the diploes align themselves with alternating field. The effect of frequency (f) on the real (ε') and imaginary part (ε") part of dielectric permittivity (ε*) and dielectric loss tangent (tan δ=ε"/ε') at different temperatures for samples with different grain sizes are illustrated in Figures 7c.2.1, 7c.2.3 and 7c.2.4. In the literature real (ε') part of dielectric constant has been reported to be 12 at 2 MHz (T=300K) for polycrystalline YIG and 12.5 at 1 MHz of frequency and 300K for single crystalline YIG [10, 11].

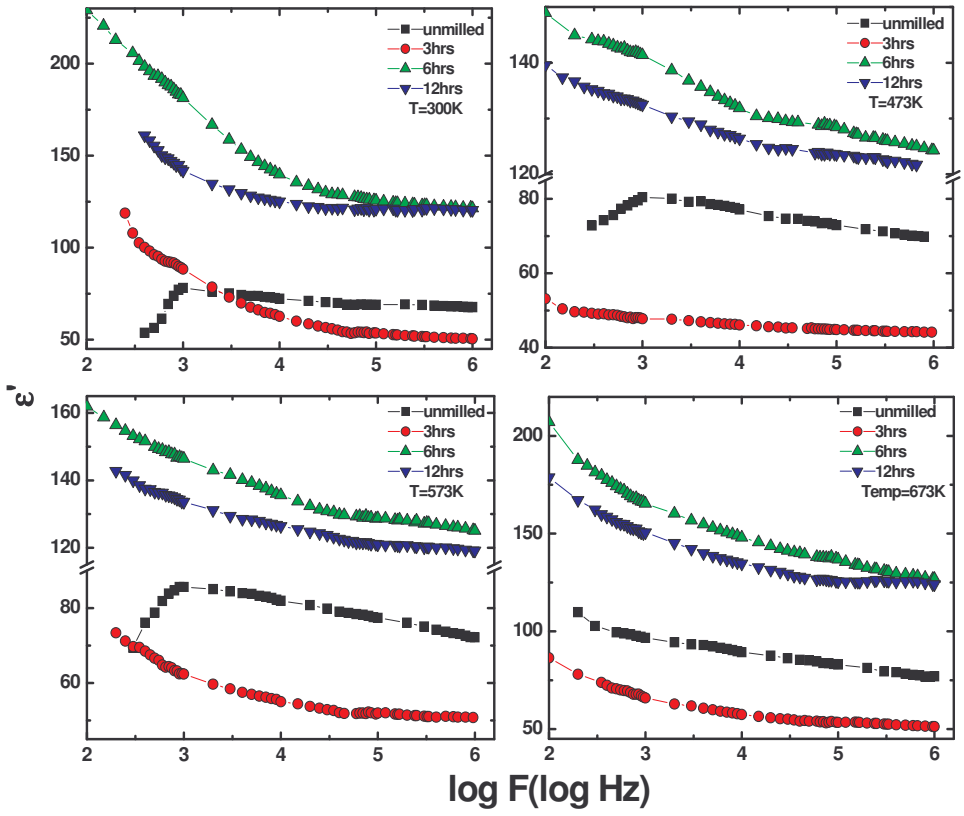

Fig.7c.2.1 Frequency dependence of real part of dielectric constant (ε') of the unmilled and milled samples of the YIG at various temperatures

In our measurements ε' is found to be ~80 at 300K (1MHz), for the bulk YIG, while it is found to be two to three times larger for the nanocrystalline YIG milled for 12 and 6hours respectively. Similarly the dielectric loss is also found to be smaller for the milled samples or found to decrease with reducing grain size.

The ε' shows an anomalous behaviour with frequency at different temperatures (300-573K) for unmilled sample. It initially increases with frequency, reaches a maximum and then decreases with further increase in frequency. In case of normal behaviour, the polarization or dielectric constant will monotonically decreases with frequency as in the case of samples milled for 3,6 and 12 hours. This happens as the electron or hole exchange between $Fe^{2+} \leftrightarrow Fe^{3+}$ or $Fe^{3+} \leftrightarrow Fe^{4+}$ can not follow the alternating field beyond a certain frequency.

The abnormal dielectric behaviour of garnets is due to the collective contribution of the two types of carriers, p- and n-type to the polarization. However, the contribution of the p-type carriers should be smaller than that from the electron exchange between $Fe^{2+} \leftrightarrow Fe^{3+}$ and also has an opposite sign. In addition, since the mobility of p-type carriers is lower than that of n-type carriers, their contribution to polarization will decease more rapidly. By summing up the contribution to both the types of carriers to the polarization, one can expect the behaviour of the dielectric constant as a function of frequency as shown in Figure 7c.2.2.

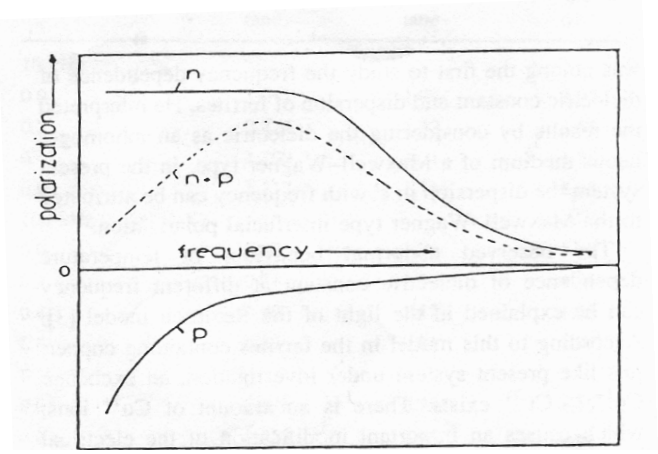

Fig. 7c.2.2 Typical behaviour of frequency dependent polarization for n-p-type of charge carriers

The decrease (for 3hrs milled sample) or increase (for 6 and 12hrs milled samples) in the value of ε' with grain size reduction can be explained on the basis of decrease or increase in the number of $Fe^{2+} \leftrightarrow Fe^{3+}$ or $Fe^{3+} \leftrightarrow Fe^{4+}$ pairs in the material on mechanical milling.

The frequency dependence of the dielectric constant ε' of milled samples of YIG at various temperatures is shown in Figure 7c.2.1. The variation of the dielectric permittivity for free dipoles oscillating in an alternating field may be described as follows. At very low frequencies ($\omega=1/\tau$, τ= relaxation time) dipoles follow the alternating field and ε' is equal to the value of dielectric constant at quasistatic fields (i.e $\varepsilon' = \varepsilon_s$). As the frequency increases with $\omega<1/\tau$, dipoles cannot follow the field or lag behind the field, hence ε' slightly decreases. When frequency reaches the characteristic frequency ($\omega=1/\tau$), the dielectric constant drops and at very high frequencies ($\omega>>1/\tau$) dipoles can no longer follow the field and $\varepsilon' \approx \varepsilon_\infty$. This nature has been observed qualitatively in Figure7c.2.1 for all the milled samples.

Figures 7c.2.3 and 7c.2.4 show frequency dependent variation of imaginary part of dielectric constant (ε'') and loss tangent (tanδ) respectively for unmilled and milled samples of the YIG at various temperatures.

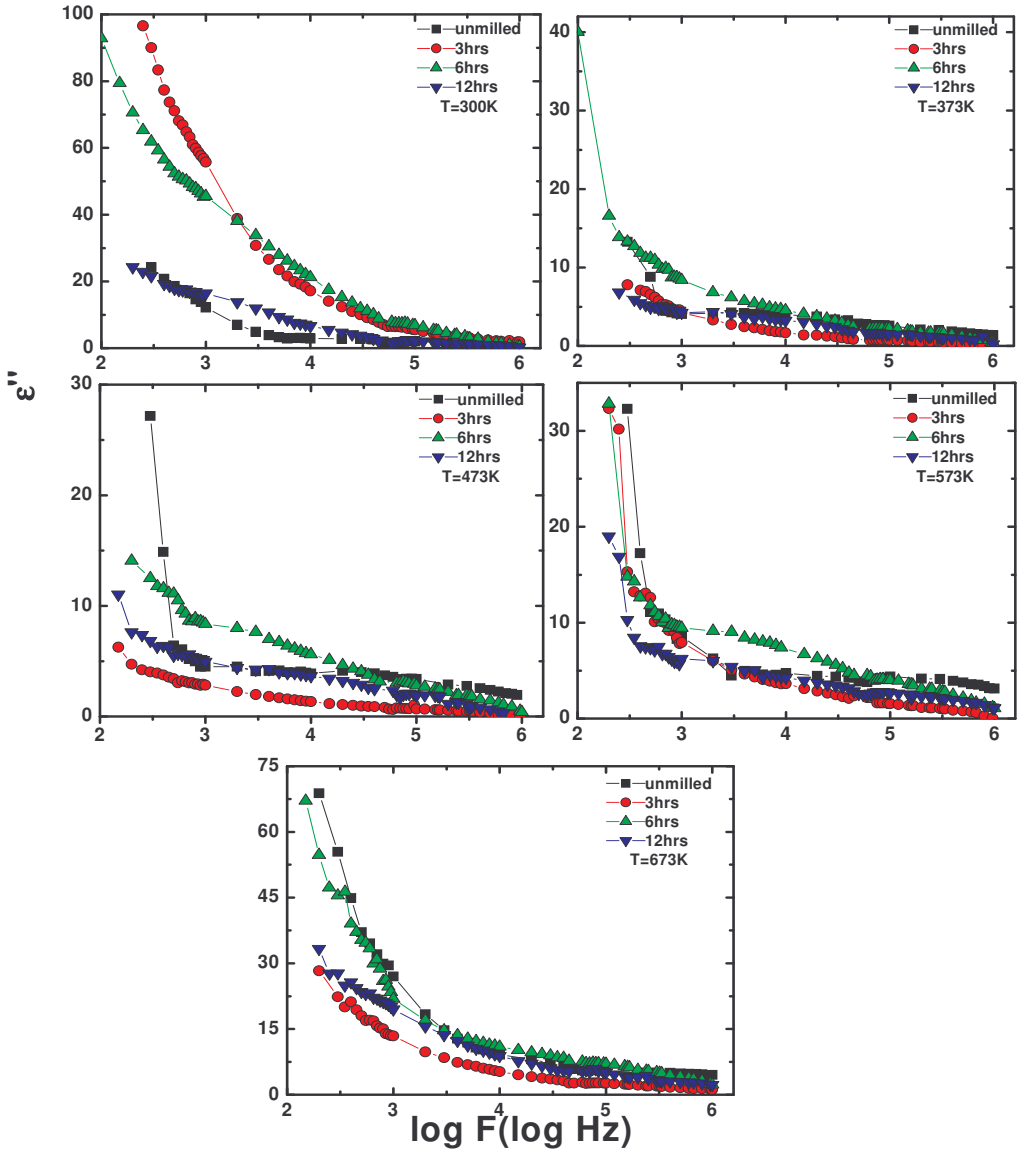

Fig. 7c.2.3 Variation in imaginary part of dielectric constant (ε'') with frequency for unmilled and milled samples at different temperatures

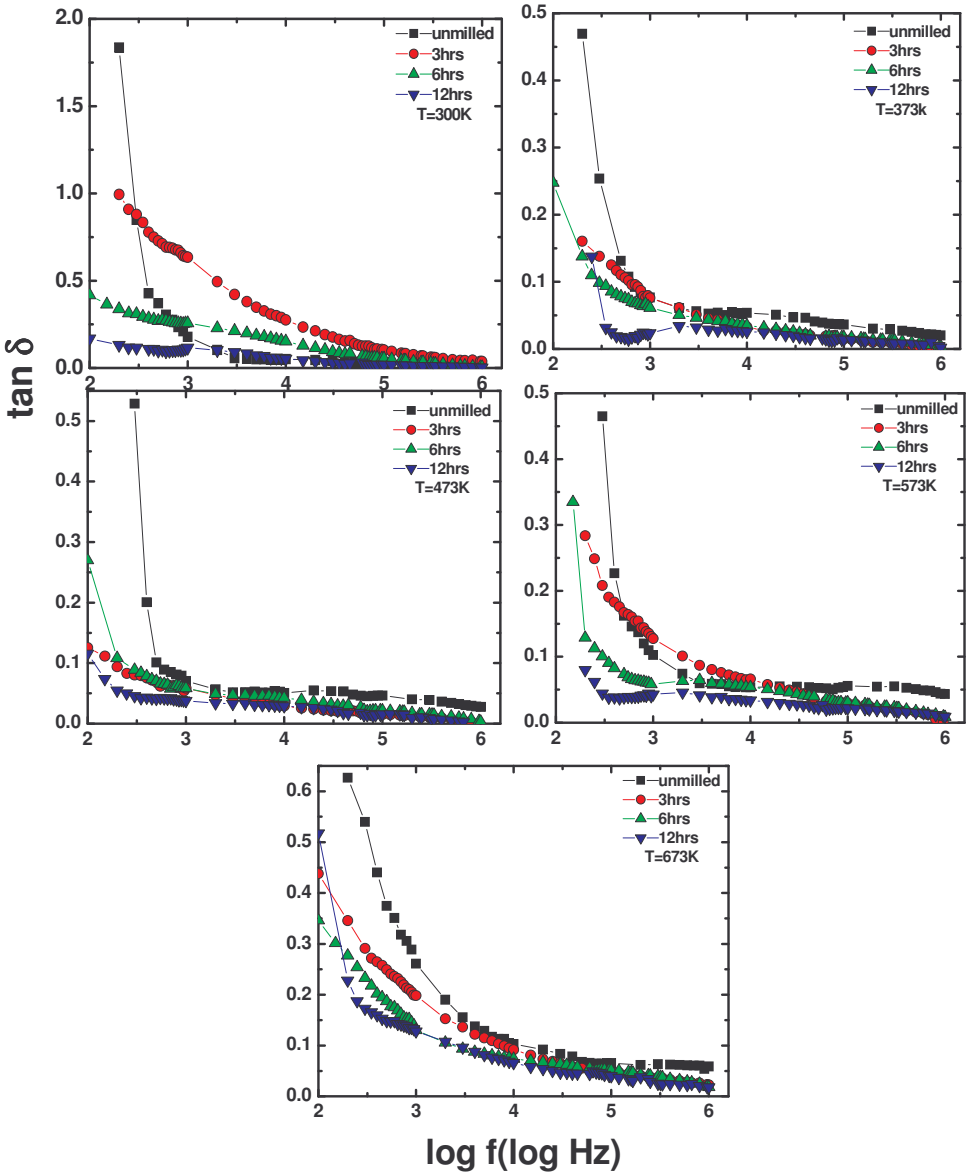

Fig. 7c.2.4 Frequency dependence of dielectric loss (tanδ) for unmilled and milled compositions of YIG at different temperatures

The dielectric loss is rather high at low frequency but falls quickly with rising frequency. The lower values of tanδ for milled samples at different frequency and temperature as compared to unmilled sample are due to higher resistivity values of milled samples as compared to unmilled sample.

Electric Modulus

The variation of real part of electric modulus M' as a function of frequency over a range of temperature is given in Figure 7c.2.5.

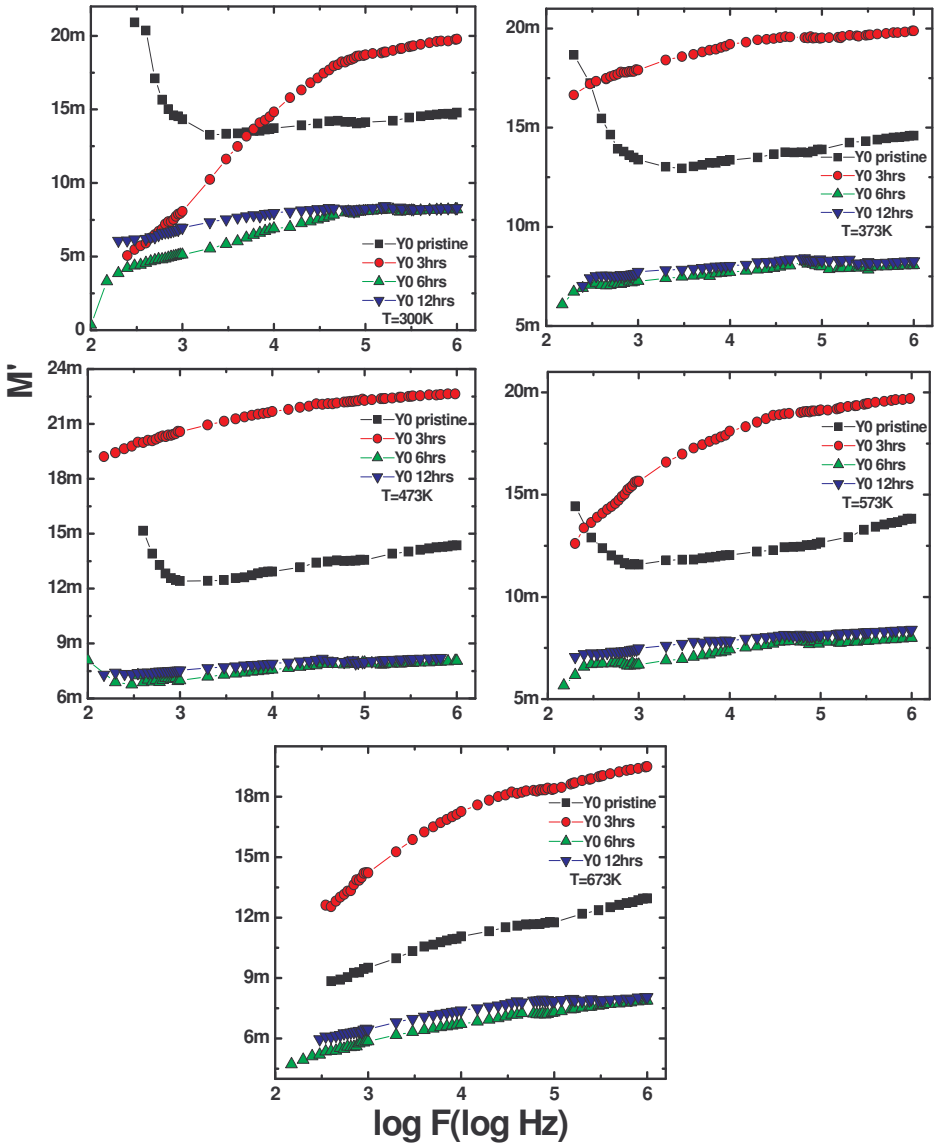

Fig.7c.2.5 Variation of real part of electric modulus M' as a function of frequency over a range of temperature

The value of M' is low in the low frequency region, as frequency increases the value of M' increases and reaches a maximum constant value of $M_\infty=1/\varepsilon_\infty$ at higher frequencies, for all temperatures. These observations

may possibly be related to a lack of restoring force governing the mobility of change carriers under the action of an induced electric field. This type of behaviour supports the conduction phenomenon due to long-range mobility of charge carriers. Further, an increase in the value of M' with increasing frequency approaching ultimately to a value M_∞ for all temperatures has been observed that support the conduction phenomenon due to short range mobility of charge carriers [12, 14].

Here, it is important to note that for 6 and 12hours milled samples variation of M' is almost independent of frequency and temperature, suggests short range mobility of charge carriers is dominant.

M'', imaginary part of electric modulus, versus log (f) at different temperature is given in Figure 7c.2.6.

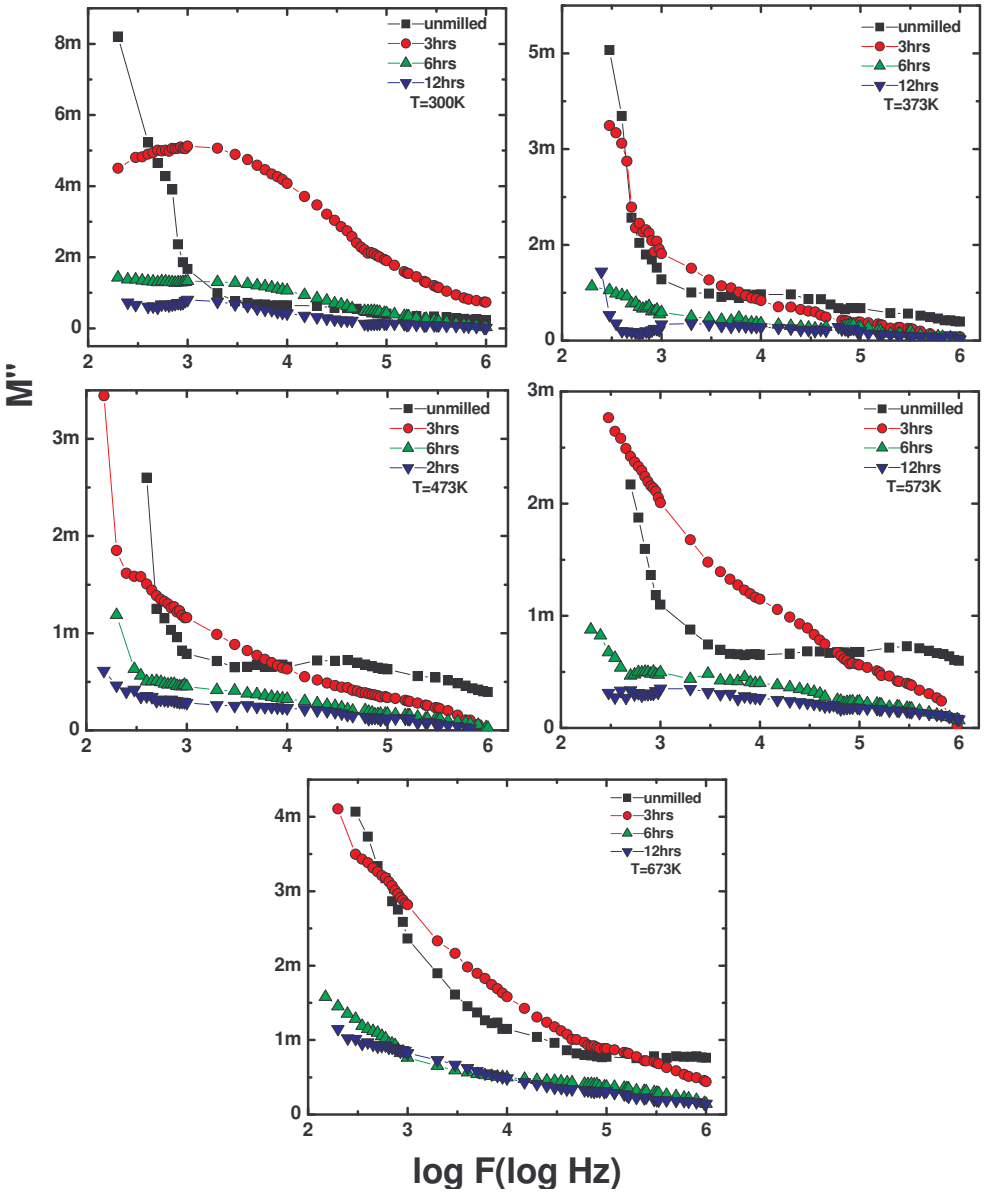

Fig. 7c.2.6 Variation of imaginary part of electric modulus M'' as a function of frequency over a range of temperature

The M''(f) curves for all the samples, except for 300K temperature show only high frequency side of the typical bell shaped M''→ f curve observed for majority of oxide compounds [15-18]. The high frequency side

represents the range of frequencies in which the charge carriers are spatially confined to their potential wells and the charge carriers can make localized motion with the well [13].

Figure 7c.2.7 displays the frequency dependence of imaginary part of electric modulus (M'') at 300K for milled samples. The stretched exponent parameter, β, has been calculated considering full width half maxima of M''(f) curve.

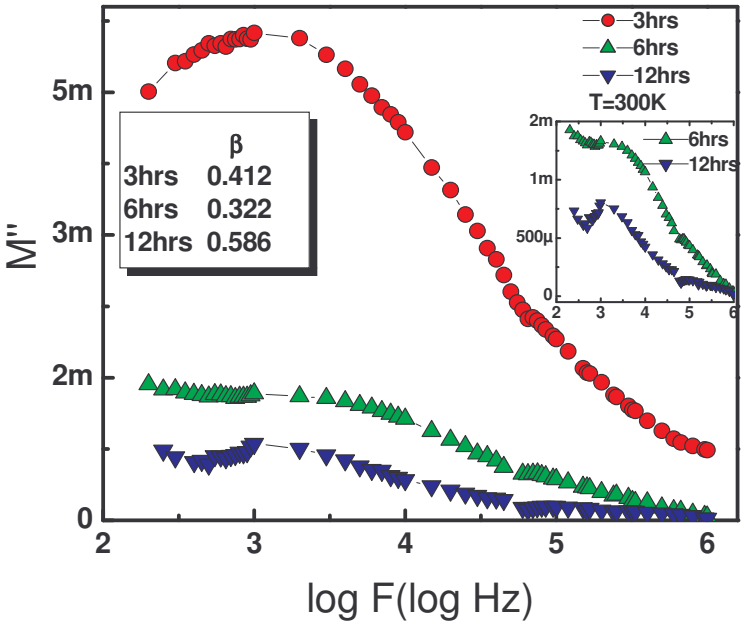

Fig.7c.2.7 Frequency dependence of imaginary part of electric modulus (M'') at 300K for milled samples

It is known that for ideal dielectric material where dipole-dipole interactions are negligible, the value of β is equal to 1, but the systems where dipole- dipole interactions are significant, the β value is always less than 1. In the present case it is found that β is 0.412 and 0.322 for 3hrs and 6hrs milled samples respectively. This is due to the fact that with increasing milling time due to grain size reduction, the grain boundary volume and the number of dipoles increase. Thus the interaction between the dipoles in the grain

boundary increases which results in slowing down the relaxation rate. It is found that for 12hrs milled sample β=0.586, this suggests that the dipoles take part in the dielectric relaxation process have narrow distribution of relaxation times may be due to homogeneous grain size and microstructure.

Figure 7c.2.8 shows the complex modulus spectra (M''(f)→M'(f)) of the unmilled and milled samples of YIG at different temperatures.

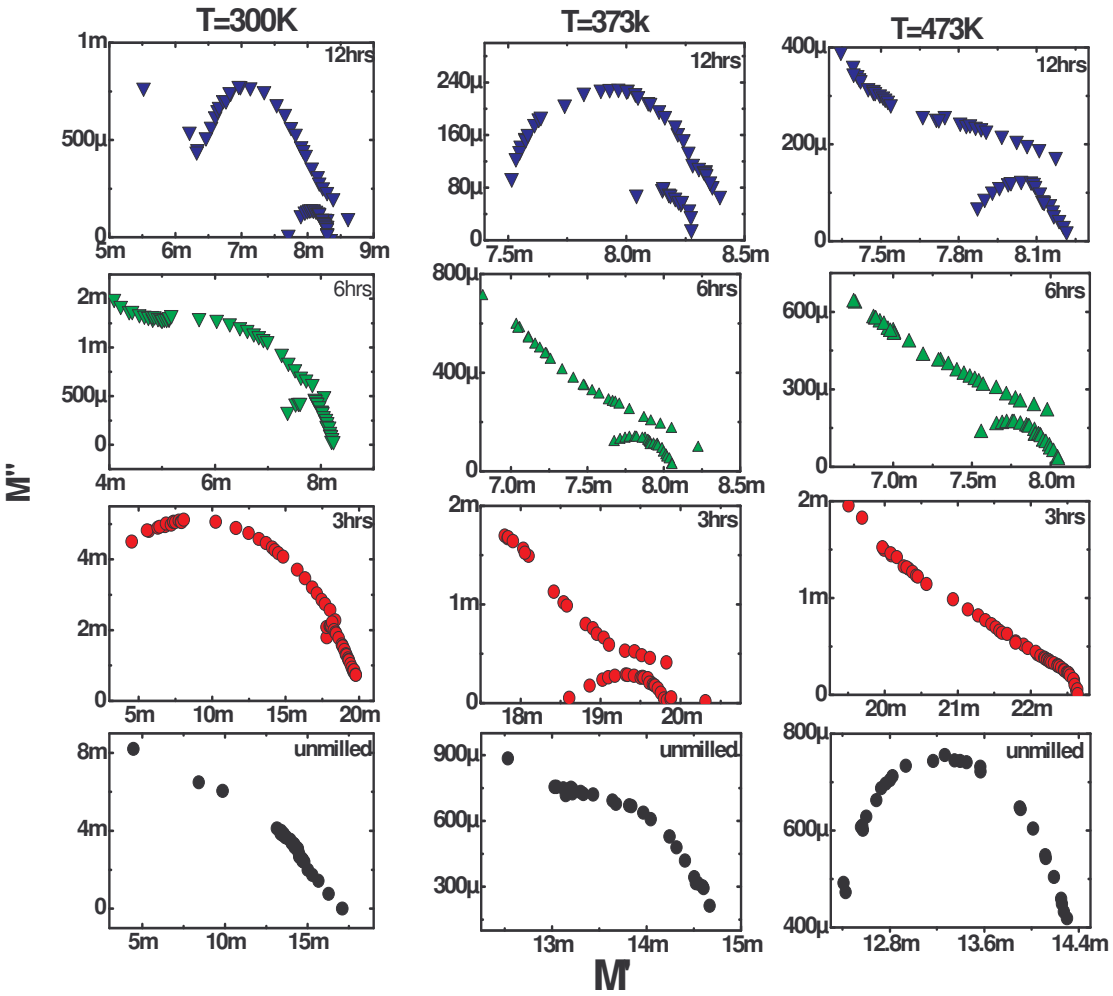

Fig.7c.2.8 Complex modulus spectra (M''(f)→M'(f)) of the unmilled and milled samples of YIG at different temperatures

These patterns indicate the presence of a single semicircular arc for unmilled sample while two semicircular arcs for all the milled samples that confirm the single phase character of unmilled sample and mixed phase

character for all the milled samples [8]. This is in good agreement with the observations made from X-ray diffraction pattern analysis.

References

1. H.W. Russel, J. Am. Ceram. Soc. 18 (1935)1.
2. K.J. Standly, Oxide Magnetic Materials, Clarendo press, Oxford, (1972).
3. A.A. Ghani, A.I. Eatah and A.A. Mohmad, Int. conf. on ferrites-3(Japan)(1980)216.
4. Osama Mohammed Hemeda, M. M. Barkao and D.M. Hemeda, Turk. J. Phys. 27 (2003)537.
5. N. Sivakumar, A. Narayanasamy, N. Ponpandian, J.M. Greneche, K. Shinda, B. Jeyadevan and K. Tohji, J. Phys. D. Appl. Phys. 39(2006)4688.
6. G.F. Goya and H.R. Rechenberg, J. Magn. Magn. Mater. 203(1999)141.
7. N. Popandian and A. Narayanasamy, J. Appl. Phys. 92 (2002)2770.
8. Mukul Pastor, J. Alloys Comps. 463(1-2)(2008)323.
9. A. Narayanasamy and N. Sivakumar Bull. Mater. 31(3)(2008)373.
10. L. Sirdeshmukh, K.K. Kumar, S. B. Laxman, A.R. Krishna and G. Sathaiah, Bull. Mater. Sci. 21(3)(1998)219
11. E.E. Anderson, J. Appl. Phys. Suppl. 30(1959)299
12. Moti Ram and S. Chakrabarti , J. Alloys. Comps. 462(1-2)(2008)204.
13. S. Saha and T.P. Sinha ,Phys. Rev. B 65(1-7)(2005)134103
14. K.P. Padmasrie, D.K. Kanchan and A.R.Kulkarni, Solid State 117 (2006) 475.
15. N.H. Vasoya, V.K.Lakhani, P.U. Sharma, K.B.Modi, Ravi Kumar, and H.H.Joshi, J. Phys. Condens. Matter. 18 (2006)8063.

16. Alo Dutta, T.P. Sinha and S. Shannigrahi, J. Appl. Phys. 104,(2008)064114.
17. Ved Prakash, S.N. Choudhary and T.P. Sinha, Physica B 403 (2008) 103.
18. Ved Prakash, Alo Dutta, S.N. Choudhary and T.P. Sinha, Mat. Sci. Engg. B. 142(2007)98.

Conclusions

The high energy milling induced structural, infrared spectral, magnetic, electrical and dielectric properties modifications in pristine $Y_3Fe_5O_{12}$ compositions have been studied by means of various experimental techniques. The important findings are summarized as:

(a) The unmilled sample possesses single phase bcc structure, on milling $Y_3Fe_5O_{12}$ decomposes into $Y_3Fe_5O_{12}$ and $YFeO_3$ phases. The lattice constant value for garnet phase is found to change while that of orthoferrite phase they remain unaffected with milling. The average grain size is found to decrease while average lattice strain, surface area and surface free energy are found to increase with milling duration.

(b) The milled samples of $Y_3Fe_5O_{12}$ show two characteristic absorption bands: high frequency absorption band is due to combine effect of asymmetric stretching vibrations of the tetrahedron of the YIG-phase and the motion of the in-plane oxygen atoms of $YFeO_3$-phase while low frequency absorption band involves bending motion of the tetrahedron of YIG phase and the apical oxygen vibrations of $YFeO_3$.

(c) SEM and TEM image analysis reveal considerable changes in grain size, shape and size distribution with milling hours.

(d) ^{57}Fe Mössbauer spectral analysis shows presence of paramagnetic singlet/doublet for milled samples due to the distribution in particle size and the super-paramagnetism exhibited by small particles at 300 K. The reduction in the magnitude of the hyperfine fields on

milling is due to the relaxation effects and also because of the surface spins of the small particles. The hyperfine parameters like Isomer shift, Quadrupole splitting/ shifting, linewidth and area ratio show remarkable change with milling.

(e) The temperature dependence of ac susceptibility for milled samples shows two magnetic transitions, one due to ferrimagnetic YIG-phase and other due to weak ferromagnetic $YFeO_3$ phase. The shift in Neel temperature with grain size reduction can be described by finite size scaling.

(f) The dc conductivity for milled specimens are lower than the unmilled sample through but the temperature range studied due to the size effect and increase in grain boundary volume and the associated impedance to the flow of charge carriers.

The low temperature transition observed in $\sigma_{dc}(T)$ curves for milled samples corresponds to yttrium orthoferrite phase while high temperature transition observed for all the samples corresponds to Neel temperature of garnet phase.

(g) The observed rise in ρ_{dc} value at higher frequency is due to presence of large polarons, on increasing temperature and milling time small polarons become the sole mobile charge carriers and ρ_{ac} shows normal behaviour.

(h) The frequency dependence of dielectric parameters (ε', ε'', $\tan\delta$, M', M'') are influenced by mechanical milling or grain size reduction. The presence of $YFeO_3$ phase is not revealed in such dielectric measurement as reflected in magnetic measurements, except M''

versus M’ plots show two semi-circular arc confirm mixed phase character of all the milled samples.